

ISSN 0911-5730

UVSOR-42

July 2015

UVSOR ACTIVITY REPORT 2014

UVSOR Facility
Institute for Molecular Science
National Institutes of Natural Sciences

UVSOR II
since 2012



Preface

This Activity Report covers the research activities carried out at the UVSOR-III Synchrotron Research Facility in FY2014 (April 2014-March 2015). This is the second volume in the blue series for the fourth decade of UVSOR, corresponding to the second year of the use of the UVSOR-III storage ring. The UVSOR-III ring has been a stable diffraction-limit light source in the VUV region in top-up operation with the beam current of 300 mA for more than two years.

The UVSOR-III Synchrotron is one of the most advanced low-energy synchrotron radiation (SR) facilities in the world and belongs to the Institute for Molecular Science (IMS), an inter-university research institute of the National Institutes of Natural Sciences (NINS). The inter-university research institutes are supported by MEXT (the Ministry of Education, Culture, Sports, Science and Technology in Japan) to provide opportunities for academic researchers to engage together in activities aimed at exploring future sciences and to utilize large-scale facilities such as SR facilities. They also serve as an international core base to promote cooperation and exchange with overseas research institutes and researchers.

The UVSOR-III Synchrotron has an electron storage ring of approximately 50 m-circumference and roughly a dozen experimental stations on 6 undulator beamlines (3 VUV and 3 in-vacuum soft X-ray undulators) and 8 dipole beamlines. The UVSOR-I ring emitted the first light in 1983, when there were not so many SR facilities in the world and the UVSOR-I Synchrotron had to construct too many branch experimental stations for increasing different kinds of users and experiments in the IR/FIR, VUV, and soft X-ray regions in Japan. Now molecular science based on chemistry is growing up as an interdisciplinary science covering not only chemical and physical sciences but also biosciences and not only molecular scale but also nano and meso scale. Since there are now 8 SR facilities in Japan, UVSOR-III can afford to focus on unique applications in advanced molecular science based on chemistry, through continuous upgrade of the light source and beamlines, as already done from UVSOR-I to UVSOR-II in 2003 and from UVSOR-II to UVSOR-III in 2012.



Professor Masahiro Katoh in Accelerator Physics Division led the UVSOR-III upgrade project to success as 6th Director of UVSOR. I appreciate his great efforts during the directorship from June 2010 to March 2014.

I have to report here two sad news. In March 2014 after we celebrated the 30th anniversary of the first light of the UVSOR-I ring in December 2013, we lost Prof. Emeritus Hiroo Inokuchi, not only one of the key founders and 3rd Director General of IMS, but also the founder and 1st Director of UVSOR. The UVSOR-III Synchrotron is in the direction of Prof. Inokuchi's idea of more than 30 years ago of making UVSOR a unique chemical machine in the world. In November 2014, we lost Mr. Kusuo Sakai who was heading the UVSOR engineer group from the very beginning and then the whole IMS Technical Division before his retirement of March 2003. I would like to express our deepest thanks and sympathies to them.

One of the missions of IMS is to cultivate younger professors and then send them to universities and research institutes. This mission is applied even to the professors who dedicate to UVSOR. In Accelerator Physics Division, Assistant Professor Taro Konomi moved to KEK in March 2015. In Photophysics Division, Associate Professor Kiyohisa Tanaka joined from Osaka University in April 2014, Assistant Professor Shinichiro Ideta joined from Tokyo University of Science in April 2015, and Assistant Professor Masaharu Matsunami will be promoted as Associate Professor of Toyota Technological Institute in June 2015.

In Technical Division, in March 2015, Chief Engineer Mr. Toshio Horigome reached the official retirement age, but is still working for UVSOR-III as a specially appointed engineer. In April 2015, Mr. Eiken Nakamura came back to succeed to the Chief Engineer position after three-year leave for Aichi Synchrotron Research Center to make full use of his rich and deep experiences at UVSOR from the very beginning.

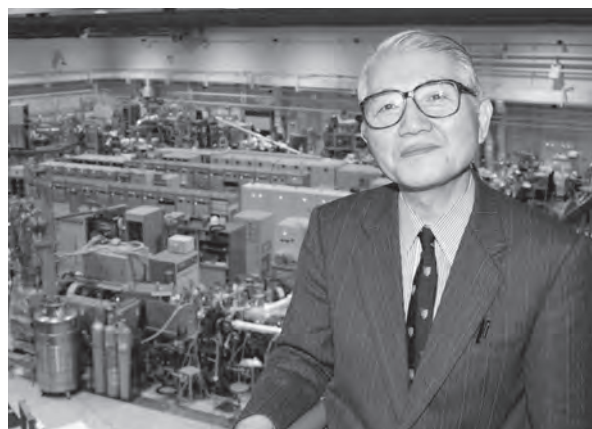
I hope many users will perform excellent work by fully utilizing UVSOR-III Synchrotron as a unique international hub for the SR research in advanced molecular science.

April 2015
Nobuhiro Kosugi
Director of UVSOR-III Synchrotron

Hiroo Inokuchi (1927-2014)

Brief Biography

- | | |
|-------------|---|
| 1927 | Born in Hiroshima, Japan |
| 1950-1959 | Research Associate, Faculty of Science, The University of Tokyo (1955-1957 Ramsay Fellow, The University of Nottingham) |
| 1956 | D.Sc., The University of Tokyo |
| 1959-1960 | Associate Professor, Faculty of Science, The University of Tokyo |
| 1960-1966 | Associate Professor, Institute for Solid State Physics, The University of Tokyo |
| 1967-1975 | Professor, Institute for Solid State Physics, The University of Tokyo |
| 1975-1987 | First Professor of IMS |
| 1983-1987 | First Director of UVSOR, IMS |
| 1987-1993 | Third Director General of IMS |
| 1993-1995 | President, Okazaki National Research Institutes (IMS, NIBB, NIPS) |
| 1995 | Emeritus Professor, IMS |
| 1996-2003 | Chief Scientist, Space Utilization Research Programme, National Space Development Agency of Japan (NASDA) |
| 2001-2014 | Academic Counselor, International Institute for Advanced Studies |
| 2003-2014 | Consultant to the President, Japan Aerospace Exploration Agency |
| 2005-2014 | Distinguished Consultant, IMS |
| 2006-2014 | Chairman, Japan Space Forum |
| 2014. 3. 20 | Passed away at the age of 87. |



Selected Awards and Honors

- | | |
|--------|--|
| 1965 | Japan Academy Prize, The Japan Academy |
| 1978 | The Chemical Society of Japan Award, The Chemical Society of Japan |
| 1989 | Fujihara Award, The Fujihara Foundation of Science |
| 1994 | Person of Cultural Merit, Japan |
| 2001 | Order of Culture, Japan |
| Member | The Japan Academy, The Chinese Academy of Science |

Kusuo Sakai (1944-2014)



Mr. Kusuo Sakai moved from National laboratory for High Energy Physics (KEK) to IMS in 1979.

In 1980, he joined the project of construction of the UVSOR facility and was involved in design of an ultra high vacuum donut tube of the storage ring.

In 1983, he moved to the UVSOR facility and worked for development of beamlines and frontends.

In 1995, he was awarded by the Chemical Society of Japan for his work on “Development of monochromators for molecular scientific researches used for synchrotron radiation”.

Brief Biography

1944	Born in Tokyo, Japan
1963	Worked at Japan Vacuum Engineering Co., Ltd. (now ULVAC, Inc.)
1972	Research Associate, National Laboratory for High Energy Physics
1979	Machine Shop Section Leader, Technical Division, IMS
1983	UVSOR Section Leader, Technical Division, IMS
1995	Head, Technical Division, IMS
2004	Retirement
2014. 11. 14	Passed away at the age of 70.

The 2014 Young Scientist Award of the Japan Society for Molecular Science



Dr. Hiroyuki Yamane, Assistant Professor working in Prof. Kosugi group, won the Young Scientist Award from the Japan Society for Molecular Science for his outstanding achievements on “systematic study on electronic structure of organic thin films and interfaces by means of photoemission spectroscopy with synchrotron radiation”.

2014 Annual Meeting Award of the Particle Accelerator Society of Japan Given to Mr. Toshiki Inagaki

Mr. Toshiki Inagaki received this award for his poster presentation on “Measurement of temporal response of transmission-type spin-polarized photocathodes (II)”. He was from Nagoya University and worked in the accelerator group of UVSOR as a research assistant. He succeeded in measuring the temporal response of the photocathode in the picosecond range. Congratulations!



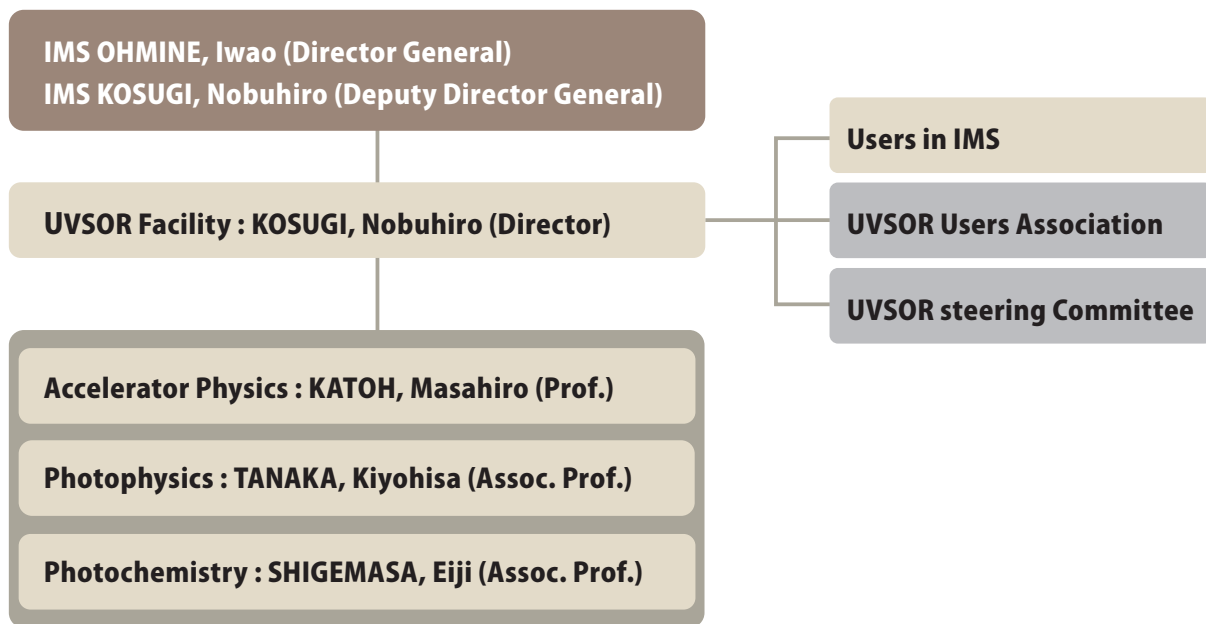
I

Organization and Staff List



UVSOR Organization

April 2015



Staff List

UVSOR Staff

Director

KOSUGI, Nobuhiro	Professor	kosugi@ims.ac.jp
------------------	-----------	------------------

Light Source Division (Accelerator Physics)

KATOH, Masahiro	Professor	mkatoh@ims.ac.jp	
OHIGASHI, Takuji	Assistant Professor	ohigashi@ims.ac.jp	
KONOMI, Taro	Assistant Professor	konomi@ims.ac.jp	(until Mar. 2015)
ITO, Atsushi	Visiting Professor		(until Mar. 2015)
YAMAZAKI, Jun-ichiro	Unit Chief Engineer	yamazaki@ims.ac.jp	
HAYASHI, Kenji	Engineer	h-kenji@ims.ac.jp	
TOKUSHI, Tetsuzyo	Supporting Engineer	tetsuzyo@ims.ac.jp	
INAGAKI, Yuichi	Supporting Engineer	yinagaki@ims.ac.jp	
HAYASHI, Kenichi	Supporting Engineer	khayasi@ims.ac.jp	
MINAKUCHI, Aki	Supporting Engineer	minakuchi@ims.ac.jp	
GUNJI, Yasuhiro	Supporting Engineer		(until Mar. 2015)

Beamline Division (Photophysics)

TANAKA, Kiyohisa	Associate Professor	k-tanaka@ims.ac.jp	
HIRAHARA, Toru	Visiting Associate Professor		(since Apr. 2015)
MATSUNAMI, Masaharu	Assistant Professor	matunami@ims.ac.jp	
IDETA, Shin-ichiro	Assistant Professor	idetas@ims.ac.jp	(since Apr. 2015)
HASUMOTO, Masami	Unit Chief Engineer	hasumoto@ims.ac.jp	
SAKAI, Masahiro	Engineer	sakai@ims.ac.jp	
KOSWATTAGE, Kaveenga Rasika	Visiting Researcher	rasika@ims.ac.jp	
HAJIRI, Tetsuya	Visiting Researcher	hajiri@ims.ac.jp	(until Aug. 2014)

Beamline Division (Photochemistry)

SHIGEMASA, Eiji	Associate Professor	sigemasa@ims.ac.jp	
IWAYAMA, Hiroshi	Assistant Professor	iwayama@ims.ac.jp	
HORIGOME, Toshio	Facility Chief Engineer	horigome@ims.ac.jp	
NAKAMURA, Eiken	Facility Chief Engineer	eiken@ims.ac.jp	(since Apr. 2015)
KONDO, Naonori	Engineer	nkondo@ims.ac.jp	
TESHIMA, Fumitsuna	Engineer	tetsu@ims.ac.jp	

Secretary

HAGIWARA, Hisayo	hagiwara@ims.ac.jp
MASUDA, Michiko	masuda@ims.ac.jp

UVSOR Steering Committee

KOSUGi, Nobuhiro	UVSOR, IMS	Chair	
KATOH, Masahiro	UVSOR, IMS		
SHIGEMASA, Eiji	UVSOR, IMS		
TANAKA, Kiyohisa	UVSOR, IMS		
ITO, Atsushi	Tokai Univ. (Visiting Prof., IMS)		(until Mar. 2015)
YOKOYAMA, Toshihiko	IMS		
KERA, Satoshi	IMS		
AKIYAMA, Shuji	IMS		
FUJI, Takao	IMS		
HARADA, Yoshihisa	Univ. of Tokyo		
NAKAGAWA, Kazumichi	Kobe Univ.		
SODA, Kazuo	Nagoya Univ.		
ADACHI, Shin-ichi	KEK-PF (IMSS)		
DAIMON, Hiroshi	NAIST		
OHASHI, Haruhiko	JASRI		
SASAKI, Shigemi	Hiroshima Univ.		

UVSOR Users Association

HIKOSAKA, Yasumasa	Toyama Univ.
HIRAHARA, Toru	Tokyo Institute of Technology
KIMURA, Shin-ichi	Osaka Univ.
KITaura, Mamoru	Yamagata Univ.
YOSHIDA, Tomoko	Nagoya Univ.

Graduate Students

ITO, Keiya	Nagoya Univ.	(since Nov. 2014)
OODAKE, Daichi	Nagoya Univ.	(since Nov. 2014)
KOUCHI, Shogo	Nagoya Univ.	(since Nov. 2014)
SUGIHAR, Shintarou	Nagoya Univ.	(since Nov. 2014)
INAGAKI, Ryo	Nagoya Univ.	(until Sep. 2014)
INAGAKI, Toshiki	Nagoya Univ.	(until Sep. 2014)
MITAMURA, Masaki	Nagoya Univ.	(until Sep. 2014)
TUIKI, Emiri	Nagoya Univ.	(until Sep. 2014)
OHNO, Yuuki	Osaka Univ.	(until Mar. 2015)

Visiting Scientists

AZIZ, Emad	Freie Universität Berlin	Jun. 2014
ROSENDAHL, Scott	McMaster University	Jun. 2014
PAN-IN, Porntip	Chulalongkorn University	Jun. 2014, Oct. 2014
SHIN, Woo Jong	Pohang University of Science and Technology	Jul. 2014, Jan. 2015
RYU, Sae Hee	Pohang University of Science and Technology	Jul. 2014
WANG, HsiaoTsu	Nation Tsinghua University	Jul. 2014
HSIEH, Shang Hsien	Tamkang University	Jul. 2014, Nov. 2014
KIM, Jimin	Pohang University of Science and Technology	Jul. 2014
KIM, Keun Su	Pohang University of Science and Technology	Jul. 2014, Feb. 2015
ARRUA, Ruben Dario	University of Tasmania	Jul. 2014, Mar. 2015
KYUNG, Wonshik	Yonsei University	Jul. 2014
KIM, Beom Seo	Yonsei University	Jul. 2014, Aug. 2014
SEO, Jungin	Yonsei University	Jul. 2014, Aug. 2014
KWON, Junyoung	Yonsei University	Aug. 2014
CHIOU, Guan Chiun	National Chiao Tung University	Aug. 2014
LIN, Ming Wei	National Synchrotron Radiation Research Center	Aug. 2014, Feb. 2015
LAI, Yu Ling	National Synchrotron Radiation Research Center	Aug. 2014, Feb. 2015
CHO, Soo Hyun	Yonsei University	Aug. 2014, Mar. 2015

PARK, Seung Ryong	Incheon National University	Aug. 2014
ASMARA Teguh Citra	National University of Singapore	Sep. 2014
FLESCH, Roman	Freie Universität Berlin	Sep. 2014
YAMAMOTO, Kenji	Freie Universität Berlin	Sep. 2014
RANCAN, Fiorenza	Charité University Medicine Berlin	Sep. 2014
RÜHL, Eckart	Freie Universität Berlin	Sep. 2014
DIAO, Cazheng	National University of Singapore	Sep. 2014
GOGOI, Pranjal Kumar	National University of Singapore	Sep. 2014
PETIT, Tristan	Helmholz-Zentrum Berlin	Oct. 2014
BIELAWSKI, Serge	University des Sciences et Technologies de Lille	Oct. 2014
SZWAJ, Christophe	University des Sciences et Technologies de Lille	Oct. 2014
WANG, Yu Fu	Tamkang University	Nov. 2014
CHIOU, Jau Wern	National University of Kaohsiung	Nov. 2014
BRANDENBURG, Tim	Helmholz-Zentrum Berlin	Nov. 2014
GOLNAK, Ronny	Helmholz-Zentrum Berlin	Nov. 2014
CHOI, Moo Yeol	Pohang University of Science and Technology	Jan. 2015
KIM, Jeong Kyu	Pohang University of Science and Technology	Jan. 2015
PARK, Min Ju	Pohang University of Science and Technology	Jan. 2015
CHANG, Lo Yueh	National tsing hua university	Feb. 2015
HITCHCOCK, Adam P.	McMaster University	Feb. 2015
SERRANO, Pauline N.	University of California, Davis	Feb. 2015
XI, Lifei	Helmholz-Zentrum Berlin	Mar. 2015
SCHWANKE, Christoph	Helmholz-Zentrum Berlin	Mar. 2015
GEE, Bruce Leland	University of California, Davis	Mar. 2015
YOO, Han Young	Yonsei University	Mar. 2015
HAN, Garan	Yonsei University	Mar. 2015

The background is a vibrant teal color. It features several overlapping circular patterns of varying shades of teal. Some circles have dashed lines or small dots around their perimeters. Diagonal light rays or streaks of a lighter teal color cut across the scene, creating a sense of motion and depth. The overall aesthetic is clean, modern, and technical.

II

Current Status of Light Sources and Beamlines

Light Source in 2014

1. Status of UVSOR Accelerators

In the fiscal year 2014, we operated UVSOR-III from June to February, for 36 weeks for users as usual. We had a shutdown period in April and May for about six weeks. This was for a upgrade program on the beam-line BL5U, which included the remodeling of the undulator U5 to an APPLE-II type polarization variable undulator and the re-construction of the photo-electron spectroscopy beam-line, BL5U.

We operated the machine for 34 weeks in the multi-bunch top-up mode, in which the beam current was kept at 300 mA with the top-up injection, and 2 weeks in the single-bunch mode, in which the machine is operated in single-bunch top-up mode with the beam current of 50 mA. The monthly statistics of the operation time and the integrated beam current are shown in Fig. 1.

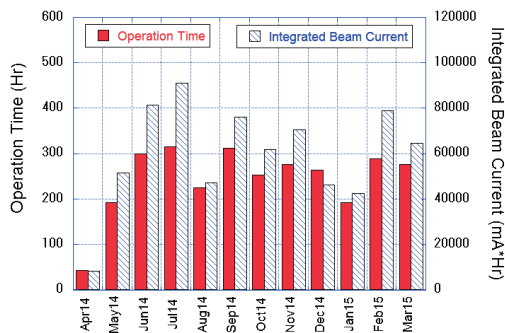


Fig. 1. Monthly statistics in FY2014.

The weekly operation schedule is as follows. On Monday, from 9 am to 9 pm, the machine is operated for machine studies. On Tuesday and Wednesday, from 9 am to 9 pm, the machine is operated for users. From Thursday 9am to Friday 9pm, the machine is operated for 36 hours continuously for users. Thus, the beam time for users in a week is 60 hours. Usually, we have a few weeks dedicated for machine study, however, in the last year, we did not have them to keep the beam time for users against the rather long shutdowns. This year we could have 5 weeks, in the middle of August, in November, just before and after the New Year vacation and the last week in FY2014. The machine study week on November is mainly dedicated for the recovery of the accelerators after the annual planned power outage.

In this fiscal year, we had a few machine troubles on the electron gun, on the RF signal generator and on the water load of the main RF cavity. However, fortunately, in all cases the beam time for users could be secured by extending the operation time in the same week.

More serious trouble happened during the shutdown period in April. During a machine

conditioning run, we observed a sudden vacuum pressure rise at the 3rd harmonic cavity, which is used for stabilizing the beam and extending the beam lifetime routinely. This happening will be described in detail in the next section.

2. Improvements and Developments

Vacuum Pressure Rise in the 3rd harmonic Cavity

In April 2014, we observed pressure rises in the 3rd harmonic RF accelerating cavity during the vacuum conditioning run. We carefully surveyed vacuum leakage on the cavity using a He leakage detector, however we could not find any suspicious part. Then, we checked the water cooling channels with the same detector one by one. Soon, we found some leakage from the water channel for one of the electrode. Since we had only a few weeks before starting the users operation, we tried to repair it using sealant. It was successful after a few trials. Then, we baked the cavity and the neighboring sections. We started the vacuum conditioning run just one week before the start of the users operation. Finally, we could start the users operation as scheduled. After one year operation, the vacuum pressure has been low enough to continue the operation. For the complete repair, we have constructed a new part for the electrode.



Fig. 2. 3rd Harmonic Cavity.

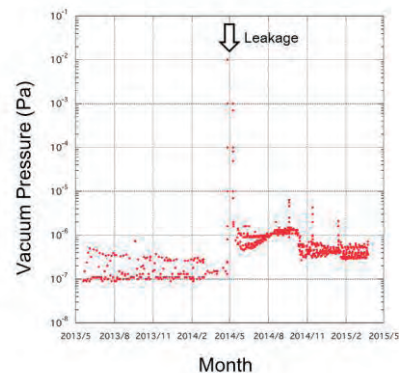


Fig. 3. Pressure History at the 3rd Harmonic Cavity.

Reconstruction of BL5U Polarization Variable Undulator

In March 2014, we remodeled the old variable polarization undulator U5. The magnetic configuration was changed to the APPLE-II one with a shorter period length, 60 mm, as utilizing the present mechanical frame. The field measurement was carried out in the storage ring. The vacuum chamber was also replaced. The new undulator was successfully commissioned and the synchrotron radiation has been being used for conditioning of the new photoelectron spectroscopy beam-line, BL5U.

Beam Injection with Pulse Quadrupole Magnets

A novel injection scheme using a pulsed sextupole magnet has been being developed[1]. Previously the sextupole magnet was installed at one of the kicker magnet by removing it temporally and replacing with the sextupole magnet every time when we carried out the machine study for the device. During the shutdown in April, a new dedicated vacuum duct for the pulsed sextupole magnet was installed just downstream of the undulator U5. With the new location, we have succeeded in injecting the beam with the efficiency of around 20 % during the first trial. We are going to improve the efficiency higher than 50% for users operation. .

Light Source Developments and Beam Physics Studies

We continue the efforts to develop coherent light sources including free electron lasers, coherent harmonic generation and coherent synchrotron radiation at the new source development station BL1U. This year, we have been improving the laser transport system to stabilize the coherent radiation intensity in cooperation with Laser Research Center at IMS and Nagoya University. Also, we are reconstructing the optical cavity for the resonator free electron laser. A gamma-ray production has been being tried in cooperation with Kyoto University for imaging study [2]. An irradiation experiment using

polarized ultraviolet has been being carried out in corporation with Tokyo University of Science.

In the beam physics study, we have succeeded in observing micro-bunching structure in the electron bunches circulating in the UVSOR storage ring during the micro-bunching instability for the first time in the world [3]. The key to the success was a novel ultrafast THz detector developed at Karlsruhe Institute of Technology. The observed results could be explained by a model developed by Lille University.

Electron gun developments towards future quantum beam sources

Electron guns of two types are being developed. One is a spin polarized electron gun. This is being developed towards inverse photo-electron spectroscopy in collaboration with Nagoya University. In FY2014, we have succeeded in measuring the temporal response of the photocathode in the picosecond range [4].

Another electron gun is a superconducting photocathode one towards future high repetition rate free electron laser. At UVSOR, the photocathode part is mainly being developed, in collaboration with KEK. A transparent and superconducting photocathode was successfully demonstrated [5].

References

- [1] N. Yamamoto *et al.*, in these reports
- [2] H. Zen *et al.*, in these reports
- [3] E. Roussel *et al.*, in these reports
- [4] T. Inagaki *et al.*, in these reports
- [5] T. Konomi *et al.*, in these reports

Masahiro KATOH (UVSOR Facility)

UVSOR Accelerator Complex

Injection Linear Accelerator

Energy	15 MeV
Length	2.5 m
Frequency	2856 MHz
Accelerating RF Field	$2\pi/3$ Traveling Wave
Klystron Power	1.8 MW
Energy Spread	~ 1.6 MeV
Repetition Rate	2.6 Hz

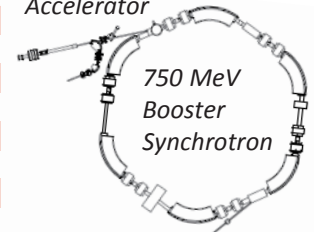
UVSOR-III Storage-Ring

Energy	750 MeV
Injection Energy	750 MeV
Maximum Storage Current	500 mA (multi bunch) 100 mA (single bunch)
Normal operation current (Top-up mode)	300 mA (multi bunch) 50 mA (single bunch)
Natural Emittance	17.5 nm-rad
Circumference	53.2 m
RF Frequency	90.1 MHz
Harmonic Number	16
Bending Radius	2.2 m
Lattice	Extended DBA $\times 4$
Straight Section	$(4 \text{ m} \times 4) + (1.5 \text{ m} \times 4)$
RF Voltage	120 kV
Betatron Tune	
Horizontal	3.75
Vertical	3.20
Momentum Compaction	0.030
Natural Chromaticity	
Horizontal	-8.1
Vertical	-7.3
Energy Spread	5.26×10^{-4}
Coupling Ratio	1%
Natural Bunch Length	128 ps

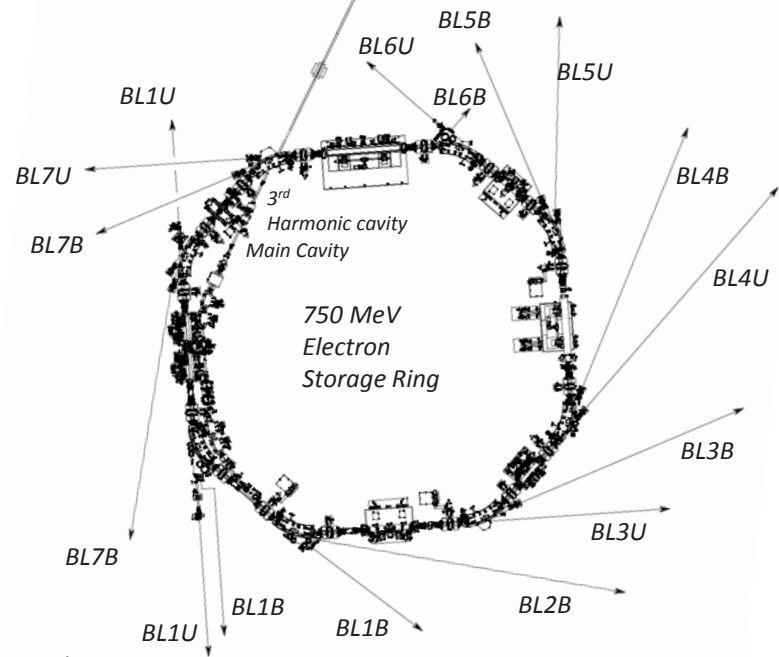
Booster Synchrotron

Energy	750 MeV
Injection	15 MeV
Frequency	32 mA (uniform filling)
Circumference	26.6 m
RF Frequency	90.1 MHz
Harmonic Number	8
Bending Radius	1.8m
Lattice	FODO $\times 8$
Betatron Tune	
Horizontal	2.25
Vertical	1.25
Momentum Compaction	0.138
Repetition Rate	1 Hz (750 MeV)

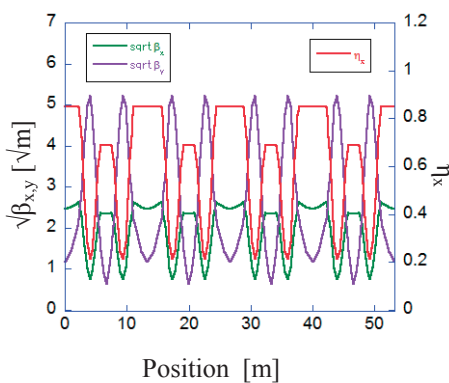
15 MeV
Linear
Accelerator



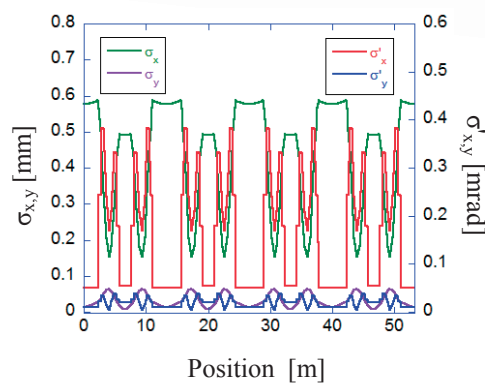
II



Electron Beam Optics of UVSOR-III Storage Ring

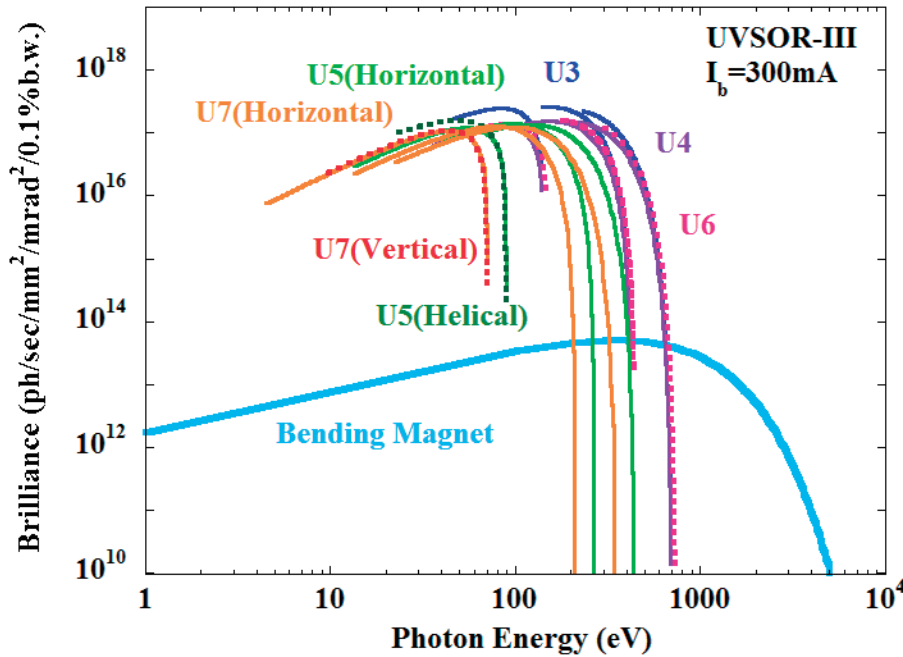


Horizontal/vertical betatron functions and dispersion function



Horizontal/vertical electron beam size and beam divergences

Insertion Device



Brilliance of radiation from the insertion devices (U3, U4, U5, U6 and U7) and a bending magnet of UVSOR-III

U1 Apple-II Undulator /

Optical Klystron

Number of Periods	10+10
Period length	88 mm
Pole Length	0.968 m + 0.968 m
Pole Gap	24-200 mm
Deflection Parameter	7.36 (Max. Horizontal) 4.93 (Max. Vertical) 4.06 (Max. Helical)

U3 In-vacuum Undulator

Number of Periods	50
Period length	38 mm
Pole Length	1.9 m
Pole Gap	15-40 mm
Deflection Parameter	2.0-0.24

U4 In-vacuum Undulator

Number of Periods	26
Period length	38 mm
Pole Length	0.99 m
Pole Gap	13-40 mm
Deflection Parameter	2.4-0.19

U5 Apple-II

Variable Polarization Undulator

Number of Periods	38
Period length	60 mm
Pole Length	2.28 m
Pole Gap	24-190 mm
Deflection Parameter	3.4 (Max. Horizontal) 2.1 (Max. Vertical) 1.8 (Max. Helical)

U6 In-vacuum Undulator

Number of Periods	26
Period length	36 mm
Pole Length	0.94 m
Pole Gap	13-40 mm
Deflection Parameter	1.78 - 0.19

U7 Apple-II

Variable Polarization Undulator

Number of Periods	40
Period length	76 mm
Pole Length	3.04 m
Pole Gap	24-200 mm
Deflection Parameter	5.4 (Max. Horizontal) 3.6 (Max. Vertical) 3.0 (Max. Helical)

Bending Magnets

Bending Radius	2.2 m
Critical Energy	425 eV

Beamlines in 2014

Eiji SHIGEMASA

UVSOR Facility, Institute for Molecular Science

Among the synchrotron radiation facilities with electron energies of less than 1 GeV, UVSOR is one of the highest-brilliance light sources in the extreme-ultraviolet region, following the successful completion of the storage ring upgrade project (the UVSOR-III project). The natural emittance of the UVSOR-III storage ring is as low as 17.5 nm-rad.

Eight bending magnets and five insertion devices are available as synchrotron light sources at UVSOR. As of 2014 there are a total of fifteen operational beamlines, which are classified into two categories. Twelve of them are the so-called “Open beamlines”, which are open to scientists from universities and research institutes belonging to the government, public organizations, private enterprises and also those from foreign countries. The remaining three beamlines are the “In-house beamlines”, and are dedicated to the use of research groups within IMS.

There is one soft X-ray station equipped with a double-crystal monochromator, eight extreme ultraviolet and soft X-ray stations with grazing incidence monochromators, three vacuum ultraviolet stations with normal incidence monochromators, two infrared (IR) stations equipped with Fourier-Transform interferometers, and one free electron laser beamline with no monochromator, as shown in the appended table (next page) for all available beamlines at UVSOR in 2014.

BL4U, equipped with a scanning transmission soft X-ray microscope (STXM), which was newly constructed in 2012, has been open to users since June 2013. Many new results have already emerged from this beamline. The performance of BL4U is close to theoretical predictions, except in the photon energy region near the C K-shell ionization threshold (~300 eV), due to the so-called “carbon contamination” of the optical elements. In 2013, the first mirror was recoated with gold, and the inner wall of the vacuum chamber as well as all parts of the mirror holder were washed with hot water to remove carbon containing elements from the surfaces. Although the photon intensity around 300 eV has tentatively been improved, it has gradually decreased with time. The grating chamber cleaning treatment was repeated during the shutdown term in the spring of 2014. As a result, the photon intensity around 300 eV has greatly been improved, and STXM analyses near the C-K edge have become feasible.

BL2B was reorganized as an open beamline in 2013, which has been conducted as one of the long-term project proposals. As an endstation of BL2B, an experimental setup for angle-resolved photoelectron spectroscopy (ARPES) of inorganic thin films was brought from Chiba University. Commissioning and performance tests were initiated in September 2014. During commissioning, vacuum

pressure rises at the first mirror chamber were frequently observed. A leak was subsequently found in the water cooling system for the first mirror. Although it takes about 20 min. to stabilize the beam position on the entrance slit, it has been decided to continue the operation of BL2B without water cooling.

The construction of a new soft X-ray beamline BL5U began in January 2014. An Apple-II type undulator, with a period length of 60 mm and total length of about 2.5 m, was selected for the new beamline. The photon energy range from 20 eV to 200 eV will be covered with the first and higher harmonic radiation. A variable included angle Monk-Gillieson mounting with an entrance slit-less configuration, which is the same as those installed at BL4U and BL6U, has been constructed. Beamline performance tests were carried out in December 2014, and it has been confirmed that the resolving power and photon intensity are very close to the expected values.

For the endstation at BL5U, an experimental setup for spin-resolved photoemission, equipped with a high-resolution hemispherical electron energy analyzer (MBS A-1) with a highly efficient ‘VLEED’ detector (very low energy electron diffraction), is under continuing development. In pursuit of realizing photoemission experiments with very high spatial resolution, a specially designed post-focusing mirror system is planned to be introduced. It is expected that a small beam spot at the sample position (less than 10 μm in diameter) will be achieved.

Owing to several serious problems during the construction period of BL5U, the commissioning has been delayed. Accordingly, BL5U will be open to users in the spring of 2016.

In order to promote beamline upgrades and developments of new experimental techniques by users, a new research proposal category, named the “long-term project proposal”, was introduced in 2012. The term of validity for this proposal category is three years. Three proposals are currently in progress. Further discussion toward formulating a basic plan on the beamline construction with users will be continued.

All users are required to refer to the beamline manuals and the UVSOR guidebook (the latest revision in PDF format uploaded on the UVSOR web site in June 2010), on the occasion of conducting the actual experimental procedures. Those wishing to use the open and in-house beamlines are recommended to contact the appropriate beamline master (see next page). For updated information on UVSOR, please see <http://www.uvsor.ims.ac.jp>.

Beamlines at UVSOR

Beamline	Monochromator / Spectrometer	Energy Range	Targets	Techniques	Contact
BL1U	Free electron laser	1.6 - 13.9 eV			M. Katoh mkatoh@ims.ac.jp
BL1B	Martin-Puplett FT-FIR	0.5 - 30 meV	Solid	Reflection Absorption	F. Teshima tetsu@ims.ac.jp
BL2A	Double crystal	585 eV - 4 keV	Solid	Reflection Absorption	N. Kondo nkondo@ims.ac.jp
BL2B	18-m spherical grating (Dragon)	24 - 205 eV	Gas	Photoionization Photodissociation	S. Kera kera@ims.ac.jp
BL3U*	Varied-line-spacing plane grating (Monk-Gillieson)	60 - 800 eV	Gas Liquid Solid	Absorption Photoemission Photon-emission	N. Kosugi kosugi@ims.ac.jp
BL3B	2.5-m off-plane Eagle	1.7 - 30 eV	Solid	Reflection Absorption	M. Hasumoto hasumoto@ims.ac.jp
BL4U	Varied-line-spacing plane grating (Monk-Gillieson)	130 - 700 eV	Gas Liquid Solid	Absorption (Microscopy)	T. Ohgashi ohgashi@ims.ac.jp
BL4B	Varied-line-spacing plane grating (Monk-Gillieson)	25 eV - 1 keV	Gas Solid	Photoionization Photodissociation Photoemission	E. Shigemasa sigemasa@ims.ac.jp
BL5U	Varied-line-spacing plane grating (Monk-Gillieson)	20 - 200 eV	Solid	Photoemission	M. Sakai sakai@ims.ac.jp
BL5B	Plane grating	6 - 600 eV	Solid	Calibration Absorption	M. Hasumoto hasumoto@ims.ac.jp
BL6U*	Variable-included-angle varied-line-spacing plane grating	30 - 500 eV	Gas Solid	Photoionization Photodissociation Photoemission	E. Shigemasa sigemasa@ims.ac.jp
BL6B	Michelson FT-IR	3 meV - 2.5 eV	Solid	Reflection Absorption	F. Teshima tetsu@ims.ac.jp
BL7U	10-m normal incidence (modified Wadsworth)	6 - 40 eV	Solid	Photoemission	M. Matsunami matunami@ims.ac.jp
BL7B	3-m normal incidence	1.2 - 25 eV	Solid	Reflection Absorption	M. Hasumoto hasumoto@ims.ac.jp
BL8B	Plane grating	1.9 - 150 eV	Solid	Photoemission	S. Kera kera@ims.ac.jp

Yellow columns represent undulator beamlines.

* In-house beamline.

† Spherical grating monochromator with translating and rotating assembly including normal incidence mount.

BL1U

Light Source Development Station

▼ Description

BL1U has been constructed for developments and applications of various photon sources including free electron laser in the range from visible to deep UV, coherent harmonic generation in the deep UV and VUV, laser Compton scattering gamma-rays and undulator radiation with various polarization properties including optical vortices.

The beam-line is equipped with a dedicated twin polarization variable undulator system with a buncher section, which can be used for a FEL oscillator and a VUV CHG. It is also equipped with a femto-second laser system synchronized with the accelerator, which is used for CHG, slicing, LCS and coherent THz radiation generation.

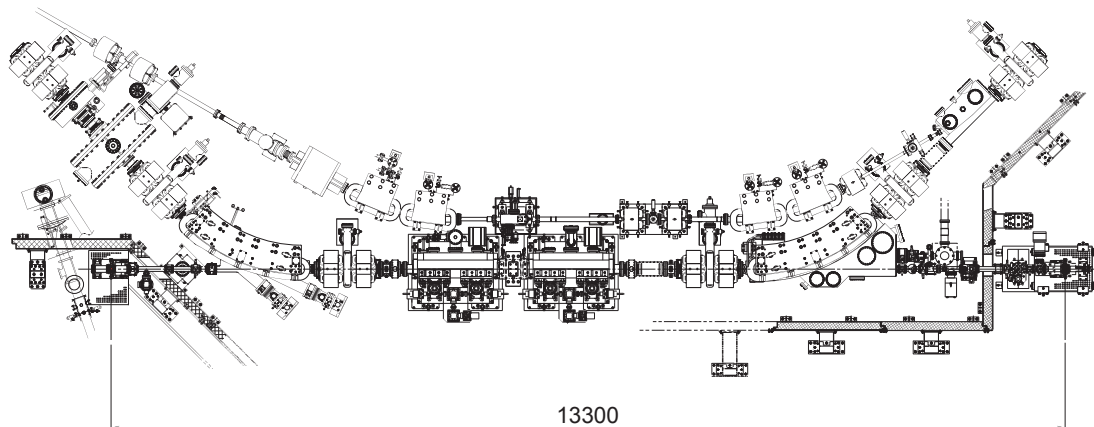


Fig. 1. Configuration of the free electron laser (under reconstruction).



Fig. 2. Twin Apple-II Undulator.

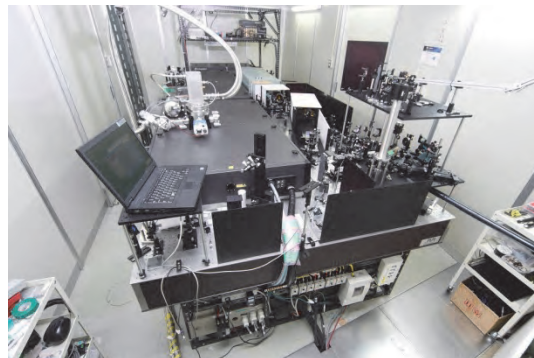


Fig. 3. Accelerator synchronized Laser System.

▼ Technical Data of FEL

Wave Length	199-800 nm
Spectral Band Width	$\sim 10^{-4}$
Polarization	Circular/Linear
Pulse Rate	11.26 MHz
Max. Ave. Power	~ 1 W

Technical Data of Ti:Sa Laser

Wave Length	800 nm
Pulse Length	130 fsec
Oscillator	90.1 MHz
Pulse Energy	2.5mJ 10mJ 50mJ
Repetition Rate	1kHz 1kHz 10Hz

BL1B

Terahertz Spectroscopy Using Coherent Synchrotron Radiation

II

▼ Description

Coherent synchrotron radiation (CSR) is a powerful light source in the terahertz (THz) region. This beamline has been constructed for basic studies on the properties of THz-CSR. However, it can be also used for measurements of reflectivity and transmission spectra of solids using conventional synchrotron radiation.

The emitted THz light is collected by a three-dimensional magic mirror (3D-MM, M0) of the same type as those already successfully installed at BL431R in SPring-8 and BL6B in UVSOR-II. The 3D-MM was installed in bending-magnet chamber #1 and is controlled by a 5-axis pulse motor stage (x , z translation; θ_x , θ_y , θ_z rotation). The acceptance angle was set at 17.5-34 degrees (total 288 mrad) in the horizontal direction. The vertical angle was set at ± 40 mrad to collect the widely expanded THz-CSR.

The beamline is equipped with a Martin-Puplett type interferometer (JASCO FARIS-1) to cover the THz spectral region from 4 to 240 cm^{-1} ($h\nu = 500 \mu\text{eV}$ -30 meV). There is a reflection/absorption spectroscopy (RAS) end-station for large samples (\sim several mm). At the RAS end-station, a liquid-helium-flow type cryostat with a minimum temperature of 4 K is installed.

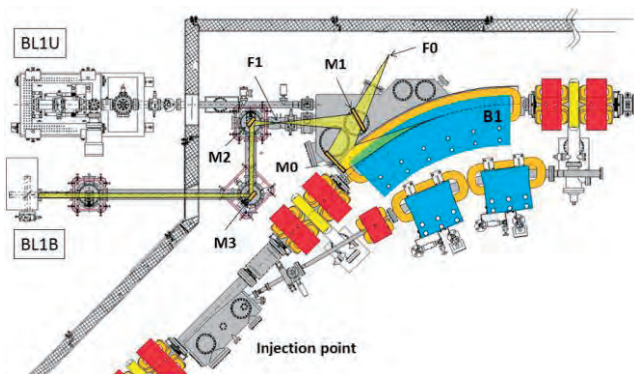


Fig. 1. Schematic top view of the beam extraction part of the THz-CSR beamline, BL1B. The three-dimensional magic mirror (3D-MM, M0) and a plane mirror (M1) are located in the bending-magnet chamber. A parabolic mirror (M2) is installed to form a parallel beam. The straight section (BL1U) is used for coherent harmonic generation (CHG) in the VUV region.

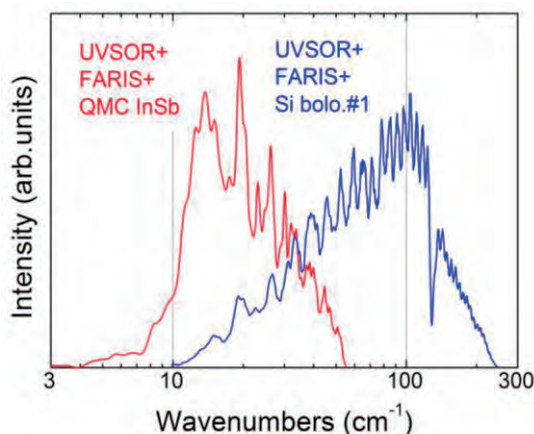


Fig. 2. Obtained intensity spectra with the combination of a light source (UVSOR), interferometer (FARIS-1), and detectors (Si bolometer and InSb hot-electron bolometer).

▼ Technical Data

Interferometer	Martin-Puplett (JASCO FARIS-1)
Wavenumber range	4-240 cm^{-1}
(Energy range)	(500 μeV -30 meV)
Resolution in cm^{-1}	0.25 cm^{-1}
Experiments	Reflection/transmission spectroscopy
Miscellaneous	Users can use their experimental system in this beamline.

BL2A

Soft X-Ray Beamline for Photoabsorption Spectroscopy

▼ Description

BL2A, which was moved its previous location as BL1A in 2011, is a soft X-ray beamline for photoabsorption spectroscopy. The beamline is equipped with a focusing premirror and a double-crystal monochromator [1]. The monochromator serves soft X-rays in the energy region from 585 to 4000 eV using several types of single crystals, such as β - Al_2O_3 , beryl, KTP (KTiOPO_4), quartz, InSb, and Ge. The throughput spectra measured using a Si photodiode (AXUV-100, IRD Inc.) are shown in Fig. 1. The typical energy resolution ($E / \Delta E$) of the monochromator is approximately 1500 for beryl and InSb.

A small vacuum chamber equipped with an electron multiplier (EM) detector is available. Photoabsorption spectra for powdery samples are usually measured in total electron yield mode, with the use of the EM detector. A silicon drift detector is also available for measuring partial fluorescence yields from solid samples.

[1] Hiraya *et al.*, Rev. Sci. Instrum. **63** (1992) 1264.

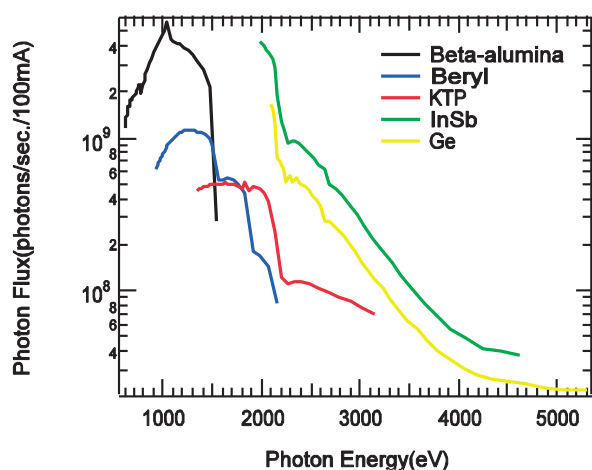


Fig. 1. throughput spectra of the double-crystal monochromator at BL2A.



Fig. 2. Side view of BL2A.

▼ Technical Data

Monochromator	Double crystal monochromator
Monochromator crystals: (2 θ value, energy range)	β - Al_2O_3 (22.53 \AA , 585–1609 eV), beryl (15.965 \AA , 826–2271 eV), KTP (10.95 \AA , 1205–3310 eV), quartz (8.512 \AA , 1550–4000 eV), InSb (7.481 \AA , 1764–4000 eV), Ge (6.532 \AA , 2094–4000 eV)
Resolution	$E / \Delta E = 1500$ for beryl and InSb
Experiments	Photoabsorption spectroscopy (total electron yield using EM and partial fluorescence yield using SDD)

BL2B

Photoelectron Spectroscopy of Molecular Solids

II

▼ Description

This beamline previously dedicated for experiments in the field of gas phase photoionization and reaction dynamics. Then, the beamline has been reconstructed for photoelectron spectroscopy of molecular solids with a new end station, and experiments can be performed from May 2014. The monochromator is a spherical grating Dragon type with 18-m focal length. High throughput (1×10^{10} photons s^{-1}) and high resolution ($E / \Delta E = 2000 - 8000$) are achieved simultaneously under the condition of the ring current of 100 mA [1]. The optical system consists of two pre-focusing mirrors, an entrance slit, three spherical gratings (G1 - G3), two folding mirrors, a movable exit slit, and a refocusing mirror [2]. The monochromator is designed to cover the energy range of 23–205 eV with the three gratings: G1 (2400 lines mm^{-1} , $R = 18$ m) at 80–205 eV; G2 (1200 lines mm^{-1} , $R = 18$ m) at 40–100 eV; G3 (2400 lines mm^{-1} , $R = 9.25$ m) at 23–50 eV. The percentage of the second-order light contamination at $h\nu = 45.6$ eV is 23% for G2 or 7% for G3.

A UHV chamber is placed downstream of the refocusing mirror chamber and equipped silicon photodiode, sapphire plate Au mesh and filters for absolute photon flux measurement, monitor the photon-beam position, relative photon flux measurements and attenuate higher order light, respectively.

The new end station consists of a main chamber with a hemispherical analyzer (SCIENTA R3000) and a liquid-He-cooled cryostat (temperature range of 15-400 K) with 5-axis stage, a sample preparation chamber with a fast-entry load-lock chamber and a cleaning chamber with LEED, ion gun for sputtering and IR heating unit.

[1] M. Ono, H. Yoshida, H. Hattori and K. Mitsuke, Nucl. Instrum. Meth. Phys. Res. A **467-468** (2001) 577.

[2] H. Yoshida and K. Mitsuke, J. Synchrotron Radiation **5** (1998) 774.

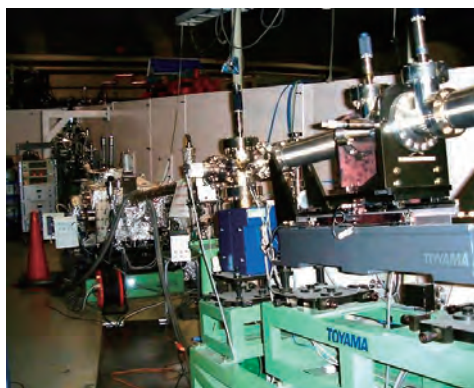


Fig. 1. 18 m spherical grating monochromator at BL2B.



Fig. 2. End station of BL2B for photoelectron spectroscopy of molecular solids.

▼ Technical Data

Monochromator	18 m spherical grating Dragon-type
Wavelength Range	23-205 eV
Resolution	2000–8000 depending on the gratings
Experiments	Angle-resolved ultraviolet photoemission spectroscopy

BL3U

Varied-Line-Spacing Plane Grating Monochromator for Molecular Soft X-Ray Spectroscopy

▼ Description

The beamline BL3U is equipped with an in-vacuum undulator composed of 50 periods of 3.8 cm period length. The emitted photons are monochromatized by the varied-line-spacing plane grating monochromator (VLS-PGM) designed for various spectroscopic investigations in the soft X-ray range including soft X-ray emission studies. Three holographically ruled laminar profile plane gratings are designed to cover the photon energy range from 60 to 800 eV. The beamline has two endstations, namely, XES setup and multi-purpose setup. The XES setup is used for soft X-ray emission spectroscopy. The beam is horizontally focused onto the sample position by a plane-elliptical mirror, M2X. In the multi-purpose setup, the beam is focused by the toroidal mirror M2. Between the sample position and M2, the differential pumping is placed. XAS of liquid samples and the application of in operando observations are performed at the experimental stage of the multi-purpose setup.

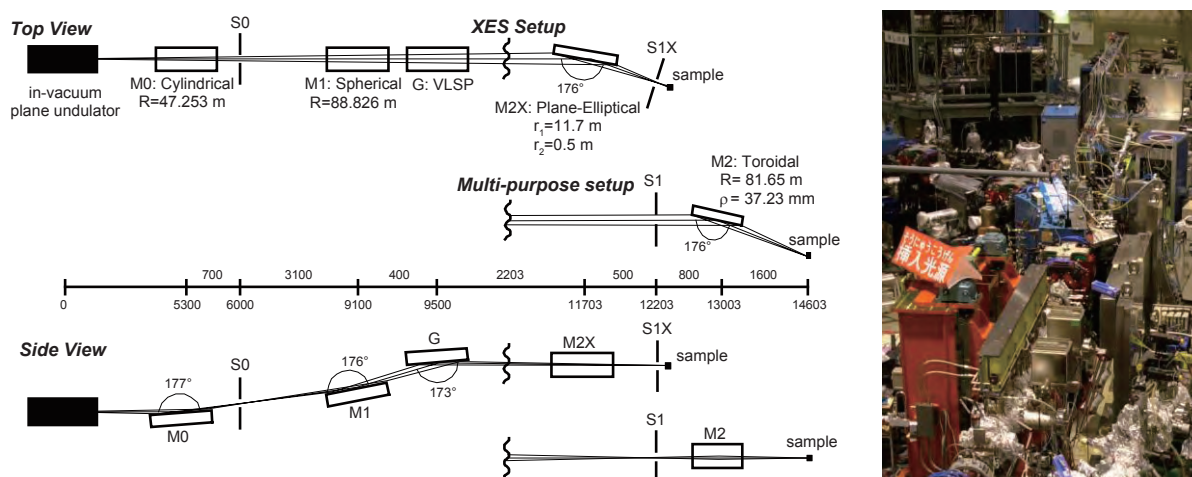


Fig. 1. Schematic layout (left) and the photography (right) of the BL3U. The distances along the beam from the center of the in-vacuum plane undulator are shown in millimeters. S1X and M2X can be replaced with the other exit slit S1 so that experiments can be carried out at either the XES or the multipurpose endstation. In the XES setup, the sample is placed 5–10 mm downstream of S1X.

▼ Technical Data

Monochromator	Varied-line-spacing plane grating monochromator
Energy Range	60-800 eV
Resolution	$E / \Delta E > 10\,000$
Experiments	Soft X-ray spectroscopy (XPS, XES, XAS)
Beam Size	Gaussian shape
(XES Endstation)	Vertical 5-20 μm ; Horizontal 41 μm (FWHM)

BL3B (HOTRLU)

VIS-VUV Photoluminescence and Reflection/Absorption Spectroscopy

II

▼ Description

BL3B has been constructed to study photoluminescence (PL) in the visible (VIS) to vacuum ultraviolet (VUV) region. This beamline consists of a 2.5 m off-plane Eagle type normal-incidence monochromator, which covers the VUV, UV, and VIS regions, i.e., the energy (wavelength) region of 1.7-31 eV (40-730 nm), with three spherical gratings having constant grooving densities of 1200, 600, and 300 l/mm optimized at the photon energies of ~ 20 , ~ 16 , and ~ 6 eV, respectively. The schematic side view and top view layouts are shown in Figs. 1(a) and 1(b), respectively. The FWHM of the beam spot at the sample position is 0.25 mm (V) \times 0.75 mm (H). Low energy pass filters (LiF, quartz, WG32, OG53) can be inserted automatically to maintain the optical purity in the G3 (300 l/mm) grating region (1.7–11.8 eV). Figure 2 shows the throughput spectra (photon numbers at a beam current of 300 mA) for each grating with entrance and exit slit openings of 0.1 mm (resolving power $E / \Delta E$ of ~ 2000 (G3, ~ 6.8 eV)). Since both slits can be opened up to 0.5 mm, a monochromatized photon flux of 10^{10} photons/s or higher is available for PL measurements in the whole energy region.

The end station is equipped with a liquid-helium-flow type cryostat for sample cooling and two detectors; one of which is a photomultiplier with sodium salicylate and the other a Si photodiode for reflection/absorption measurement. For the PL measurements in the wide energy region from VIS to VUV, two PL monochromators, comprising not only a conventional VIS monochromator but also a VUV monochromator with a CCD detector, are installed at the end station.

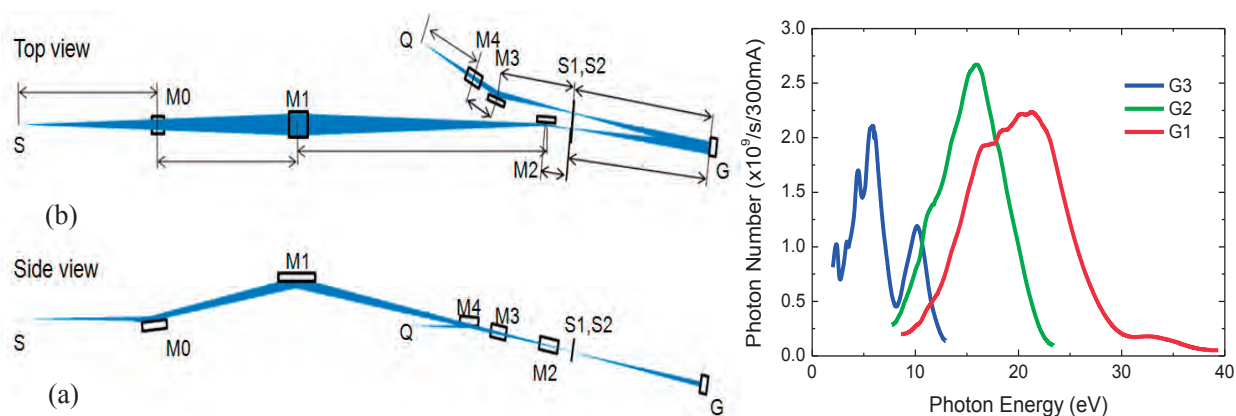


Fig. 1. Schematic layout of the BL3B (a) side view and (b) top view.

▼ Technical Data

Monochromator	-2.5 m normal-incidence monochromator
Energy range	1.7-31 eV (40~730 nm)
Resolution ($\Delta h\nu / h\nu$)	≥ 12000 (at ~ 6.9 eV, 0.02 mm slits, G1 (1200 l/mm))
Experiments	Photoluminescence, reflection, and absorption spectroscopy, mainly for solids

BL4U

Scanning Transmission X-Ray Microscopy in the Soft X-Ray Region

▼Description

In the soft x-ray region, there are several absorption edges of light elements and transition metals. The near edge X-ray absorption fine structure (NEXAFS) brings detailed information about the chemical state of target elements. A scanning transmission X-ray microscope (STXM) in the soft X-ray region is a kind of extended technique of the NEXAFS with high spatial resolution. The STXM has a capability of several additional options, for example, in-situ observations, 3-dimensional observation by computed tomography and ptychography, by utilizing the characteristics of the X-rays. The STXM can be applied to several sciences, such as polymer science, material science, cell biology, environmental science, and so on.

This beamline equips an in-vacuum undulator, a varied-line-spacing plane grating monochromator and a fixed exit slit. The soft X-ray energy range from 130 to 770 eV with the resolving power ($E / \Delta E$) of 6,000 is available. The aperture size of the fixed exit slit determines not only the resolving power but also the size of a microprobe. A Fresnel zone plate is used as a focusing optical device through an order select aperture and its focal spot size of ~ 30 nm is available at minimum. An image is acquired by detecting intensities of the transmitted X-rays by a photomultiplier tube with scintillator with scanning a sample 2-dimensionally. By changing the energy of the incident beam, each 2-dimensional NEXAFS image is stacked. A main chamber of STXM is separated from the beamline optics by a silicon nitride membrane of 100-nm thickness; therefore, sample folders can be handled in vacuum or in helium.

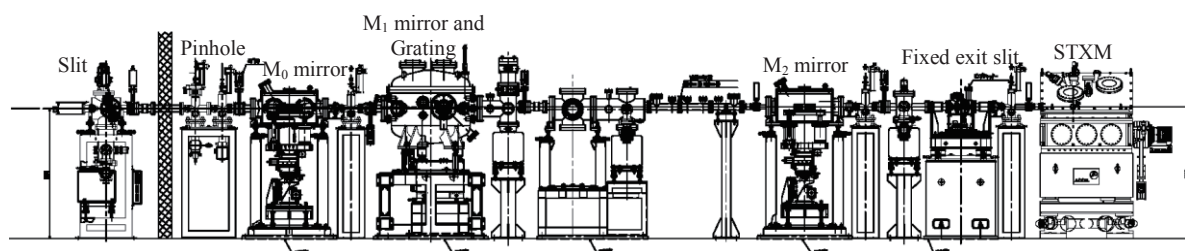


Fig. 1. Schematic image of BL4U.

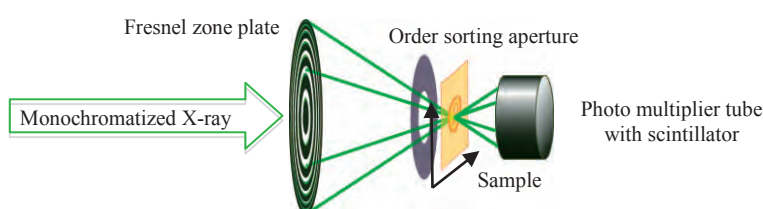


Fig. 2. Schematic image of the STXM.

▼Technical Data

Energy range (E)	130 -770 eV
Resolving power ($E / \Delta E$)	~ 6000
Focusing optical element	Fresnel zone plate
Spatial resolution	~ 30 nm
Experiments	2-dimensinal absorption spectroscopy
Measurement environment	standard sample folder in vacuum or in helium, specially designed sample cell in ambient condition

BL4B

Varied-Line-Spacing Plane Grating Monochromator for Molecular Soft X-Ray Spectroscopy

II

▼ Description

The beamline BL4B equipped with a varied-line-spacing plane grating monochromator (VLS-PGM) was constructed for various spectroscopic investigations in a gas phase and/or on solids in the soft X-ray range. Three holographically ruled laminar profile plane gratings with SiO₂ substrates are designed to cover the photon energy range from 25 to 800 eV. The gratings with groove densities of 100, 267, and 800 l/mm cover the spectral ranges of 25–100, 60–300, and 200–1000 eV, respectively, and are interchangeable without breaking the vacuum. Figure 1 shows the absolute photon flux for each grating measured using a Si photodiode (IRD Inc.), with the entrance- and exit-slit openings set at 50 and 50 μm, respectively. The maximum resolving power ($E / \Delta E$) achieved for each grating exceeds 5000.

There is no fixed endstation on this beamline. A small vacuum chamber equipped with an electron multiplier (EM) detector is available. Soft X-ray absorption spectra of solid samples are usually measured by means of the total electron yield method using EM, and the partial fluorescence yield method using a silicon drift detector (SDD).

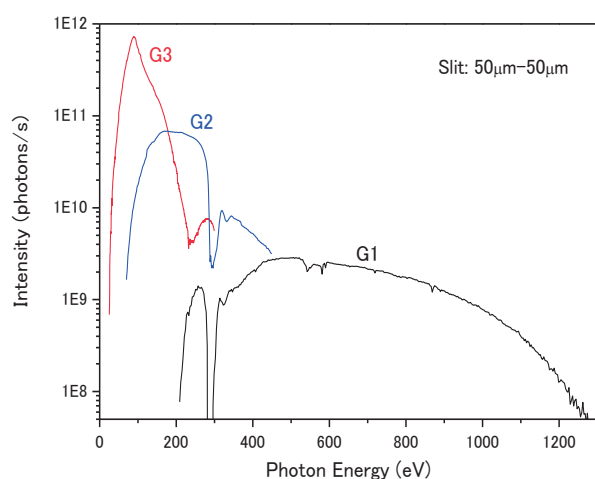


Fig. 1. Throughput from the VLS-PGM monochromator on BL4B.

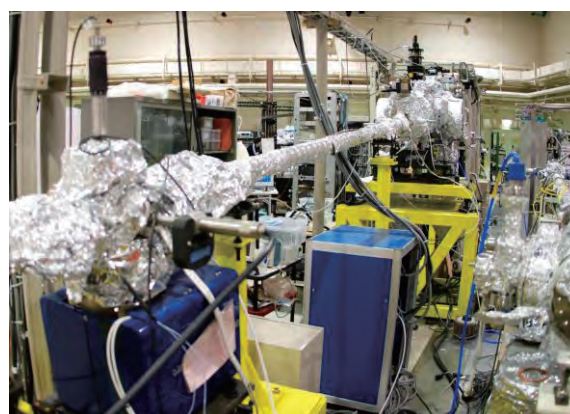


Fig. 2. Photo of BL4B.

▼ Technical Data

Monochromator	Varied-line-spacing Plane Grating Monochromator
Energy range	25-1000 eV
Resolution	$E / \Delta E > 5000$ (at maximum)
Experiments	Soft X-ray spectroscopy (mainly, photoabsorption spectroscopy for solid targets by means of total electron yield method using EM and partial fluorescence yield method using SDD)

BL5U

Photoemission Spectroscopy of Solids and Surfaces

▼Description

This beamline was originally used for angle-resolved photoemission spectroscopy (ARPES) study of solids and surfaces. After Jan 2014, the beamline has been shutdown for upgrade. The whole beamline, including the undulator and the endstation, will be renewed to perform higher energy resolution ARPES experiments. This beamline will also have new capability to obtain spin- and spatial-dependence of the electronic structure of solids using new spin detector and micro-focused beam. This beamline will be open for users from FY2016.



Fig. 1. Pictures of BL5U on May 2014.

▼Technical Data (Expected Performance)

Monochromator	Monk-Gillieson VLS-PGM
Energy Range	20-200 eV
Resolution	$h\nu/\Delta E > 10,000$ for $< 10 \mu\text{m}$ slits
Experiment	ARPES, Spin-resolved ARPES, Space-resolved ARPES
Flux	$< 10^{12}$ photons/s for $< 10 \mu\text{m}$ slits (at the sample position)
Beam spot size	400 (H) x 5-20 (V) μm , 10 (H) x 4-6 (V) μm (microscope)
Main Instruments	Hemispherical photoelectron analyzer (MBS A-1), Liq-He flow cryostat with 5-axis manipulator (5-400 K)

BL5B

Calibration Apparatus for Optical Elements and Detectors

II

▼ Description

BL5B has been constructed to perform calibration measurements for optical elements and detectors. This beamline is composed of a plane grating monochromator (PGM) and three endstations in tandem. The most upstream station is used for the calibration measurements of optical elements, the middle one for optical measurements for solids, and the last for photo-stimulated desorption experiments. The experimental chamber at the most downstream station is sometimes changed to a chamber for photoemission spectroscopy. The calibration chamber shown in Fig. 2 is equipped with a goniometer for the characterization of optical elements, which has six degrees of freedom, X-Y translation of a sample, and interchanging of samples and filters. These are driven by pulse motors in vacuum. Because the polarization of synchrotron radiation is essential for such measurements, the rotation axis can be made in either the horizontal or vertical direction (s- or p-polarization).

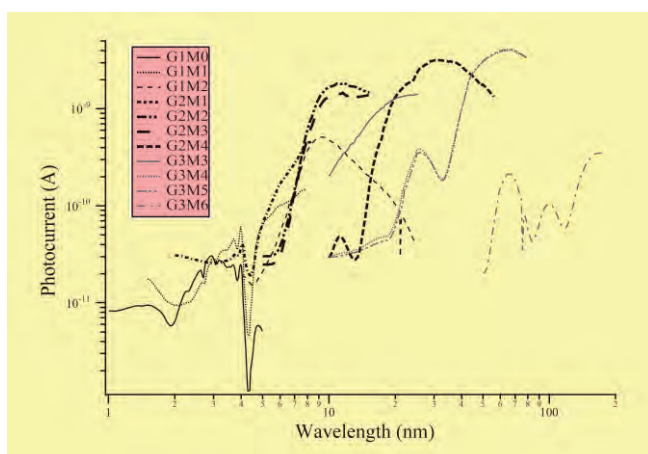


Fig. 1. Throughput spectra for possible combinations of gratings and mirrors at BL5B measured by a gold mesh.

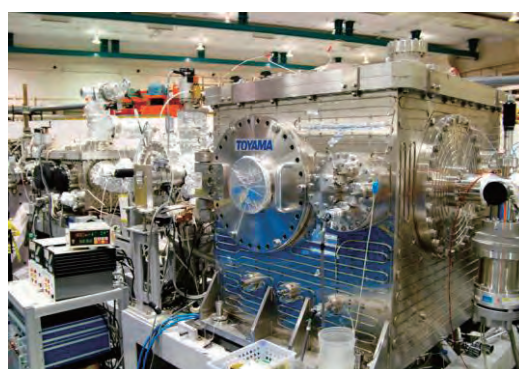


Fig. 2. A side view of the experimental chamber for calibration measurements.

▼ Technical Data

Monochromator	Plane Grating Monochromator
Energy range	6-600 eV (2-200 nm)
Resolution	$E / \Delta E \sim 500$
Experiments	Calibration of optical elements, reflection and absorption spectroscopy mainly for solids

BL6U

Variable-Included-Angle VLS-PGM for Molecular Soft X-Ray Spectroscopy

▼Description

The beamline BL6U equipped with a variable-included-angle Monk-Gillieson mounting monochromator with a varied-line-spacing plane grating was constructed for various spectroscopic investigations requiring high-brilliance soft X-rays in a gas phase and/or on solids. Through a combination of undulator radiation and sophisticated monochromator design (entrance slit-less configuration and variable-included-angle mechanism), using a single grating, the monochromator can cover the photon energy ranging from 30 to 500 eV, with resolving power of greater than 10000 and photon flux of more than 10^{10} photons/s. Figure 1 shows an example of the monochromator throughput spectra measured using a Si photodiode, with the exit-slit opening set at 30 μm , which corresponds to the theoretical resolving power of 10000 at 80 eV.

There is no fixed endstation on this beamline.

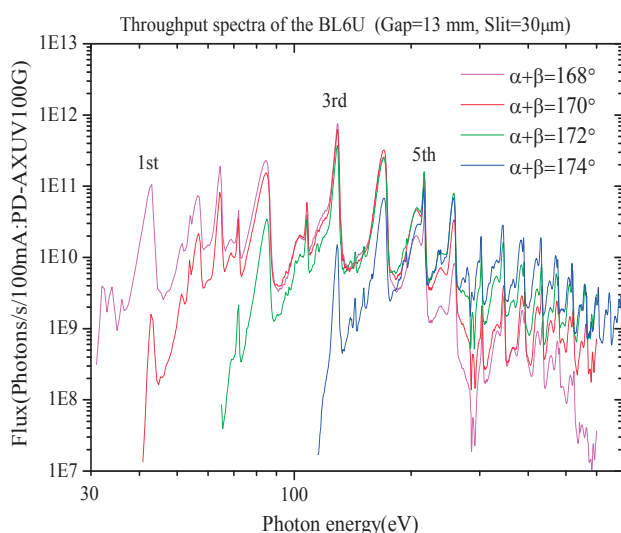


Fig. 1. Throughput spectra of the BL6U monochromator at various included angles.



Fig. 2. Photo of BL6U.

▼Technical Data

Monochromator	Variable-included-angle Varied-line-spacing Plane Grating Monochromator
Energy range	40-500 eV
Resolution	$E / \Delta E > 10000$ (at maximum)
Experiments	High-resolution soft X-ray spectroscopy (mainly photoelectron spectroscopy for gaseous and solid targets)

BL6B

Infrared and Terahertz Spectroscopy of Solids

II

▼Description

Synchrotron radiation (SR) has good performance (high brilliance and high flux) not only in the VUV and soft X-ray (SX) regions but also in the infrared (IR) and THz regions. BL6B covers the IR and THz regions. The previous beamline, BL6A1, which was constructed in 1985, was the pioneer in IRSR research. The beamline was deactivated at the end of FY2003 and a new IR/THz beamline, BL6B (IR), was constructed in FY2004. The front-end part including bending duct #6 was replaced with a new part having a higher acceptance angle ($215 \text{ (H)} \times 80 \text{ (V)} \text{ mrad}^2$) using a magic mirror, as shown in Fig. 1.

There are two Michelson type interferometers in this endstation; with first one (Bruker Vertex70v), which covers a wide spectral region from 30 to $20,000 \text{ cm}^{-1}$ ($h\nu = 4 \text{ meV}-2.5 \text{ eV}$), reflection/absorption spectroscopy measurements of large samples (up to several mm) and IR/THz microscopy measurements of tiny samples (up to several tens of μm) can be performed. For reflection/absorption spectroscopy measurements, a liquid-helium-flow type cryostat with a minimum temperature of 4 K is installed. The other interferometer (Jasco FT/IR-6100), which covers 350 to $15,000 \text{ cm}^{-1}$ ($h\nu = 45 \text{ meV}-1.8 \text{ eV}$), has been available for IR microscopy imaging measurements from FY2014. One can also perform ATR measurements using diamond ATR prism.

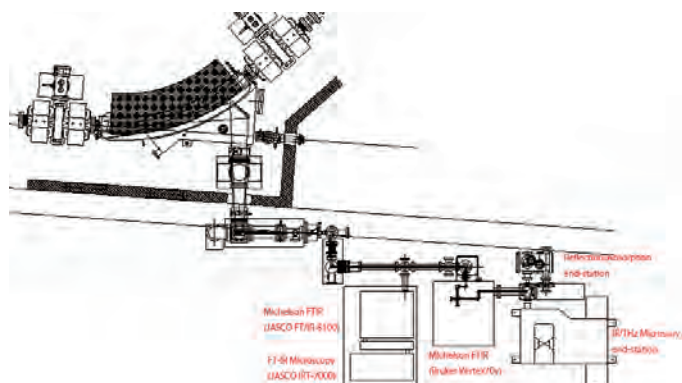
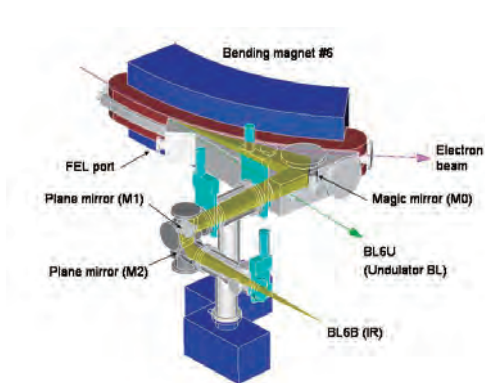


Fig. 1. Design of the optics and front end of BL6B. Fig. 2. Schematic top view of BL6B.

▼Technical Data

Interferometer	Michelson (Bruker Vertex70v)	Michelson (Jasco FT/IR-6100)
Wavenumber Range (Energy range)	$30-20,000 \text{ cm}^{-1}$ ($4 \text{ meV}-2.5 \text{ eV}$)	$350-15,000 \text{ cm}^{-1}$ ($45 \text{ meV}-1.8 \text{ eV}$)
Resolution in cm^{-1}	0.1 cm^{-1}	0.5 cm^{-1}
Experiments	Reflectivity and transmission spectroscopy THz Microspectroscopy	IR microscopy imaging (JASCO IRT-7000) ATR spectroscopy

BL7U (SAMRAI)

Angle-Resolved Photoemission of Solids in the VUV Region

▼ Description

Beamline 7U, named the Symmetry- And Momentum-Resolved electronic structure Analysis Instrument (SAMRAI) for functional materials, was constructed to provide a photon flux with high energy resolution and high flux mainly for high-resolution angle-resolved photoemission spectroscopy of solids [1]. An APPLE-II-type variable-polarization undulator is installed as the light source. The undulator can produce intense VUV light with horizontal/vertical linear and right/left circular polarization. The undulator light is monochromatized by a modified Wadsworth type monochromator with three gratings (10 m radius; 1200, 2400, and 3600 lines/mm optimized at $h\nu = 10, 20, \text{ and } 33 \text{ eV}$). The energy resolution of the light ($h\nu / \Delta h\nu$) is more than 10^4 with a photon flux of 10^{11} - 10^{12} ph/s or higher on samples in the entire energy region.

The beamline has a photoemission end-station equipped with a 200 mm-radius hemispherical photoelectron analyzer (MB Scientific AB, A-1 analyzer) with a wide-angle electron lens and a liquid-helium-cooled cryostat with 6-axis pulse motor control (AVC Co., Ltd., i-GONIO). The main function of the beamline is to determine the three-dimensional Fermi surface and electronic structure of solids at low temperatures and their temperature dependence in order to reveal the origin of their physical properties.

[1] S. Kimura, T. Ito, M. Sakai, E. Nakamura, N. Kondo, K. Hayashi, T. Horigome, M. Hosaka, M. Katoh, T. Goto, T. Ejima and K. Soda, "SAMRAI: A variably polarized angle-resolved photoemission beamline in the VUV region at UVSOR-II," Rev. Sci. Instrum. **81** (2010) 053104.

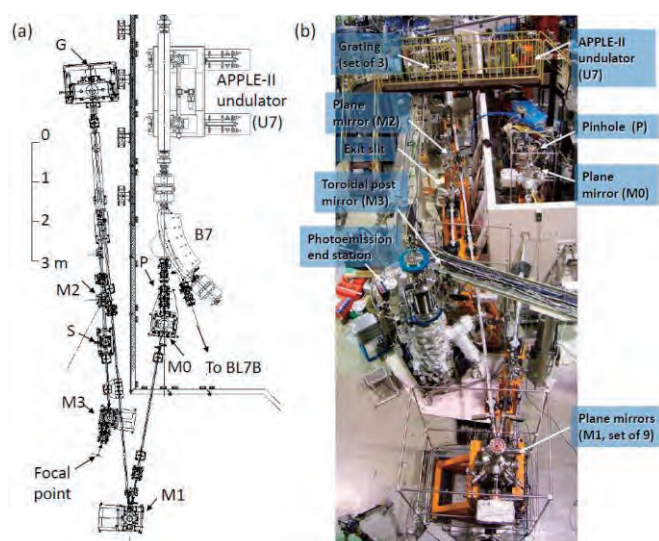


Fig. 1. Layout (a) and photograph (b) of the SAMRAI beamline consisting of an APPLE-II type undulator (U7), a modified Wadsworth type monochromator (M0-S), and a high-resolution photoemission analyzer at the focal point. The monochromator has five major optical components: two plane mirrors (M0 and M1) with water cooling, one set of three spherical gratings (G), an exit slit (S), and one toroidal refocusing mirror (M3). The spherical gratings have a radius of 10 m and are located 22 m from the center of the undulator. There is no entrance slit. S is located 6.47 m from G. A second branch for a VUV microscope end-station is planned to be constructed after the plane mirror (M2) located between G and S.

▼ Technical Data

Light source	APPLE-II type undulator ($\lambda_u = 76 \text{ mm}$, $N = 36$) vertical/horizontal linear, right/left circular
Monochromator	10 m normal-incidence monochromator (modified Wadsworth type)
Photon energy range	6-40 eV ($\lambda = 30\sim 200 \text{ nm}$)
Resolution ($h\nu / \Delta h\nu$)	1×10^4 - 5×10^4
Photon flux on sample	$\geq 10^{12}$ - 10^{11} ph/s (depending on $h\nu$)
Beam size on sample	$200 \text{ (H)} \times 50 \text{ (V)} \mu\text{m}^2$
Experiments	Angle-resolved photoemission of solids (MB Scientific A-1 analyzer, acceptance angle: $\pm 18 \text{ deg}$)

BL7B

3 m Normal-Incidence Monochromator for Solid-State Spectroscopy

II

▼ Description

BL7B has been constructed to provide sufficiently high resolution for conventional solid-state spectroscopy, sufficient intensity for luminescence measurements, wide wavelength coverage for Kramers–Kronig analyses, and minimum deformation to the polarization characteristic of incident synchrotron radiation. This beamline consists of a 3-m normal incidence monochromator, which covers the vacuum ultraviolet, ultraviolet, visible, and infrared, i.e., the wavelength region of 50–1000 nm, with three gratings (1200, 600, and 300 l/mm). Two interchangeable refocusing mirrors provide two different focusing positions. For the mirror with the longer focal length, an LiF or a MgF₂ window valve can be installed between the end valve of the beamline and the focusing position. Figure 1 shows the absolute photon intensity for each grating with the entrance and exit slit openings of 0.5 mm. A silicon photodiode (AXUV-100, IRD Inc.) was utilized to measure the photon intensity and the absolute photon flux was estimated, taking the quantum efficiency of the photodiode into account.

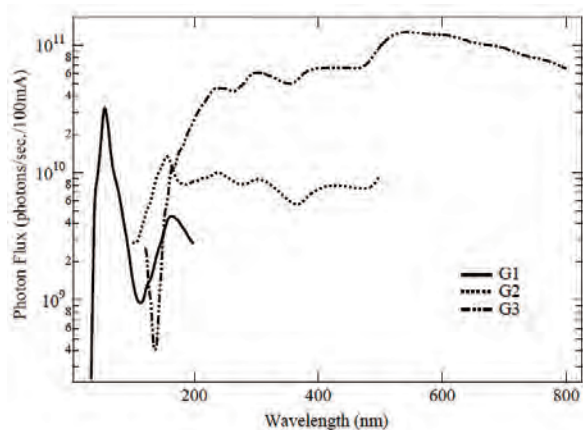


Fig. 1. Throughput spectra of BL7B measured using a silicon photodiode.



Fig. 2. Photo of BL7B.

▼ Technical Data

Monochromator	3 m Normal-Incidence Monochromator
Wavelength Range	1.5-25 eV (50-1000 nm)
Resolution	$E / \Delta E = 4000-8000$ for 0.01 mm slits
Experiments	Absorption, reflection, and fluorescence spectroscopy, mainly for solids

BL8B

Angle-Resolved Ultraviolet Photoelectron Spectrometer for Solids

▼ Description

BL8B is a beamline for the angle-resolved ultraviolet photoemission spectroscopy (ARUPS) system, which is designed to measure various organic solids such as molecular crystals, organic semiconductors, and conducting polymers. This beamline consists of a plane-grating monochromator (PGM), a sample preparation chamber with a fast-entry load-lock chamber, a measurement chamber (base pressure 1×10^{-10} Torr), a cleaning chamber (base pressure 1×10^{-10} Torr), and a sample evaporation chamber (base pressure 3×10^{-10} Torr). The cleaning chamber is equipped with a back-view LEED/AUGER, an ion gun for Ar^+ sputtering, and an infrared heating unit. The PGM consists of premirrors, a plane grating, focusing mirror, and a post-mirror, with an exit slit. It covers the wide range from 2 to 130 eV with two exchanging gratings (G1: 1200 l/mm, G2: 450 l/mm) and five cylindrical mirrors. The toroidal mirror focuses the divergent radiation onto the sample in the measurement chamber. The spot size of the zeroth-order visible light at the sample surface is approximately $1 \times 1 \text{ mm}^2$. Figure 1 shows the throughput spectra of PGM (slit = 100 μm). The energy resolution at a slit width of 100 μm was found to be $E / \Delta E = 1000$ in the wavelength range from 2 to 130 eV. A hemispherical electron energy analyzer of 75 mm mean radius with an angular resolution less than 2° can be rotated around the vertical and horizontal axes. The sample mounted on a manipulator (temperature range 14–320 K) can also be rotated around two axes.

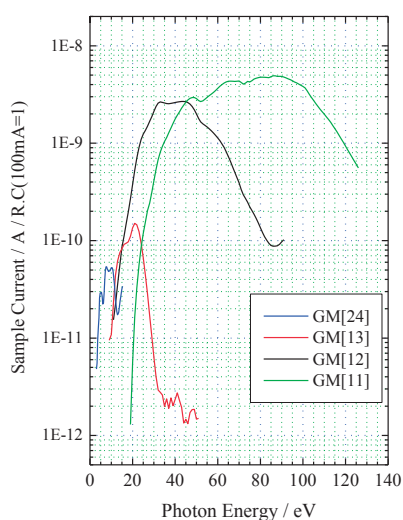


Fig. 1. Throughput spectra of plane-grating monochromator at BL8B (slit = 100 μm).

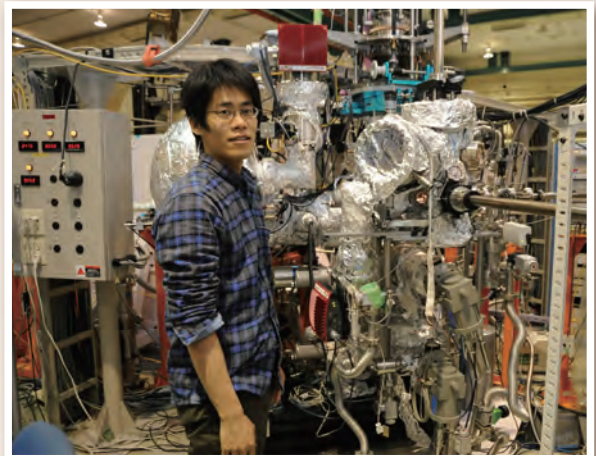
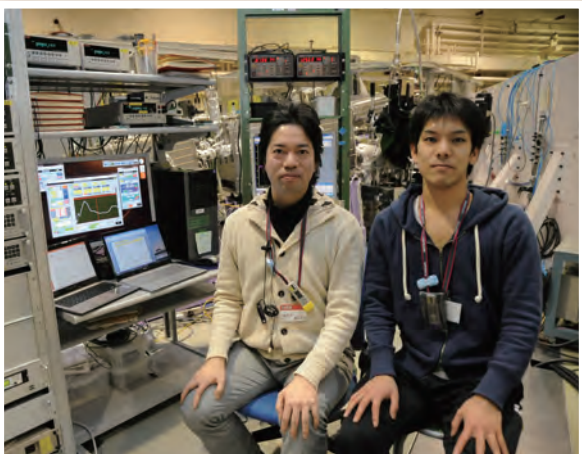
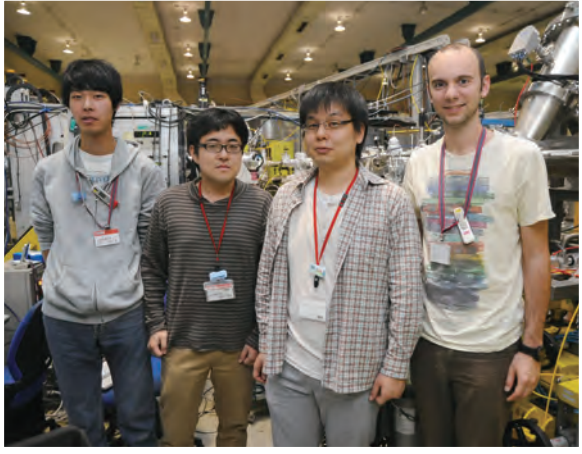


Fig. 2. A photo of BL8B.

▼ Technical Data

Monochromator	Plane-grating monochromator
Wavelength Range	9-600 nm
Resolution	$E / \Delta E = 1000$
Experiments	Angle-resolved ultraviolet photoemission spectroscopy

UVSOR User 2



III-1

Accelerators and
Instruments

Light sources

Measurement of Temporal Response of Transmission-Type Spin-Polarized Photocathodes

T. Inagaki¹, N. Yamamoto¹, T. Konomi², Y. Okano³, M. Adachi⁴, X. G. Jin¹,
M. Hosaka¹, Y. Takashima¹ and M. Katoh^{2,3,1}

¹Nagoya University, Nagoya 464-8601, Japan

²UVSOR Facility, Institute for Molecular Science, Okazaki 444-8585, Japan

³Laser Research Center for Molecular Science, Okazaki 444-8585, Japan

⁴High Energy Accelerator Research Organization (KEK), Tsukuba 305-0801, Japan

We have developed transmission-type spin polarized photocathodes with negative electron affinity (NEA). The spin-polarized electron beam is essential for “International Linear Collider” and so on. It is also expected to be applied for “Spin-resolved Inverse Photoemission Spectroscopy” [1].

In order to measure the temporal response of photocathodes, we developed the electron pulse length measurement system with 20 kV DC gun (Fig. 1). In this system by using an rf deflecting cavity, the electron beam is kicked transversely according to the rf phase position and the longitudinal pulse structure is projected to the transverse plane. We have employed the resonance mode of TM120. The resonance frequency is 2614 MHz for the rf cavity and the resonance frequency corresponds to the multiple of RF acceleration frequency of UVSOR storage ring, so the laser can be synchronized with UVSOR accelerator is used for the pump laser [2]. Temporal response of the photocathodes is evaluated by comparing the electron pulse structure and the pump laser pulse length. The pump laser pulses are provided by a mode-locked Ti:sapphire oscillator. In the present system by using a pulse stretcher, the pulse length of the pump laser can be selected in the range between 6.1 and 45 ps.

After the installation of the rf cavity to electron gun system, we carried out the measurement test with the GaAs/GaAsP superlattice photocathode with thickness of 96 nm. To evaluate its temporal response, the longitudinal pulse structure of electron beam projected by an rf deflecting cavity is fitted with a temporal response function which has two decay time constants, fast and slow temporal response times (Fig. 2). The measurement is carried out with pump laser length of less than 10 ps. As the results, two decay time constants are 3.1 ± 0.9 and 14 ± 1 ps, respectively. We considered that this result is consistent in a prior research with almost the same active layer thickness on front irradiation type [3].

Finally, in near future we are planning to reduce electron beam size before it is projected to the transverse plane in order to realize more precisely temporal response measurement and we will make systematic measurement for the various transmission-type photocathodes.

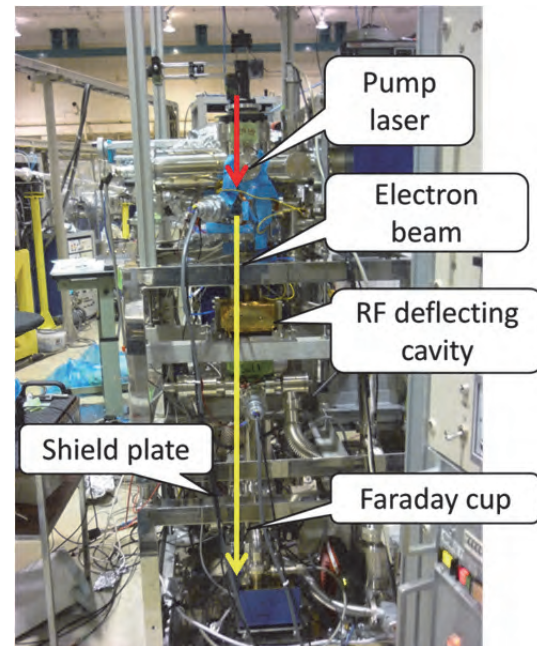


Fig. 1. 20 kV DC electron gun.

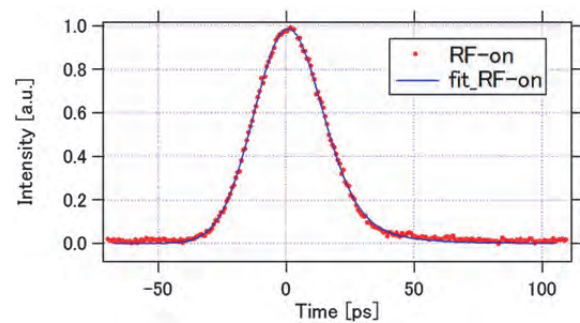


Fig. 2. Experimental data and fitted curves for a longitudinal pulse structure of electron beam.

[1] N. Yamamoto, doctoral thesis, Nagoya University (2007).

[2] T. Niwa, master's thesis, Nagoya University (2013).

[3] X. G. Jin *et al.*, “Picosecond electron bunches from GaAs/GaAsP strained superlattice photocathode” *Ultramicroscopy* **130** (2013) 44.

Light Sources

Narrow Band Coherent Edge Radiation from UVSOR-III Storage Ring

M. Hosaka¹, D. Oodake², N. Yamamoto^{1,2}, T. Konomi^{3,4}, J. Yamazaki³, K. Hayashi³,
Y. Takashima^{1,2} and M. Katoh^{3,4}

¹Synchrotron Radiation Research Center, Nagoya University, Nagoya 464-8603, Japan

²Graduate School of Engineering, Nagoya University, Nagoya 464-8603, Japan

³UVSOR Facility, Institute for Molecular Science, Okazaki 444-8585, Japan

⁴School of Physical Sciences, The Graduate University for Advanced Studies (SOKENDAI), Okazaki 444-8585, Japan

We have already succeeded in producing narrow band coherent THz radiation by manipulating the interaction between a relativistic electron bunch and an amplitude modulated laser [1]. In the former experiment, the radiation from a bending magnet where electrons moving along a circular trajectory, is extracted. As next step we planned to extract the radiation from edges of bending magnets, where electrons experience rapid change of magnetic field. The radiation is called edge radiation and has distinctive features as compared to normal synchrotron radiation: highly collimation even in long wavelength region, annular radiation pattern and radial polarization. Applying our technique of amplitude modulation laser, intense narrow band edge radiation is expected to be generated. Moreover, radially polarized light can be converted to Z-polarized one by using a high NA lens. Novel new applications of the radiation, such as surface science and solid state physics are expected.

The experiment to observe narrow band edge radiation was carried out with an electron beam of 600 MeV. Amplitude modulated Ti:Sa of 3 mJ was injected to BL1U undulator where the interaction between the laser and the electron bunch occurs. We have installed a simple beamline consisting of a mirror and a window port at 0 degree of BL2 to extract edge radiation from the edges of the bend 1 and bend 2. The edge radiation from the beamline was detected using an InSb hot-electron bolometer. In the initial experiment, we confirmed that the radiation intensity is proportional to the square of stored beam current, as is peculiar to coherent radiation (the figure is not seen in this report). Then we measured radiation intensity as a function of the THz frequency adjusted by the laser modulation frequency. Figure 1 shows the experimental result compared with efficiency calculations taking account of optical parameters of UVSOR-III magnetic lattice. As seen in the figure they agree well except for very low frequency region ($\sim 5 \text{ cm}^{-1}$) where multi-turn effect [2] dominates, which we did not take into account in the calculation. We observed spatial intensity distribution of the radiation by moving the bolometer which is located at distance of about 7 m from the radiation source point.

In the experiment, we employed a polarizer to extract only horizontal polarized component. Figure 2

shows the spatial distribution obtained in the experiment with the wavelength adjusted to 20 cm^{-1} . We expected horizontally separated distribution (Fig. 2 (b)); however, the experimental result does not clearly reproduce the expected distribution. We think the spatial distribution is affected by diffraction due to a narrow beam duct. We are planning a similar experiment with shorter THz wavelength. We are also going to make a simulation taking account of the diffraction effect.

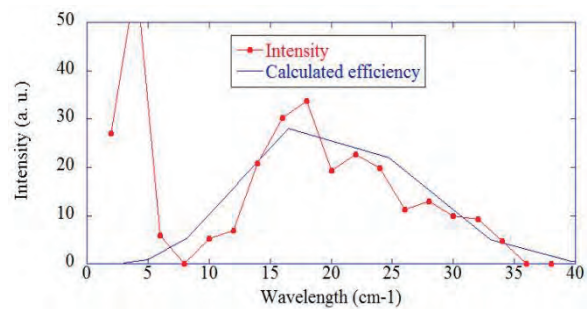


Fig. 1. Intensity of edge radiation as a function of wavelength.

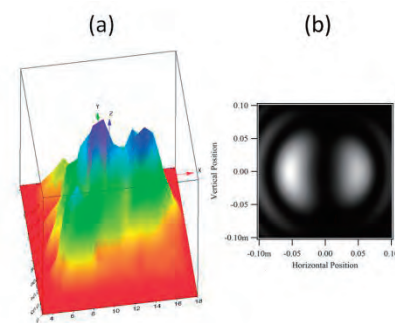


Fig. 2. Spatial distribution of horizontal polarized component of edge radiation: (a) experiment (b) calculation.

[1] S. Bielawski *et al.*, Nat. Phys. Rev. Lett. **4** (2008) 390.

[2] C. Evain *et al.*, Phys. Rev. ST Accel Beam **12** 9 (2010) 090703.

Light sources

Beam Injection with a Pulsed Multipole Magnet at UVSOR-III

N. Yamamoto¹, H. Zen², M. Hosaka¹, M. Adachi⁴, K. Hayashi³,
J. Yamazaki³, Y. Takashima¹ and M. Katoh^{3,1}

¹Synchrotron Radiation Research Center, Nagoya University, Nagoya 464-8603, Japan

²Institute of Advanced Energy, Kyoto University, Uji 611-0011, Japan

³UVSOR Facility, Institute for Molecular Science, Okazaki, 444-8585, Japan

⁴High Energy Accelerator Research Organization, Tsukuba 305-0801, Japan

The pulsed multipole injection scheme was developed at KEK-PF and KEK-AR [1,2]. In this scheme, the injection beam is captured into the accelerator acceptance as a result of pulsed multipole kicks, and the stored beam passes through the center of the multipole magnet, where the field strength is almost zero. The scheme thus avoids exciting coherent oscillation in the stored beam and delivers a high quality photon beam for synchrotron radiation users.

To introduce pulsed multipole injection into the UVSOR-III storage ring, we designed a rectangular-shaped pulsed multipole magnet (Fig.1) and tested it for electron beam injection[3]. The goal of the design was to compensate for residual magnetic fields by using thin ferrite bars applied to the pre-manufactured magnet.

The injection experiments demonstrated that multiturn injection, which uses the pulsed multipole magnet, is successful technique for UVSOR-III. This is the successful result of the pulsed multipole injection in case of as many as 7–9 kicks being applied to the same injected bunch on consecutive turns.

After optimizing the injection conditions, we obtained a maximum injection efficiency of 23% and an electron beam injection up to 300 mA. The injection efficiency obtained was less than expected from beam simulations, but the efficiency was sufficient to maintain the top-up operation at 300 mA. We suggest that the quality of the injection beam may have caused the lower injection efficiency because an injection efficiency lower than expected also occurred when using conventional dipole magnets. Thus, to obtain a higher injection efficiency, we shall focus our future investigations on the injector system.

Finally, this work demonstrates that the field-compensation technique based on using thin ferrite bars to cancel the residual magnet field is an economical and powerful way to improve performance. Coherent oscillations were drastically suppressed by applying this technique to pre-manufactured magnet (Fig. 2).

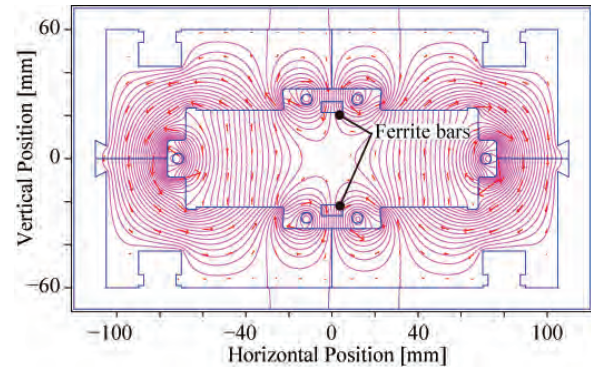


Fig. 1. Cross-section of the pulsed multipole magnet with calculated magnetic field.

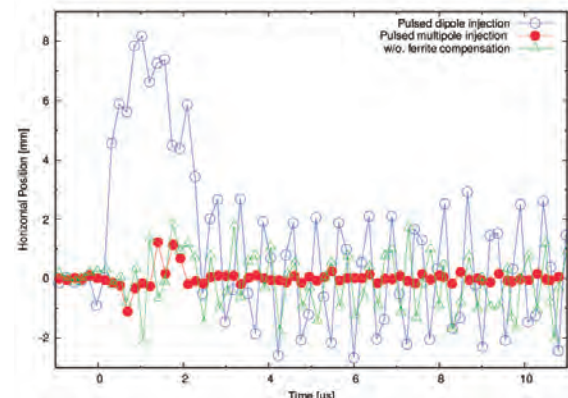


Fig. 2. Measured stored beam movements with pulsed dipole magnet (open circles) and pulsed multipole magnet with ferrite bars (close circles) and without ferrite bars (open triangles).

- [1] K. Harada, Y. Kobayashi, T. Miyajima and S. Nagahashi, Phys. Rev. ST-AB **10** (12) (2007) 123501.
 [2] H. Takaki, N. Nakamura, Y. Kobayashi, K. Harada, T. Miyajima, A. Ueda, S. Nagahashi, M. Shimada, T. Obina and T. Honda, Phys. Rev. ST-AB **13** (2010) 020705.
 [3] N. Yamamoto, H. Zen, M. Hosaka, T. Konomi, M. Adachi, K. Hayashi, J. Yamazaki, Y. Takashima and M. Katoh, Nucl. Inst. and Meth. A **767** (2014) 26.

Others

Performance Evaluation of Mass Production Nuclear Emulsion for 2015 Balloon-Borne Experiment

N. Otsuka¹, H. Kawahara¹, H. Rokujo¹, K. Ozaki², S. Aoki², E. Shibayama², S. Takahashi², S. Tawa², F. Mizutani², K. Yamada², Y. Tateishi², T. Kosaka² and GRAINE collaboration

¹Graduate School of Science, Nagoya University, Nagoya 464-8602, Japan

²Department of Human Environment Science, Kobe University, Kobe 657-8501, Japan

We are promoting GRAINE project. GRAINE project is a balloon-borne experiment to explore the gamma-ray astrophysics. We load a balloon with nuclear emulsion to observe cosmic gamma-rays. Nuclear emulsion is able to record the 3-dimensional trajectory of a charged particle within a 1-um accuracy. Nuclear emulsion is made of a plastic base and silver halide emulsion which is coated on a plastic base. After development the emulsion films, we can observe track made of silver grain by charged particles under a microscope. We observed electron-pair which created of cosmic gamma-rays in emulsion and reconstruct each gamma-ray to determine which way the gamma-ray come from. Figure 1 shows how track of charged particle look like in nuclear emulsion under microscope.

We produced nuclear emulsion at Nagoya University for next balloon-borne experiment. Next balloon-borne experiment will operate in May 2015, Australia. We were required to product about fifty square meters of nuclear emulsion for 2015 experiment. Mass production of silver halide emulsion for 2015 experiment is started at February 2014 and it finished in January 2015. Figure 2 shows time profile of the total amount of produced emulsions. We produce emulsion with R&D machine (1L tank) until November 2014. Thereafter, we introduced mass production machine (3L tank).

We need to evaluate performance of each silver halide emulsion. I will explain how to evaluate performance of silver halide emulsion. We expose electron beam to films made of silver halide emulsion to evaluate at UVSOR. Exposed film has trajectories of electron. We measured Grain Density (GD), counts of silver grains per 100um, by observed trajectories in emulsion under microscope. GD would be high when emulsion has high sensitivity to charged particle.

Figure 3 shows results of measurement of GD for all emulsions. The high density silver halide emulsion has an average GD of 50.6 and the middle density silver halide emulsion has an average GD of 45.8. Since next experiment demand more than 40 for GD, mass production of emulsion was stable. Moreover, the mass production machine is able to produce emulsion as the R&D machine.

Sufficient performed emulsions were coated on plastic bases at Nagoya University. These films are become detector for 2015 experiment.

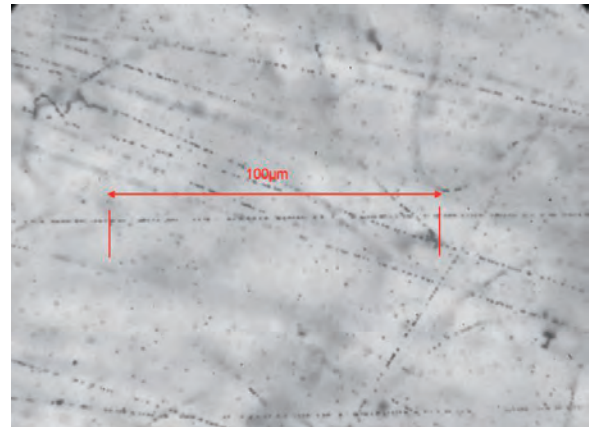


Fig. 1. Microscopic view of emulsion recorded charged track.

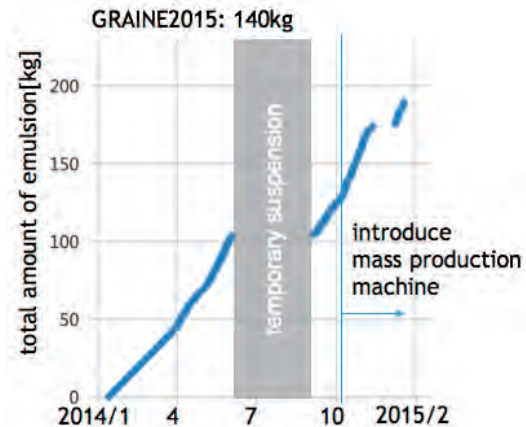


Fig. 2. Time profile of mass production for 2015 experiment.

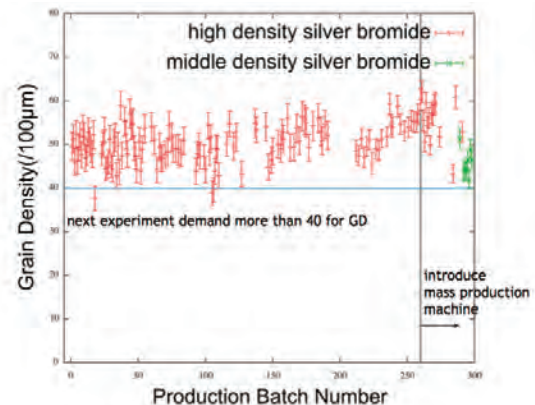


Fig. 3. Performance of produced silver bromide emulsions.

Others

Development of the Backward-Illuminated Photocathode for SRF GUN

T. Konomi¹, R. Inagaki², M. Hosaka³, N. Yamamoto³, Y. Takashima^{2,3} and M. Katoh^{1,3}

¹UVSOR Facility, Institute for Molecular Science, Okazaki 444-8585, Japan

²Graduate School of Engineering, Nagoya University, Nagoya 464-8603, Japan

³Nagoya University Synchrotron Radiation Research Center, Nagoya 464-8603, Japan

Photocathode electron gun is a key component of the high brightness synchrotron radiation source such as free electron laser, energy recovery linac, etc. Superconducting RF gun has advantages on the high gradient and high duty operation because CW high power RF operation is capable. Figure 1 shows the superconducting RF gun cavity under development [1]. The cavity is made of pure niobium, and RF surface resistance is 1/1,000,000 compared with pure copper cavity. Therefore the gun can accelerate high current beam with high accelerating field.

Backward illumination with a transparent photocathode is desirable from the good laser operability point of view because it gives better laser pointing stability, laser shape operability with fiber bundle and a high numerical aperture lens. Figure 2 shows the scheme of the gun. The excitation light (laser) is illuminated to the backside of the photocathode, and the electron beam emitted from front side of the photocathode and accelerated in RF field.

We studied the backward illumination for the transparent photocathode in a superconducting RF gun and we found that a combination of a transparent superconductor LiTi₂O₄ and the high brightness photocathode K₂CsSb is a candidate. Figure 3 shows the structure of the photocathode. The transparent superconductor LiTi₂O₄ is epitaxially grown on transparent substrate MgAl₂O₄ [2]. RF is reflected at LiTi₂O₄ because RF Skin depth of the superconductor is several hundred nm. It's possible to protect the substrate with the insulation breakdown voltage.

Photocathode parameter was measured separately. The critical RF magnetic field was measured by SQUID (Fig.4). The operation RF magnetic field of SRF gun is 4.3 mT on the photocathode. The photocathode has double margin about RF field at 5K.

The quantum efficiency has the peak at green wavelength range (Fig.5).

We will develop SRF gun development such as laser development by using these cathode data.



Fig. 1. Superconducting RF gun cavity.

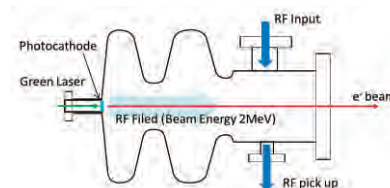


Fig. 2. Scheme of developed electron gun.

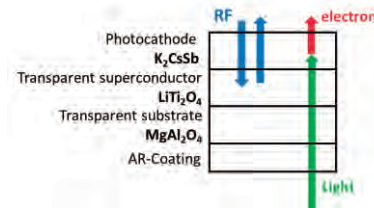


Fig. 3. The photocathode structure.

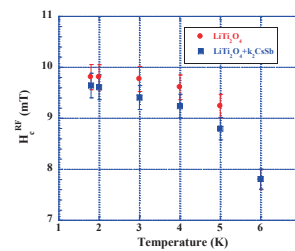


Fig. 4. Critical RF magnetic Field of LiTi₂O₄.

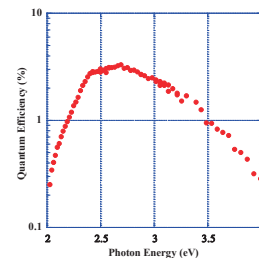


Fig. 5. Quantum efficiency of the photocathode.

[1] R. Matsuda *et al.*, PASJ11, MOOL13, 2014.

[2] A. Kumatani *et al.*, Appl. Phys. Lett. **101** (2012) 123103.

BL1U, Accelerators

Generation of Laser Compton Scattered Gamma-Ray Using a 1.95- μm Fiber Laser at UVSOR Facility

H. Zen¹, Y. Taira², T. Konomi^{3,4}, J. Yamazaki³, T. Hayakawa⁵, T. Shizuma⁵, T. Kii¹,
H. Toyokawa², M. Katoh^{3,4} and H. Ohgaki¹

¹Institute of Advanced Energy, Kyoto University, Uji 611-0011, Japan

²National Institute of Advanced Industrial Science and Technology (AIST), Tsukuba 305-8568, Japan

³UVSOR Facility, Institute for Molecular Science, Okazaki 444-8585, Japan

⁴School of Physical Sciences, The Graduate University for Advanced Studies (SOKENDAI), Okazaki 444-8585, Japan

⁵Japan Atomic Energy Agency, Tokai-mura 319-1184, Japan

High energy and quasi-monoenergetic gamma-rays can be generated by Compton backscattering between high energy electron beams and laser beams [1]. The gamma-rays are called as LCS (Laser Compton Scattering) gamma-ray and have unique and good features such as energy tunability, variable polarization and good directivity. Therefore, the LCS gamma-rays are very useful for various purposes. In order to generate narrowband and intense LCS gamma-ray, high current, low emittance and small energy spread electron beam must be provided.

In the UVSOR facility, high current (300 mA, top-up), low emittance (17.5 nm-rad) and small energy spread (5.26×10^{-4}) electron beam circulating in the UVSOR-III storage ring with electron energy of 750 MeV is available [2]. Those features of electron beam are very good for generating narrowband and intense LCS gamma-ray. Therefore, we proposed development of LCS gamma-ray source in the UVSOR facility.

In this fiscal year, we installed a 1.95- μm fiber laser in the downstream side of BL1U and performed LCS gamma-ray generation experiment. The experimental setup is shown in Fig. 1. Laser beam with 1.95- μm wavelength was injected from downstream side of BL1U and scattered by electron beam circulating in the storage ring. The characteristics of the fiber laser are listed in Table 1. The energy spectrum of generated LCS gamma-ray include detector efficiency is shown in Fig. 2. We have successfully generated LCS gamma-rays whose maximum energy of about 5.4 MeV. The gamma-ray yield with the beam current of 300 mA and laser power of 5 W is expected to be about 3×10^5 photons/s in 3% bandwidth.

Table 1. Characteristics of the 1.95- μm Fiber Laser

Parameter	Specification
Operation mode	CW
Operation wavelength	1950 nm
Max. output power	5 W
Spectral linewidth	< 1 nm
Beam quality, M^2	< 1.1
Output polarization	Linear

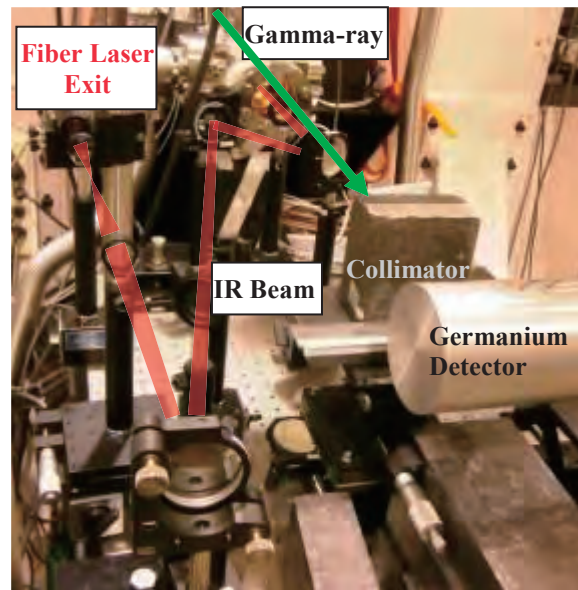


Fig. 1. Setup of LCS experiment at the downstream of BL1U.

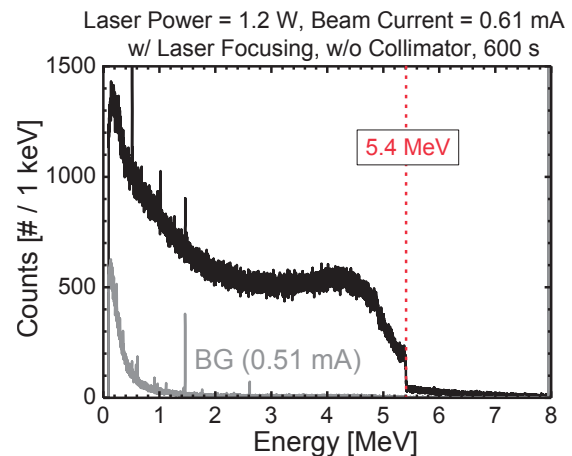


Fig. 2. Measured gamma-ray spectrum with and without laser injection.

[1] F. V. Hartemann *et al.*, Phys. Rev. ST Accel. Beams **8** (2005) 100702.

[2] M. Adachi *et al.*, J. Phys.: Conf. Ser. **425** (2013) 042013.

BL1U

Observation of Light's Orbital Angular Momentum from Helical Undulator Harmonics

S. Sasaki¹, A. Miyamoto¹, M. Hosaka², N. Yamamoto², T. Konomi³ and M. Katoh³

¹Synchrotron Radiation Center, Hiroshima University, Higashi-Hiroshima 739-0046, Japan

²Nagoya University Synchrotron Radiation Research Center, Nagoya, 464-8603, Japan

³UVSOR Facility, Institute for Molecular Science, Okazaki, 444-8585, Japan

The phenomenon of higher harmonic radiation from a helical undulator carrying orbital angular momentum (OAM)[1] attracts a great deal of attention because this novel property may be used as a new probe for synchrotron radiation science[2] that would be performed in a diffraction limited light source facility.

Although a diffraction limited x-ray source does not yet exist, the 750 MeV UVSOR-III is already a diffraction limited light source in the ultra violet (UV) wavelength region. In this ring, a tandem-aligned double-APPLE undulator system similar to that in BESSY-II [3] is installed for FEL and coherent light source experiments. Using this set-up, we observed spiral interference patterns between two different harmonic radiations with a scanning fiber multi-channel spectrometer and a CCD camera placed at the end of BL1U Beamline. By these measurements, various interference patterns such as single, double, and triple spirals were observed which concur with the theoretical prediction for every mode in the right or left circular polarization[4]. Figure 1 shows the layout of undulator system and beamline.

A schematic view of experimental set-up for the interference measurements with a CCD camera is shown in Fig. 2.

Figure 3 shows examples of interference patterns.

The rotation of an interference pattern by rotating a polarizer was also observed as shown in Fig.4.

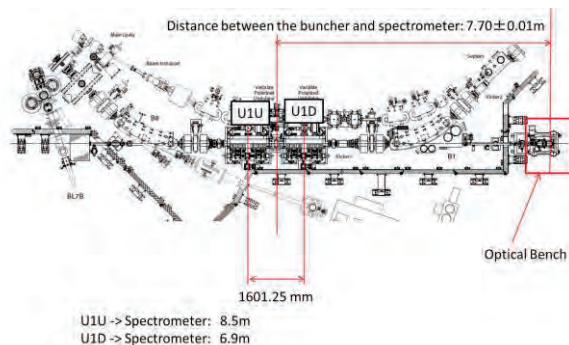


Fig. 1. Drawings of undulators and BL-1U beamline.

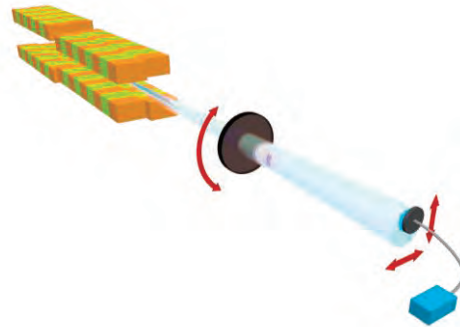


Fig. 2. Experimental set-up for interference measurements with a CCD camera.

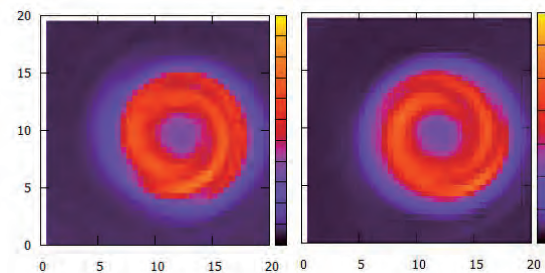


Fig. 3. Double spiral by interference between 1st & 3rd harmonic. $E = 500$ MeV, $\varepsilon_0 = 8$ nrad, $\lambda = 250$ nm.

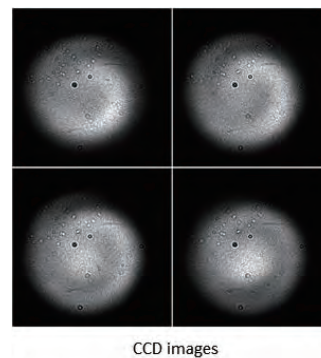


Fig. 4. Spiral rotation, 1st & 2nd harm.interference. Rot. Angle: TL: 0°, TR: 30°, BL: 60°, BR: 90°.

[1] S. Sasaki and I. McNulty, Phys. Rev. Lett. **100** (2008) 124801.

[2] M. VanVeenendaal and I. McNulty, Phys. Rev. Lett. **98** (2007) 157401.

[3] J. Bahrtdt, *et al.*, Phys. Rev. Lett. **111** (2013) 034801.

[4] S. Sasaki, A. Miyamoto, M. Hosaka, N. Yamamoto, T. Konomi and M. Katoh, to be published.

BL2B

Reconstruction of the Beamline BL2B for Development of Photoelectron Spectroscopy for Organic Materials II

S. Kera^{1,2}, K. R. Koswattage³, K. Yonezawa², Y. Nakayama², K. K. Okudaira² and H. Ishii^{2,3}¹Institute for Molecular Science, Okazaki 444-8585, Japan²Graduate School of Advanced Integration Science, Chiba University, Chiba 263-8522, Japan³Center for Frontier Science, Chiba University, Chiba 263-8522, Japan

The beamline BL2B has been reconstructed for characterizing the wide range of molecular materials *via* angle-resolved photoelectron spectroscopy (ARPES) to achieve the fundamental understanding of charge transport properties, adsorption properties, interface energetics, chemical reactivity and so on, since September 2013.

The BL2B originally consists of M0, and M1 pre-focusing mirrors, entrance slit, monochromator, movable exit slit and M4 refocusing mirror. The monochromator consists of G1, G2, and G3 spherical gratings and M2 and M3 plane mirrors system [1, 2]. The monochromator was designed to cover the energy range of 23 – 205 eV and used for gas phase experiments till 2012.

In the initial process, the beamline was mainly reconstructed solving a malfunction of the M2 and M3 mirror system in the monochromator, introducing a UHV chamber (monitoring chamber) downstream of the M4 mirror chamber, building a new interlock system, placing a new end-station for the ARPES equipped with a hemispherical analyzer (SCIENTA R3000) [3]. Then, the beam line was carefully aligned starting from adjusting M0, M1, and subsequently adjusting the optics in the monochromator and M4 mirror. A typical spot size after the M4 refocusing mirror is roughly estimated to be about 1.5 mm × 0.8 mm (vertical × horizontal) for exist slit of 300 μm by a four directional slit (in between the M4 mirror & the monitoring chamber) edges scan.

The photon flux for an exit slit width of 300 μm are estimated to be $1 \times 10^{10} - 3 \times 10^{10}$, $4 \times 10^{10} - 2 \times 10^{11}$, and $1 \times 10^{10} - 2 \times 10^{10}$ photons/s for G1 (80 – 150 eV), G2 (50– 120 eV) and G3 (25 – 55 eV) gratings, respectively using a silicon photodiode (AXUV-100, IRD) and Au mesh in the monitoring chamber. The estimated photon flux is one order of magnitude smaller than the expecting value from the references [1, 2] and the decrement may be due to contamination of the optics, a slight misalignment of the light and so on.

The contribution of the second order light was estimated to be 10% at 28 eV and it can be reduced to 2.4% by inserting a metal filter (Al20nm/Mg300nm /Al20nm/Ni70nm, LUXEL) in the monitoring chamber. The accuracy of the photon energy at 28 eV was checked by measuring Fermi edge of gold considering the first and second order light, leading a difference of -0.04 eV.

The beamline resolution was determined by measuring Fermi edge of gold at low temperature ~13 K. Refereeing a preciously determined energy resolution of the analyzer ($\Delta R=2.3\text{meV}$ at pass energy (E_p) of 2eV and analyzer slit of 0.2mm) by Xe gas cell experiments, the photon energy resolution is estimated to be 14 ± 1 meV at 28 eV, and the value is consistent with the literature ($E/\Delta E = 2,000$ @Slit 500μm) [1]. Consequently, one can obtain the ARPES data for a Au(111) surface as shown in Fig.1.

M0 mirror is cooled by water cooling system to improve the stability of the synchrotron light, however currently the cooling system having a problem where the mirror system cannot be cooled. Thus, the stability of the photon energy and flux has been carefully checked repeatedly measuring the binding energy and intensity of Au 4f at the photon energy of 110 eV. The result confirms that a stability to a certain extent of the light for a 24 hours continuous measurements which may not be a drawback for future experiments at BL2B.

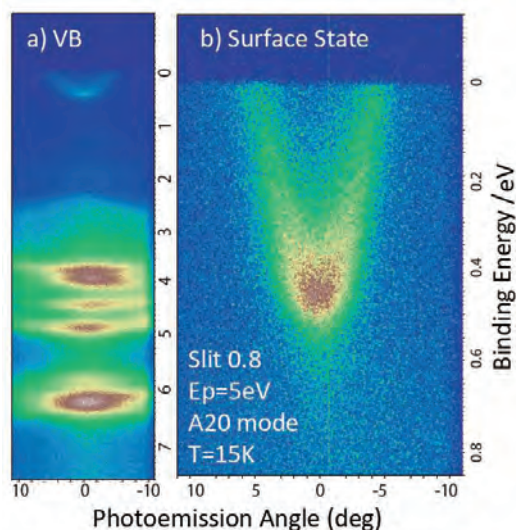


Fig. 1. ARPES of a clean Au(111) surface taken at 15 K and $h\nu = 28$ eV. (a) Valence band (VB) region is recorded for 5min and (b) surface state region is recorded for 40min to obtain an image.

[1] H. Yoshida and K. Mitsuke, *J. Synch. Rad.* **5** (1998) 774.

[2] M. Ono, H. Yoshida and K. Mitsuke *Nucl. Instrum. Meth. Phys. Res. A* **467-468** (2001) 577.

[3] S. Kera *et al.*, *UVSOR Act. Repo2013* **41** (2014) 38.

BL6B, BL1U

Microbunching Instability in Relativistic Electron Bunches: Direct Observations of the Microstructures Using Ultrafast YBCO Detectors

E. Roussel¹, C. Evain¹, C. Szwaj¹, S. Bielawski¹, J. Raasch², P. Thoma², A. Scheuring², M. Hofherr², K. Ilin², S. Wunsch², M. Siegel², M. Hosaka³, N. Yamamoto³, Y. Takashima³, H. Zen⁴, T. Konomi⁵, M. Adachi⁵, S. Kimura⁵ and M. Katoh⁵

¹Laboratoire PhLAM, Université Lille 1, 59655 Villeneuve d'Ascq, France

²Institute of Micro- and Nanoelectronic Systems, Karlsruhe Institute of Technology, 76187 Karlsruhe, Germany

³Synchrotron Radiation Research Center, Nagoya University, Nagoya 464-8603, Japan

⁴Institute of Advanced Energy, Kyoto University, Uji 611-0011, Japan

⁵UVSOR Facility, Institute for Molecular Science, Okazaki 444-8585, Japan

During the synchrotron radiation process, each electron is exposed to the radiation emitted by the others. At high electron bunch charge, this collective effect is at the origin of an instability that leads to the spontaneous formation of spatial structures inside the electron bunch: the microbunching instability (or CSR instability). This very fundamental electromagnetic phenomenon is known as a limitation in various types of accelerators, and at the same time as a great opportunity for the generation of giant pulses of Terahertz radiation (Coherent Synchrotron Radiation or CSR). This phenomenon is also suspected to be at the origin of coherent emission in solar flares.

Although this is a well-known fact, direct experimental observations of the structures, or the field they emit (CSR), remained up to now an open problem. In the present work, we attempted to observe directly such a structure in a storage ring, and follow its evolution over many turns.

The experimental setup is displayed in Fig. 1. The UVSOR-III storage ring was operated in single bunch, above the microbunching instability threshold. The spontaneously formed structure (with ~ 9 nm wavelength) emitted a coherent radiation (at the same wavelength). This radiation was detected using an ultrafast detector developed by the Institute of Micro- and Nanoelectronic Systems (KIT, Germany). This detector has the capability to measure the total electric field evolution, with a time resolution that is better than fastest oscilloscope speeds (17 ps at the time).

The experimental recordings immediately revealed that we had access to the full shape of the CSR pulses (including envelope and carrier), and which are a direct “image” of the microstructures (Fig. 2). Then, the data quickly appeared as a powerful and severe reference for the tests of theoretical models. Comparison with numerical simulations quickly revealed model limitations, and how the models should be refined to reproduce the experimental data. These studies were also performed in presence of laser perturbations, using the slicing setup installed at BL1U (see Ref. [1] for details).

More generally, the possibility to “see” directly the

microstructures shape and its evolution at each turn opens the way to tests of models, and control strategies that were not possible before.

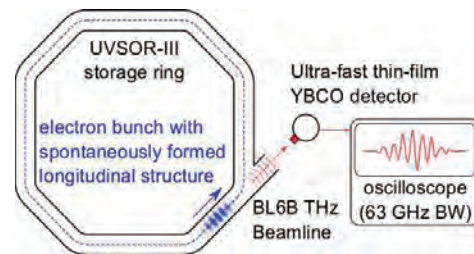


Fig. 1. Experimental setup.

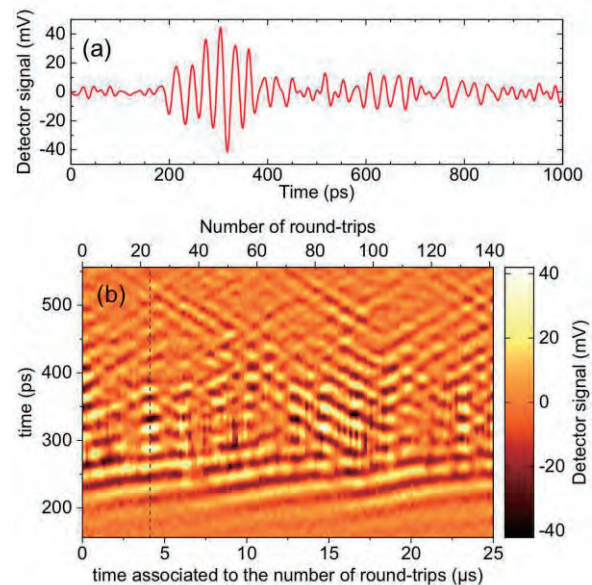


Fig. 2. (a) Typical pulse shape associated to a burst of CSR radiation that carries the information on the electron bunch microstructure. (b). Series of pulse shapes at successive round-trips in the ring.

[1] E. Roussel *et al.*, Phys. Rev. Lett. **113** (2014) 094801.

<http://dx.doi.org/10.1103/PhysRevLett.113.094801>.

BL7B

Evaluation of the VUV Coating Performed on the Flight Mirrors of the CLASP Sounding Rocket

N. Narukage¹, M. Kubo¹, R. Ishikawa¹, Y. Katsukawa¹, S. Ishikawa¹, T. Kobiki¹, G. Giono¹,
R. Kano¹, T. Bando¹ and S. Tsuneta²

¹National Astronomical Observatory of Japan, Mitaka 181-8588, Japan

²Institute of Space and Astronautical Science, Japan Aerospace Exploration Agency, Sagami-hara 252-5210, Japan

Our team consisting of Japan, US, Spain, France, and Norway is developing a Chromospheric Lyman-Alpha SpectroPolarimeter (CLASP), which is proposed to fly with a NASA sounding rocket in 2015 [1, 2]. CLASP will explore the magnetic fields in the solar atmosphere (the upper chromosphere and transition region) via the Hanle effect in the Lyman-alpha ($\text{Ly}\alpha$) line (121.6 nm) for the first time. This experiment requires precise spectropolarimetric observations with a polarimetric sensitivity of $3\sigma \sim 0.1\%$ and a wavelength resolution of 0.01 nm.

In order to achieve the polarimetric sensitivity of $3\sigma \sim 0.1\%$, CLASP requires the high throughput for suppressing the photon noise. For this purpose, CLASP consists of minimum number of reflective mirrors [3]. And, we have developed three types of high-efficiency VUV reflective coatings, namely, a reflective narrow band filter coating [4], a high reflectivity polarizing coating [5], and a high reflectivity mirror coating.

In 2014, we fabricated the flight mirrors and performed the high-efficiency VUV reflective coatings on such flight mirrors. In order to evaluate the performance of the flight coatings, witness samples (whose diameters are 1 inch or 30 mm) were coated simultaneously with the flight mirrors. Using these witness samples, we evaluated the performance of the flight coatings at UVSOR BL7B with our measurement system shown in Fig. 1 (see the details in Narukage *et al.* [5]).

The reflective narrow band filter coating was applied to the 290 mm diameter primary mirror (see Fig. 2). The measured reflectivity in $\text{Ly}\alpha$ is about 56%. Meanwhile, the reflectivity in visible light and infrared is less than 5 % in average. Hence, this coating can efficiently remove the unwanted visible light and heat, which are the dominant components in the solar spectrum. Additionally, this coating is enough uniform across the entire 290 mm diameter to suppress the polarization caused by the non-uniformity of the coating to less than $10^{-3}\%$ [6].

The high reflectivity polarizing coating on the flight polarization analyzer has a performance of $R_s \sim 55\%$ and $R_p \sim 0.3\%$ at their Brewster's angle of 68 degree in $\text{Ly}\alpha$, where R_s and R_p are reflectivity for s- and p-polarized beam, respectively. This coating has ~ 2.5 times higher efficiency than MgF_2 , and high polarization power ($\equiv (R_s - R_p) / (R_s + R_p)$) of 98.9 %.

Other mirrors, namely, secondary mirror and two

camera mirrors, were coated with the high reflectivity mirror coating. The measured reflectivity is more than 80 % in $\text{Ly}\alpha$.

On the bases of these measurements with BL7B, we confirmed that all of the coatings on the CLASP flight mirrors satisfy the specifications determined for the polarimetric sensitivity of $3\sigma \sim 0.1\%$.

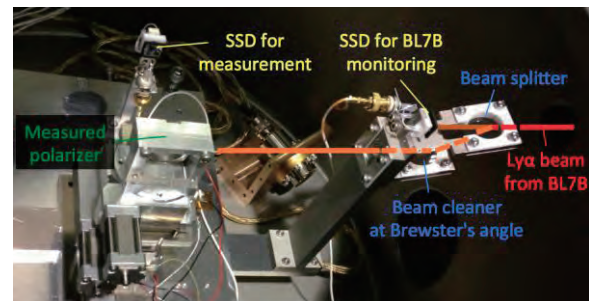


Fig. 1. Photo of our measurement system.

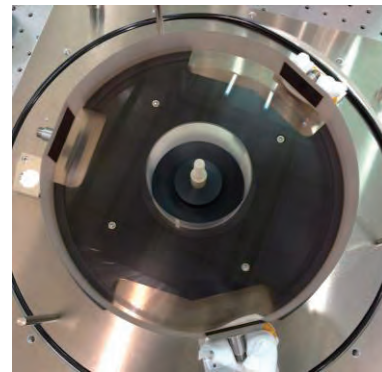


Fig. 2. Photo of the CLASP primary mirror.

- [1] R. Kano *et al.*, SPIE **8443** (2012) 84434F.
- [2] K. Kobayashi *et al.*, Proc. Fifth Hinode Science Meeting, Astronomical Society of the Pacific Conference Series **456** (2012) 233.
- [3] N. Narukage *et al.*, Applied Optics **54** (2015) 2080.
- [4] N. Narukage *et al.*, UVSOR Activity Report 2012 **40** (2013) 46.
- [5] N. Narukage *et al.*, UVSOR Activity Report 2012 **40** (2013) 47.
- [6] R. Ishikawa *et al.*, Solar Physics **289** (2014) 4727.

BL7B

The Improvement and Evaluation of VIS-VUV Ellipsometry

Y. Kubo¹, K. Fukui¹, K. Yamamoto², T. Saito³ and T. Horigome⁴

¹Department of Electrical and Electronics Engineering, University of Fukui, Fukui 910-8507, Japan

²FIR Center, University of Fukui, Fukui 910-8507, Japan

³Department of Environment and Energy, Tohoku Institute of Technology, Sendai 982-8577, Japan

⁴UVSOR Facility, Institute for Molecular Science, Okazaki 444-8585, Japan

Recently, the need for quantitative measurements of ultraviolet (UV) - vacuum UV (VUV) radiation is increasing with the expanding applications of the radiation for sterilization, curing, *etc.*. However, most widely used Si photodiodes, have a serious problem of degradation under UV exposure. To develop stable new UV detectors, accurate optical constants of alternative materials, especially of wide bandgap ones, composing a detector are necessary. Although commercially available spectroscopic ellipsometers (SE) are known as a powerful tool to obtain optical constants with high accuracy, the highest photon energy limit is typically in the near UV. Therefore, we are improving a visible (VIS) – VUV SE which is designed by an AIST group [1] to optimizing for the use at BL7B. In this report, we show present status of a VIS-VUV SE at BL7B.

Figure 1 shows the side view of VIS-VUV SE. In this SE, an oblique incident photodiode and a sample chamber are rotated along the incident beam axis (β and α rotations) instead of the rotations of an analyzer and a polarizer, respectively. Then, both rapid and accurate 5-axis adjustable mechanical system to align mechanical α rotation axis with the light axis is required. To realize computer controlled adjustable mounting at the narrow working space of BL7B, we design and construct a mount using parallel link mechanism. Measurement accuracy drastically increases after installing this mount.

Figure 2 shows both the refractive index n and the extinction coefficient k of Au mirror as a function of photon energy. Color symbols represent measurement results under various experimental conditions. The solid lines show the standard table data of Au [2] for comparison. Although measurement errors mainly affect the accuracy of extinction coefficient k according to the measurement principles, k shows good agreement with reference data in the whole measurement photon energy range. However, the accuracy of n is not enough at present and further improvement is needed, though absolute values of n are in agreement with rough surface Au thin film [3]

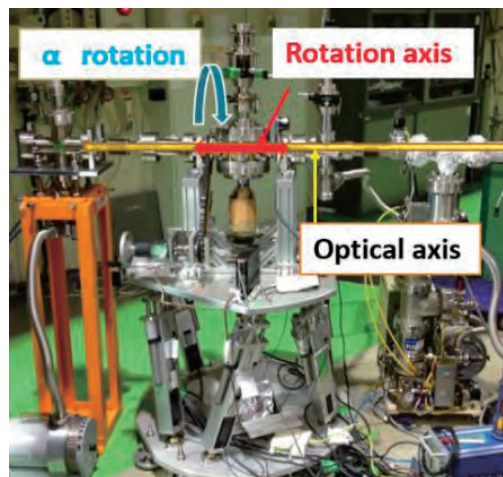


Fig. 1. Side view of a visible - vacuum ultraviolet spectroscopic ellipsometer at BL7B.

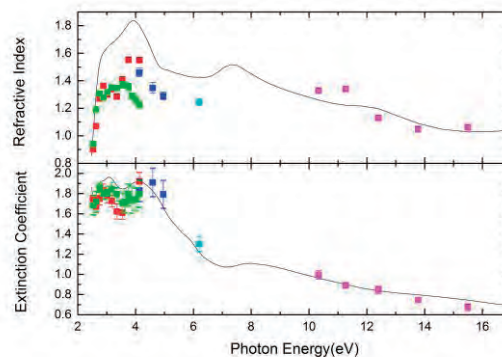


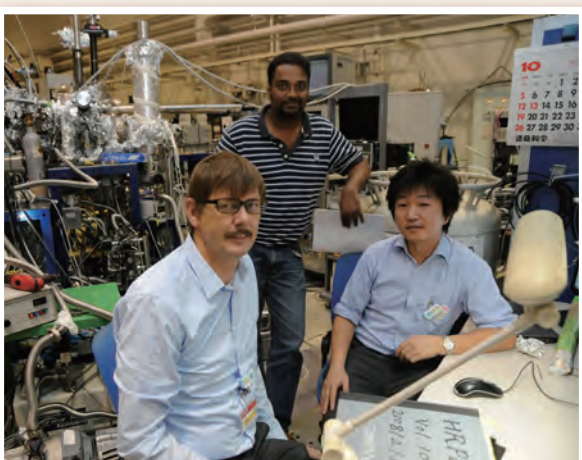
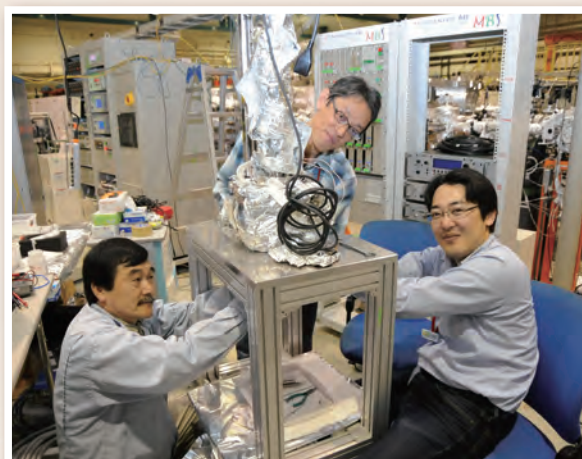
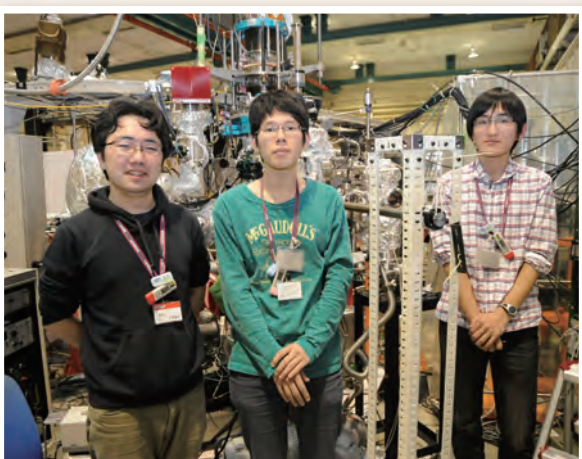
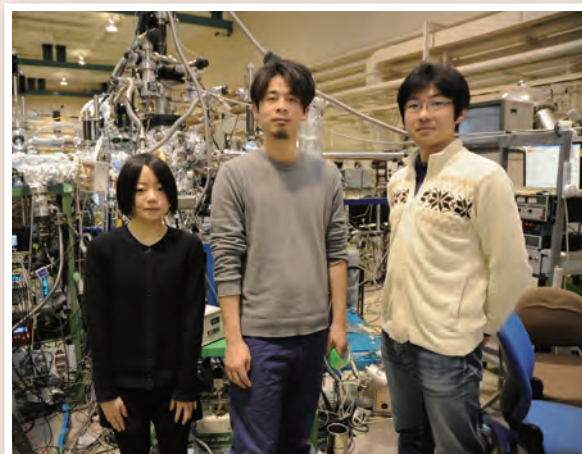
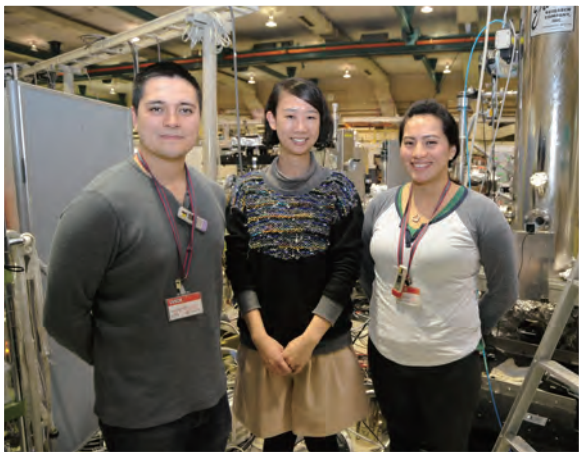
Fig. 2. Photon energy dependences of both refractive index and extinction coefficient of Au mirror.

[1] T. Saito, M. Yuri and H. Onuki, *Rev. Sci. Instrum.* **66** (1995) 1570.

[2] D.E. Gray *ed.*, *American Institute of Physics Handbook 3rd edition* (McGraw-Hill, 1972) 6-136.

[3] M. L. Theye, *Phys. Rev. B* **2** (1970) 3060.

UVSOR User 3



The background is a vibrant blue. In the upper right, there is a large, semi-transparent circular graphic composed of several concentric rings. The outermost ring features a series of small, light-blue circles. Below this graphic, the text 'III-2' is prominently displayed in a large, white, serif font. Underneath the main title, the words 'Materials Sciences' are written in a smaller, white, sans-serif font. The bottom half of the page is filled with a fine, light-blue grid of small dots.

III-2

Materials Sciences

BL1B

Terahertz Reflectivity Spectra of Superionic Conductors

T. Awano

Faculty of Engineering, Tohoku Gakuin University, Tagajo 985-8537, Japan

Superionic conductors are solids which have high ionic conductivity as liquids or electrolyte solutions. I have measured their reflectivity spectra at millimeter wave and far-infrared region to investigate motions of mobile and immobile ions [1-7]. Ionic plasmonic feature in energy loss function spectra were observed in millimeter wave region of these superionic conductors.

Terahertz spectral region is the frequency region between vibration and translation motion of the mobile ion. The “attempt mode” of conduction ion were also observed in these superionic crystals. This vibrational mode is directly connected with translational movement of conduction ion. Namely, silver ion surrounded by iodine tetrahedron try to move out at this frequency, c.a. 20 cm^{-1} .

On the other hand, the attempt mode was not clear in AgI-based superionic conductive glasses. Therefore, precise measurement of reflectivity spectra of these glasses was executed at the new terahertz beam line BL1B.

Reflectivity spectra of $(\text{AgI})_{0.5}(\text{AgPO}_3)_{0.5}$ glasses and $(\text{AgI})_{0.75}(\text{Ag}_2\text{MoO}_4)_{0.25}$ glasses were measured by FARIS Martin-Puplett interferometer and QMC InSb hot electron bolometer. The spectral region is suitable for the observation of the attempt mode of silver ion.

Figure 1 shows spectra of four glass samples at room temperature. The attempt mode was observed in #1 sample of each glass. In contrast, #2 samples showed no such absorption at 20 cm^{-1} . This difference seems to be due to the difference of glass structure. Much AgI-clusters may exist in the #1 glass samples. Characterization of the glass structure is necessary to make it clear.

Proton conductors are interested because of the use in fuel cells. The $\text{Cs}_2(\text{HSO}_4)(\text{H}_2\text{PO}_4)$ crystal is a newly discovered room temperature proton conductor[8]. It keeps high ionic conductivity once after heating above 380 K. It is interesting to make clear the mechanism of such conductivity dependence by thermal history. Figure 2 shows reflectivity spectra of $(\text{AgI})_{0.5}(\text{AgPO}_3)_{0.5}$ glasses at room temperature. Anisotropic peaks were observed as shown in the Fig. 2. The measurement of the change of these absorption bands after the heating is underway.

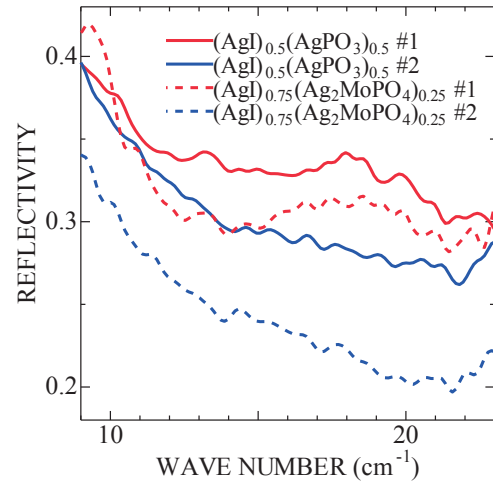


Fig. 1. Reflectivity spectra of $(\text{AgI})_{0.5}(\text{AgPO}_3)_{0.5}$ and $(\text{AgI})_{0.75}(\text{Ag}_2\text{MoO}_4)_{0.25}$ glasses.

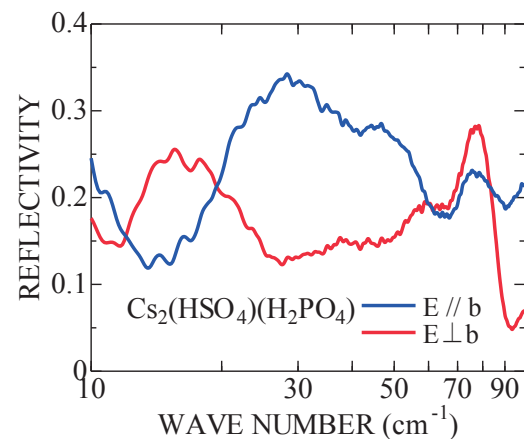


Fig. 2. Reflectivity spectra of $\text{Cs}_2(\text{HSO}_4)(\text{H}_2\text{PO}_4)$ crystal.

- [1] T. Awano, T. Nanba, M. Ikezawa, T. Matsuyama and H. Yamaoka, *Solid State Ionics* **53-56** (1992) 1269.
- [2] T. Awano, *Infrared Phys. Tech.* **51** (2008) 458.
- [3] T. Awano and T. Takahashi, *J. Phys. Soc. Jpn.* **79** suppl.A (2010) 118.
- [4] T. Awano and T. Takahashi, *Journal of Physics: Conference Series* **148** (2009) 012040.
- [5] T. Awano and T. Takahashi, *Proc. 13th Asian Conference on Solis State Ionics*, World Scientific (2012) 569.
- [6] T. Awano, T. Nanba and M. Ikezawa, *UVSOR Activity Report 1992* **20** (1993) 146.
- [7] T. Awano, *UVSOR Activity Report 2011* **39** (2012) 91.
- [8] C. R. I. Chisholm and S.M. Haile, *Acta Cryst.* **B55** (1999) 937.

BL1B

THz Spectra of Hole-Doped $\text{CeOs}_2\text{Al}_{10}$

H. Takao¹, S. Kamei¹, Y. Yamada², J. Kawabata², T. Takabatake² and S. Kimura^{3,1}

¹Department of Physics, Osaka University, Toyonaka 560-0043, Japan

²ADSM, Hiroshima University, Higashi-Hiroshima 739-8530, Japan

³Graduate School of Frontier Biosciences, Osaka University, Suita 565-0871, Japan

Kondo insulators/semiconductors (KIs) are materials with a tiny energy gap at the Fermi level (E_F) owing to the hybridization between conduction and localized $4f$ electrons, namely c - f hybridization. Because of the strong c - f hybridization intensity, KIs do not order magnetically by the Ruderman-Kittel-Kasuya-Yosida (RKKY) interaction. However, recently observed KIs, $\text{Ce}M_2\text{Al}_{10}$ ($M = \text{Ru}, \text{Os}$), have an antiferromagnetic magnetic ordering at the temperature (T_0) of about 27 K [1]. Since the ordering temperature is too high compared with that expected from the de Gennes factor [2], another mechanism of the magnetic ordering besides the RKKY interaction is anticipated.

One of such TIs, $\text{CeOs}_2\text{Al}_{10}$ has a clear energy gap below the photon energy of about 50 meV [3]. T_0 of this material is strongly suppressed by the hole doping due to the substitution of Os by Re, $\text{Ce}(\text{Os}_{1-x}\text{Re}_x)_2\text{Al}_{10}$, and disappears at $x = 0.05$ [4]. Then we have investigated the relation of the c - f hybridization gap to the magnetic ordering using the material of $x = 0.05$.

$\text{Ce}M_2\text{Al}_{10}$ s have anisotropic crystal and electronic structures as well as the anisotropic c - f hybridization intensity [5]. The energy gap owing to the c - f hybridization clearly appears along the c axis. Then we measured the temperature-dependent polarized reflectivity [$R(\omega, T)$] spectra of $x = 0.05$ along the c axis at the beamline 1B using an automatic measurement system [6].

The obtained $R(\omega, T)$ spectra divided by that at 80 K in the terahertz region of 3 – 10 meV (0.7 – 2.4 THz) are shown in Fig. 1. Since the spectrum at 80 K is almost unity in this energy region because of its metallic conductivity, the $R(\omega, T)/R(\omega, 80 \text{ K})$ spectra are nearly equal to $R(\omega, T)$. The $R(\omega, T)$ spectrum strongly depends on temperature in this region. This origin is considered to be the temperature-dependent Drude weight due to carriers excited over an energy gap. This is the evidence of the existence of the energy gap.

The energy gap originates from the c - f hybridization, which remains at $x = 0.05$ even though the magnetic ordering disappears. This suggests that the c - f hybridization is not the sufficient condition for the magnetic ordering. However, in the case of other $\text{RM}_2\text{Al}_{10}$ ($R = \text{other rare-earth ions}$), which has no c - f hybridization, magnetic ordering temperature obeys the de Gennes factor indicating the RKKY interaction [2]. Therefore the c - f hybridization is basically

needed for the appearance of the high ordering temperature T_0 . These facts suggest that the unusual magnetic ordering of $\text{Ce}M_2\text{Al}_{10}$ does not directly originate from but indirectly relates to the c - f hybridization.

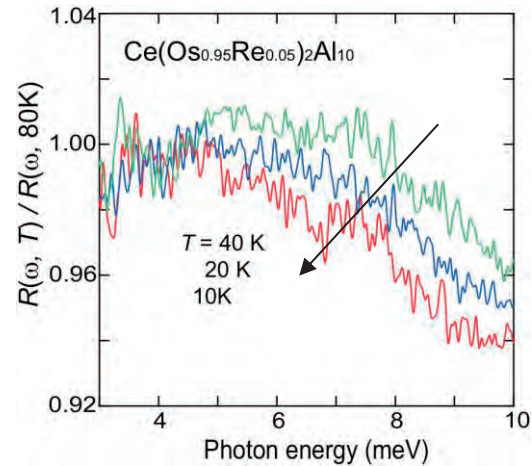


Fig. 1. Temperature dependence of relative reflectivity spectrum of $\text{Ce}(\text{Os}_{0.95}\text{Re}_{0.05})_2\text{Al}_{10}$ divided by that at 80 K in the photon energy region of 3 – 10 meV (0.7 – 2.4 THz). The observed Drude spectral weight is suppressed with decreasing temperature.

[1] T. Nishioka, Y. Kawamura, T. Takesaka, R. Kobayashi, H. Kato, M. Matsumura, K. Kodama, K. Matsubayashi and Y. Uwatoko, *J. Phys. Soc. Jpn.* **78** (2009) 123705.

[2] Y. Muro, J. Kajino, T. Onimaru and T. Takabatake, *J. Phys. Soc. Jpn.* **80** (2011) SA021.

[3] S. Kimura, T. Iizuka, H. Miyazaki, A. Irizawa, Y. Muro and T. Takabatake, *Phys. Rev. Lett.* **106** (2011) 056404.

[4] J. Kawabata, T. Takabatake, K. Umeo and Y. Muro, *Phys. Rev. B* **89** (2014) 094404.

[5] S. Kimura, Y. Muro and T. Takabatake, *J. Phys. Soc. Jpn.* **80** (2011) 033702.

[6] S. Kimura, *JASCO Report* **50** (2008) 6 [in Japanese].

BL2A

Local Structure Investigation around P Atom in Ag and Cu Doped Hydroxyapatite

M. Sato¹, H. Sakaguchi², Y. Inoue² and A. Nakahira^{2,3}

¹Institute for Materials Research, Tohoku University, Sendai 980-8577, Japan

²Graduate school of Engineering, Osaka Prefecture University, Sakai 599-8531, Japan

³Kansai Center for Industrial Materials Research, Tohoku University, Sakai 599-8531, Japan

Hydroxyapatite ($\text{Ca}_{10}(\text{PO}_4)_6(\text{OH})_2$, HAp) is a chief inorganics of our hard tissue and it has been widely used in medical field as artificial hard tissue due to its excellent biocompatibility and osteo-conductivity. However, there is the most significant problem of infection during the displacement surgery or after the operation[1]. When such infections occurred, it is necessary to repeat a surgery to replace the alternate implants. This is a significant burden for patient. In order to overcome these problems, imparting the antibacterial property to the implants is expected as one of the efficient method, and the development of alternate materials of hard tissue having antibacterial property have been strongly desired [2]. Therefore, Cu and Ag doped HAp, which are expected having an excellent antibacterial property, has been prepared by hydrothermal technique to prevent some infections during surgery, and the local structure around P atom of these sample was investigated by XAFS measurement at BL-2A in UVSOR.

Ag and Cu doped HAp samples were prepared by 0.1 mol/L $\text{Ca}(\text{NO}_3)_2$, $(\text{NH}_4)_2\text{HPO}_4$, CuCl_2 and AgNO_3 solutions, respectively. The Ca/P ratio was fixed at 1.67 and the amount of Ag and Cu changed in the range from 0 mol% to 10 mol% for Ca concentration of HAp. The pH value of each solutions were regulated by ammonia solution and tris buffer solution, respectively. Obtained slurry was filtrated and then dried at 323 K for overnight. The P K-edge XAFS spectra was corrected in BL-2A of UVSOR. The XAFS data of sample was obtained by fluorescence mode using InSb double crystal monochrometer and SDD detector. In a present study, unfortunately, the EXAFS spectra did not obtained due to the influence of absorption of M-edge of Au mesh which is using as an I_0 measurement.

Figure 1 shows P K-edge XANES spectra of Ag-HAp prepared by HT process. The obtained XANES spectra resembled to that of commercial HAp (HAp-200, Taihei Chemical Industrial Co., Ltd.), and the shape of XANES spectra did not change by increasing the Ag ratio. This result indicate that the secondary phase such as silver phosphate does not generate and the local structure around P atom does not changed by Ag addition.

Figure 2 shows P K-edge XANES spectra of Cu-HAp samples prepared by HT process. The P-K edge spectra of sample showed similar spectra to HAp-200 and $\text{Cu}_3(\text{PO}_4)_2$. This result means that the added Cu ion exists into HAp structure or forms

$\text{Cu}_3(\text{PO}_4)_2$. It is thought that since the local structure around P atom in both HAp and $\text{Cu}_3(\text{PO}_4)_2$ resembles each other, the obtained XANES spectra of HAp-200 and $\text{Cu}_3(\text{PO}_4)_2$ had similar shape. Therefore, it is difficult to decide that the Cu ion exists into HAp structure or forms $\text{Cu}_3(\text{PO}_4)_2$ from P-K XANES spectra only. In order to obtain the structural knowledge of Cu-HAp in detail, the measurement in EXAFS region is necessary in a future study. In Ag-L edge measurement, good spectra could not obtain in this measurement period.

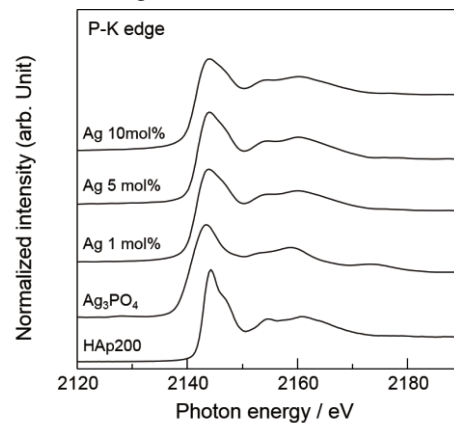


Fig. 1. P K-edge XANES spectra of Ag-HAp samples.

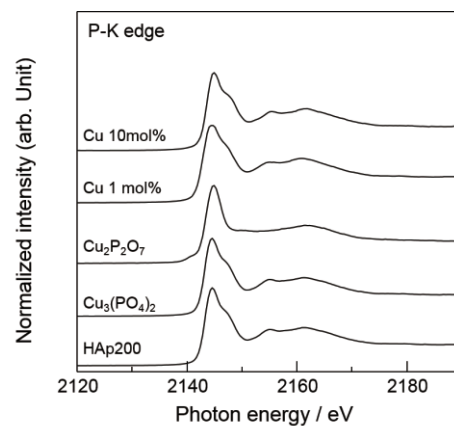


Fig. 2. P K-edge XANES spectra of Cu-HAp samples.

[1] M. Stigter, J. Bezemer, K. de Groot and P. Layrolle, *Journal of Controlled Release* **99** (2004) 127.

[2] L. Zhao, P. K. Chu, Y. Zhang and Z. Wu, *Journal of Biomedical Materials Research Part B: Applied Biomaterials* **91** (2009) 470.

BL2A

Study of Formation Processes of Active Mo Species over V-Doped Mo/H-AlGaMFI by Mo L_{III}-Edge XANES

H. Aritani¹, S. Mogi¹, N. Naijo¹, T. Sugawara¹, T. Kawai¹ and A. Nakahira²

¹Department of Life Science & Green Chemistry, Saitama Institute of Technology, Fukaya 369-0293 Japan

²Graduate School of Engineering, Osaka Prefecture University, Sakai 599-8531 Japan

Mo-modified H-MFI is a typical catalyst for MTB (Methane to Benzene) reaction, *i.e.*, methane dehydroaromatization. Although the MTB reaction is revolutionary for direct conversion of natural gas, deactivation due to coking over the catalyst cannot be avoided during the methane conversion. Clarification of the deactivation process over the catalysts is one of an important point for develop of highly active and durable MTB catalysts. In this study, time course of the formation and activation of active Mo species on H-MFI supports is investigated. The effects of Ga-doping onto MFI (GaAlMFI) support and Mo-V co-doping on GaAlMFI are also studied.

Catalyst samples were prepared by impregnation of each H-GaAlMFI (Si/Al₂=40) support with MoO₂(acac)₂-VO(C₅H₇O₂)₃-CHCl₃ solution (5wt% as MoO₃), and followed by dried and calcined at 773 K. GaAlMFI (Al/Ga=50-100) supports were synthesized hydro-thermally at 413 K for a week, and followed by ion-exchanging with NH₄Cl and calcined at 873 K. The catalytic MTB reactivity was evaluated by means of fixed-bed flow reaction at 1023 K, as described in a separate paper [1]. Mo L_{III}-edge XANES spectra were measured in BL2A of UVSOR-IMS in a total-electron yield mode using InSb double-crystal monochromator. Photon energy was calibrated by using Mo metal-foil, and normalized XANES spectra and their derivatives are presented. REX-2000 (Rigaku Co.) software was used by normalization of each XANES spectrum.

Figure 1 shows the XANES spectra of various Mo-V/GaAl-MFI catalysts after MTB reaction for 60 and 200 min. After the reaction for 60 min with highly catalytic activity, the edge energy (shown in Table 1) is almost as same as that of α -Mo₂C over the whole catalysts. At the same instant, the white lines peaked at ca. 2524 eV can be shown, indicating the formation excess carbonized Mo species. It suggests the formation of Mo-carbonaceous species in catalytically active state. After the reaction for 200min in deactivated state, the edge energy values over Mo/H-MFI and Mo-V/GaAlMFI, which are highly active and durable catalysts, are almost kept on at ca. 2522 eV. For significantly deactivated catalysts, Mo/GaAl-MFI and Mo-V-H-MFI, the edge energy values are almost as same as that of α -Mo₂C. Indeed, the Mo-V/GaAlMFI is the most highly active and durable catalyst for MTB, which is the least amount of deposited carbonaceous species analyzed by thermogravimetry. In contrast, Mo/H-MFI (V- and

Ga-free) catalysts show high activity only an initial state, and large amount of deposited carbonaceous species are shown over the catalysts. It is concluded that Both Ga-doping onto H-MFI and V-doping with Mo bring about the high and durable activity for MTB reaction by way of stable Mo-carbonaceous species without carbon deposition.

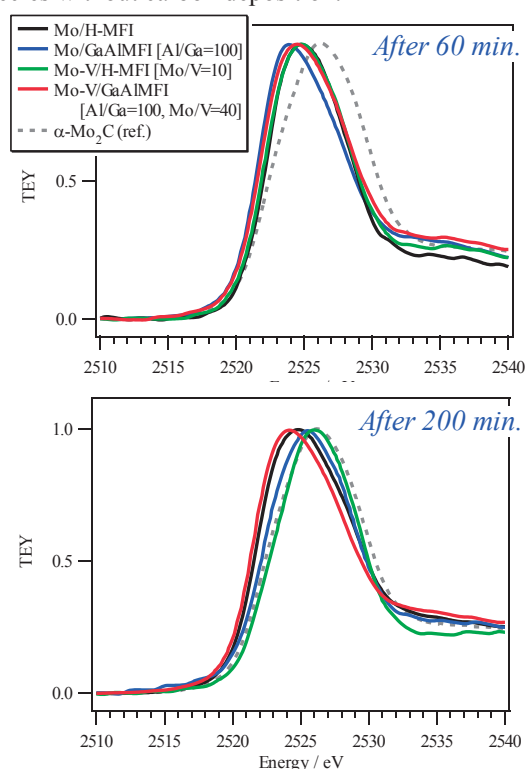


Fig. 1. Mo L_{III}-edge XANES of Mo-V/H-GaAlMFI catalysts after MTB reaction for 60 (top) and 200 (bottom) minutes at 1023 K.

Table 1. Edge energy value of the catalysts after MTB reaction for 60/200 min.

Catalyst	Time / min.	Edge Energy / eV
Mo/H-MFI40	60	2522.63
	200	2521.75
Mo/Ga(100)Al-MFI40	60	2521.75
	200	2522.35
Mo-V(10)/H-MFI40	60	2521.98
	200	2523.52
Mo-V(40)/Ga(100)Al-MFI40	60	2521.87
	200	2521.65
α -Mo ₂ C		2522.13

[1] H. Aritani, H. Shibasaki, H. Orihara and A. Nakahira, J. Environm. Sci. **21** (2009) 736.

BL2A

Local Environment Analysis of Mg Ions Doped in CaZrO₃:Tb

H. Fukaya¹, Y. Kubo¹ and T. Yamamoto^{1,2}

¹Faculty of Science and Engineering, Waseda University, Tokyo 169-8555, Japan

²Institute of Condensed-Matter Science, Waseda University, Tokyo 169-8555, Japan

Phosphor is a very attractive material in the combined use of the light emitting device (LED) and then a lot of researches have been already carried out for this material. One of the common strategies to synthesize stable phosphors for the industrial applications is the doping of the rare-earth ions in the matrix oxides. Among these, Tb doped CaZrO₃ was found to show bright green-light emission by UV irradiations [1]. In addition, it was reported that Mg co-doping into this material can increase the brightness of the green-light emission [1]. In order to understand the mechanism of this kind of change in brightness, it is important to know the local environment of doped ions in the matrix oxides. For such purpose, XANES analysis is quite powerful and we could successfully analyze wide variety of functional materials [2, 3]. In the current study, local environment of co-doped Mg ions in CaZrO₃:Tb is investigated by the X-ray absorption near-edge structure measurements at Mg K-edge.

Mg co-doped CaZrO₃:Tb was prepared by the conventional solid-state reaction method. Reagent grade CaCO₃, ZrO₂, Tb₄O₇ and MgO powders were used as starting materials. These powders were weighed changing the molar ratio of cations and mixed in an agate mortar. These mixed powders were pressed into cylindrical pellets, which were sintered in air at 1673 K for 6 hrs. Resultant specimens were ground and were provided to photoluminescence measurements. A concentration of the dopants with the most bright luminescence was 0.03 for both Tb and Mg, i.e., CaZr_{0.94}Tb_{0.03}Mg_{0.03}O₃. This sample was examined by the XRD measurements, which showed its crystal structure is single-phased and orthorhombic perovskite structure without any precipitates.

Mg-K XANES spectra of Mg co-doped CaZrO₃:Tb, MgO and Mg(OH)₂ were observed at BL2A in UVSOR by total electron yield method. The incident beam was monochromatized with a beryl (10T0) (2d = 15.965 Å) double crystal monochromator. Sample powders were put on the carbon adhesive tape, which are attached on the first Cu-Be dinode of the electron multiplier.

Observed Mg-K XANES spectra of Mg co-doped CaZrO₃:Tb (CaZr_{0.94}Tb_{0.03}Mg_{0.03}O₃) is shown in Fig. 1 together with those of MgO and Mg(OH)₂. Mg-K XANES profile of the Mg co-doped CaZrO₃:Tb shows similar one as that of MgO, but is quite different from that of Mg(OH)₂. From this comparison, it is suggested that the local environment of Mg ions in Mg co-doped CaZrO₃:Tb is similar to that in MgO, which is the 6-coordination of oxygen

ions. Such environment exists in CaZrO₃ as Zr⁴⁺ site. Finally, we could determine the local environment of Mg ions in CaZrO₃:Tb by the Mg-K XANES analysis.

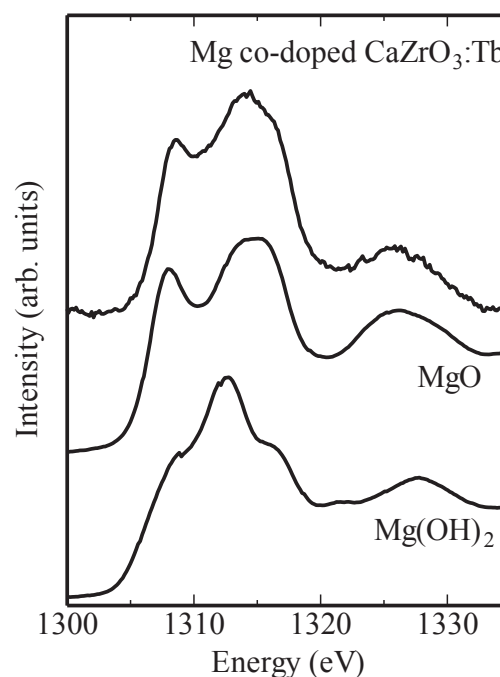


Fig. 1. Mg-K XANES spectra of Mg co-doped CaZrO₃:Tb, MgO and Mg(OH)₂.

- [1] Y. Shimizu *et al.*, Mater. Sci. Eng. B **161** (2009) 100.
- [2] T. Yamamoto, *et al.*, J. Phys.: Condens. Matter **21** (2009) 104211.
- [3] I. Tanaka *et al.*, J. Am. Cer. Soc. **88** (2005) 2013.

BL2A

Local Structure Analysis of the Charge-Discharge Process for Conversion Reaction of the Binary Metal Oxide Containing Aluminum Ion by XAFS Measurement

N. Sonoyama¹, Y. Ogasawara¹, T. Mizuno¹ and T. Tukada²

¹Graduate School of Engineering Science, Nagoya Institute of Technology, Nagoya, 466-8555, Japan

²Nagoya Institute of Technology Institute for Molecular Science, Okazaki 444-8585, Japan

Tarascon et al. reported that 3d transition metal oxides (MO, where M is Fe, Co, Ni, and Cu etc.) nanoparticles could reversibly react with lithium to achieve high theoretic capacities as high as 700 mAh g⁻¹ in 2000 [1–4]. The mechanism of the “conversion reaction” involves the formation and decomposition of Li₂O accompanied by a large amount of lithium ion reaction toward metal oxide nano particles. In this study, we have investigated the electrochemical reaction of Al³⁺ ion doped NiO which was synthesized using layered double hydroxide as a precursor by ex-situ XAFS measurement.

The solid solution of multiple metal oxides, Al^{III} dissolved NiO was prepared according to the method mentioned in the previous papers [9,10]. The ratio of divalent metal and other valent metals (Ni²⁺:Al³⁺) is 2:1 otherwise noted. X-ray absorption spectroscopy measurements were performed at the BL-2 in UV-SOR under the vacuum condition. Measurements are carried out by fluorescence method and photoelectric yield method. The electrochemical reacted samples are removed from the cell and rinsed with dimethyl carbonate and set in transfer vessel.

In Fig. 1, XANES spectra of as prepared Ni-Al oxide comparing with alumina power and aluminum foil. The absorption edge of as prepared Al-Ni oxide appeared at lower energy region than alumina power. This would be brought by the crystal structure of Ni-Al oxide.

In Fig. 2, XANES spectra of Ni-Al oxide reduced by discharging until 30 mV. The XANES spectrum of Ni-Al oxide hardly changed in comparison with pristine sample. This result is inconsistent with the increased capacity by aluminum introduction. This suggests that the reduction of aluminum ion is limited, not until metal state.

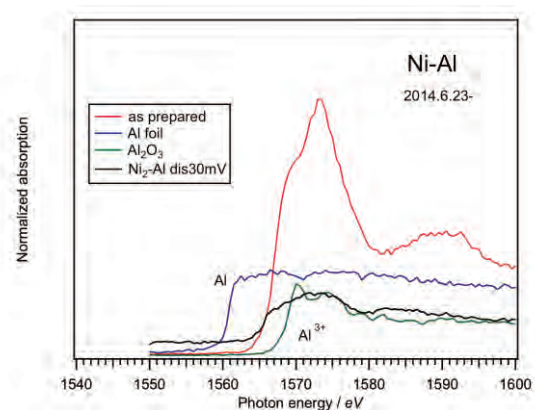


Fig. 1. Al k edge XANES spectra of as prepared Al-Ni oxide, Al foil and alumina.

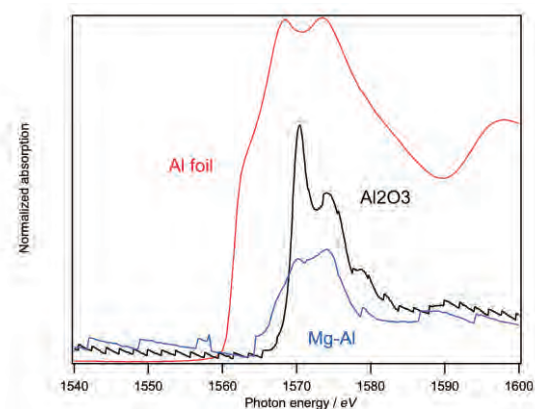


Fig. 2. Al k edge XANES spectra of as prepared Al-Ni oxide and reduced one.

- [1] P. Poizot, S. Laruelle, S. Grugeon, L. Dupont and J. Tarascon, *Ionics* **6** (2000) 321.
- [2] P. Poizot, S. Laruelle, S. Grugeon, L. Dupont and J.-M. Tarascon, *Nature* **407** (2000) 496.
- [3] S. Grugeon, S. Laruelle, R. Herrera-Urbina, L. Dupont, P. Poizot and J. M. Tarascon, *J. Electrochem. Soc.* **148** (2001) A285.
- [4] S. Laruelle, S. Grugeon, P. Poizot, M. Dollé L. Dupont and J.-M. Tarascon, *J. Electrochem. Soc.* **149** (2002) A627.

BL2A

Evaluation of Local Structure of Si for Perlite Synthesized from Natural Mineral

A. Nakahira^{1,2}, S. Togo¹, M. Kasai^{1,3}, Y. Kobayashi³, T. Morinaga¹, Y. Inoue¹,
M. Sato⁴ and H. Aritani⁵

¹Faculty of Engineering, Osaka Prefecture University, Sakai 599-8531, Japan

²Osaka Center, IMR, Tohoku University, Sakai 599-8531, Japan

³Mitsui Mining & Smelting Co., Ltd., Perlite Division, Tokyo 141-8584, Japan

⁴Institute of Materials Research, Tohoku University, Sendai 980-8577, Japan

⁵Saitama Institute of Technology, Fukaya 369-0293, Japan

In general, perlite is considered to be a volcanic glass typically formed by the hydration of obsidian. Therefore, perlite minerals have a relatively high water content and soften by heat-treatments on rotary kiln furnace around the temperatures range of 1000 °C. Since on the heat-treatments water trapped in the perlite structure is vaporized, the rapid foam phenomena for perlite material arise. As a consequence, inorganic foam materials with unique porous-structures are easily produced in large amounts. Perlite is one of most versatile natural products. Large amounts of porous foam with amorphous structure is commercially useful for its significantly light weight and low thermal conductivity due to the unique porous structure and its compositions. These perlites are used in a lot of commercial fields as lightweight plasters, mortar, concrete, tiles and thermal insulation materials. In special, the large amounts of consumption of LNG leads to the construction of LNG tanks and consequently the usage of perlite for heat insulation in LNG tanks rapidly increase. Furthermore, the recycle of waste material from perlite insulator in LNG tanks emerges as a severe problem in Japan and other countries.

In order to solve the recycle of perlite waste after insulator usage, we have continued to develop the efficient use of perlite wastes. For example, perlite wastes may be used for a silica source for inorganic materials and ceramics like silica, mullite, zeolite, glass and so on.

In this study, we attempted to investigate the structure for naturally perlite products. However, perlite has amorphous structures and the detailed characterization of perlite microstructures are insufficiently carried out. In special, the relations of perlite structure and synthetic parameter for useful ceramics are not well clarified.

Powders of natural perlite ore were prepared by the crushers and the ball-milling process before the rotary heat-treatments from natural ore minerals. Several perlite powders were prepared for rotary heat-treatments. Perlite powders were thrown into the heat-treatment furnace at 1073K to 1273K under air atmosphere. Foamed perlites were crashed by ball-milling and aligned to some grades of average

particle size.

Obtained products were characterized by XRD method, FT-IR and TG-DTA. The microstructures of products were observed by SEM. The local structures around Si for the obtained products were characterized by measuring X-ray adsorption near edge structure (XANES) at BL02A in UV-SOR.

Various foamed perlite powders were synthesized though heat-treatments at 1073 to 1273K in air atmosphere. The evaluation of XRD for foamed perlite powders was done. XRD results showed that foam products obtained from perlite powders were amorphous. Figure 1 shows XANES spectra of products and reference materials. As shown in Fig. 1, XANES spectra of sample obtained the same spectra as amorphous silica gel. These results suggest that LTA products obtained from perlite possess the same local structure of Si for commercial amorphous silica gel.

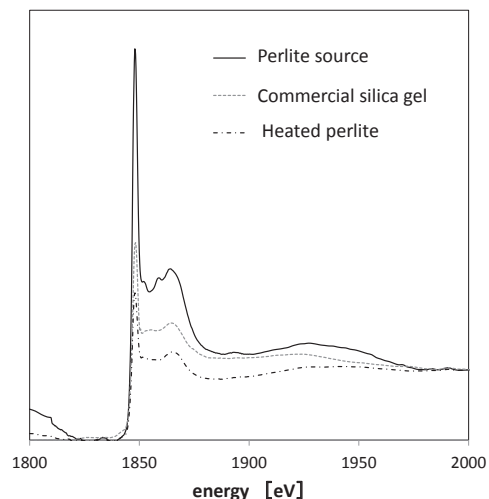


Fig. 1. Si XANES spectra of perlite and reference materials: product and silica gel.

BL2A

XANES Analysis of Methylene Blue Adsorbed on WO₃ Nanomaterials

T. Yoshida¹, K. Komori², M. Yamamoto², C. Tsukada², S. Yagi¹, M. Yajima², S. Kajita¹ and N. Ohno²

¹EcoTopia Science Institute, Nagoya University, Nagoya 464-8603, Japan

²Graduate School of Engineering, Nagoya University, Nagoya 464-8603, Japan

Recently, formation of dendritic nanostructures was found on W surface by He plasma irradiation in certain plasma conditions [1]. We have applied the dendritic nanostructured W to a photocatalyst which can mineralize the organic compounds in water or atmosphere under light irradiation.

In our previous research, we partially oxidized the surface of the nanostructured W and obtained a nanostructured WO₃/W composite material. The material showed photocatalytic decolorization reaction of methylene blue (MB: C₁₆H₁₈ClN₃S nH₂O, n≈3) aqueous solution under near infrared light irradiation. However, we should confirm whether MB decolorization reflects the photoinduced mineralization of MB molecules or the sensitization effect of MB adsorbed on WO₃/W composite material. Therefore, in the present study, we investigate the chemical state of MB molecules after photoinduced reaction by XAFS measurements.

The dendritic nanostructure was fabricated by He plasma irradiation to a monocrystal W plate. After the plasma irradiation, the surface of the sample was partially oxidized on exposure to air at room temperature. We prepared two samples in this manner through the oxidation for 90 days, and the surface oxidation ratios (*x*) of the samples were estimated by XPS measurements as 70 %. Another two samples with *x* =100 % were prepared by further heat-treatment at 773 K for 2 hour in air. These samples are referred to as WO₃(*x*)/W.

S K-edge XANES measurements were conducted for the adsorbed species on the surfaces of WO₃(70)/W and WO₃(100)/W after photocatalytic decolorization reaction of MB by total electron yield or fluorescence X-ray yield method at BL2A in UVSOR and BL6N1 in Aichi Synchrotron Radiation Center.

Figure 1 shows S K-edge XANES spectra of a MB solid powder and a MB aqueous solution. The peaks at 2471.4 eV and 2473.4 eV are respectively assigned to $\pi^*(S-C)$ and $\sigma^*(S-C)$ excitations [2]. Noticeable difference among the two spectra is observed for the $\pi^*(S-C)$ peak. The XANES spectrum of a MB powder shows a sharp $\pi^*(S-C)$ peak, because MB molecules in the solid state are stacked each other by the $\pi-\pi$ interaction [3] to form a high symmetric structure. On the other hand, $\pi^*(S-C)$ peak is lower in the spectrum of a MB aqueous solution rather than the solid state

Figure 2 shows S K-edge XANES spectra of the surfaces of WO₃(70)/W and WO₃(100)/W kept with

MB aqueous solutions under light irradiation or in the dark. The $\pi^*(S-C)$ peaks for both samples in the dark are much higher than the peak for MB molecule in aqueous solution (Fig. 1). Such characteristic feature of XANES spectra is similar to that of a MB solid powder. Therefore, in the dark reaction, MB molecules would be aggregated and stacked by $\pi-\pi$ interactions each other. The intensities of $\pi^*(S-C)$ and $\sigma^*(S-C)$ peaks decrease by the light irradiation for both samples, indicating the break of S-C bonds of MB molecules adsorbed on the samples. Thus, XANES measurements clearly demonstrate the difference in the chemical state of MB molecules between the photoinduced reaction under NIR light irradiation and the adsorption reaction in the dark.

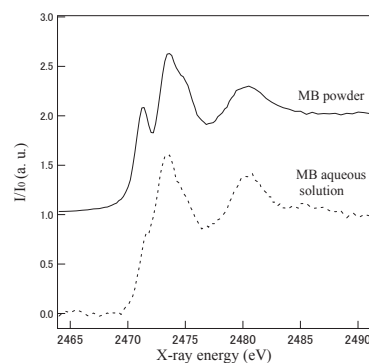


Fig. 1. S K-edge XANES spectra of a MB solid powder and a MB aqueous solution.

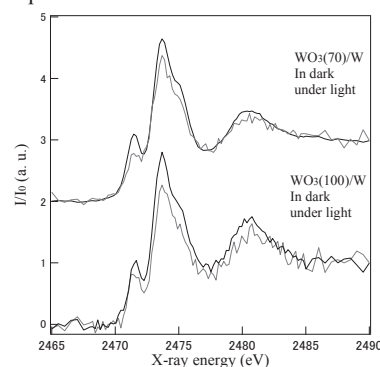


Fig. 2. S K-edge XANES spectra of the MB adsorbates on the surfaces of WO₃(70)/W and WO₃(100)/W. These samples were kept with MB aqueous solutions under near infrared light for 225 min (black) or in the dark for 350 min (gray).

[1] S. Takamura, N. Ohno, D. Nishijima and S. Kajita, *J. Plasma Fusion Res.* **1** (2006) 051.

[2] G. N. George *et al.*, *J. Phys. Chem. A* **118** (2014) 7796.

[3] H. E. Marr III and J. M. Stewart, *Acta Cryst.* **B29** (1973) 847.

BL2A

Local Structure Investigation around P Atom in Mn Substituted LiFePO₄

M. Sato¹, M. Togo², Y. Inoue² and A. Nakahira^{2,3}

¹Institute for Materials Research, Tohoku University, Sendai 980-8577, Japan

²Graduate school of Engineering, Osaka Prefecture University, Sakai 599-8531, Japan

³Kansai Center for Industrial Materials Research, Tohoku University, Sakai 599-8531, Japan

Lithium-ion battery has been used in many mobile devices as high performance battery due to its high energy density and repeatable property. However, there are some problems to be overcome such as a stability in harsh environment and a significant cost saving. LiFePO₄ is anticipated as a novel positive electrode material to reduce the materials cost and to exhibit the high thermal stability. Among the 3d transition elements, which are essential for the cathode active material, iron is the one of ideal elements in terms of cost and resources. LiFePO₄ has reversible potential of 3.5 V and theoretical capacity of 170 mAhg⁻¹, which are comparable energy density to a bedded salt type LiCoO₂. The doping of multiply-charged ion and the substitution of foreign element to Fe site are to be a good approach to improve the conductivity and to enhance the electrode potential of LiFePO₄. In this study, Mn substituted LiFePO₄ was synthesized by hydrothermal process, and the effect of Mn substitution on the local structure around P atom was investigated by XAFS measurement.

LiOH/H₂O, (NH₄)₂HPO₄, FeSO₄/7H₂O and MnSO₄/5H₂O were used as starting materials. Each starting materials were weighted to become a molar ratio of Li : P : Fe : Mn = 2 : 1 : 1-x : x (x = 0, 0.25, 0.50, 0.75, 1.0). After measurement, they were put into distilled water in a Teflon vessel and vigorously mixed for a few minutes. Teflon vessel with mixed solution was encapsulated into autoclave and was hydrothermally treated at 473 K for 6 hours. Obtained slurry was filtrated and then dried at 323 K for overnight. The P K-edge XAFS spectra was corrected in BL-2A of UVSOR. The XAFS data of sample was obtained by fluorescence mode using InSb double crystal monochromator and SDD detector. In a present study, unfortunately, the EXAFS spectra did not obtained due to the influence of absorption of M edge of Au mesh which is using as an I₀ measurement.

Figure 1 shows P K-edge XANES spectra of LiMn_xFe_{1-x}PO₄ (x = 0, 0.25, 0.5, 0.75, 1). Obtained sample had similar XANES spectra to that of commercial LiFePO₄, and the XANES spectra of sample did not change by Mn addition. These results indicate that the Mn based secondary phase such as MnPO₄ does not generated by Mn addition during a synthesis and the local structure around P atom does not change by Mn substitution.

Figure 2 shows P K-edge XANES spectra of samples after charge-discharge cycle test. The

shoulder was appeared around 2148 eV on the XANES spectra of after 100 cycles, and it was observed more clearly after 1000 cycles. This result indicate the generation of FePO₄ phases and the quantitative increment of FePO₄ phase with increasing the cycles. Therefore, it is suggested that the reaction of eq.1 became difficult to occur by repeating the charge-discharge cycle test.

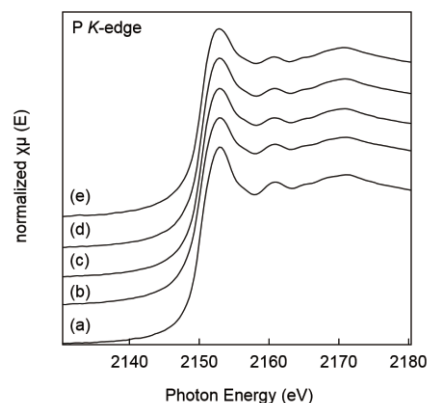
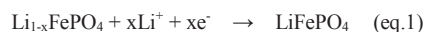


Fig. 1. P K-edge XANES spectra of LiMn_xFe_{1-x}PO₄ samples prepared by hydrothermal process. (a) x = 0, (b) x = 0.25, (c) x = 0.5, (d) x = 0.75, (e) x = 1.

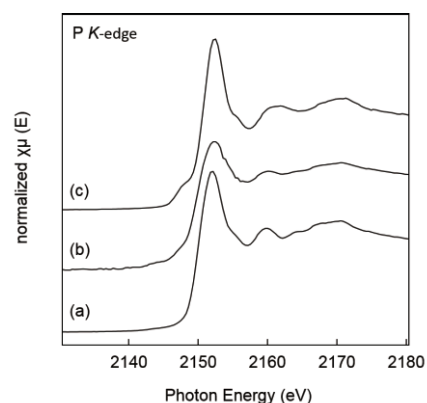


Fig. 2. P K-edge XANES spectra of samples after charge-discharge cycle test. (a) 0 cycle, (b) 100 cycles, (c) 1000 cycles.

[1] Aniruddha Deb *et al.*, J. Synchrotron Rad. **11** (2004) 497.

BL2A

Structural Evaluation of Local Structure of Si for LTA-Type Zeolite from Perlite Source

A. Nakahira^{1,2}, M. Kasai^{1,3}, S. Togo¹, Y. Kobayashi³ and H. Aritani⁴

¹Faculty of Engineering, Osaka Prefecture University, Sakai 599-8531, Japan

²Osaka Center, IMR, Tohoku University, Sakai 599-8531, Japan

³Mitsui Mining & Smelting Co., Ltd., Perlite Division, Tokyo 141-8584, Japan

⁴Saitama Institute of Technology, Fukaya 369-0293, Japan

Perlite is a volcanic glass that is typically formed by the hydration of obsidian. Perlite with a relatively high water content softens at temperatures of 1000 °C and water trapped in the perlite structure of the material vaporizes, leading to the expansion of the material and unique porous-structure. Because perlite has a high water content and amorphous structure, it is commercially applicable to many fields from the advantage of its significantly light weight after foam processing. Many commercial applications for perlite have been developed as lightweight plasters, mortar and concrete, ceiling tiles and insulation materials.

In this study, we attempted to synthesize the zeolite from naturally perlite products. Zeolites have the unique 3D microporous networks. They are one of aluminosilicate minerals commonly used as various commercial adsorbents and other applications in petroleum industry as a catalyst and oxygen purification and water purification. In this experiments, perlite was used for a silica source for zeolite. Especially we focused on LTA-type zeolite with low Si/Al zeolite having unique properties such as high ion exchange capacity, catalytic activity, and sorption ability etc.[1-2] In case of synthesis of zeolite, the microstructure of perlite plays an important role for stability of many zeolite phase. As, however, perlite has amorphous structures, the relations of perlite structure and synthetic parameter for LTA-type zeolite are not well clarified.

Perlite powders were prepared by the ball-milling process for rotary heat-treatments from natural products. Foamed perlites were crashed by ball-milling and aligned to some grades of average particle size. Sodium aluminate (NaAlO₂) was used as an alumina source and added into perlite powder for the adjustment of Si/Al ratio. Perlite powder and sodium aluminate were mixed in NaOH solution and aged for 6 hours. Then mixed solution was poured into vessel and heated at 363K Hydrothermal synthesis for perlite was carried out at 363K for 24 hours. After hydrothermal treatments under some synthetic conditions, the products were filtered and sufficiently washed with de-ionized water and dried.

Obtained products were characterized by XRD method, FT-IR and TG-DTA. The microstructures of products were observed by SEM. The local structures around Si for the obtained products were characterized by measuring X-ray adsorption near

edge structure (XANES) at BL02A in UV-SOR.

Various zeolites were synthesized though hydrothermal treatment of perlite with alkaline solutions in order to facilitate effective use of the discarded perlite. The evaluation of XRD for products was carried out. XRD results showed that products obtained from perlite powders with 2.5 micron of average particle size were also identified to be LTA type without another phase. These results indicated that the obtained fine-zeolite products were LTA type zeolites. Using perlites powders after the mechanical mixing by ball-milling process monolithic LTA zeolite powders were successfully synthesized by after the mechanical mixing processing for 24 hours.

Figure 1 shows the XANES spectra of products and reference materials. As shown in Fig. 1, XANES spectra of sample obtained the same spectra as the commercial LTA. These results suggest that LTA products obtained from perlite possess the good crystallinity and also the same local structure of Si for commercial LTA.

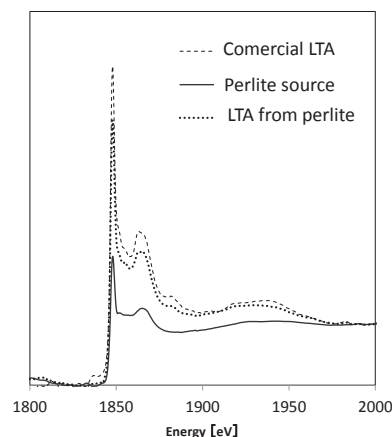


Fig. 1. Si XANES spectra of zeolites and reference materials: perlite, product and commercial LTA.

[1] D. Novembre, B. D.Sabatino, D. Gimeno and C. Pace, "Synthesis and characterization of Na-X, Na-A and Na-P zeolites and hydroxysodalite from metakaolinite", *Clay Minerals* **46** (2011) 339.

[2] G.M. Khan, D.M.Y. Arafat, S.M.S. Razzaque and Md. S. Alam, *Indian Journal of Chemical Technology* **17** (2010) 303.

BL2A

Studies on Electronic Structure of Aluminum Oxide Thin Film under Voltage Applied Conditions by Near-Edge X-Ray Absorption Fine Structure

E. Kobayashi¹, K. K. Bando², O. Takahashi³ and T. Okajima¹

¹Kyushu Synchrotron Light Research Center, Tosu 841-0005, Japan

²National Institute of Advanced Industrial Science and Technology, Tsukuba 305-8565, Japan

³Institute for Sustainable Science and Development, Hiroshima University, Higashi-Hiroshima, 739-8526, Japan

Aluminum oxide is recognized as an important material because it is the prototype of metal oxides and of wide-gap insulator. The aluminum oxide is also used in a wide field of industrial applications such as an insulating material. However, there is no report on the electronic structure of aluminum oxide under voltage applied conditions. Although Al *K*-edge NEXAFS spectra of aluminum oxide have been obtained in total electron yield mode, the method is difficult under voltage applied conditions. Then we have observed an electronic state by detecting x-ray fluorescence from the sample while scanning photon energy.

Al *K*-edge NEXAFS spectra of aluminum oxide thin film were measured at the beamline 2A of the UVSOR in the Institute of Molecular Science. An alumina film was made on a stainless steel plate by dip-coating with a diluted alumina sol (Kawaken Fine Chemicals, F1000). The coated plate was dried at 333 K and calcined at 573 K in an oven. The NEXAFS spectra were obtained using the partial fluorescence yield (PFY) mode at room temperature.

Figure 1 shows the Al *K*-edge NEXAFS spectra of aluminum oxide obtained from PFY mode at various applied voltage. This sample was discharged at 160 V. Two strong peaks are observed at around 1569.3 eV (A) and 1571.8 eV (B), respectively. The spectral features are also similar to the obtained for Gibbsite [1]. The intensity of peak A and peak B change gradually with applied voltage. Figure 2 shows the applied voltage dependence of the intensity of peak A and peak B for aluminum oxide thin film. The intensity of the two peaks tends to become weak with increasing applied voltage and the peaks become broad. This result indicates that the content of an amorphous phase increased in alumina with applied voltage.

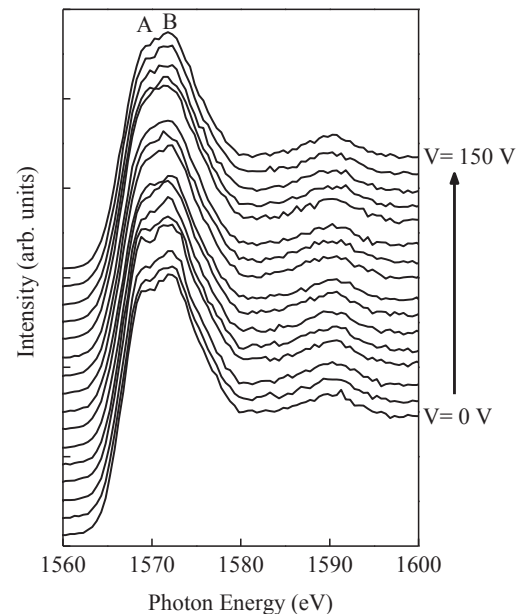


Fig. 1. Al *K*-edge NEXAFS spectra of aluminum oxide thin film obtained from PFY mode at various applied voltage.

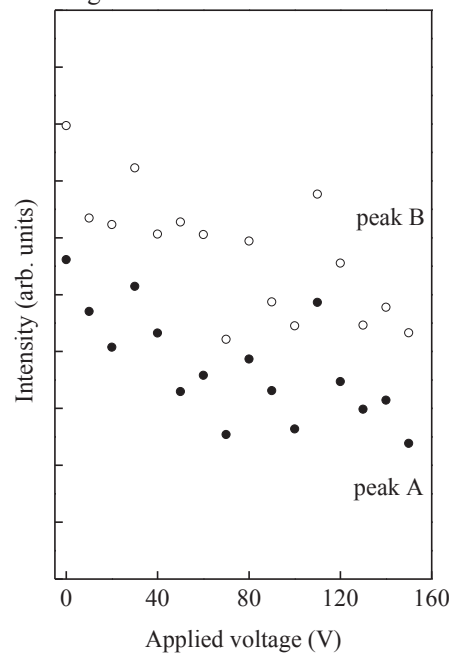


Fig. 2. Applied voltage dependence of the intensity of peak A and peak B for aluminum oxide thin film.

[1] C. S. Doyle *et al.*, *J. Synchrotron Rad.* **6** (1999) 621.

Temperature Dependence of Self-Trapped Exciton Emission and Energy Transfer in Binary Rare-Earth Borates upon Vacuum UV Excitation

N. Kodama, A. Abe, M. Kudo and T. Takahashi

Graduate School of Engineering and Resource Science, Akita University, Akita 010-8502, Japan

We report the temperature and material dependence of the intrinsic luminescence from self-trapped excitons (STEs) and energy transfer to RE^{3+} ($RE^{3+} = Sm^{3+}, Gd^{3+},$ or Tb^{3+}) ions observed in three kinds of undoped binary borates $LaSc_3(BO_3)_4$ (LSB), $YSc(BO_3)_2$ (YSB), and $LuSc(BO_3)_2$ (LuSB) under vacuum ultraviolet (VUV) excitation. In addition, we examine the temperature dependence and the dynamics of energy transfer from STEs in RE^{3+} -doped LSB, YSB, and LuSB samples.

The time-resolved spectra were measured using a pulse with a width of 10 ns from an F_2 pulsed laser operating at 157 nm, and the decay times were determined.

Figures 1(a), 1(b), and 1(c) show the temperature dependence of the luminescence spectra in undoped LSB, YSB, and LuSB, respectively. As can be seen, at 293 K, three, two, and one distinct emission bands were observed for LSB, YSB, and LuSB, respectively, and were located at energies corresponding to the STE bands. The peaks of the STE luminescence bands in all samples (LSB, YSB, LuSB) shifted to longer wavelengths with increasing temperature from 15(or 14) to 293 K.

Figure 2 shows the temperature dependence of the STE intensities for the undoped samples. In the undoped LSB, the STE(I) intensity decreased gradually from 15 to 160 K, and then remained nearly constant. Accompanying this decrease in the STE(I) intensity, the intensities of STE(II) and (III) increased, reached their maxima at 180 K, and then decreased monotonically for higher temperatures. This decrease in the STE(II) and STE(III) intensity likely resulted from a thermal quenching process, such as an intrinsic quenching or a partial energy transfer to nonradiative “killer” centers due to the presence of defects or impurities. Undoped YSB exhibited an STE(I) intensity that increased gradually as the temperature increased to 125 K, above which the intensity decreased. The STE(II) luminescence appeared at 180 K, and the intensity increased with increasing temperature to 293 K. In the undoped LuSB, the intensity of STE(I) passed through a maximum at 200 K, which is similar to the temperature dependence of the STE(II) and STE(III) luminescence for LSB and that of STE(I) for YSB. As the STE(I) emission intensity decreased in LSB and YSB, the STE(II) and STE(III) emission intensity increased, accompanied by the appearance of the STE(II) emissions. These facts suggest that there are multiple (three in LSB, two in YSB) local minima on the adiabatic potential energy surfaces, i.e., the barriers for the exciton self trapping in LSB and YSB. Multi-step transitions correspond to the evolution from STE(I) to STE(II) and further to STE(III).

Figure 3 compares the temperature dependence of the rate of decrease in the STE(I), (II), and (III) emissions in the RE^{3+} -doped and undoped samples of LSB and YSB.

For a high RE^{3+} doping concentration (5%), the rate of decrease did not show notable changes, or gradually decreased up to approximately 200 K, followed by a gradual increase as temperature rose, whereas for low Sm^{3+} doping (1%), the rate of decrease increased monotonically with increasing temperature. These results suggest that for the low RE^{3+} doping, the thermally assisted energy transfer process related to the exciton (STE) mobility was activated as the temperature increased.

In the case of LSB at a temperature of 293 K, the energy transfer rates determined from time-resolved measurements were $1.9 \times 10^6 s^{-1}$ (STE(II)) and $1.8 \times 10^5 s^{-1}$ (STE(III)) for 5 at.% Sm^{3+} doping, $1.6 \times 10^6 s^{-1}$ (STE(II)) and $0.8 \times 10^5 s^{-1}$ (STE(III)) for 5 at.% Gd^{3+} doping, and $2.2 \times 10^6 s^{-1}$ (STE(II)) and $0.8 \times 10^5 s^{-1}$ (STE(III)) for 5 at.% Tb^{3+} doping. The energy transfer rates in the YSB at 293 K were $1.9 \times 10^7 s^{-1}$ (STE(I)) and $5.6 \times 10^5 s^{-1}$ (STE(II)) for 5 at.% Gd^{3+} doping and $6.5 \times 10^6 s^{-1}$ (STE(II)) and $1.5 \times 10^5 s^{-1}$ (STE(III)) for 1 at.% Tb^{3+} doping. The observed energy transfer rates were the same magnitude as, or within an order of magnitude of, the estimates based on dipole-dipole energy transfer.

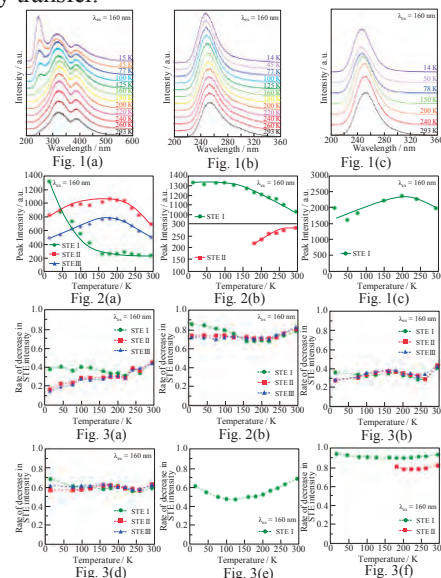


Fig. 1. Temperature dependence of intrinsic luminescence spectra in (a) undoped LSB, (b) YSB, and (c) LuSB in the range 15(or 14)–293 K.

Fig. 2. Temperature dependence of STE intensity for undoped samples: (a) LSB, (b) YSB, and (c) LuSB.

Fig. 3. Temperature dependence of rate of decrease in STE(I), (II), and (III) emissions in RE^{3+} -doped and undoped samples for LSB and YSB: (a) 1% Sm -doped LSB, (b) 5% Sm -doped LSB, (c) 5% Gd -doped LSB, (d) 5% Tb -doped LSB, (e) 5% Gd -doped YSB, and (f) 5% Tb -doped YSB.

BL3B

Charging States of Oxygen Vacancies in Yttria-Stabilized Zirconia Analyzed by the Decay of Photoluminescence

S. Kaneko, T. Morimoto and Y. Ohki
Waseda University, Tokyo 169-8555, Japan

In yttria-stabilized zirconia (YSZ), ZrO_2 is partly replaced by Y_2O_3 . This means that oxygen vacancies are present in YSZ with the same ratio as that of Y_2O_3 [1]. In order to examine the electronic energy structure of the oxygen vacancy in YSZ, the decaying behavior of photoluminescence (PL) was observed in YSZ.

It has been known that the PL with a peak energy of 2.8 eV appearing in YSZ as shown in Fig. 1 is due to the oxygen vacancy and that the oxygen vacancy can take three different charging states [1-3]. However, the charging state from which the PL is emitted is unclear.

Using the single-bunch mode of synchrotron radiation at BL3B line in the UVSOR facility as an excitation photon source, we observed the decay of the 2.8-eV PL excited by 5.2-eV photons in a ns-range. As shown in Fig. 2(a), the decay constant of the PL can be estimated as 7 ns. In addition, we measured the decay in a ms-range using a fluorescence spectrometer FP-8500 (Jasco). As shown by the black open circles in Fig. 2(b), the 2.8-eV PL decays with a lifetime of around 0.3 ms. Note that red open squares show the decay in intensity of the excitation photons induced by the movement of a mechanical shutter.

When an oxygen atom is removed from a certain site, the site would be effectively charged positively. Therefore, the site attracts electrons. Regarding this, the oxygen vacancy capturing no electrons is called the F^{2+} center, while the ones capturing one and two electrons are called the F^+ center and the F center, respectively.

The PL, which has been attributed to oxygen vacancies, has been reported for many oxides. It has been known that the F centers in alumina [4] and $YAlO_3$ [5] induce phosphorescence with a time constant of the order of ms, while the F^+ centers have been assigned to the origin of fluorescence with a time constant of the order of ns. Taking these facts into account, the 2.8-eV PL in YSZ would be ascribable to both the F^+ and F centers.

However, it is unlikely that both the F^+ and F centers with different charging states emit photons with the same energy. In this regard, we assume the following luminescent mechanism as a plausible model. Namely, the 2.8-eV PL in YSZ is induced by the F^+ centers with the decay constant of 7 ns. One important fact is that the F^+ centers can be generated if one electron is released from the F centers in addition to those originally present in YSZ. If the

release of electrons needs a certain long time, the 2.8-eV PL must have a large decay constant like 0.3 ms when it is originated from the F centers.

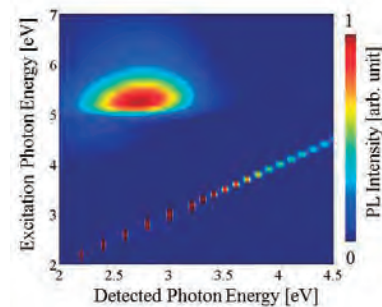
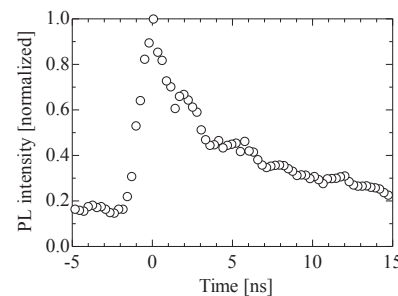
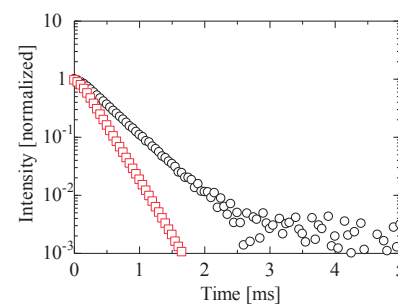


Fig. 1. Distribution of PL energy and PL excitation energy observed for YSZ at 10 K.



(a)



(b)

Fig. 2. Decay profiles of the 2.8-eV PL observed in YSZ; (a) in a ns range and (b) in a ms range (\circ) in comparison with the decay of excitation photons with an energy of 5.2 eV (\square), normalized by their respective initial values.

- [1] J. M. Costantini, *et al.*, *J. Nucl. Mater.* **440** (2013) 508.
- [2] H. Nakajima, *et al.*, *J. Alloys Compd.* **408** (2006) 728.
- [3] T. Morimoto, *et al.*, *Jpn. J. Appl. Phys.* **47** (2008) 6858.
- [4] A. I. Surdo, *et al.*, *Radiat. Meas.* **33** (2001) 587.
- [5] Y. V. Zorenko, *et al.*, *Opt. Spectrosc.* **96** (2004) 532.

BL3B

Band Gap of B1-Type $M_xZn_{1-x}O$ ($M = Mg, Mn, Fe, Co, Ni$) Synthesized under High Pressures

K. Takahama¹, K. Usui¹, D. Shimada², M. Kato¹, K. Niwa², K. Kusaba²,
M. Hasegawa² and K. Soda¹

¹Department of Quantum Engineering, Graduate School of Engineering, Nagoya University,
Nagoya 464-8603, Japan

²Department of Crystalline Materials Engineering, Graduate School of Engineering, Nagoya University,
Nagoya 464-8603, Japan

Wide gap semiconductor ZnO is one of promising materials for light emitting devices, transparent conducting electrodes, catalysis, solar cells, and so on [1]. There have been many proposals and efforts for controlling such as a band gap width and energy positions of conduction band minimum and valence band maximum, and hence its functional properties, by forming mixed crystals with other metal oxides [2, 3]. Recently B1(NaCl)-type mixed crystals $M_xZn_{1-x}O$ ($M = Mg, Mn, Fe, Co, Ni$) have been successfully synthesized under high pressures [4], where ZnO transforms the B4(wurtzite)-type structure to B1-type. In this report, we have investigated their reflectance spectra to estimate their band gaps.

Measurement of reflectance spectra was performed at BL3B for polycrystalline specimens of about 1 mm in thickness and ~2 mm in diameter synthesized at 1173 K under a pressure of 6.5 GPa with DIA-type cubic anvil cell. The band gaps were estimated with the Tauc plot for an indirect transition [5].

Figure 1 compares the estimated band gap (red circle) with those experimentally evaluated from valence band photoelectron measurements (PES, blue circles) [6, 7] for the present specimens as well as experimental values of ZnO and MgO (black circles) in ref. [3] and calculated with the first principle calculations [2, 7, 8]. Here, theoretical direct and indirect band gaps are shown by solid and broken lines, respectively, which were calculated with full potential linearized augmented plane wave method with generalized gradient approximation (GGA) by Perdew-Burke-Ernzerhof (PBE) and Engle-Vosko (EV) [2] and with full potential linear muffin-tin orbital method (LMTO) [8]. Experimental results are also presented by open black circles for B1-type $Mg_xZn_{1-x}O$ films grown by pulsed laser deposition [9].

The present band gaps agree quantitatively well with those obtained by PES and qualitatively with theoretical predictions, taking into account that the underestimation of the band gap is well known for these calculations. The agreement of both the present and PES experimental estimations of the band gap indicates the n-type nature of the specimens, which was assumed for the previous estimation from PES. For $x = 0.75$, band gaps for the bulk specimens are considerably different from those reported for the

film. This may be due to effects of Zn as an impurity for the Mg-rich films or different crossover between indirect and direct band gaps of the films on a substrate from the bulk specimens, although the reason has not been clarified at present yet.

Results will be reported elsewhere on other mixed crystals.

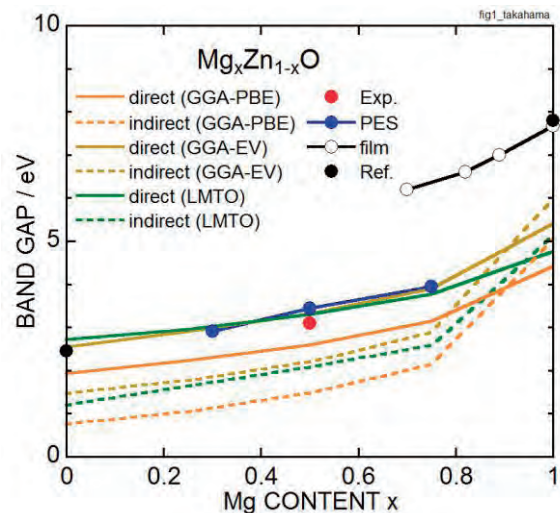


Fig. 1. Band Gaps of B1-type $Mg_xZn_{1-x}O$.

- [1] H. Q. Ni *et al.*, *J. Appl. Phys.* **91** (2002) 1339.
- [2] B. Armani *et al.*, *Compt. Mater. Sci.* **40** (2007) 66.
- [3] D. K. Kanan and E. A. Carter, *J. Phys. Chem. C* **116** (2012) 9876.
- [4] D. Simada, Master thesis (Nagoya University, 2013).
- [5] J. Tauc *et al.*, *Phys. Status Solidi* **15** (1966) 627.
- [6] K. Takahama *et al.*, UVSOR Activity Report 2013 **41** (2014) 83.
- [7] K. Soda *et al.*, Aichi SR Report (2013) 2504026.
- [8] F. Z. Aoumeur-Benkabou *et al.*, *Model. Num. Sim. Mater. Sci.* **2** (2012) 60.
- [9] R. Schmidt-Grund *et al.*, *AIP Conf. Proc.* **772** (2005) 201.

BL3B

Energy Transfer from Tl^+ Centers to In^+ Centers in Co-Doped $NaCl:Tl^+, In^+$ Crystals

A. Iguchi and T. Kawai

Graduate School of Science, Osaka Prefecture University, Sakai 599-8531, Japan

Alkali halide crystals have the wide band-gap up to the vacuum ultraviolet energy region and are a suitable candidate host for doping of impurity ions. Among a lot of impurity ions, Tl^+ -type ions that have the ns^2 electronic configuration in their ground state are well-known as impurity ions doped in alkali halides [1,2]. Although many experimental studies have been performed on Tl^+ -type centers in alkali halides, energy transfer between Tl^+ -type centers in alkali halides are comparatively less studied. In this study, we have investigated the energy transfer from Tl^+ centers to In^+ centers in $NaCl$ crystals co-doped with the Tl^+ and In^+ ions at the BL-3B line of UVSOR.

Figure 1 shows the absorption spectrum of $NaCl:In^+$ and the luminescence spectrum of $NaCl:Tl^+$ in the energy range from 3.6 to 4.8 eV. In $NaCl:In^+$, the A absorption band having doublet structure and the B absorption band appearing as a shoulder are observed at 4.1 and 4.6 eV, respectively. The C absorption band is located around 5.1 eV in the higher energy region than the B absorption band. In $NaCl:Tl^+$, the A' luminescence band due to the Tl^+ centers is observed around 4.25 eV. The A' luminescence band in $NaCl:Tl^+$ has a large overlap with the A absorption band in $NaCl:In^+$. The fact indicates the potential of the energy transfer from the Tl^+ centers to the In^+ centers in co-doped $NaCl:Tl^+, In^+$ crystals. According to the Förster model [3,4], the critical distance between both centers for resonant energy transfer is estimated to be 17.5 Å from the overlap with the luminescence and absorption bands.

Figure 2 shows the excitation spectra in $NaCl:Tl^+$, $NaCl:In^+$, and co-doped $NaCl:Tl^+, In^+$ crystals at room temperature (RT). The A' luminescence band in $NaCl:Tl^+$ is efficiently excited in the energy region around 4.8 eV and 6.1 eV, where the A, B, and C absorption bands of the Tl^+ centers are located. In $NaCl:In^+$, the luminescence band at 3.00 eV, which corresponds to the A' luminescence band of the In^+ centers, is efficiently excited at the A, B, and C absorption bands of the In^+ centers.

In the co-doped $NaCl:Tl^+, In^+$ crystal, the excitation spectrum for the A' luminescence band of the In^+ centers has the broad band around 6.10 eV in addition to the A, B, and C bands of the In^+ centers. Since the 6.10 eV band corresponds to the excitation band for the A' luminescence band in $NaCl:Tl^+$, the fact implies the existence of the energy transfer from the Tl^+ centers to the In^+ centers in the co-doped $NaCl:Tl^+, In^+$ crystal. In order to clarify the energy

transfer mechanism from the Tl^+ centers to the In^+ centers in the co-doped $NaCl:Tl^+, In^+$ crystals, the measurements of the decay kinetics of the luminescence are needed.

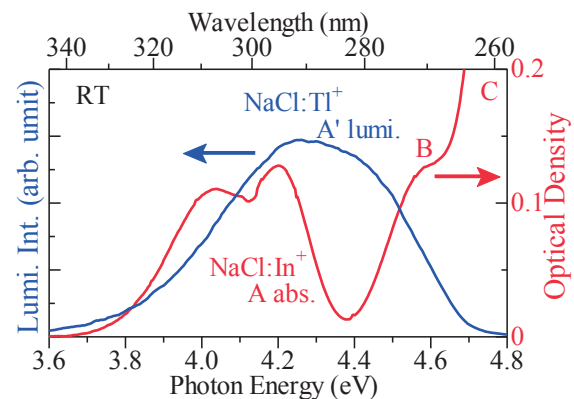


Fig. 1. Luminescence spectrum (blue) of $NaCl:Tl^+$ and absorption spectrum (red) of $NaCl:In^+$ at RT.

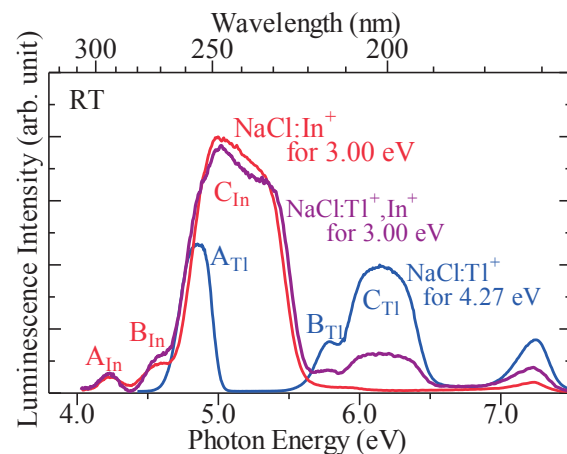


Fig. 2. Excitation spectra of $NaCl:Tl^+$ (blue), $NaCl:In^+$ (red), and co-doped $NaCl:Tl^+, In^+$ (purple).

- [1] A. Ranfagni *et al.*, *Advances in Physics* **32** (1983) 823.
- [2] P. W. M. Jacobs, *J. Phys. Chem. Solids* **52** (1991) 35.
- [3] T. Förster, *Disc. Faraday Soc.* **27** (1959) 7.
- [4] D. L. Dexter, *J. Chem. Phys.* **21** (1953) 836.

BL3B

Luminescence Band with a Zero-Phonon Line in NaCl:TI⁺ Crystals

T. Kawai

Graduate School of Science, Osaka Prefecture University, Sakai 599-8531, Japan

TI⁺ centers in alkali halide crystals are well-known as a strong electron-phonon interaction system and exhibit the broad luminescence band with a large Stokes shift. Though lots of the optical studies have been performed for the TI⁺ centers in alkali halides [1,2], the optical measurements with high-resolution are considerably less. We have performed the optical measurements with high-resolution for NaCl:TI⁺ crystals at the BL-3B line of UVSOR.

Figure 1 shows the absorption spectrum up to the vacuum ultraviolet energy region at low temperature in NaCl:TI⁺. The broad absorption bands called A, B, and C are observed at 4.87, 5.77, and 6.19 eV, respectively. The A, B, and C absorption bands are attributed to the intra-ionic transitions from the ground ¹A_{1g} state to the excited ³T_{1u}, ³T_{2u}+³E_u, and ¹T_{1g} states in the TI⁺ centers, respectively[1,2].

Figure 2 shows the luminescence and absorption spectra measured by high-resolution spectroscopy in the vicinity of the A band in NaCl:TI⁺. The broad luminescence band called A' appears with a Stokes shift. It should be noted that the A' luminescence band has a weak zero-phonon line at 4.622 eV. On the other hand, the A absorption band has no zero-phonon line and no overlap with the A' luminescence band. This odd spectra can be explained on the basis of a fact that the A' luminescence band is composed of two luminescence bands.

In general, the A' luminescence band of the TI⁺ centers comes from the radiative transitions from the relaxed excited states of ³A_{1u} and ³T_{1u}. The excited ³A_{1u} state is located at the slightly lower energy position than the ³T₁ state. Since the transition from the ¹A_{1g} state to the ³A_{1u} state is strongly forbidden, the absorption band due to the ³A_{1u} state is not usually observed on the absorption spectrum. Therefore, the A absorption band observed in the absorption spectra comes from the transition from the ¹A_{1g} state to the ³T_{1u} state. On the other hand, the radiative transition from the relaxed excited state of ³A_{1u} occurs with the long decay time constant of a few milliseconds. If the lattice-relaxation of the excited ³A_{1u} state is considerably smaller than that of the excited ³T_{1u} state, the luminescence band from the relaxed excited state of ³A_{1u} would appear at the higher energy position than that from the excited relaxed state of ³T_{1u}. Then, the luminescence band with a zero-phonon line might be observed with an apparent Stokes shift, as shown in Fig. 2. Therefore, the zero-phonon line at 4.622 eV in NaCl:TI⁺ is attributed to the radiative transition from the ³A_{1u} state.

The luminescence band from the relaxed excited

state of ³T_{1u} has the shorter decay time constant of a few ten nanoseconds. The fact implies that the time-resolved luminescence spectroscopy would allow us to decompose the A' luminescence band into the slowly decaying luminescence band and the fast-decaying luminescence band, which correspond to the luminescence bands from the relaxed excited states of ³A_{1u} and ³T_{1u}, respectively. In order to confirm the above idea, we are planning to perform a time-resolved luminescence spectroscopy.

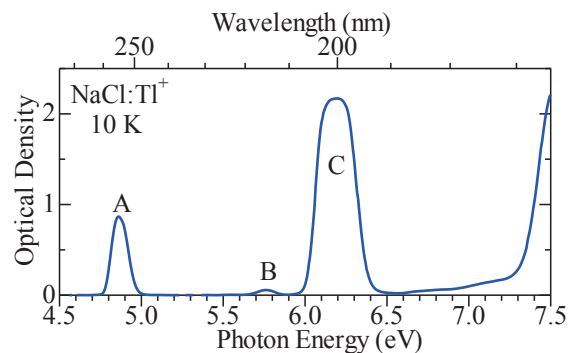


Fig. 1. Absorption spectrum of a NaCl:TI⁺ crystal.

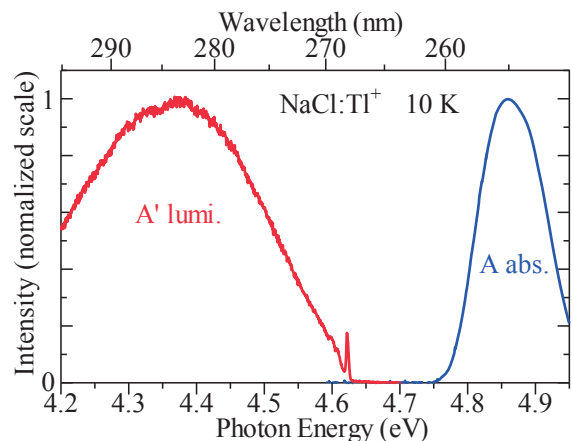


Fig. 2. The A' luminescence band and the A absorption band obtained by using a high-resolution spectroscopy.

[1] A. Ranfagni *et al.*, *Advances in Physics* **32** (1983) 823.

[2] P. W. M. Jacobs, *J. Phys. Chem. Solids* **52** (1991) 35.

BL3B

Anomalous Excitons and Screenings Unveiling Strong Electronic Correlations in $\text{SrTi}_{1-x}\text{Nb}_x\text{O}_3$

P. K. Gogoi^{1,2,3}, L. Sponza⁴, D. Schmidt¹, T. C. Asmara^{1,2,3}, C. Diao¹, J. C. W. Lim^{1,2}, S. M. Poh¹, S. Kimura⁶, P. E. Trevisanutto^{1,3,5}, V. Olevano⁷ and A. Rusydi^{1,2,3}

¹Singapore Synchrotron Light Source, National University of Singapore, 117603, Singapore

²NUSNNI-NanoCore, National University of Singapore, 117576, Singapore

³Department of Physics, National University of Singapore, 117542, Singapore

⁴Laboratoire des Solides Irradiés, École Polytechnique, CNRS, F-91128 Palaiseau, France

⁵Centre for Advanced 2D Materials and Graphene Research Centre, National University of Singapore, 117546, Singapore

⁶Graduate School of Frontier Biosciences, and Department of Physics, Osaka University, Suita 565-0871, Japan

⁷Institut Néel, CNRS, BP 166, F-38042 Grenoble, France

Strong electronic correlations in transition metal oxides are known to drive rich phenomena such as superconductivity, colossal magnetoresistance and metal insulator transitions [1]. An example of a model transition metal oxide is the perovskite-type SrTiO_3 (STO). Indeed, STO in various bulk forms and recently its heterostructures with other oxides, have shown exotic phenomena such as superconductivity, magnetisms, metal-insulator transitions and two-dimensional electron gas. However the role of electronic correlations, particularly electron-hole (e-h) and electron-electron (e-e) interactions, remains unclear. Then we measured the temperature dependence of the optical conductivity spectra of STO and $\text{SrTi}_{1-x}\text{Nb}_x\text{O}_3$ with $x = 0.005$ (STNO) and obtained the spectral weight transfer.

In Fig. 1a (1b), the real part of the optical conductivity, is plotted for STO (STNO) for temperatures of 4.2, 200 and 350 K. The energy range is divided into 9 separate ranges for convenience of analysis. As can be seen in Fig. 1c (1d) the spectral weight of the first excitonic region (Ex1) (shown as Region 2) decreases monotonically with a slight dip in the temperature range of 75 – 150 K. STO has a phase transition from cubic to tetragonal around 105 K with a very slight change of the c axis [2]. These dips, both in STO and STNO, could be due to this phase change which has been reported to occur over a range of 60 K previously [3]. Here the spectral weight of the band-edge region (shown as Region 3) remains almost constant for both STO and STNO. A similar trend is seen for the second excitonic region (Ex2) (shown as Region 5) and the corresponding next region (shown as Region 6) respectively in Fig. 1e (1f). Also plotted are the spectral weight functions for the energy range before the excitonic region in this case (as Region 4). Importantly it has opposite spectral weight transfer as that of the excitonic region and it is seen that the spectral weight for Region 4 and Region 5 are almost conserved together. These spectral weight analysis sheds further light on the various general aspects of the excitonic effects present in STO and STNO.

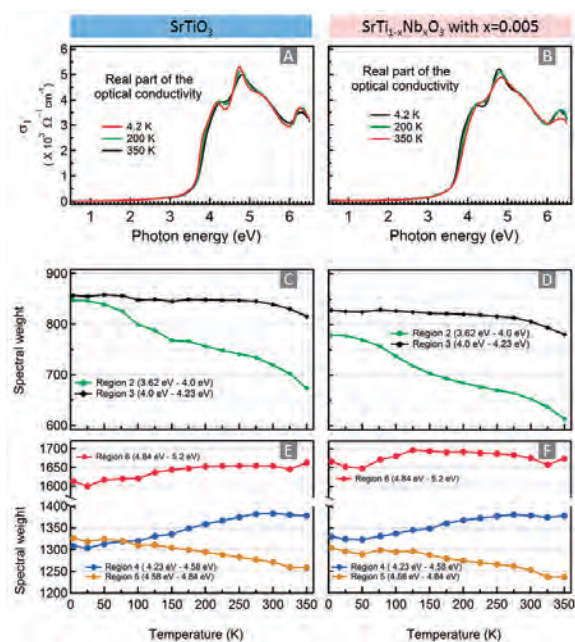


Fig. 1. Real part of the optical conductivity and spectral weight transfer. Real part of the optical conductivity at selected temperatures for (a) STO and (b) STNO. Temperature dependence of spectral weight for the first direct inter-band (Region 3) transition and for associated excitonic spectra around peaks Ex1 (Region 2) for (c) STO and (d) STNO. Temperature dependence of spectral weight for regions around and including excitonic peak Ex2 for (e) STO and (f) STNO.

[1] D. N. Basov *et al.*, Rev. Mod. Phys. **83** (2011) 471.

[2] K. A. Müller, W. Berlinger and F. Waldner, Phys. Rev. Lett. **21** (1968) 814.

[3] K. W. Blazey, Phys. Rev. Lett. **27** (1971) 146.

BL3B

Ultraviolet Photoluminescence of Gd³⁺ in Gd³⁺-Pr³⁺ Co-Doped Yttrium Aluminate under Vacuum Ultraviolet Excitation

K. Ueda¹, Y. Shimizu¹, A. Takiguchi¹, Y. Taira² and Y. Inaguma²

¹ Department of Materials Science, Graduate school of Engineering, Kyushu Institute of Technology, Kitakyushu 804-8550, Japan

² Department of Chemistry, Faculty of Science, Gakushuin University, Tokyo 171-8588, Japan

It is known that a Gd³⁺ center shows a sharp emission peak at approximately 310 nm in UV-B region, which is attributed to the 4f-4f transition from ⁶P_J to ⁸S_{7/2} states. The sharp emission from Gd³⁺ is anticipated as a new light source for medical application such as phototherapy for skin disease [1] and transilluminator for DNA analysis [2]. In the recent studies, Pr³⁺ co-doping was found to give a large excitation band for Gd³⁺ emission in some materials such as LaPO₄ [2] and YAlO₃ [3]. Although the excitation band is considered to be derived from the Pr³⁺ 4f-5d absorption, the details are unknown yet. In this study, Gd³⁺ and Pr³⁺ co-doped YAlO₃ were prepared and the fundamental UV photoluminescence (PL) properties were investigated by VUV excitation.

The polycrystalline samples of (Y_{1-x-y}Gd_xPr_y)AlO₃ (x=0.00-0.07 and y=0.00-0.03) were prepared by a polymerized complex method, using Y₂O₃, Gd₂O₃, Pr₆O₁₁, Al(NO₃)₃·9H₂O as starting materials. Citric acid monohydrate and propylene glycol were used to form the polymerized complex gels. The sample powders were obtained by heating at 1400 °C in air. The obtained powders were pressed into pellets and sintered at 1400 °C in air. The phases in the samples were identified by the powder X-ray diffraction (XRD) using a Rigaku RINT 2500 diffractometer (CuKα radiation). The emission and excitation spectra were measured at the beamline BL3B in UVSOR.

Each sample was identified as a distorted perovskite type phase with a space group Pnma. Because no impurity phases were observed in their XRD patterns, it was confirmed that both Gd³⁺ and Pr³⁺ were dissolved into the host lattices. Figure 1 shows PL spectra observed in (Y_{1-x-y}Gd_xPr_y)AlO₃ at room temperature along with the PL intensities as a function of x or y. All Gd³⁺ doped samples showed Gd³⁺ emission peaks at 314 nm originating from ⁶P_{7/2} to ⁸S_{7/2} transition. The maximum PL intensity was observed at x=0.07 and y=0.03. It is noteworthy that even a small amount of Pr³⁺ co-doping such as y=0.01 enhanced the Gd³⁺ emission.

Figure 2 shows PL excitation spectra of (Y_{1-x-y}Gd_xPr_y)AlO₃. An intense band, that was assignable to host lattice excitation, was observed at 157 nm for a Gd³⁺ single doped sample. In contrast, another intense band was observed at approximately 220 nm for Gd³⁺ and Pr³⁺ co-doped samples. The shape of the excitation spectra for Gd³⁺-Pr³⁺ co-doped

samples agreed well with the one for a Pr³⁺ single doped sample that monitored Pr³⁺ 5d-4f emission at 243 nm. As the result, the Gd³⁺ emission mechanism in Gd³⁺-Pr³⁺ co-doped samples was found to be considerably different from that in the Gd³⁺ single doped one. The Gd³⁺ emission in Gd³⁺-Pr³⁺ co-doped samples occurred through energy transfer from Pr³⁺ to Gd³⁺, even on the excitation of the host lattices.

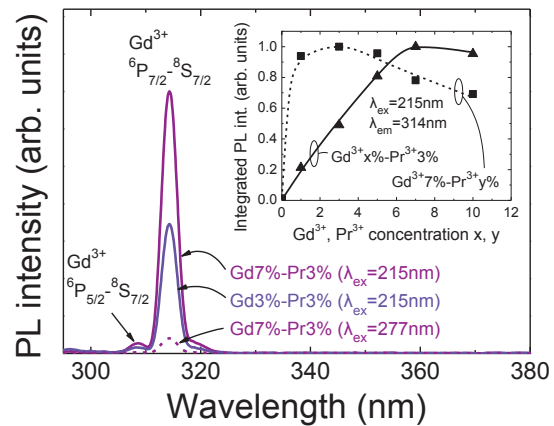


Fig. 1. Gd³⁺ PL spectra in (Y_{1-x-y}Gd_xPr_y)AlO₃. Inset shows the PL intensities as a function of Gd³⁺ and Pr³⁺ concentration x, y.

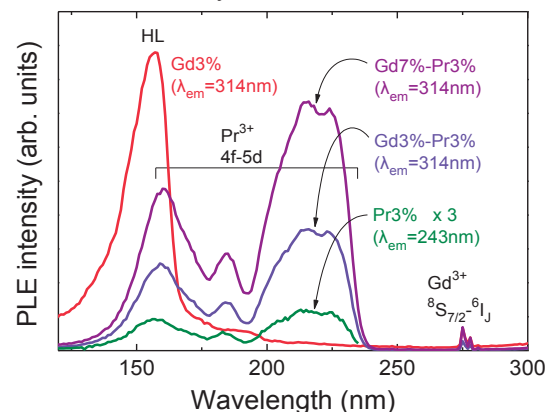


Fig. 2. PL excitation spectra of (Y_{1-x-y}Gd_xPr_y)AlO₃. Only the spectrum of (Y_{0.97}Pr_{0.03})AlO₃ is magnified.

- [1] R. P. Sonekar, S. K. Omanwar, S. V. Moharil, S. M. Dhopte, P. L. Muthal and V. K. Kondawar, *Opt. Mater.* **30** (2007) 622.
- [2] S. Okamoto, R. Uchino, K. Kobayashi and H. Yamamoto, *J. Appl. Phys.* **106** (2009) 013522.
- [3] Y. Shimizu, Y. Takano and K. Ueda, *J. Lumin.* **141** (2013) 44.

BL3B

Excitation and Emission Spectra of Ce^{3+} in $\text{Ba}_3\text{Y}_2\text{B}_6\text{O}_{15}$

M. Yoshino, M. Hotta and S. Watanabe

Graduate School of Engineering, Nagoya University, Nagoya 464-8603, Japan

The trivalent lanthanide ions (e.g., Nd^{3+} , Er^{3+} , Yb^{3+}) in Oxide crystals have drawn attentions due to their application for luminescent materials in NIR to UV regions such as solid-state lasers or phosphors. The trivalent cerium ion, Ce^{3+} , has also attracted attentions as luminescence centers. In this work, the $4f-5d$ excitation spectra and emission spectra for Ce^{3+} in $\text{Ba}_3\text{Y}_2\text{B}_6\text{O}_{15}$ crystal have been measured. For the comparison, the excitation spectra and emission spectra for Pr^{3+} -doped $\text{Ba}_3\text{Y}_2\text{B}_6\text{O}_{15}$ have been also measured. The Ce doped and Pr doped samples are produced by solid state reactions. The concentration of dopants in the samples are 0.5 and 1.0 mol%. Figure 1 shows the excitation spectrum monitored 440 nm for $\text{Ba}_3(\text{Y}_{0.995}\text{Ce}_{0.005})_2\text{B}_6\text{O}_{15}$. The peaks B and C originate in the absorption of the $4f-5d$ transitions of Ce^{3+} . The peak A originates in the absorption of the $\text{Ba}_3\text{Y}_2\text{B}_6\text{O}_{15}$ host crystal. The peaks related to the absorption in the host and the $4f-5d$ transition of lanthanide ion are seen also in the excitation spectrum for Pr^{3+} -doped sample. They are shown as A and B in Fig. 2, respectively. The emission spectra for Ce^{3+} in $\text{Ba}_3\text{Y}_2\text{B}_6\text{O}_{15}$ are shown in Fig. 3 and 4. The emission intensity in 0.5 mol% sample is higher than in 1.0 mol% sample due to the concentration quenching. Each emission spectra have shoulder and may consist of two peaks due to the two final states of $4f$ energy levels. As shown in Fig. 4, the shape of the two emission spectra with excited in other Ce^{3+} absorption wavelength, 336 and 356 nm, are different. From this result, these two transitions occur in Ce^{3+} on the different sites. On the other hand, similarity in the emission excited with 336 and 187 nm indicates preferential energy transfer from host to Ce^{3+} in the particular site.

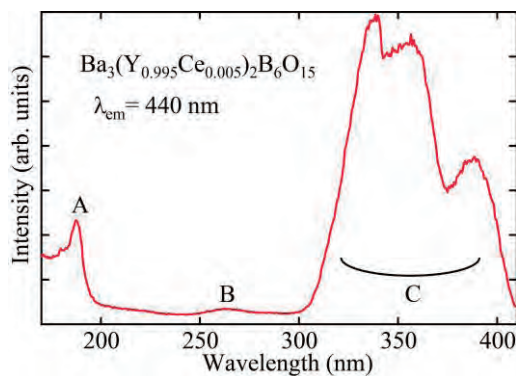


Fig. 1. Excitation spectrum of $\text{Ba}_3(\text{Y}_{0.995}\text{Ce}_{0.005})_2\text{B}_6\text{O}_{15}$.

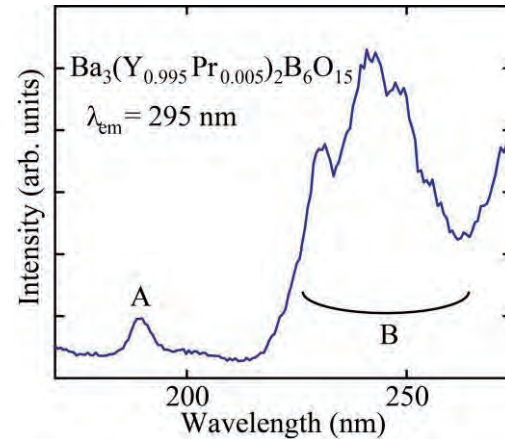


Fig. 2. Excitation spectrum of $\text{Ba}_3(\text{Y}_{0.995}\text{Pr}_{0.005})_2\text{B}_6\text{O}_{15}$.

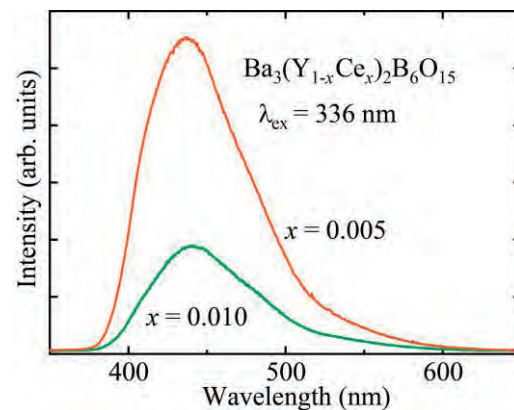


Fig. 3. Emission spectra of Ce-doped $\text{Ba}_3\text{Y}_2\text{B}_6\text{O}_{15}$.

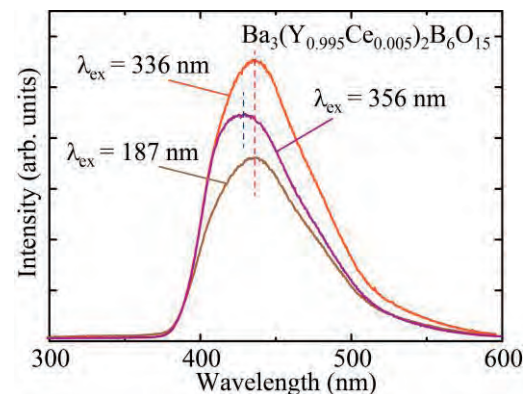


Fig. 4. Emission spectra of $\text{Ba}_3(\text{Y}_{0.995}\text{Ce}_{0.005})_2\text{B}_6\text{O}_{15}$.

BL3B

Optical Spectroscopy of Nd and Cr Codoped $Y_3Sc_xGa_yAl_{5-x-y}O_{12}$ Single Crystals

M. Yamaga, T. Kishita, S. Fujiwara, Y. Takeda and A. Ogata

Department of Mathematical and Design Engineering, Gifu University, Gifu 501-1193, Japan

Garnet crystals codoped with Nd and Cr are a candidate of solar-pumped laser materials. In order to improve pumping efficiency of Nd^{3+} luminescence and energy transfer of Cr^{3+} to Nd^{3+} , substitutional disordered crystals $Y_3Sc_xGa_yAl_{5-x-y}O_{12}$ were prepared. The prepared garnet crystals were denoted by YAG ($x=0, y=0$), YSAG ($x=0.2, y=0$), YGAG ($x=0, y=0.2$). The substitution produces inhomogeneous broadening of the Nd^{3+} and Cr^{3+} optical spectra. Enhancement of overlapping between the Cr^{3+} absorption and solar spectra and between the Cr^{3+} luminescence bands and the Nd^{3+} absorption lines lead to an increase of the pumping efficiency and the energy transfer rates, respectively.

Figure 1 shows the absorption spectra of Nd:Cr:YGAG, Nd:Cr:YSAG in comparison with that of Nd:Cr:YAG. The base lines are shifted for clarity. The sharp lines observed in the ultraviolet (UV), visible, and near infrared (IR) regions for three crystals are due to the optical transitions from the $^4I_{9/2}$ multiplet ground state of Nd^{3+} to the multiplet excited states. Three broad bands with peaks at 270, 430, and 600 nm are assigned to the optical transitions from the 4A_2 ground state of Cr^{3+} to the $^4T_1(2)$, $^4T_1(1)$, and 4T_2 excited states, respectively. The difference in the absorption spectra of (Nd:Cr:YGAG, Nd:Cr:YSAG) and Nd:Cr:YAG in Fig. 1 is inhomogeneous broadening of the Nd^{3+} lines in Nd:Cr:YGAG or Nd:Cr:YSAG caused by substitution of Ga^{3+} or Sc^{3+} for Al^{3+} , respectively. The absorption coefficients of Cr^{3+} bands and Nd^{3+} lines in Nd:Cr:YGAG and Nd:Cr:YSAG were (2.5, 0.7) or (0.7, 0.1) times compared with those in Nd:Cr:YAG, respectively. This estimated ratios are nearly equal to the concentration ratios of Cr and Nd contained in these samples, respectively.

Figure 2 shows the normalized luminescence spectra excited at 430 nm in the $^4T_1(1)$ absorption band of Cr^{3+} for three crystals. These spectra consist of sharp intense R lines around 690 nm and phonon-absorbed and phonon-emitted side bands around 678 and 707 nm of Cr^{3+} and weak near IR lines around 885 nm due to the optical transitions from the metastable $^4F_{3/2}$ excited state of Nd^{3+} to the $^4I_{9/2}$ lowest state.

Figure 3 shows the excitation spectra of the Nd^{3+} luminescence lines at 885 nm for three crystals. The excitation spectra are the superposition of the Cr^{3+} absorption bands and the Nd^{3+} absorption lines. The observation of the Cr^{3+} bands in the Nd^{3+} excitation spectrum gives evidence on the energy transfer from Cr^{3+} to Nd^{3+} .

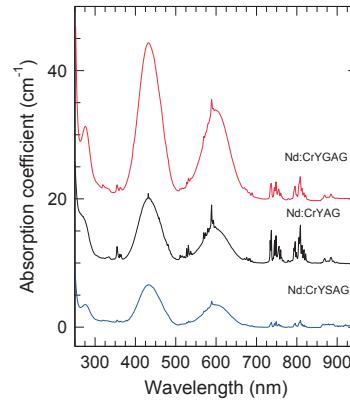


Fig. 1. Absorption spectra for three garnet crystals.

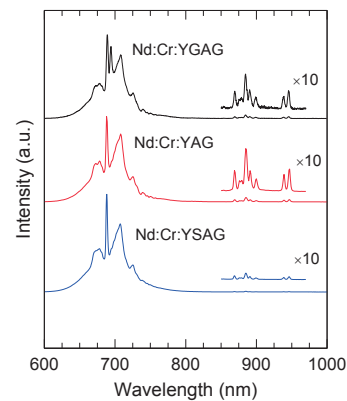


Fig. 2. Emission spectra for three garnet crystals.

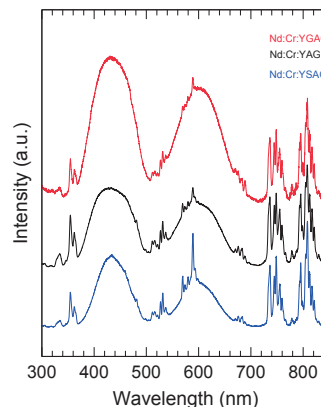


Fig. 3. Excitation spectra for three garnet crystals.

BL3B

Relaxed Exciton Luminescence of RbCl Heavily Doped with RbI

N. Ohno and K. Sakae

Graduate School of Engineering, Osaka Electro-Communication University, Neyagawa 572-8530, Japan

Extensive studies have been made on luminescence arising from localized relaxed excitons in alkali chlorides containing iodine impurities. Dilute Γ -doped crystals stimulated with VUV light or X-rays produces characteristic luminescence bands. The luminescence bands have been well explained in terms of localized relaxed excitons at ICl^- molecule (Γ^- monomer) and a complex of two iodine ions (Γ^- dimer) [1,2]. However, optical and luminescence properties of heavily iodine-doped alkali chloride crystals have not been examined sufficiently so far. Recently our group have studied luminescence properties of KCl heavily doped with KI as reported in ref. [3]. The present report describes the results of RbCl heavily doped with RbI.

The crystals of RbCl:I were grown by the Bridgeman method from reagent grade RbCl added with an appropriate amount of RbI (up to 5 mol %). The optical measurements were made at 15 K at BL3B station.

In dilute crystals, the photoluminescence spectra were almost the same as those of the previous studies [4,5]: three luminescence bands peaking at 2.46 eV (monomer emission), 4.38 eV (dimer emission) and at 5.76 eV (NE emission). Photoexcitation spectra for the dimer emission are shown in Fig. 1 for various RbI mol % crystals detected at 4.38 eV. The each spectrum has been normalized at unity at the maximum. The excitation peaks at 6.25 and 6.78 eV of 0.01 mol % crystal move toward the lower energy side with increasing RbI concentration. The low energy shift of the excitation bands suggests that there coexist dimers, trimers and larger sizes of I^- ions (RbI cluster) in heavily-doped RbCl:I crystal as can be observed in heavily-doped KCl:I [3].

The luminescence energies of the trimers and clusters of I^- ions in heavily doped RbCl:I crystals are expected to be different from that of Γ^- dimers. We have examined the photoluminescence spectra excited at various photon energies. The results for 1 mol % crystal are shown in Fig. 2. It is clearly confirmed that the peak energy of the luminescence band moves towards the low energy side when excited with lower photon energy. These luminescence bands are supposed to be the composite bands due to radiative annihilation of the relaxed exciton at dimers, trimers and clusters of I^- ions [3].

In RbCl crystals containing RbI around 1 mol %, there exists a small amount of dimer centers as compared with monomers, and moreover the amount of trimers and clusters of RbI is extremely smaller than

those of monomers and dimers. However, the

luminescence intensities of such large-sized centers are found to be comparable with that of the dimer emission. This fact suggests that the excitons trapped in RbI clusters in heavily doped RbCl:I crystals would give the high luminescence efficiency.

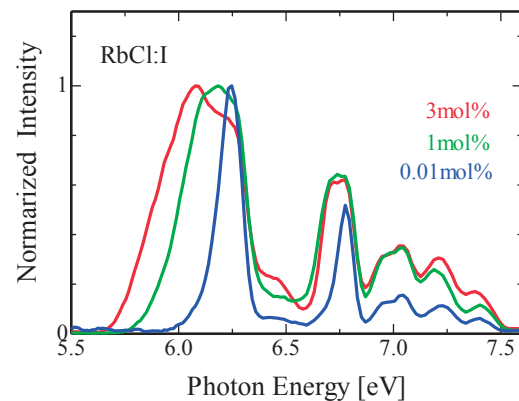


Fig. 1. Photoexcitation spectra of RbCl:I crystals detected at 4.38 eV for various RbI mol % at 15 K.

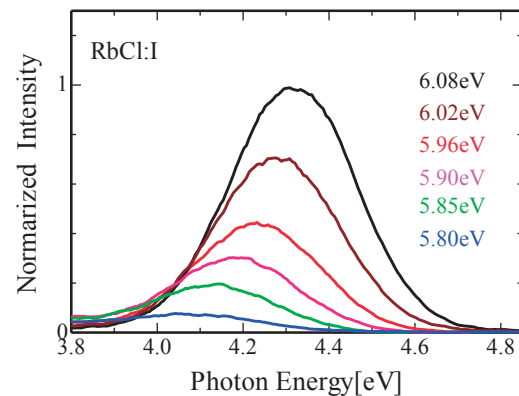


Fig. 2. Photoluminescence spectra of RbCl:I (1 mol%) crystal excited with various photon energies at 15 K.

- [1] N. Nagasawa, *J. Phys. Soc. Jpn.* **27** (1969) 1535.
- [2] K. Kan'no, K. Tanaka and T. Hayashi, *Rev. Solid State Sciences* **4** (1990) 383, and references therein.
- [3] A. Ohno and N. Ohno, *Phys. Status Solidi C* **8** (2011) 112.
- [4] O. Arimoto, K. Sasaki, H. Nakatani, K. Kan'no and Y. Nakai, *J. Lumin.* **31&32** (1984) 333.
- [5] K. Kan'no, H. Nakatani, T. Mukai, O. Arimoto, and Y. Nakai, *J. Phys. Soc. Jpn.* **55** (1986) 2433.

BL3B

Near Band Edge Absorption Spectra and Green Band Excitation Spectrum of Boron-Doped Diamond Films

S. Kondou¹, K. Fukui¹, K. Yamamoto² and T. Inushima³

¹Department of Electrical and Electronics Engineering, University of Fukui, Fukui 910-8507, Japan

²FIR Center, University of Fukui, Fukui 910-8507, Japan

³Department of Electronics, Tokai University, Hiratsuka 259-1292, Japan

Boron (B) is one of the best elements for p-type impurity of the diamond semiconductor devices. Boron-doped diamond (BDD) is also known as the blue diamond. Then, we have been measuring the CEES (Combined Excitation Emission Spectroscopy) around the band-gap (excitation energy 4.5 ~ 7.0eV) in order to clarify the electron state of BDD whose B concentrations is in the metal like - semiconductor transition region. In this study, we have focused on the CEES pattern differences of between BDDs and non B doped diamond (substrate) around the H3 emission band which consists of several sharp peaks and has the maximum peak at 2.47 eV.

The BDD films used in this study are grown on Ib-synthesized diamond substrates by the MPCVD (Microwave Plasma Chemical Vapor Deposition) method and their B concentration are 1000, 5000 and 10000 ppm [1]. All CEES measurements including the diamond substrate (0 ppm) have been performed at BL3B (and BL7B).

Figure 1 show the CEES patterns of both 1000 ppm and 10000 ppm BDD samples at 9 K. The horizontal and the vertical axes correspond to the emission photon energy and the excitation photon energy, respectively. Strong emissions around 2.4eV at low excitation photon energy region (<~6.0eV) are H3 emission band which are due to the nitrogen dimer defect (H3) centers in the substrate. The drastic intensity increases of the H3 emissions at 5.5 eV in Fig. 1 suggest that the indirect band gap locates at about 5.5 eV. On the other hand, at high excitation photon energy region (>~6.0eV), no H3 emission band has been observed in any samples without 0 ppm, because the excitation light cannot reach substrates through BDD thin films due to the strong absorption of BDD at high excitation photon energy region. However, 1000 ppm only show a different Gaussian type emission band whose peak locates at 2.3 eV. This emission band is probably assigned as the Green emission band that is often observed in the BDD. Figure 2 shows the excitation spectrum of the Green emission band. We believe that this is the first excitation spectrum of this emission band.

From the above description, the excitation photon energy dependence of the H3 emission band intensity represents the photon energy dependence of the transmittance of the BDD thin film. Then, we try to make the near band edge absorption spectra of the BDD thin films. Figure 3 shows the absorption

spectra of 1000 ppm, 5000 ppm and 10000 ppm BDD thin films.

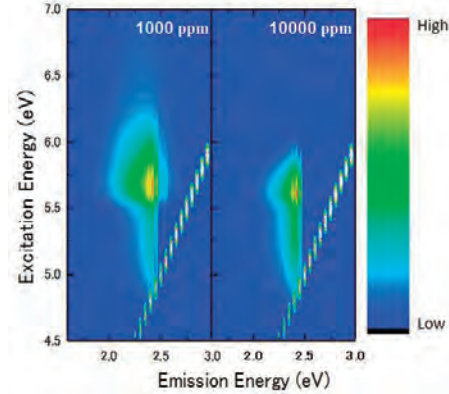


Fig. 1. CEES patterns of 1000 ppm (left) and 10000 ppm (right) BDD samples at 9 K.

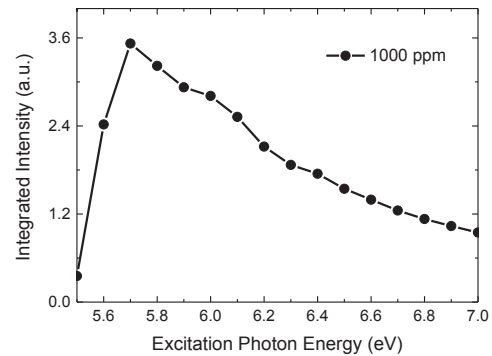


Fig. 2. Excitation spectrum of the Green emission band.

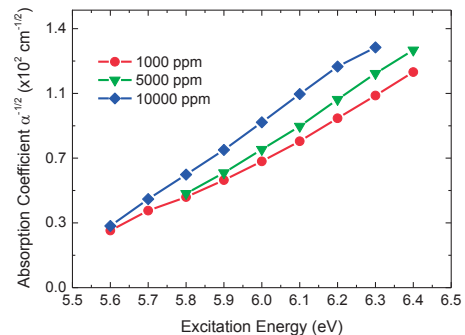


Fig. 3. Absorption spectra of 1000 ppm, 5000 ppm and 10000 ppm BDD thin films.

[1]A. Ogasawara, T. Inushima, T. Shiraishi, S. Ohya, S. Karasawa and H. Shiomi, *Diamond Related Mater.* **6** (1997) 835.

BL3B

Optical Properties of SrCeO₃ Crystals

H. Numata¹, M. Kitaura², S. Watanabe³, S. Kurosawa⁴, K. Yubuta⁴ and A. Ohnishi²

¹School of Science and Technology, Yamagata University, Yamagata 990-8560, Japan

²Department of Physics, Faculty of Science, Yamagata 990-8560, Japan

³Department of Materials, Physics and Energy Engineering, Graduate School of Engineering, Nagoya University, Nagoya 464-8063, Japan

⁴Institute for Materials Research, Tohoku University, Sendai 980-8577, Japan

From analogy with CeO₂, the electronic state of SrCeO₃ is considered to be in the mixed-valence state due to mixing between $4f^0$ and $4f^1L^{-1}$ configurations, where L^{-1} denotes the hole in valence band mainly composed O-2p orbitals [1]. The mixed valence state results from hybridization between O-2p and Ce-4f orbitals. Basically, Ce-4f electrons have localized character. However, it is considered that they have itinerant character, owing to the mixed valence state. Since either localization or itinerancy should be reflected in the conductive behavior of Ce-4f electrons, photoconductivity experiment is favorable to investigate the dynamical behavior of Ce-4f electrons in photoexcited SrCeO₃. As a first step, we have measured photoabsorption (PA), photoluminescence (PL), PL excitation (PLE) spectra of SrCeO₃ crystals, in order to obtain fundamental optical properties. These data provide us information on creation and relaxation processes of Ce-4f electrons and O-2p holes.

SrCeO₃ crystals were grown in air by a Floating zone method. They were annealed under oxygen atmosphere for 24h at 1070K. Crystal surfaces were mechanically polished. Experiment was performed at the beamline BL3B in UVSOR facility. PA spectra were obtained by detecting incident and transmitted light with a calibrated silicon photodiode. PL and PLE spectra were measured using the combination of a grating monochromator and a CCD detector or a photomultiplier, respectively. PLE spectra were corrected for the energy distribution of excitation light source.

Figure 1 shows PA (green line), PL (blue line) and PLE (red line) spectra, which were measured at 9 K. The PA spectrum exhibits the fundamental absorption edge at 2.46 eV. According to the electronic structure calculation reported previously, such a rapid increase is ascribed to the formation of the charge transfer (CT) excitons which are composed of Ce-4f electrons and O-2p holes. A PL band appears around 2.30 eV under excitation at 4.81 eV. A similar band is observed in PL spectra of Sr₂CeO₄ [4]. The PLE spectrum for the 2.30 eV band shows that it is excited in the energy region above 3.46 eV. The intensity of the 2.30 eV band reaches the maximum at 4.07 eV, and is gradually decreased with increasing photon energy.

The 2.30 eV band is excited in the fundamental absorption region. This result suggests that the 2.30

eV band is an intrinsic feature in SrCeO₃. This band has the Stoke shift of 0.30 eV. It is likely to consider that the 2.30 eV band originates from the relaxed state of a CT exciton, which may localizes on a octahedral (CeO₆)⁸⁻ complex ion.

The threshold for excitation of the 2.30 eV band is not agreement with the fundamental absorption edge. Such a disagreement implies that CT excitons annihilate nonradiatively under photoexcitation near the fundamental absorption edge. There are two possible explanations for this. One is that CT excitons transfer their energy to lattice imperfections before lattice relaxation. The other is that CT excitons immediately relax to the ground state without emitting 2.30 eV band. The missing of 2.30 eV band is an open problem to be solved, and details of it will be clarified by photoconductivity experiment.

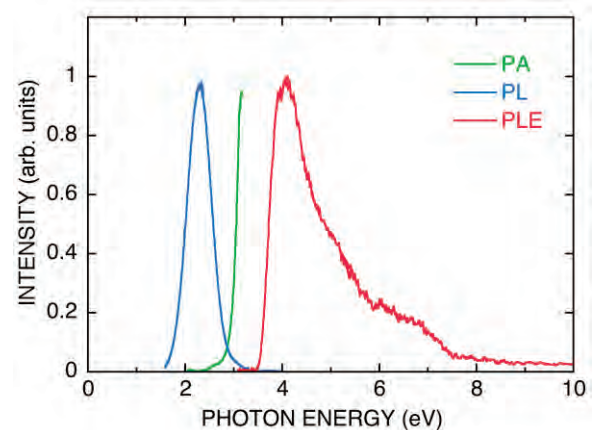


Fig. 1. PA (green line), PL (blue line), and PLE (red line) spectra of SrCeO₃ crystals measured at 9K.

- [1] A. Fujimori *et al.*, Phys. Rev. B **28** (1983) 2281.
- [2] M. Niwano *et al.*, J. Phy. Soc. Jpn. **57** (1988) 1489.
- [3] H. Numata *et al.*, UVSOR Activity Report 2013 **41** (2014) 63.
- [4] L. V. Peterson *et al.*, J. Electrochem. Soc. **147** (2000) 4688.

BL3B

VUV Absorption Spectra of Alanine Single Crystals

S. Tanaka, M. Kitaura, A. Ohnishi and M. Sasaki

Department of Physics, Faculty of Science, Yamagata University, Yamagata 990-8560, Japan

Amino acids are simple chiral molecules with L- and D-forms. Protein molecules are composed of only L-amino acids. This is called “homochirality”, which has attracted much attention in relation to the mystery of life. It has been generally accepted that the homochirality of proteins come from the creation of L-amino acids by circularly polarized VUV light in outer space region. So far, VUV absorption spectra of amino acids have been studied using their aqueous solutions [2] and thin films [3]. To our knowledge, there is no report on VUV absorption spectra of amino acid single crystals. In the present study, VUV absorption spectra of alanine crystals have been measured to provide the true absorption spectrum of it, and to verify the validity of natural circular dichroism spectra already reported [4].

The alanine single crystals were obtained by the slow evaporation from saturated aqueous solution of commercial L-alanine reagent (SIGMA-ALDRICH, purity > 99.5%). The photograph of an alanine single crystal used in our experiment is shown in Fig. 1. The crystal structure of alanine is orthorhombic, and orthogonal crystalline axes exist in the cleavage place. They were distinguished by two polarizers arranged in a cross Nicole alignment. However, it could not be determined which are they among *a*, *b* and *c* crystalline axes.

Figure 2 shows the VUV absorption spectra of an alanine single crystal for different configurations of linearly polarized light. These data were obtained by the Kramers-Kronig analysis from the VUV reflectivity spectra in 5-30 eV range measured at room temperature. A number of peaks are observed in 5-10 eV range. They show remarkable linear dichroism, which has not been found in Refs. 2 and 3. A broad peak is observed in around the 14.0 eV. This peak has been reported in Ref. 4. The VUV absorption spectra of an alanine crystal are shown in an expanded scale of 5-12 eV. They are composed of peaks around 6.0, 6.8, 7.5, 8.0, 9.2, and 10.0 eV. In Ref. 4, the natural circular dichroism spectrum of a L-alanine deposit thin film exhibited peaks at 6.8 and 8.0 eV and dips at 6.2 and 7.5 eV. Since the energies are in good agreement with those of absorption peaks in Fig. 3, we can say that there is no doubt on the validity of natural circular dichroism spectra in Ref. 4.



Fig. 1. Photograph of an alanine crystal used in our experiment.

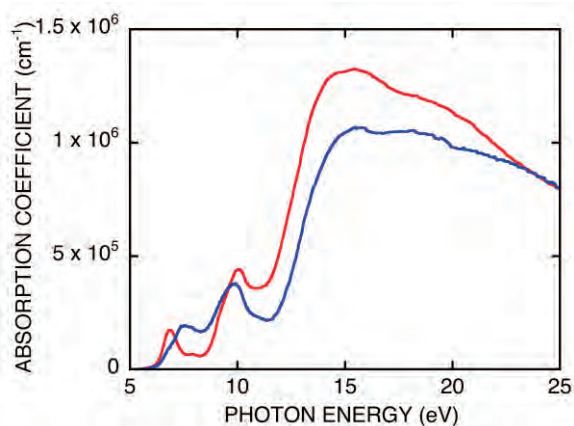


Fig. 2. VUV absorption spectra of an alanine crystal, which were obtained by the Kramers-Kronig analysis from reflectivity spectra in 5-30 eV range measured at room temperature.

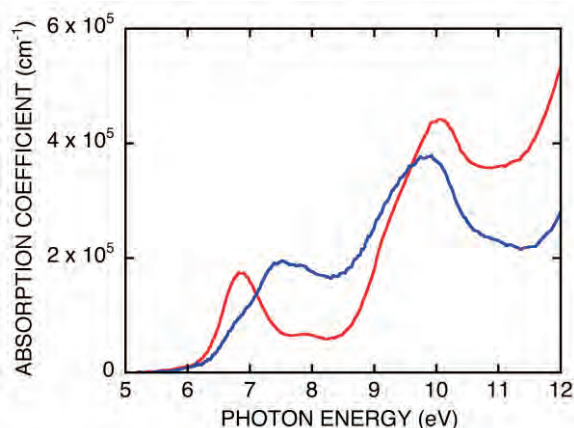


Fig. 3. VUV absorption spectra of an alanine crystal in an extended scale of 5-12 eV.

- [1] P. A. Snyder *et al.*, *Biopolymers* **12** (1973) 975.
- [2] T. Inagaki *et al.*, *Biopolymers* **12** (1973) 1353.
- [3] M. Tanaka *et al.*, *J. Electron Spectrosc. Relat. Phenom.* **181** (2001) 177.
- [4] F. Kaneko *et al.*, *J. Phys. Soc. Jpn.* **78** (2009) 013001.

BL3B

Temperature Dependence of Absorption Spectra for Ce³⁺-Doped Y₃Al₅O₁₂ Single Crystals

S. Watanabe¹, M. Nakaya¹, J. Onoe¹, M. Kitaura², K. Kamada³ and A. Ohnishi²

¹Department of Materials, Physics and Energy Engineering, Graduate School of Engineering, Nagoya University, Nagoya 464-8603, Japan

²Department of Physics, Faculty of Science, Yamagata University, Yamagata 990-8560, Japan

³New Industry Creation Hatchery Center, Tohoku University, Sendai 980-8579, Japan

Ce³⁺-doped Y₃Al₅O₁₂ (Ce:YAG) have been widely studied for application as a yellow phosphor used in white light LEDs. The basic research on optical properties for Ce:YAG is important issues for development of luminescent materials. In addition, the detailed analysis based on a first-principles calculation is useful for understanding the optical properties of luminescent materials.

In this study, we have performed experimental and theoretical investigation of the temperature dependence of the 4*f*-5*d* absorption spectra for Ce:YAG single crystals.

The single crystals of Ce:YAG were grown by the micro pulling down method. The concentration of Ce³⁺ was 1 mol%. The 4*f*-5*d* absorption spectra were measured at 9 and 312 K. These absorption spectra were analyzed by using a first-principles configuration interaction calculation [1,2]. The effects of lattice relaxation due to the substitution of Y³⁺ by Ce³⁺ were considered using the optimized structure estimated by a first-principles DFT calculation.

Figure 1 shows the experimental 4*f*-5*d* absorption spectra of Ce:YAG at 9 and 312 K, respectively. Three major peaks A, B and C were observed in both spectra. These peaks can be attributed to the Ce³⁺ 4*f*-5*d* absorption peaks. The peak intensities depend upon temperature. As shown in Fig. 1, the intensity of peak B at 9 K increases, compared with that at 312 K. In order to investigate the effects of thermal excitation, we calculated the oscillator strengths for the transitions from two different initial states since the Ce³⁺ 4*f*_{5/2} level slightly splits due to the crystal field. Figure 2 shows the theoretical 4*f*-5*d* absorption spectra of Ce:YAG. Figure 2(a) shows the oscillator strengths from the lowest 4*f*_{5/2} level, and Fig. 2(b) shows the oscillator strengths from the higher-lying 4*f*_{5/2} level which is 0.108 eV higher than the lowest level. The oscillator strength of the peak B for the transition from the higher-lying 4*f*_{5/2} level is significantly strong, compared to that from the lowest level. This result clearly indicates that the origin of the strong temperature dependence of the peak B in the experimental spectra can be ascribed to the change of re-distribution of electron population inside the 4*f*_{5/2} level by the initial state due to the thermal excitation.

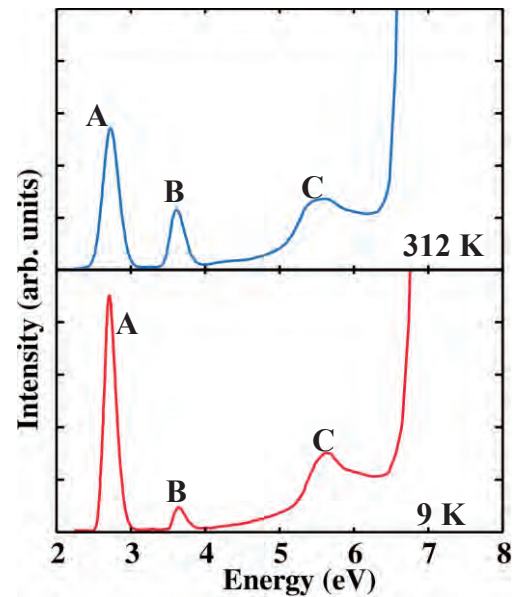


Fig. 1. Experimental absorption spectra of Ce:YAG at 9 and 312 K.

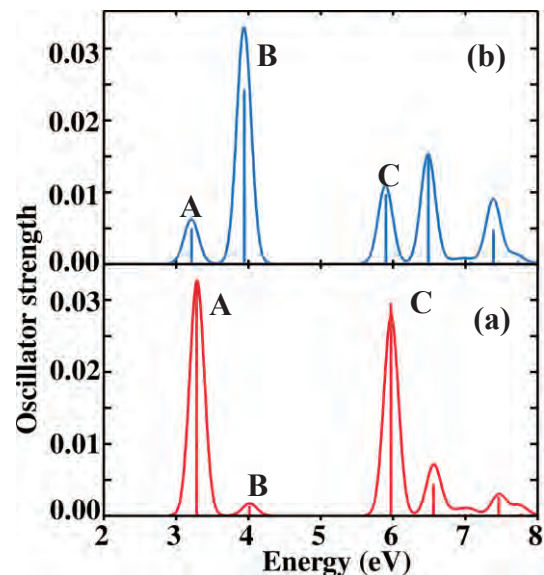


Fig. 2. Theoretical absorption spectra of Ce:YAG. (a) Oscillator strengths from the ground state of 4*f*_{5/2} level. (b) Oscillator strengths from second-lowest 4*f*_{5/2} level.

[1] K. Ogasawara *et al.*, Phys. Rev. B **64** (2001) 143.

[2] S. Watanabe *et al.*, Phys. Rev. B **81** (2010) 125128.

BL3B

Two-Band Luminescence from an Intrinsic Defect in Spherical and Terraced MgO Nanoparticles

P. V. Pikhitsa¹, C. Kim¹, S. Chae¹, S. Shin¹, S. Jung¹, M. Kitaura²,
S. Kimura³, K. Fukui⁴ and M. Choi¹

¹Global Frontier Center for Multiscale Energy Systems, Division of WCU Multiscale Mechanical Design, School of Mechanical and Aerospace Engineering, Seoul National University, Seoul 151-744, Korea

²Department of Physics, Faculty of Science, Yamagata University, Yamagata 990-8560, Japan

³UVSOR Facility, Institute for Molecular Science and the Graduate University for Advanced Studies, Okazaki 444-8585, Japan

⁴Department of Electrical and Electronics Engineering, Faculty of Engineering, University of Fukui, Fukui 910-8507, Japan

Magnesium oxide nanocubes obtained by the self-combustion of Mg metal have long exhibited only a broad 2.9 eV cathodoluminescence (CL) band owing to oxygen vacancies (F centers). In our work, a room-temperature ultraviolet 4.8 eV CL band has been observed coincident with a 2.5 eV band of the same intensity from an unexplored intrinsic defect in MgO terraced nanocubes and nanospheres produced from Mg metal during combustion in an H_2/O_2 flame. Synchrotron radiation excitation spectra reveal that the excitation energy at the onset of both bands is just above the bandgap energy of 7.7 eV, where electrons and holes are generated (see Fig. 1).

Figure 1 compares the PL spectra, taken at 8 K, for photon excitation energies swept through the forbidden band and up to 10 eV from the UV-MgO (Fig. 1(a)) and the non-UV-MgO cubes (Fig. 1(b)). It is clear that the two PL bands observed in CL arise simultaneously at 7.7 eV and persist as the excitation energy sweeps deeper into the conduction band (Fig. 1(a)). This is a strong indication that both bands (marked by red circles in Fig. 1(a)) have the same origin and that electrons and holes from the conduction band are solely responsible and necessary for the excitation of the two bands, similar to the electron and hole “shower” in CL, when it is understood that a photon of 8 eV leads to the formation in MgO of a conduction electron and a hole that do not undergo transformation into a self-trapped state.

We determine that a defect, responsible for both emission bands, creates proximal anion-cation vacancy pairs named P centers that may appear instead of F centers because of changes in the MgO nanoparticle growth conditions.

The discovery of two-band room-temperature CL from spherical and terraced MgO nanoparticles may find applications in defect-center lasers based upon MgO and in spectral transformers.¹ The two-band CL may also have applications in the geosciences because its presence or absence should be useful to distinguish the history of MgO formation in the Earth's mantle or in planetary nebula.

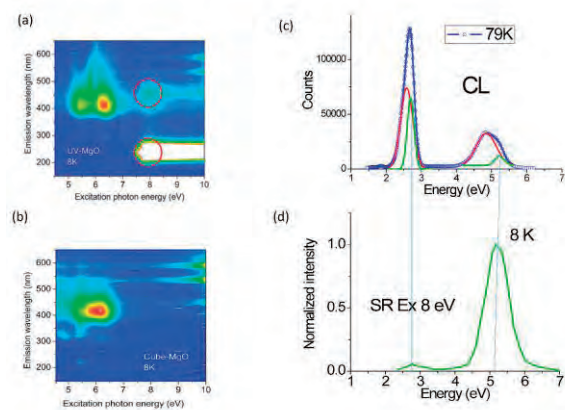


Fig. 1. Photoluminescence spectra vs. excitation energy from synchrotron radiation (intensity grows from blue to red). (a) Red circles marking correlated emission bands at 4.8 eV (upper) and 2.5 eV (lower) from UV-emitting MgO. The F^+ band at 420 nm is from the non-UV-MgO present in the powder sample. (b) Emission from non-UV-MgO cubes, where the F^+ band at 420 nm is present but the 4.8 and 2.5 eV bands are absent. (c) CL spectrum for UV-MgO taken at 79 K (blue) and the deconvoluted spectral peaks (red and green curves). The additional two-band spectrum (green curve) is compared with (d) the two-band synchrotron radiation spectrum (not corrected for intensity magnitude) excited at 8 eV and 8 K taken from (a).

[1] A. Lushchik, E. Feldbach, R. Kink, Ch. Lushchik, M. Kirm and I. Martinson, Phys. Rev. B **53** (1996) 5379.

BL4U

Scanning Transmission X-Ray Microscopy Study on Fluorescence Mechanism of Nanocarbon-Silica Composites

S. Kawasaki, H. Song and Y. Takeuchi

Nagoya Institute of Technology, Nagoya 466-8555, Japan

Mesoporous carbon-silica (MPCS) composites synthesized by tri-constituent co-assembly method have fascinating nano-space structures. We have investigated Li-ion battery anode and EDLC electrode properties of the composites. In the course of the investigation we found that mesoporous carbon-silica composites exhibit very intense visible photoluminescence under low-energy ultra-violet light irradiation.[1-5] Now, a class of stable, efficient, inexpensive and less toxic photoluminescent materials which emit white light under long-wavelength UV light is strongly required to replace fluorescent lamps by LED lamps. The composites we synthesized satisfy the required conditions and are the promising materials from the environmental point of view. However, detailed mechanism of the fluorescence property of MPCS has not been understood well. Then, in order to understand the mechanism, we performed scanning transmission x-ray microscopy (STXM) measurements of MPCS samples.

MPCS samples were prepared by tri-constituent co-assembly method. Tetraethyl orthosilicate (TEOS) and resol are used as silica and carbon sources, respectively. Tri-block co-polymer (BASF F-127) was used as a soft template. Carbonization was done in nitrogen atmosphere at 1170 K. Oxidation was done in air at 720 K. The obtained MPCS samples were characterized by TEM, SEM, XRD, Raman, and N₂ adsorption measurements. STXM measurements were performed at BL-4U of UV-SOR of Institute for Molecular Science, Okazaki, Japan.

Figure 1 shows the observed C K-edge X-ray absorption spectrum of MPCS sample. For usual bulk carbon samples, sharp π^* absorption peak is observed at around 285 eV. However, as shown in Fig. 1, for MPCS sample, the peak at around 285 eV is very broad and the peak-top is observed at about 288 eV. The cluster size of nanocarbons remained in MPCS sample after the oxidation treatment should be very small. If π conjugation scale is decreased, π - π^* gap should be widen. This would be the reason why the peak-top of π^* absorption of MPCS sample is observed at higher energy than usual bulk carbon samples. To confirm the validity of this hypothesis, we should perform STXM measurements of several kinds of MPCS samples having different carbon cluster sizes.

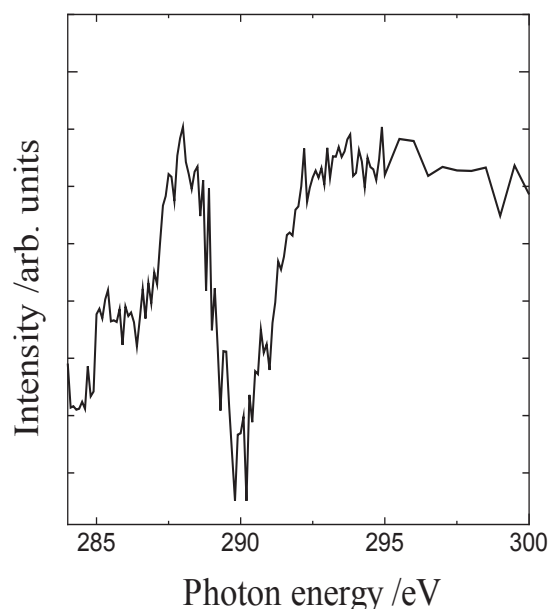


Fig. 1. Carbon K-edge X-ray absorption spectra of mesoporous carbon-silica composite sample.

- [1] Y. Ishii, A. Matsumura, Y. Ishikawa and S. Kawasaki, *Jpn J. Appl. Phys.* **50** (2011) 01AF06-1.
- [2] Y. Ishikawa, K. Sato, S. Kawasaki, Y. Ishii, A. Matsumura and S. Muto, *physica status solidi (a)* **209** (2012) 1022.
- [3] K. Sato, Y. Ishikawa, Y. Ishii, S. Kawasaki, S. Muto and Y. Yamamoto, *Jpn. J. Appl. Phys.* **51** (2012) 08240.
- [4] Y. Ishikawa, S. Kawasaki, Y. Ishii, K. Sato and A. Matsumura, *Jpn. J. Appl. Phys.* **51** (2012) 01AK02.
- [5] Y. Ishii, Y. Nishiwaki, A. Al-zubaidi and S. Kawasaki, *J. Phys. Chem. C* **117** (2013) 18120.

BL4U

The Effect of Carbon Bombardment of ZnO Probed by Scanning Transmission X-Ray Microscopy

Y. F. Wang¹, S. H. Hsieh¹, J. W. Chiou², W. F. Pong¹, T. Ohigashi³ and N. Kosugi³

¹Department of Physics, Tamkang University, Tamsui 251, Taiwan

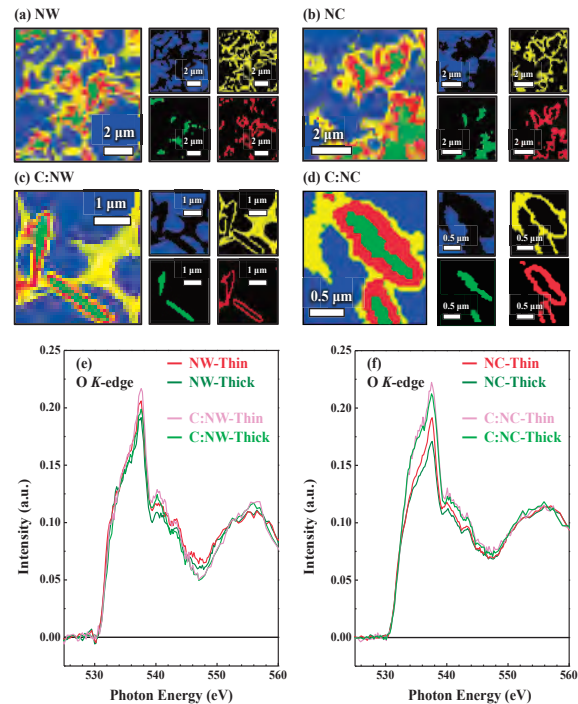
²Department of Applied Physics, National University of Kaohsiung, Kaohsiung 811, Taiwan

³UVSOR Facility, Institute for Molecular Science, Okazaki 444-8585, Japan

In the present work, the effect of carbon bombardment of ZnO nanowires (NW) and nanocactus (NC) has been studied using X-ray-based microscopic and spectroscopic techniques. Figures 1(a-d) display the O *K*-edge scanning transmission X-ray microscopy (STXM) stack mappings of randomly selected sample regions of ZnO NW and NC before and after carbon bombardment (C:NW and C:NC). The stack mappings are decomposed into blue, yellow, red and green maps (right panels), which correspond to the regions that are associated with different thickness and spectroscopic variations of the samples. Overall, the divisions of the mappings into thick (green), thin (red), carbon lacing (yellow) and background (blue) regions were generated via principle component analysis (PCA) for cluster analysis based on spectroscopic differences. The O *K*-edge STXM-XANES (X-ray Absorption Near-Edge Structure) spectra in the Figs. 1(e) and 1(f) are the sum of the corresponding XANES spectra of the thick (green) and thin (red) regions of ZnO NW and NC before and after C bombardment, respectively.

As displayed in Figs. 1(e) and 1(f), according to the dipole-transition selection rule, the near features at ~535-550 eV in the O *K*-edge STXM-XANES spectra are attributed to the electron excitations from O $1s$ -derived states to $2p_{\sigma}$ -derived (along the bilayer) and O $2p_{\pi}$ -derived (along the c axis) states, which are approximately proportional to the density of the unoccupied O $2p$ -derived states. The O *K*-edge STXM-XANES spectra clearly reveal that the intensities of near features in the thin regions are higher than those in the thick regions of ZnO NC/NW and C:NC/C:NW. The enhanced intensities of the near features in the O *K*-edge STXM-XANES spectra can result in a higher population of defects in the thin or surface/edge regions because of the non-stoichiometric chemical composition or dangling bonds.[1]

Additionally, the intensities of near features of ZnO C:NC/C:NW samples (after C bombardment) are also higher than those in ZnO NC/NW samples (before C bombardment), further suggesting that the bombarding C atoms may play an important role to enhance density of the unoccupied O $2p$ -derived states.



Figs. 1. (a)-(d): O *K*-edge scanning transmission X-ray microscopy (STXM) stack mappings of randomly selected sample regions of ZnO NW and NC before and after carbon bombardment (C:NW and C:NC). The spatial distribution of background (blue), carbon lacing (yellow), thick (green) and thin (red) regions of samples. (e) and (f): The O *K*-edge STXM-XANES spectra are the sum of the corresponding XANES spectra between the thin (red) and thick (green) regions of ZnO NW and NC before and after C bombardment, respectively.

[1] S. B. Singh *et al.*, *Nanoscale* **6** (2014) 9166.

BL4U

Chemical Redox of Mesoscopic NiO/CH₃NH₃PbI₃ Perovskite Heterojunction by Scanning Transmission X-Ray Microscopy

M. W. Lin¹, K. C. Wang², L. T. Chang¹, Y. L. Lai¹, T. Ohigashi³, N. Kosugi³, P. Chen² and Y. J. Hsu^{1,2}

¹National Synchrotron Radiation Research Center, Hsinchu 300, Taiwan

²Department of Photonics, National Cheng Kung University 701, Tainan, Taiwan

³Institute for Molecular Science, Okazaki 444-8585, Japan

Organometal trihalide perovskite-based solar cells have exhibited high power conversion efficiencies when incorporated into mesoscopic NiO (NiO_{nc}) hole-transport layers [1]. Herein we studied the origin of such high efficient carrier transport in terms of electronic and chemical properties of perovskite-NiO_{nc} heterojunction by x-ray photoelectron spectroscopy (XPS), Near-edge X-ray absorption fine structure (NEXAFS), and scanning transmission X-ray microscopy (STXM).

From our previous studies, we found a pronounced chemical redox between CH₃NH₃PbI₃ perovskite-NiO_{nc} heterojunction that PbI₂ is oxidized to PbO and subsequently produce hole-dopant CH₃NH₃PbIO at the heterojunction. From the O *K*-edge spectra in an auger-electron-yield (AEY) mode, we observed an extra distinct peak at 535 eV for ITO/NiO_{nc}/CH₃NH₃PbI₃ in comparison to pristine NiO_{nc}. This additional peak is apparently produced by the contact reaction at heterojunction of NiO_{nc}/CH₃NH₃PbI₃. As a result, the generation of hole-doping CH₃NH₃PbIO at NiO_{nc}/perovskite heterojunction plays a critical role to facilitate the carrier transport, and thus enhance the solar cell efficiencies.[2]

To further confirm the redox reaction at NiO_{nc} and CH₃NH₃PbI₃ perovskite heterojunction, chemical maps of oxygen distributions within microaggregates of SiN/NiO_{nc}/CH₃NH₃PbI₃ are studied by STXM. Figure 1 displays the STXM images of SiN/NiO_{nc}/CH₃NH₃PbI₃, which are optical density (OD) maps obtained at (a) 532.1 eV and (b) 535.1 eV, the characteristic absorption peaks of NiO_{nc} and CH₃NH₃PbIO, respectively as mentioned above. The Pb OD map of the SiN/NiO_{nc}/CH₃NH₃PbI₃ as shown in Figure 1b is obtained at 610 eV. These image mappings of O and Pb on SiN/NiO_{nc}/CH₃NH₃PbI₃ show similar elemental distribution in morphology and size except the contrast. As a result, we anticipate that the Pb is bonded with O and located on the mesoporous structure of NiO_{nc}. The image acquired at 532.1 eV which is composed of major characters of O 2p and Ni 3d orbitals, exhibits weaker image contrast than that obtained at 535.1 eV, indicating the NiO_{nc} is involved in the interfacial redox reaction at heterojunction. The more redox occurs, the lower the peak intensity of 532.1 eV and thus the weaker the contrast displays.

The corresponding micro NEXAFS spectra as the cross marks shown in Figure 1 are displayed in Figure 2a and 2b for O *K*-edge and Pb *N*-edge, respectively. In comparison with pristine NiO_{nc} (as shown in the inset of Figure 2b), the spectra show decreased peak intensity at 532.1 eV and broader peak width between 535-545 eV. The micro NEXAFS of Pb *N*-edge in Figure 2c express similar shape and intensity. Our results suggest that the redox is occurred at heterojunction and the formation of perovskite is located in the mesoporous structure of NiO_{nc}.

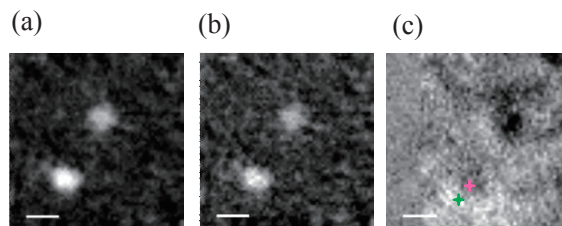


Fig. 1. The OD images of O *K*-edge at (a) 532.1 eV, (b) 535.1 eV, and (c) Pb *N*-edge at 654 eV from SiN/NiO_{nc}/CH₃NH₃PbI₃.

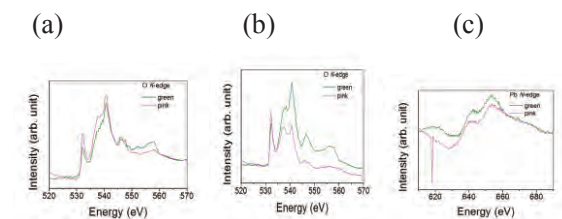


Fig. 2. Micro-NEXAFS spectra of the O *K*-edge and Pb *N*-edge extracted from the Figure 1a, 1b, and 1c, respectively. The inset in Figure 2a shows the O *K*-edge NEXAFS of pristine NiO_{nc}.

[1] K. C. Wang, J. Y. Jeng, P. S. Shen, Y. C. Chang, E. W.-G. Diau, C. H. Tsai, T. Y. Chao, H. C. Hsu, P. Y. Lin, P. Chen, T. F. Guo and T. C. Wen, *Sci. Rep.* **4** (2014) 4756.

[2] Ming-Wei Lin, Kuo-Chin Wang, Yu-Ling Lai, Takuji Ohigashi, Nobuhiro Kosugi, Peter Chen, Tzung-Fang Guo and Yao-Jane Hsu, "Chemical Redox of Mesoscopic NiO/CH₃NH₃PbI₃ Perovskite Interfaces for High Efficient Solar Cell", in preparation.

BL4U

Characterization of Monolithic Polymers Containing Nanoparticles by Scanning Transmission X-Ray Microscopy (STXM)

D. Arrua¹, C. Desire¹, A. Khodabandeh¹, T. Ohgashi², N. Kosugi² and E. Hilder¹

¹Australian Centre for Research on Separation Science (ACROSS), School of Chemistry, University of Tasmania, Private Bag 75, Hobart 7001, Australia

²UVSOR Facility, Institute for Molecular Science, Okazaki 444-8585, Japan

Monolithic polymers are a new generation of stationary phases for chromatography, offering significant benefits over currently particle-based materials. The main characteristic of these materials is the presence of large through-pores which permits the use of high flow rates at low backpressures [1]. However, improvements in this technology rely on being able to accurately characterize the porous structure and new characterization techniques are needed to better understand the polymer morphology and its optimization. In this sense, the relatively high penetration power of X-rays would allow a comprehensive analysis of the radial and longitudinal heterogeneity of the monolithic materials developed in our research group.

The characterization by STXM of polymer monoliths was performed at the BL4U beamline of the UVSOR synchrotron radiation facility. To obtain a suitable sample for STXM studies, the macroporous styrene-divinylbenzene (Sty-DVB) monolith with encapsulated hydroxyapatite (HAP) and titanium dioxide (TiO₂) nanoparticles was embedded with an aliphatic epoxy resin specially designed for STXM analysis [2]. The experiments were performed at the C-K, Ca-L and Ti-L edges. Figure 1 shows the NEXAFS spectra for both the HAP and TiO₂ nanoparticles. Both spectra show several peaks which are a result of the combination of spin-orbit splitting between the 2p and 3d orbitals [3, 4].

The spectrum of the Sty-DVB polymer has a peak at 285.2 eV which corresponds to the C 1s → π*_{C=C} transition of aromatic systems (spectrum not shown).

These spectroscopic differences allowed identification and mapping of each type of nanoparticle within the polymer monolith. Figure 2 presents STXM optical density (OD) images at three different energies of a monolith containing 5% wt/wt of each nanoparticle. It is possible to see the HAP nanoparticles at 349 eV (Fig. 2. panels a and d), the TiO₂ nanoparticles at 460.4 eV (Fig. 2. panels b and e) and the polymer scaffold at 285.2 eV (Fig. 2. panels c and e). These OD images display the spatial distribution of each type of nanoparticle within the polymeric scaffold.

Ongoing studies in our research group are focused in the application of these composite materials as solid supports for liquid chromatography and solid phase extraction.

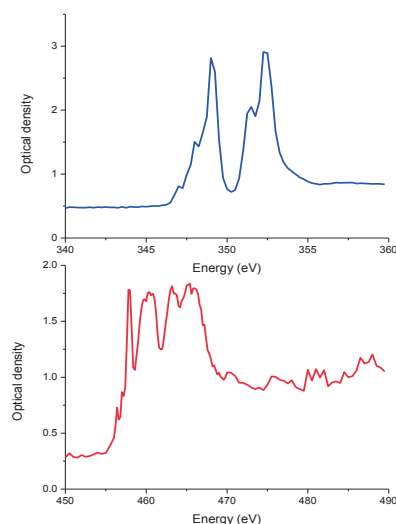


Fig. 1. NEXAFS spectra of HAP (top) and the TiO₂ (bottom) nanoparticles.

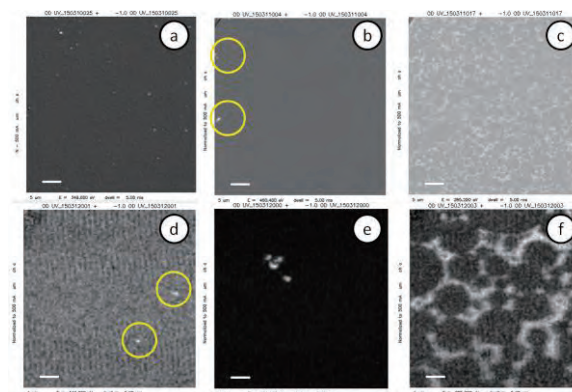


Fig. 2. STXM optical density (OD) images at (a and d) 349, (b and e) 460.4 and (c and f) 285.2 eV. Scale bars = 5 μm (a-c) and 1 μm (d-e).

- [1] R. D. Arrua *et al.*, *Analyst* **137** (2012) 5179.
- [2] A. P. Hitchcock *et al.*, *J. Electron Spectrosc.* **156** (2007) 467.
- [3] S. Hanhan *et al.*, *J. Electron Spectrosc. Relat. Phenom.* **172** (2009) 44.
- [4] H. Zhang *et al.*, *J. Chem. Phys.* **136** (2012) 174701.

BL4B

O K-Edge Spectroscopy of High Valence State Mn(V) Oxides

Y. Aoki, T. Kobayashi, K. Kuroda, E. Tsuji and H. Habazaki
 Faculty of Engineering, Hokkaido University, Sapporo 060-8628, Japan

In naturally occurring photosystem II (PSII), the water oxidation reaction proceeds with extraordinary high catalytic activity, where a μ -oxo bridged tetrameric Mn cluster (Mn_4CaO_5) serves as the multielectron oxidation catalyst within a complex protein environment [1,2]. Thus, the Mn clusters of photosynthetic organisms have triggered extensive research efforts to develop efficient water oxidation catalysts composed of the inexpensive and abundant element Mn. In a recent year, various manganese oxides, such as MnO_2 , BaMnO_3 , LaMnO_3 etc. has been reported to show an excellent electrocatalytic properties for oxygen evolution by electrochemical water splitting [3, 4]. Suntivich *et al* reported that hole on oxygen make an important role for oxygen evolution catalysis of manganese oxide [4]. Such a hole probably evolves by mixing of ligand-to-metal charge transfer (LMCT) state which tends to be involved in high valence state metal oxides due to the covalency of metal-O bonding. In fact, it is reported high valence state $\text{Mn}^{\text{V}}=\text{O}$ intermediates are involved during water oxidation cycle (S-cycle) and make an important role for O-O bond formation from two water molecules [5].

$\text{Ba}_3\text{Mn}_2\text{O}_8$ is Mn(V) oxides and is thermally stable in ambient atmosphere. Recently, we found that $\text{Ba}_3\text{Mn}_2\text{O}_8$ electrodes facilitate O-O peroxide species under the anodic polarization in neutral solutions. K-edge XAS spectroscopy can direct evidence of unoccupied state of solids. Accordingly, it is of fundamental and technological important to study the manganese oxide system by using this technique in order to clarify the relationship between oxygen hole and electrocatalysis. In this study, we investigate O K-edge spectra of $\text{Ba}_3\text{Mn}_2\text{O}_8$ samples treated by anodic polarization at various potentials.

$\text{Ba}_3\text{Mn}_2\text{O}_8$ powders were prepared by calcining BaCO_3 and MnO_2 mixture at 950°C in dry air. $\text{Ba}_3\text{Mn}_2\text{O}_8$ -base electrodes were prepared by mixing $\text{Ba}_3\text{Mn}_2\text{O}_8$ and carbon powders with a teflon binder and uniaxially-pressed at 100 MPa. The electrodes were polarized at a constant anodic potential with an Ag/AgCl (sat. KCl) reference electrode in neutral NaClO_4 solution (0.1 M).

O K-edge XAS spectra were recorded in a total electron yield mode by measuring bulk current through the irradiated samples. The spectra of the manganese oxide samples were shown in Fig. 1. The Mn atoms in $\text{Ba}_3\text{Mn}_2\text{O}_8$ take tetrahedral coordination with oxygen atoms. Therefore, the pre-edge peaks at around 529 eV can be assigned to the transition to anti-bonding t_{2g} states. In case of KMnO_4 , the Mn-O clusters take tetrahedral coordination, so that the

peaks at around 530 eV can be assigned to the transition to anti-bonding t_2 states. The apparent changes in O K-edge spectra are not observed in the samples after the polarization at various potentials, as shown in Fig. 1. This might be due to the deterioration of the polarized specimens by exposing to air.

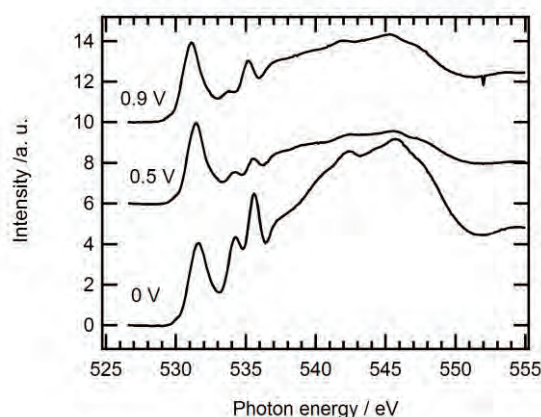


Fig. 1. O K-edge spectra of $\text{Ba}_3\text{Mn}_2\text{O}_8$ treated by anodic polarization in neutral solution at various potentials.

- [1] J. H. Alstrum-Acevedo *et al.*, *Inorg. Chem.* **44** (2005) 6802.
- [2] G. C. Dismukes, R. Brimblecombe, G. A. N. Felton, R. S. Pryadun, J. E. Sheats, L. Spiccia and G. F. Swiegers, *Acc. Chem. Res.* **42** (2009) 1935.
- [3] F. Jiao and H. Frei, *Energy Environ. Sci.* **3** (2010) 1018.
- [4] J. Suntivichi *et al.*, *J. Phys. Chem. C* **118** (2014) 1856.
- [5] F. A. Armstrong, *Phil. Trans. R. Soc. B* **363** (2007) 1263.

BL4B

XANES Analysis of Valence State of Co Doped in CeO₂

T. Oomori¹, K. Tarui¹ and T. Yamamoto^{1,2}

¹Faculty of Science and Engineering, Waseda University, Tokyo 169-8555, Japan

²Institute of Condensed-Matter Science, Waseda University, Tokyo 169-8555, Japan

A lot of researches on dilute magnetic materials (DMMs), which are processed by doping dilute (a few at%) magnetic elements into the non-magnetic materials, have been carried out after the discovery of the ferromagnetism in InAs:Mn [1]. Among DMMs, there are two type of the models for the doped magnetic ions, i.e., substituted and precipitated ones. In order to understand the mechanism of the appearance of ferromagnetism in DMMs, it is essential to know the local environment of the doped magnetic elements. We have successfully studied the valence state of Mn and Fe ions by measuring the Mn and Fe-L₃ X-ray absorption near edge structure (XANES) analysis at BL4B in UVSOR [2]. In the present study, charge state of doped Co in Co-doped CeO₂, which shows room-temperature ferromagnetism, was investigated by the XANES analysis at Co-L₃ edge.

Co doped CeO₂ was prepared by the conventional solid-state reaction method. Reagent grade CeO₂ and Co₃O₄ powders were used as starting materials. These powders were firstly weighed with a molar ratio of Ce:Co = 0.95:0.05, which are mixed and ground in an agate mortar and fired in air at 1273 K for 10 hours. After cooling down to the room temperature, these specimen was annealed in Ar(97%)-H₂(3%) atmosphere at 723 K for an hour. Co-L₃ XANES spectra of Co-doped CeO₂, Co-foil and Co₃O₄ were measured at BL4B in UVSOR by total electron yield method. The incident beam was monochromatized with a varied-line-spacing plane grating (800 lines/mm). Energy resolution (E/ΔE) of the incident beam was set to 3000. Sample powders and foil were put on the carbon adhesive tape, which are attached on the first Cu-Be diode of the electron multiplier.

Prior to the XANES analysis, synthesized specimen was examined by the X-ray diffraction. No extra peaks appeared after doping the Co and peak position did not change. If Co is substituted at Ce site, peak position should change, because ionic radius of Co is much smaller than that of Ce ion. This result suggests Co exists as nano-sized precipitates.

Observed Co-L₃ XANES spectra of Co₃O₄, Co-foil and Co-doped CeO₂ are shown in Fig. 1. Fine structures of the reference samples, i.e., Co and Co₃O₄, show different profiles and we can clearly distinguish these two. A profile of Co-L₃ XANES of Co-doped CeO₂ show similar profile as Co-foil, which suggests that doped Co exists as metallic charge state. Combining the results by XRD and XANES, we can conclude that doped Co exists as nano-sized metallic precipitate.

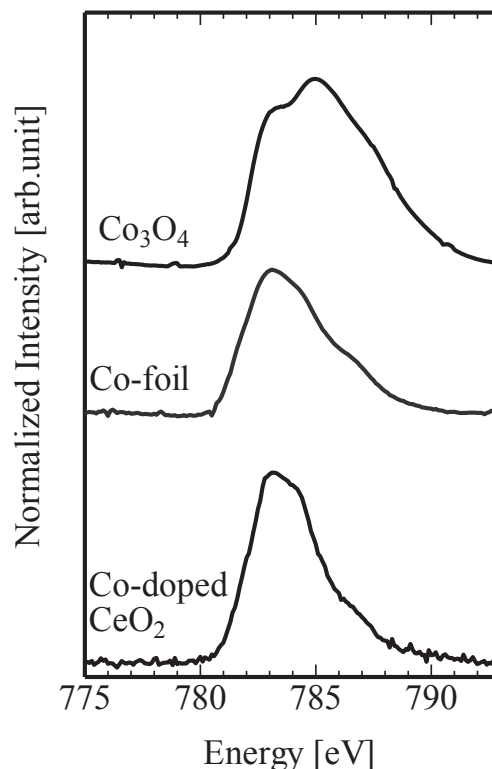


Fig. 1. Co-L₃ XANES spectra of Co₃O₄, Co-foil and Co-doped CeO₂.

[1] H. Ohno *et al.*, Phys. Rev. Lett. **68** (1992) 2664.

[2] T. Okazaki *et al.*, Solid State Comm. **151** (2011) 1749.

BL4B

Investigation on the Surface Structure of LiNbO_3 -Coated LiCoO_2 Using the Soft X-Ray XANES Measurement

H. Kobayashi, T. Okumura and M. Shikano

Research Institute for Ubiquitous Energy Devices, National Institute of Advanced Industrial Science and Technology (AIST), Ikeda, 563-8577, Japan

Realization of the all-solid-state Li-ion battery (LIB) consisting of non-flammable inorganic solid electrolytes is desired because of their high safety. To improve energy and power densities of the all-solid-state LIB, the decrease of the interfacial resistance between the electrode and solid electrolyte is required as well as the synthesis of solid electrolyte with high Li-ion conductivity. It has been reported that $\text{Li}_4\text{Ti}_5\text{O}_{12}$ -coated LiCoO_2 reduced the interfacial resistance between LiCoO_2 positive electrode and sulfide electrolyte and enhanced the rate capability to be compatible to that of commercial LIB with liquid electrolyte [1]. Recently we also reported that the mechanochemical Al_2O_3 -coating process was an effective way of improving the cycle performance at high temperature in the cell of $\text{Li}/1\text{M LiPF}_6$ in $\text{EC}:\text{DMC}$ (1:2)/ $\text{Li}_{1.20}\text{Mn}_{0.55}\text{Ni}_{0.16}\text{Co}_{0.09}\text{O}_2$ [2]. In this paper, LiNbO_3 -coating LiCoO_2 was prepared and these surface structure were investigated using the soft X-ray XANES measurement.

LiNbO_3 -coated LiCoO_2 were prepared with an ethanol solution of ethoxides of Li and Nb using tumbling fluidized bed granulating-coating machines (POWREX Co.) and heated for 30 min. in air between 573 and 773 K. The particle morphology and containing transition metal were confirmed by SEM and EDAX measurements. Electronic structures were investigated by XANES measurement at the beamline BL4B in UVSOR.

The SEM and EDAX results clarified that the sizes of pristine LiCoO_2 particles were in the range of 1-10 μm (an average particle size: 6 μm) and no transition metal except Co was observed. The EDAX results showed the existence of Nb in the LiNbO_3 -coated LiCoO_2 particles, but gave no information of the distribution of Nb on the surface of LiNbO_3 -coated LiCoO_2 particle. Therefore, the soft X-ray XANES was measured to check the surface structure on LiCoO_2 . The Co *L*-edge XANES spectra clarified that the samples after heat treatment showed weaker intensities of the A and B peaks compared with the pristine sample as shown in Fig. 1. The O *K*-edge XANES spectra clarified that the shape of the C and D peaks for the samples after heat treatment was close to that of LiNbO_3 with increasing heat temperature as shown in Fig. 2. These results indicated that the surface of LiNbO_3 -coated LiCoO_2 after heat treatment at 773 K was covered uniformly by LiNbO_3 layer and that the soft X-ray XANES measurement was an effective way of confirming the

surface structure of coated samples.

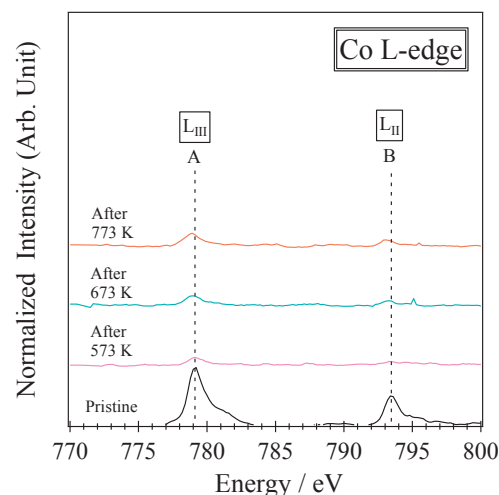


Fig. 1. Co *L*-edge XANES spectra for pristine and LiNbO_3 -coated samples after heat treatment.

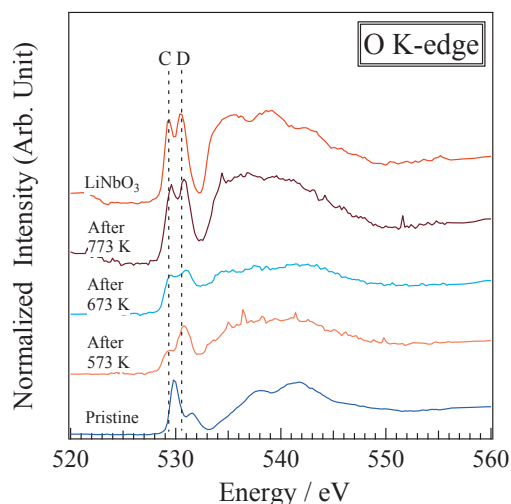


Fig. 2. O *K*-edge XANES spectra for pristine and LiNbO_3 -coated samples after heat treatment together with LiNbO_3 .

[1] N. Ohta *et al.*, *Adv. Mater.* **18** (2006) 2226.

[2] H. Kobayashi *et al.*, *Solid State Ionics* **262** (2014) 43.

BL4B

Perpendicular Magnetic Anisotropy in Mn₄N Studied by X-Ray Magnetic Circular Dichroism

G. Shibata¹, J. Okabayashi², A. Chikamatsu³, A. Fujimori¹ and T. Hasegawa³

¹Department of Physics, The University of Tokyo, Tokyo 113-0033, Japan

²Research Center for Spectrochemistry, The University of Tokyo, Tokyo 113-0033, Japan

³Department of Chemistry, The University of Tokyo, Tokyo 113-0033, Japan

Transition-metal nitrides such as Co₄N, Fe₄N, and Mn₄N have been investigated as novel materials for applications in spintronic devices because of the room-temperature ferro- or ferrimagnetism. Especially, the perpendicular magnetic anisotropy (PMA) in metallic Mn₄N is one of the interesting topics since it has benefits of enhanced thermal stability and low current magnetization switching. Anti-perovskite type Mn₄N consists of two kinds of inequivalent Mn sites (Mn_A: 3.85 μ_B /f.u. and Mn_B: -0.9 μ_B /f.u.) which occupy the corner and face-centered positions of the unit cell with tetragonal distortion. The large PMA energy of 0.16 MJ/m³ in Mn₄N was reported at room temperature [1]. However, the origin for the appearance of PMA in Mn₄N has not been clarified yet. For fundamental understanding of PMA in Mn₄N, the electronic and magnetic structures have to be clarified explicitly. In order to investigate PMA energy, it is necessary to evaluate the orbital magnetic moments along parallel and perpendicular directions to the surface. Here, we report the x-ray magnetic circular dichroism (XMCD) of Mn₄N in order to discuss the origin of PMA.

Samples were grown by pulsed laser deposition method on MgO (001) substrates. The 40-nm-thick Mn₄N was deposited under the substrate temperature of 500 °C. Although there is a lattice mismatch of 7.0 % at the interface, coherent growth was observed by transmission electron microscope [1]. It is reported that the 4-nm-thick MnO_x layer is formed on the Mn₄N surface [1]. In order to suppress the formation of such an oxidization layer, the sample surface was capped with 2-nm-thick Al₂O₃. The saturation magnetic field of the Mn₄N thin film along the magnetically hard axis was estimated to be ~ 3 T [1]. XMCD measurements were done at UVSOR BL-4B under the conditions of 5 K [2]. A magnetic field of ± 5 T using a superconducting magnet was applied along the incident polarized soft x-ray, which is enough to saturate the magnetization along the magnetically hard axis direction. The total electron yield mode was adopted. Normal incidence (NI) and grazing incidence (GI) geometries were employed to deduce the anisotropic orbital magnetic moments.

Figures 1(a) and 1(b) show Mn *L*-edge x-ray absorption spectra (XAS) and XMCD in the NI and GI setups, respectively. In XAS, a shoulder structure is observed at 632 eV. In the Mn *L*₃ XMCD spectra, in addition to the negative XMCD peak

located at the main absorption peak (628.5 eV), a positive XMCD signal is observed around 630 eV. In Mn₄N, two kinds of XMCD components originating from the Mn_A and Mn_B sites are overlapped antiferromagnetically, which brings the complicated XMCD spectral line shapes. Since the decomposition into each component has not succeeded yet, magneto-optical sum rules cannot be applied at this moment. The asymmetry in XMCD between the *L*₃ and *L*₂ peaks at the NI setup is larger than that in the GI setup, suggesting that the anisotropic orbital magnetic moments are induced. These results suggest that the anisotropic orbital magnetic moments might be related to the PMA in this system as explained by Bruno's relationship [3]. In order to deduce the site specific spin and orbital magnetic moments, we are planning to measure the substitution dependence of XMCD spectral line shapes in (Mn_{1-x}M_x)₄N (*M* = nonmagnetic metal), which will provide information about the electronic states and magnetism of each Mn site.

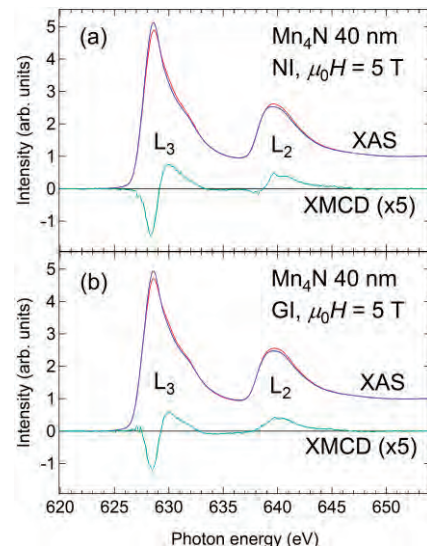


Fig. 1. X-ray absorption spectra (XAS) and XMCD of Mn₄N thin film at the Mn *L* edge in (a) normal incidence (NI) and (b) grazing incidence (GI) setups at 5 K and 5 T.

[1] X. Shen, A. Chikamatsu, K. Shigematsu, Y. Hirose, T. Fukumura and T. Hasegawa, *Appl. Phys. Lett.* **105** (2014) 072410.

[2] T. Yokoyama, Y. Takagi and K. Nakagawa, *Int. Rev. Phys. Chem.* **27** (2008) 449.

[3] P. Bruno, *Phys. Rev. B* **39** (1989) 865.

BL4B

Investigating Orbital Magnetic Moments in Spinel-Type MnV_2O_4 Using X-Ray Magnetic Circular Dichroism

J. Okabayashi^{1*}, S. Miyasaka², K. Henmi², K. Tanaka^{2,3}, S. Tajima²,
H. Wadati⁴, A. Tanaka⁵, Y. Takagi³ and T. Yokoyama³

¹Research Center for Spectrochemistry, University of Tokyo, Tokyo 113-0033, Japan

²Department of Physics, Osaka University, Toyonaka 560-0043, Japan

³Institute of Molecular Science, Okazaki, 444-8585, Japan

⁴Institute for Solid State Physics, University of Tokyo, Kashiwa, 227-8581, Japan

⁵Department of Quantum Matter, Hirshima University, Higashi-Hiroshima 739-8530, Japan

Couplings between orbital and spin degrees of freedom in transition metal (TM) oxides exhibit a wide variety of interesting physical phenomena studied in strongly correlated electron systems. The orbital degeneracy of t_{2g} or e_g orbitals, split by the crystal field in TM oxides, gives rise to the orbital ordering phenomena in perovskite-type Mn or V oxides accompanied by Jahn-Teller distortion. Spinel-type MnV_2O_4 is a good candidate to study orbital ordering since orbital magnetic moments of Mn^{2+} (d^5) are nearly quenched with relatively large spin moments in high spin states. An unresolved issue related to orbital ordering of spinel-type vanadium oxides is the relationship between the orbital magnetic moments in vanadium sites and orbital ordering. In this study, we investigated the element specific electronic and magnetic properties of MnV_2O_4 using XAS and XMCD, and examined the relationship between orbital magnetic moments and orbital ordering.

Single crystals were grown by the floating-zone method. Details of the sample preparation and the fundamental physical properties are described in Ref. [1]. The magnetic and orbital ordering temperatures of MnV_2O_4 were estimated to be 59 and 54 K, respectively. The XAS and XMCD measurements were performed at BL-4B, UVSOR, Institute of Molecular Science. Total photoelectron yield mode by directly detecting the sample current was adopted. A magnetic field of ± 5 T was applied along the direction of the incident polarized soft x-ray.

Figure 1(a) shows XAS, XMCD, and the integrated XMCD spectra of V $L_{2,3}$ -edge regions taken at 5 K, which is sufficiently lower than the orbital ordered transition temperature. The resulting residuals from the XMCD integrals for both L_2 and L_3 edges are shown at the bottom of Fig. 1 (a), suggesting that the finite values of orbital magnetic moments remained in the V^{3+} states. Using the integrals over XAS spectra and assuming that the V $3d$ electron number to be 2, we deduced the orbital magnetic moments (m_l) to be less than $0.01 \mu_B$ /(V atoms) from the orbital sum rule. This value is close to zero but finite. This result indicates that unquenched orbital magnetic moments contribute to complex wave functions in V sites.

Figure 1(b) shows the calculated XAS and XMCD spectra of V L -edges obtained using the cluster

models with configuration interaction. In the case of V L -edges, qualitatively similar spectral line shapes with both XAS and XMCD spectra in Fig. 1(a) were reproduced by the cluster-model calculation. Tetragonal local lattice distortion around the V sites must also be considered. The t_{2g} states are split into two levels by the tetragonal distortion and the lowest xy states are occupied by one of the electrons. The other electron occupies the yz or zx states. We determined the tetragonal distortion value for the V $3d$ states (D_{tet}) to be 0.02 eV in order to reproduce the complicated XMCD spectral line shapes qualitatively. The existence of the small but finite orbital magnetic moments in the V sites can be explained by the (i) complex orbital ordering as discussed in the case of FeV_2O_4 , (ii) domain formation, and (iii) mixing of the real and complex orbital orderings due to the trigonal distortion around the V sites [2].

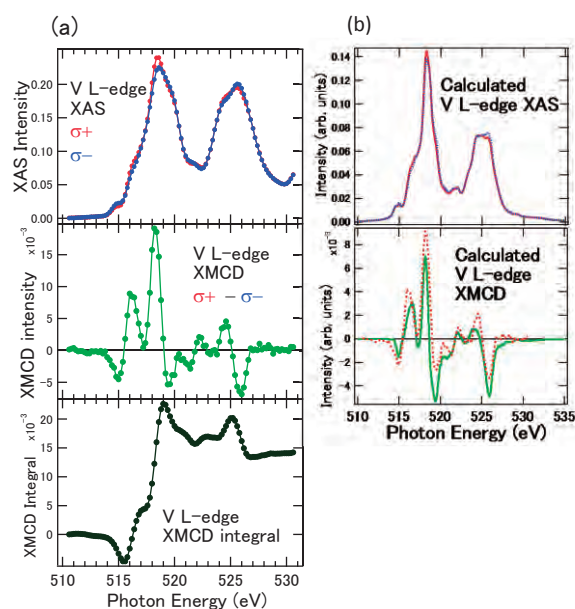


Fig. 1. V L -edge XAS, XMCD, and XMCD integrated spectra in MnV_2O_4 (a). Cluster model calculations are also shown in (b).

[1] K. Henmi *et al.*, J. Phys. Soc. Jpn. **81** (2012) SB030.

[2] J. Okabayashi *et al.*, submitted.

*e-mail: jun@chem.s.u-tokyo.ac.jp

BL5B

Study of Ultrafast Spin-Switching of a Ferrimagnetic Alloy by Resonant Magneto-Optical Kerr Effect

S. Yamamoto¹, M. Taguchi², Y. Kubota¹, S. Ito¹, M. Hasumoto³,
E. Shigemasa³ and I. Matsuda¹

¹Institute for Solid State Physics, The University of Tokyo, Chiba 277-8581, Japan

²Nara Institute of Science and Technology (NAIST), Ikoma 630-0192, Japan

³UVSOR Facility, Institute for Molecular Science, Okazaki 444-8585, Japan

A crystal of GdFeCo is a ferrimagnetic metallic alloy, composed of rare-earth and transition metal sublattices that couple anti-ferromagnetically. It has been reported that the material shows ultrafast spin-switching by irradiation of a femtoseconds-pulse of either circularly or linearly polarized infrared light. Recently, we have carried out time-resolved measurement of resonant magneto-optical Kerr effect (RMOKE) [1] at the Fe *M*-shell absorption edge by soft x-ray free electron laser and succeeded in directly detecting dynamic variations of magnetic signal during the spin-switching. However, the RMOKE data have lacked spectroscopic information to make a proper interpretation of the phenomena.

In the present research, we carried out the RMOKE experiment at BL-5B at UVSOR to measure spectra of absorption intensity and Kerr rotation angle of a crystal of GdFeCo. Kerr rotation angle was determined by the rotating-analyzer ellipsometry method (Fig. 1). Figure 2(a) shows a schematic drawing of the sample system. A 20 nm-thick Gd₂₁(Fe₉₀Co₁₀)₇₉ film was grown on a Ta/Si(SiO₂) substrate and capped with a 2 nm-thick Ta layer.

Figure 2(b) shows absorption spectrum of the GdFeCo sample that shows peaks of various core-levels of Ta, Fe, and Co atoms. In the measurements, perpendicular magnetic field of +/- 0.5 T was applied with a permanent magnet. As shown in the figure, the simulated Fe 3*p* spectra, based on the resonant scattering theory [1], almost completely reproduces spectral feature of the Fe 3*p* absorption peak. The Kerr rotation angles (θ_k 's) of the Fe *M*-shell absorption edge were evaluated as in Fig. 2(c). The θ_k value becomes as large as 3-4 degrees at the photon energy ($h\nu$) around 50 eV and it is reasonably reproduced by the simulation [1]. The discrepancy at $h\nu > 60$ eV is likely due to the contribution from the Co 3*p* level that has not been considered in the calculation. On the other hand, the difference at the pre-edge in Fig.2(c) seemingly originates from the film structure that has been reported previously in the Ni nanofilm [1]. The smaller θ_k value of the Fe *M*-edge, compared with the Ni *M*-edge, was likely due to the smaller spin-orbit interaction for the lighter element.

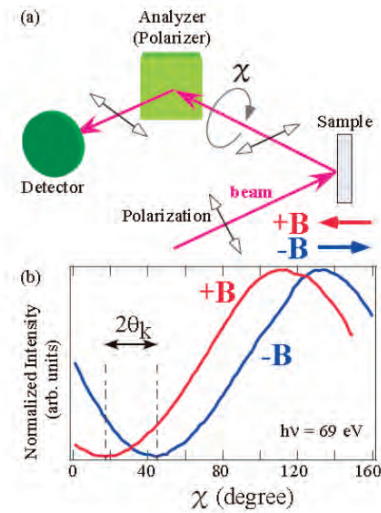


Fig.1. (a) Geometry for rotating-analyzer ellipsometry (RAE) to measure the polar MOKE. The light beam is *p*-polarized by the surface, and the magnetic field (**B**) is applied along the surface normal. (b) Typical results of the intensity variation with rotation angle, χ . The Kerr rotation angle, θ_k , can be determined from $2\theta_k = |\theta(+B) - \theta(-B)|$.

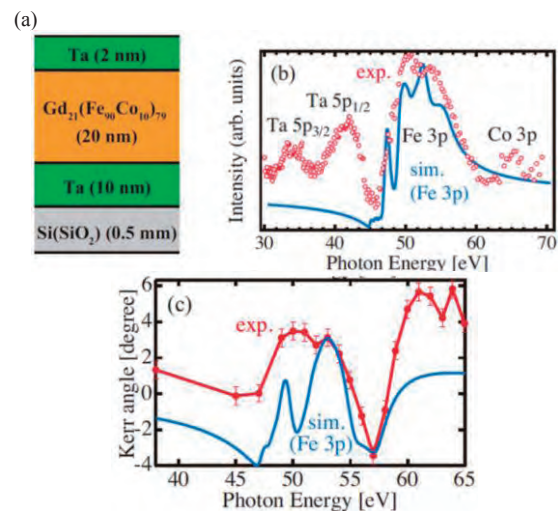


Fig.2. (a) Schematic drawing of the GdFeCo sample system. (b) The absorption spectrum at $h\nu=30-70$ eV. (c) Photon energy dependence of the Kerr-rotation angle (θ_k).

[1] Sh. Yamamoto *et. al.*, Phys. Rev. B. **89** (2014) 064423.

BL6B

Infrared Spectroscopy of Photo-Induced Defects in Ce³⁺:GAGG Crystals

R. Inaba¹, M. Kitaura¹, K. Kamada², S. Kurosawa^{2,3}, A. Ohnishi¹ and K. Hara⁴

¹Department of Physics, Faculty of Science, Yamagata University, Yamagata 990-8560, Japan

²New Industry Creation Hatchery Center, Tohoku University, Sendai 980-8579, Japan

³Institute for Materials Research, Tohoku University, Sendai 980-8577, Japan

⁴Research Institute of Electronics, Shizuoka University, Hamamatsu 422-8529, Japan

The Ce-doped Gd₃Al₂Ga₃O₁₂ (Ce:GAGG) crystal was developed as a scintillator for radiation detector. These crystals exhibit a high light yield, high-energy resolution, and short decay time, as compared to other inorganic scintillator crystals [1]. On the other hand, it has been pointed out that trapping of photo-excited carriers due to crystal defects causes the occurrence of phosphorescence and decrease in light yield [2,3]. In order to improve the performance of scintillators, it is necessary to clarify the origin of crystal defects. We have measured infrared (IR) absorption spectra of Ce:GAGG crystals under UV-irradiation.

Ce:GAGG crystals were grown from a melt in oxygen or hydrogen atmosphere by the CZ method. The concentration of cerium ion was set to 1.0 mol%. Experiment was performed at the beamline BL6B. The UV-irradiation was performed at 3.31 eV with a picosecond light pulser, which is located in the Ce³⁺ 4f → 5d₂ absorption band. The sample temperature was set to 9K.

Figure 1 shows stationary IR absorption spectra of oxygen- and hydrogen-annealed Ce:GAGG crystals. As indicated by a blue line, the IR absorption spectrum of oxygen-annealed Ce:GAGG crystal is structureless. On the other hand, one can see a broad band above 6000 cm⁻¹ in the IR absorption spectrum drawn with a black line.

Figure 2 shows IR absorption spectra of an oxygen-annealed Ce:GAGG crystal. A black line represents the IR absorption spectrum without UV-irradiation. When UV-irradiation is turned on, the IR spectrum exhibits a broad band above 6000 cm⁻¹, as indicated by a blue line. This band is the same as the stationary IR absorption band for a hydrogen-annealed Ce:GAGG crystal, which was shown in Fig. 1.

The UV-irradiation at 3.31 eV results in the creation of excited electrons in the conduction band and Ce⁴⁺ ions [2-4]. The excited electrons will be captured immediately by lattice imperfections [2]. Therefore, it is likely that the photo-induced IR absorption band in Fig. 1 is caused by the formation of trapped electrons.

There are few candidates for the origin of trapped electrons in multicomponent oxides with garnet structure. The present experiment demonstrates that the photo-induced IR absorption band for an oxygen-annealed Ce:GAGG crystal is the same as the stationary IR absorption band for a hydrogen-annealed Ce:GAGG crystal. In general, it

has been accepted that oxygen vacancies are easily introduced in hydrogen-annealed oxide crystals. On this basis, we assign the photo-induced IR absorption band to electrons trapped at oxygen vacancies. This finding is valuable as a guiding principle to grow high-quality scintillator crystals.

A part of this work was carried out under the Cooperative Research Project Program of the Research Institute of Electrons, Shizuoka University.

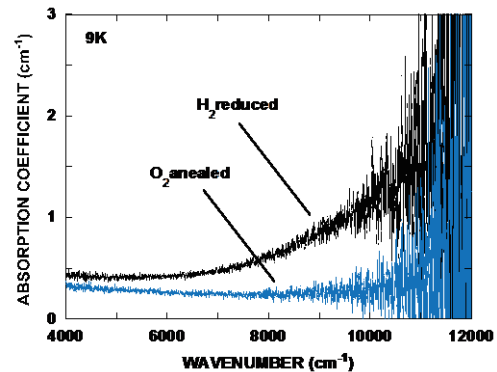


Fig. 1. Stationary IR absorption spectrum of oxygen- and hydrogen-annealed Ce:GAGG crystals measured at 9K.

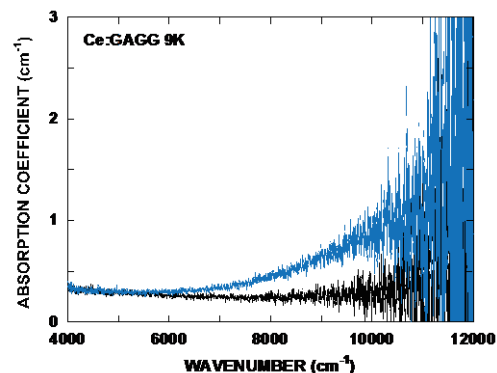


Fig. 2. IR absorption spectrum of an oxygen annealed Ce:GAGG crystal measured at 9K under UV-irradiation (blue line). The data obtained under unirradiation was also shown (black line).

- [1] K. Kamada *et al.*, *J. Cryst. Growth* **352** (2012) 88.
- [2] M. Kitaura *et al.*, *J. Appl. Phys.* **115** (2014) 083517.
- [3] A. Satoh, *et al.*, *Jpn. J. Appl. Phys.* **53** (2014) 05FK01.
- [4] P. Dorenbos, *J. Lumi.* **134** (2014) 310.

BL6B

Formation Mechanism of Ultrashallow Thermal Donors Formed in Carbon- and Hydrogen-Doped Czochralski Silicon Crystals

A. Hara and T. Awano

Department of Electronic Engineering, Tohoku Gakuin University, Tagajo 985-8537, Japan

We previously reported on ultrashallow thermal donors (USTDs) in carbon- and hydrogen-doped Czochralski silicon (CZ Si) crystals [1]. The following formation mechanism was tentatively proposed: in the first stage, STD(H)s are formed at a high rate; in the second stage, carbon diffuses in a thermally activated process via an interstitial or interstitialcy mechanism and modulates the electronic structure of STD(H)s by combining with them to form USTDs. In this study, we evaluated the formation process of USTDs in order to clarify the previously proposed model.

Figure 1 shows the behavior of USTDs and STD(H)s after carbon- and hydrogen-doped CZ Si crystals were annealed at 480 °C for various durations of time [1]. USTDs were slowly generated, and their spectral intensity increased with the annealing time up to 40 h. However, some lines for the group-1 USTDs began to reduce their intensity after further annealing, and a strong line eventually became dominant. In contrast, one strong line was dominant in the group-2 USTDs. The STD(H) line intensities were strong even after short-term annealing for 3 h and were maximized after annealing for 10 h. This indicates that the formation speed of STD(H)s is very high compared to that of USTDs. It is significant that the STD(H) lines began to decrease in intensity when the annealing continued beyond 10 h.

To investigate the generation of USTDs and reduction of STD(H)s at 480 °C for various annealing times, as shown in Fig. 1, we used Lorentzian curve fitting to examine the variation in area intensity of each line. For the group-1 USTDs, an area intensity of $1s-2p_{\pm}$ lines was used. For the group-2 USTDs, $1s-2p_0$ lines were used for curve fitting because of the following reasons. The $1s-3p_{\pm}$ spectral lines of the group-1 USTDs and $1s-2p_0$ lines of the STD(H)s overlapped with the $1s-2p_{\pm}$ lines of the group-2 USTDs. According to the effective mass theory, the ratio of intensity between the $1s-2p_0$ and $1s-2p_{\pm}$ lines should be 4:10. Thus, we determined the area intensity of the $1s-2p_{\pm}$ lines of group-2 to be 2.5 times the area intensity of the $1s-2p_0$ spectral lines derived from curve fitting. The curves of the $1s-2p_{\pm}$ STD(H) lines were fitted by using two main peaks and five satellite lines.

Figure 2 summarizes the variation in area intensity of the $1s-2p_{\pm}$ lines for the group-1 and group-2 USTDs and the STD(H)s; the figure also shows the sum of these donors as a function of the annealing time at 480 °C. The summation of the USTD and

STD(H) line areas showed a weak dependency on the annealing time when the duration was longer than 10 h at 480 °C. This result supports our model, which shows that STD(H)s are changed to USTDs.

In summary, we validated our model for the formation mechanism of USTDs based on the variations in the area intensities of USTDs and STD(H)s using curve fitting. In the first stage, STD(H)s form at a high rate; in the second stage, carbon modulates the electronic structure of STD(H)s by combining with them to form USTDs.

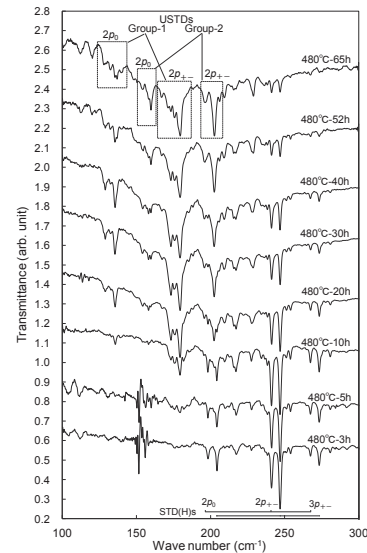


Fig. 1. Variation in USTD and STD(H) spectra in carbon- and hydrogen-doped CZ Si as function of annealing duration at 480 °C.

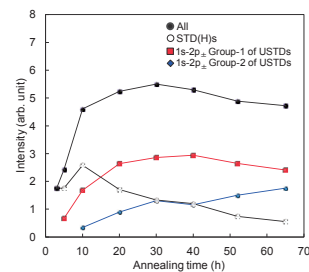


Fig. 2. Variation in spectral intensity area for STD(H)s, group-1 and group-2 USTDs, and the sum of these as function of annealing duration at 480 °C.

[1] A. Hara and T. Awano: UVSOR ACTIVITY REPORT 2013 **41** (2014) 88.

BL6B

Domain Structure of Alkali Niobate Piezoelectrics by Far-Infrared Reflective Method

Y. Taniguchi, T. Yamazaki, M. Kato and K. Kakimoto

Graduate School of Engineering, Nagoya Institute of Technology, Nagoya 466-8555, Japan

Orthorhombic $(\text{Na,K})\text{NbO}_3$ (NKN) piezoelectrics have attracted much attention as substitute materials for $\text{Pb}(\text{Zr,Ti})\text{O}_3$. We have examined that Li-doped NKN revealed the existence of a monoclinic Pm phase, and concluded that the Pm phase is the main factor of good piezoelectric properties[1][2]. However, there is no detailed report about the domain structure of NKN, which could explain the origins of the improved properties. Electrical measurements, like the impedance measurement, allow only for the evaluation of grains and grain boundaries. However, it is impossible to evaluate domains and domain walls. Therefore, spectroscopic methods need to be used, because they provide the structural deformation of the perovskite structure at a local scale about NbO_6 octahedron and alkali-ion movements. Via Raman spectroscopy, large changes in the vicinity of domain walls have been obtained, both in the Raman shift and its peak intensity. In this work, we evaluated the domain wall from the change of the permittivity using Infrared(IR) reflectivity measurements.

$(\text{Na}_{0.55}\text{K}_{0.45})(\text{Nb}_{0.995}\text{Mn}_{0.005})\text{O}_3$ crystals were prepared by the floating zone method. The obtained crystals were orthorhombic and had stripe domains with a width of $\sim 50 \mu\text{m}$. The samples were cut and polished for IR measurements. By means of a FT-IR spectrometer (Bruker, VERTEX 70v), IR measurements were performed every $10 \mu\text{m}$ vertically to the domain structure by using a line mapping technique. The spectra were fitted by the following equation:

$$\varepsilon(\omega) = \varepsilon_\infty + \sum_n \frac{\omega_{pn}^2}{\omega_{on}^2 - \omega^2 - i\gamma_n\omega} \quad (1)$$

where, ε_∞ is the high-frequency dielectric constant, ω_p and ω_o the plasma and longitudinal frequencies, and γ the damping constant. The complex dielectric function is related to the reflectivity spectrum by the equation

$$R = \left| \frac{\sqrt{\varepsilon(\omega)} - 1}{\sqrt{\varepsilon(\omega)} + 1} \right|^2 \quad (2)$$

Figure 1 shows the IR reflectivity spectra of Mn-NKN crystals at R.T. using two apertures of different diameter. The spectra in the case of the aperture with a diameter of 0.5 mm showed no change. In comparison, when the diameter is 0.25 mm, the spectra slightly changed with the position of the measurement. This result shows that the structure evaluation of domains and domain walls is enabled by using the aperture with the smaller diameter.

Figure 2 shows the permittivity of Mn-NKN crystals at different positions. With the diameter of 0.25 mm, the permittivity ε' showed a maximum value at the $0 \mu\text{m}$ position. The main reason for this behavior could be the multitude of the polar axis at the domain wall. This result suggests that the domain wall could be evaluated via the increase of the permittivity during IR reflectivity measurement.

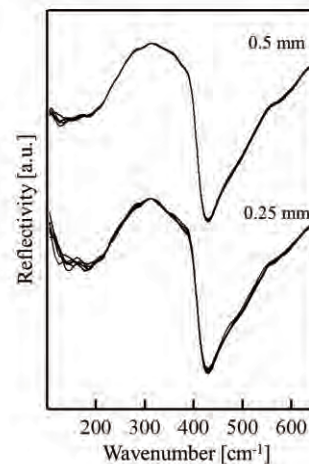


Fig. 1. IR reflectivity spectra of Mn-NKN crystals at R.T. using the aperture diameters of 0.5 mm and 0.25 mm

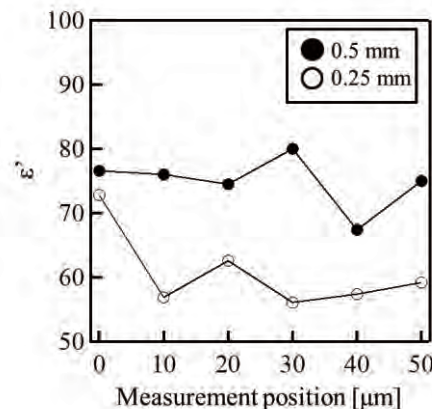


Fig. 2. Permittivity of Mn-NKN crystals at R.T. at different positions for the aperture diameters of 0.5 mm and 0.25 mm

[1] T. Nishi, K. Tsuchida, K. Kato, N. Kato, M. Watanabe and K. Kakimoto, UVSOR Activity Report 2012 **40** (2013) 140.

[2] T. Yamazaki, M. Kato, K. Tsuchida and K. Kakimoto, UVSOR Activity Report 2013 **41** (2014) 87.

BL6B

Spatial Distribution of Carrier Density of $\text{Sm}_{1-x}\text{Y}_x\text{S}$ ($x = 0.17$)

 S. Kamei¹, H. Takao¹, Y. Ohtsubo^{2,1}, H. Miyazaki³, K. Imura⁴, N. K. Sato⁴ and S. Kimura^{2,1}
¹ Department of Physics, Osaka University, Toyonaka 560-0043, Japan

² Graduate School of Frontier Biosciences, Osaka University, Suita 565-0871, Japan

³ Department of Frontier Materials, Nagoya Institute of Technology, Nagoya 466-8555, Japan

⁴ Department of Physics, Nagoya University, Nagoya 464-8603, Japan

Physical properties of some materials are drastically changed at the first-order phase transition by tuning external parameters of temperature, pressure, magnetic field, and chemical pressure. At the first-order transition, phase separations as well as phase coexistence are sometimes observed [1]. Since the phase separation is strongly related to the origin of the first-order transition, the origin of the phase separations is under debate in some materials.

Samarium monosulfide SmS is known to be a material with a pressure-induced first-order insulator-to-metal transition accompanied with the color change from black to golden-yellow, namely black-golden phase transition (BG transition), at the critical pressure of about 0.7 GPa [2]. The origin of the BG transition is known as the valence transition from Sm^{2+} with larger ionic radius to Sm^{3+} with smaller radius owing to the external pressure. When a part of Sm^{2+} -ions are replaced to Y^{3+} -ions of smaller ionic radius, namely $\text{Sm}_{1-x}\text{Y}_x\text{S}$, a similar BG transition is realized at ambient pressure [3]. At the border of the BG transition of $x \sim 0.17$, the black and golden phase separation (BG separation) is observed [4]. To investigate the origin of the BG separation, we measured a micro X-ray fluorescence (XRF) imaging (10- μm step) of Y $K\alpha$ line to check the spatial distribution of Y-atoms. In addition, to clarify the relation of the insulator-to-metal transition to the BG transition, the carrier density distribution was also measured by using an IR micro-imaging (6.25- μm step, about 26,000 points in total) [5]. The obtained reflectivity spectra at all measured points were fitted by the combination of the Drude and Lorentz functions using a nonlinear least-square method and the spatial distribution of the effective carrier density

(N_{eff}) in the Drude function was mapped on the sample surface.

Figure 1a shows the visible image of the BG separation of $\text{Sm}_{0.83}\text{Y}_{0.17}\text{S}$. Some golden-yellow areas, which indicate the appearance of the golden phase, are observed. The spatial distribution of the Y-ion probed by the XRF imaging is shown in Fig. 1b. The spatial distribution is almost flat on the whole sample surface except for the sample edge. The Y-ion distribution at golden-yellow areas is similar to that at black areas (for instance, the open solid circles in Fig. 1). This implies that the BG transition as well as the BG separation does not originate from the spatial concentration distribution of Y-ions.

Figure 1c shows the spatial distribution of N_{eff} . N_{eff} at the golden-yellow area reasonably increases from that at the black area. However, we can recognize that some part of the black area has larger N_{eff} than the other black area (for instance, the open dashed circle in Fig. 1), i.e., the metallic conduction appears even in the black phase. This result suggests that the insulator-to-metal transition of $\text{Sm}_{1-x}\text{Y}_x\text{S}$ does not relate to the BG transition.

[1] e.g. L. Zhang *et al.*, *Science* **298** (2002) 805.

[2] P. Wachter, In *Handbook on the Physics and Chemistry of Rare Earth*, edited by K. A. Gschneidner *et al.*, (North-Holland, Amsterdam, 1994), Vol. 19, p. 383.

[3] K. Imura *et al.*, *J. Korean Phys. Soc.* **62** (2013) 2028.

[4] S. Kimura *et al.*, *UVSOR Activity Report 2013* **41** (2014) 90.

[5] S. Kimura *et al.*, *UVSOR Activity Report 2012* **40** (2013) 45.

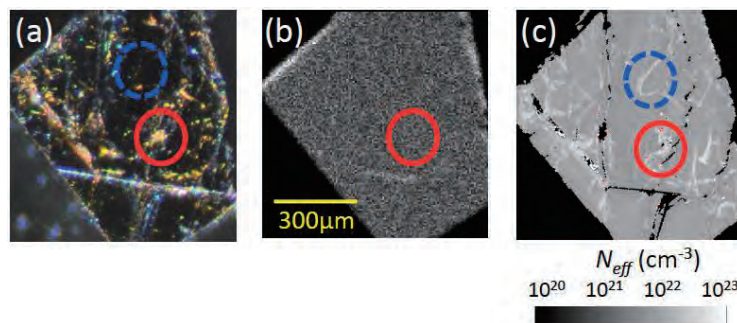


Fig. 1. (a) Visible image of a measured sample of $\text{Sm}_{0.83}\text{Y}_{0.17}\text{S}$. (b) Spatial distribution of the intensity of the Y $K\alpha$ line probed by X-ray fluorescence imaging. (c) Spatial distribution of the effective carrier density (N_{eff}) from the Drude and Lorentz fitting of reflectivity spectra. Open solid (red) and dashed (blue) circles indicate the points of a typical golden phase area and a black phase area with different carrier density, respectively, discussed in the text.

BL7U

Local Electron-Phonon Coupling in Organic Single Crystals: Angle-Resolved Ultraviolet Photoemission Study

F. Bussolotti¹, J. Yang², T. Yamaguchi², Y. Nakayama², H. Ishii², M. Matsunami¹, N. Ueno² and S. Kera^{1,2}

¹Department of Photomolecular Science, Institute of Molecular Science, Okazaki 444-8585, Japan,

²Department of Nanomaterial Science, Graduate School of Advanced Integration Science, Chiba University, Chiba 263-8522, Japan

A detailed understanding of the electronic and transport properties of organic semiconductors is crucial for the optimization of any real organic-based (opto)electronic devices. Despite huge research efforts important open issues still remain, as mainly related to the role played by the electronic delocalization and electron-phonon coupling effects on the charge transport mechanism in organic materials [1]. In this work, we clearly revealed the impact of electron-phonon coupling on the electronic band dispersion of rubrene single crystals (SCs) by angle-resolved ultraviolet photoelectron spectroscopy (ARUPS).

The ARUPS study was conducted at BL7U. The photon energy ($h\nu$) was set to $h\nu=8$ eV. During photoemission measurements the SCs were continuously irradiated with laser light (photon energy=3.06 eV, power=14 mW) to avoid sample charging [2]. The energy and angular resolution was 10 meV and 0.15° respectively.

Figure 1(a) shows the UPS spectra of the highest occupied molecular orbital (HOMO) of rubrene SC as acquired along the ΓY symmetry direction at 307 K (room temperature). In particular, a “kink”-like dispersive behavior is observed at $\theta \sim 20^\circ$. This striking spectral feature is more clearly revealed by the $E(k_{\parallel})$ band mapping of the HOMO dispersion [Fig. 1(b)]. The kink structure is centered at $k_{\parallel}^{\text{kink}} = \sim 0.23 \text{ \AA}^{-1}$ with an energy width of ~ 130 meV, which nearly coincides with the characteristic energy of the rubrene intramolecular vibrations ($h\nu_0^{\text{rub}} = 130$ meV) [3]. Upon crossing the kink structure (from Γ to Y) a clear broadening of the HOMO peak is observed [Fig. 1(c), left panel].

The occurrence of kink structures in the electronic band dispersions of organic molecular solids was theoretically predicted by Ciuchi *et al.* [4] as a result of the interaction of electrons with high frequency intramolecular vibrations [4]. This *local* electron-phonon coupling introduces “cuts” in the electronic band dispersion at multiple of the intramolecular vibrational energy, resulting in kink structures as those observed in the present rubrene SC.

According to the above picture, electron-phonon scattering events are allowed only for $k_{\parallel} > k_{\parallel}^{\text{kink}}$ (i.e. at higher binding energies) where they cause the observed increase of the HOMO linewidth [Fig. 1(c), left panel]. These *local* electron-phonon coupling

effects are substantially temperature independent in the [307K–110K] temperature range ($kT < 26$ meV) as the rubrene intramolecular vibrations ($h\nu_0^{\text{rub}}=130$ meV) cannot be excited when $kT \ll h\nu_0^{\text{rub}}$.

According to our ARUPS results, the electronic band structure of rubrene SC is significantly affected by *local* electron-phonon coupling effects. The most salient spectral features come from the interaction of electrons with high-frequency intramolecular vibrations which causes the appearance in (i) kink structure in the electron band dispersion and (ii) scattering of higher binding energies electrons.

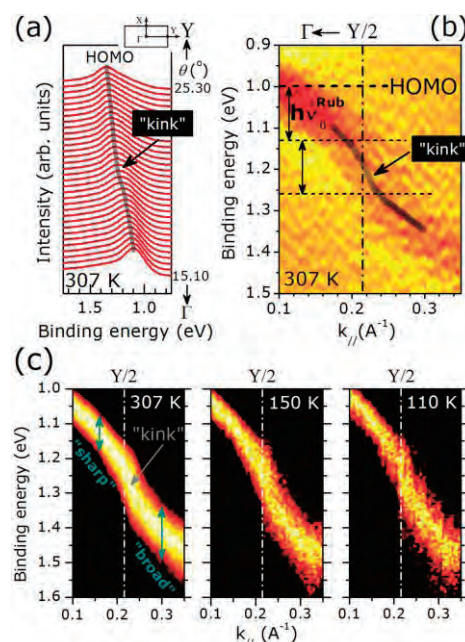


Fig. 1. (a) θ -dependence of the HOMO-UPS spectra of rubrene single crystal along ΓY direction (see inset) ($h\nu=8$ eV). (b) $E(k_{\parallel})$ map of the HOMO band dispersion (second derivative intensity plot, ΓY direction). (c) $E(k_{\parallel})$ map of the HOMO band dispersion at 307 K, 150 K and 110 K. The spectral intensities were normalized to the intensity of the HOMO peak.

[1] N. Ueno *et al.*, Prog. Surf. Sci. **83** (2008) 490.

[2] S. Machida *et al.*, Phys. Rev. Lett. **104** (2010) 156401.

[3] S. Duhm *et al.*, Adv. Mat. **24** (2012) 901.

[4] S. Ciuchi *et al.*, Phys. Rev. Lett. **106** (2011) 166406.

BL7U

Valence Band Dispersion of the Pentacene Single Crystal

Y. Nakayama¹, M. Yamamoto², Y. Mizuno², M. Matsunami³, H. Ishii^{2,4} and N. Ueno²

¹Department of Pure and Applied Chemistry, Faculty of Science and Technology, Tokyo University of Science, Noda 278-8510, Japan

²Graduate School of Advanced Integration Science, Chiba University, Chiba 263-8522, Japan

³UVSOR Facility, Institute for Molecular Science, Okazaki 444-8585, Japan

⁴Center for Frontier Science, Chiba University, Chiba 263-8522, Japan

Pentacene (C₂₂H₁₄) is one of the most vigorously studied organic semiconductors because a practical magnitude of the field effect mobility of conductive holes ($\mu_h > 1 \text{ cm}^2\text{V}^{-1}\text{s}^{-1}$) at room temperature (RT) was discovered for the first time for organic thin film transistors [1]. In particular, the single crystal phase of pentacene is attracting notable interest because further greater μ_h ($35 \text{ cm}^2\text{V}^{-1}\text{s}^{-1}$ at RT and over $50 \text{ cm}^2\text{V}^{-1}\text{s}^{-1}$ at 225 K) was reported [2]. As a primary factor for such excellent electric conduction properties, the valence band dispersion structures of the pentacene single crystal (Pn-SC) have been intriguing researchers of fundamental as well as applied science fields. However, experimental demonstration of the valence band structures of *insulating* organic semiconductor single crystal samples has been problematic due to “sample charging”. Photoconductivity of organic semiconductors provides one solution against this drawback, actually *k*-integrated density-of-states of the Pn-SC were disclosed by means of photoelectron spectroscopy under laser light illumination [3,4]. In the present study, we elucidated the valence band structures of the Pn-SC by a photoconductivity-assisted angle-resolved ultraviolet photoelectron spectroscopy (ARUPS) technique.

Oblong plates (typically several mm² wide and a few μm thick) of the Pn-SC produced by a physical vapor transport technique were selected and posted individually onto conductive carbon tape to prepare specimens. Ag glue was additionally pasted at the rim of each crystal to ensure good electric conductivity. ARUPS measurements were carried out at BL7U in UVSOR, where the excitation photon energy ($h\nu$) was set at 10 eV in this study. In order to cancel sample charging, the sample was shined by continuous wave laser light (405 nm) during the measurements [5].

Figure 1(a) shows the ARUPS spectra taken at RT toward a diagonal direction of the surface Brillouin zone of the Pn-SC where the widest energy dispersion of the valence band is theoretically expected [6]. The upper and lower valence bands originating from the highest occupied states of two crystallographically inequivalent pentacene molecules exhibit clear energy dispersion to split each other by tilting the photoelectron take-off angle (θ) from the surface normal. It is worth mentioning that this dispersion direction is opposite to that of another crystalline polymorph (so called “thin-film” phase) of pentacene,

where the two bands split at the Γ point (normal emission) and degenerate each other for the grazing emission [7], but agrees with the trend of one other phase (“bulk” phase) [8]. Cooling the sample temperature down to 115 K resulted in expansion of the band width by *ca.* 20 % as shown in Fig. 1(b) and (c), which should be attributed to reduced electron-phonon coupling at lower temperature [9].

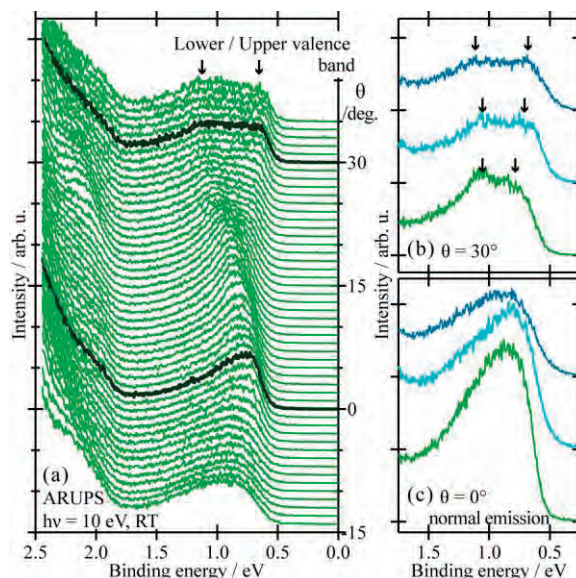


Fig. 1. (a) ARUPS spectra of a Pn-SC sample. (b) and (c) Temperature dependent evolution of UPS spectra (green: RT, light blue: 211 K, blue: 115 K) at electron take-off angles of 30° and 0° , respectively.

- [1] Y.-Y. Lin *et al.*, IEEE Electron Device Lett. **18** (1997) 606.
- [2] O. Jurchescu *et al.*, Appl. Phys. Lett. **84** (2004) 3061.
- [3] A. Vollmer *et al.*, Euro. Phys. J. E **17** (2005) 339.
- [4] Y. Nakayama *et al.*, Jpn. J. Appl. Phys. **53** (2014) 01AD03.
- [5] S. Machida *et al.*, Phys. Rev. Lett. **104** (2010) 156401.
- [6] H. Yoshida *et al.*, Phys. Rev. B **77** (2008) 235205.
- [7] M. Ohtomo *et al.*, Appl. Phys. Lett. **95** (2009) 123308.
- [8] H. Kakuta *et al.*, Phys. Rev. Lett. **98** (2007) 247601.
- [9] N. Koch *et al.*, Phys. Rev. Lett. **96** (2006) 156803.

BL7U

Angle-Resolved Photoemission Study on Quasi-One Dimensional Organic Conductor (TMTTF)₂PF₆

T. Ito^{1,2}, M. Mitamura¹, H. Horikawa¹, T. Hajiri¹, S. Kimura^{3,4} and T. Nakamura⁵

¹Graduate School of Engineering, Nagoya University, Nagoya 464-8603, Japan

²Nagoya University Synchrotron Radiation Research Center, Nagoya University, Nagoya 464-8603, Japan

³Graduate School of Frontier Biosciences, Osaka University, Suita 565-0871, Japan

⁴Department of Physics, Osaka University, Suita 565-0871, Japan

⁵Institute for Molecular Science, Okazaki 444-8585, Japan

The Bechgaard salts (TMTCF)₂X (C = S, Se; X = PF₆, AsF₆, etc.) belong to a family of quasi-one-dimensional (Q1D) organic conductors. These materials allow for a variety of ground states from antiferro magnetism, a Peierl's-like spin density wave, to a superconducting state by tuning the chemical pressure with the combination of TMTSF/TMTTF and anion X [1].

In this study, we have performed temperature dependent angle-resolved photoemission spectroscopy (ARPES) on single-crystalline (TMTTF)₂PF₆ to clarify the relation between the electric structure and the thermodynamic properties. ARPES measurement were performed at UVSOR-III BL7U by utilizing the bulk-sensitive low photon energy ($h\nu = 8\text{ eV}$) as well as the micro focus beam ($15 \times 100 \mu\text{m}^2$).

Figure 1 (a) and (b) shows the ARPES spectra and image along the ΓX direction of (TMTTF)₂PF₆ at $T = 30\text{ K}$ (charge ordering state: CO). We found highly dispersive band (h) folded around $k = 0.27 \text{ \AA}^{-1}$ (red arrow) at 0.4 eV, the dispersive broad feature (s) and the broad shoulder (p) below the Fermi level (E_F). From the comparison with the previous ARPES study on (TMTSF)₂X [2, 3], we have expected that the observed three features are attributed to holon, spinon and polaron band, respectively. It should be noted that the holon/spinon bands shift away from E_F relative to (TMTSF)₂PF₆ in consistent with the insulating properties of (TMTTF)₂PF₆ at CO states.

Figure 3 shows temperature dependent ARPES spectrum at $k = 0.27 \text{ \AA}^{-1}$ from $T = 30\text{ K}$ (CO), 100 K, 200 K (charge localization state: loc) to 300 K (metallic state: M) [4]. With increasing temperature, the main peak at 0.4 eV becomes weak and almost disappears at $T = 300\text{ K}$. As a result, the band structure at the metallic state dominates with the high-energy bound states (loc in Fig. 1) below 1 eV. On the other hand, we found that the spectral weight at E_F increases from $T = 30\text{ K}$ to 300 K, which is consistent with the thermodynamic properties of (TMTTF)₂PF₆. We have found the good reproducibility of the observed temperature dependence with decreasing temperature, which ensure the less radiation damage effect during the present ARPES measurement.

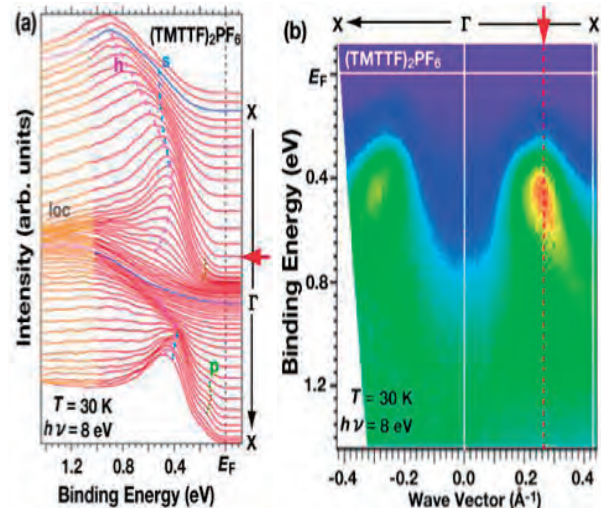


Fig. 1. ARPES spectra (a) and image of (TMTTF)₂PF₆ along ΓX direction at $T = 30\text{ K}$. Dashed lines are guide for eyes. Red arrow indicates the top of the holon dispersion.

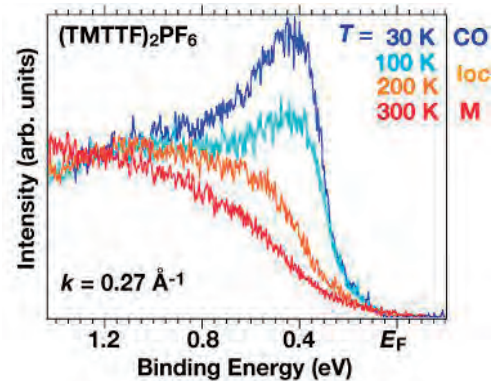


Fig. 2. Temperature dependent ARPES spectrum of (TMTTF)₂PF₆ at the top of the holon dispersion ($k = 0.27 \text{ \AA}^{-1}$).

[1] T. Ishiguro *et al.*, *Organic Superconductors* (Springer-Verlag, Berlin, 1998).

[2] S. Hirate *et al.*, UVSOR Activity Report 2011 **39** (2012) 97.

[3] M. Mitamura *et al.*, UVSOR Activity Report 2012 **40** (2013) 110.

[4] E. Rose *et al.*, *J. Phys.: Condens. Mat.* **25** (2013) 014006.

BL7U

Carrier Concentration Dependence of Superconducting Gap of $\text{Bi}_{1.7}\text{Pb}_{0.4}\text{Sr}_2\text{Ca}_{1-x}\text{Y}_x\text{Cu}_2\text{O}_{8+\delta}$

H. Sakamoto¹, A. Yamamoto² and T. Takeuchi^{2,3}

¹*Department of Crystalline Materials Science, Nagoya University, Nagoya 464-8603, Japan*

²*Toyota Technological Institute, Nagoya 468-8511, Japan*

³*Promoting Individual Research to Nurture the Seeds of Future Innovation, Japan Science and Technology Agency, Tokyo 102-8666, Japan*

Despite a huge number of investigations being performed after the discovery of high- T_c cuprate superconductors, the collective excitation leading to the formation of Cooper-pairs has not been fully identified yet. In order to gain deep insight into such collective excitation, it is of great importance to know the temperature-, momentum-, and carrier concentration- dependences of superconducting gap. Unfortunately, however, the pseudogap developing at the underdoped condition has made it difficult to reveal the temperature-, momentum-, and carrier concentration- dependences of superconducting gap. In this study, therefore, we carefully investigated the energy-width of superconducting-gap $\Delta(\varphi, p) = \Delta_0(p)\cos\varphi$ for $\text{Bi}_{1.7}\text{Pb}_{0.4}\text{Sr}_2\text{Ca}_{1-x}\text{Y}_x\text{Cu}_2\text{O}_{8+\delta}$ using ultra-high-energy-resolution laser induced angle resolved photoemission spectroscopy (ARPES) measurements. Here φ and p indicate the angle from the $(0, 0)$ - (π, π) direction and the introduced hole-concentration from the half-filled condition at $p = 0$. By additionally employing the synchrotron radiation ARPES measurements at BL7U in UVSOR, we estimated the carrier concentration of the employed samples using the area surrounded by the Fermi surface.

Figure 1 shows a symmetrized \mathbf{k}_F -ARPES spectrum of $\text{Bi}_{1.7}\text{Pb}_{0.4}\text{Sr}_2\text{Ca}_{0.9}\text{Y}_{0.1}\text{Cu}_2\text{O}_{8+\delta}$ at $\varphi \approx 23^\circ$ as a typical example. The magnitude of $\Delta(\varphi, p)$ was defined as the energy difference between two peaks in a symmetrized spectrum. The magnitude of $\Delta(23^\circ, p)$ of $\text{Bi}_{1.7}\text{Pb}_{0.4}\text{Sr}_2\text{Ca}_{0.9}\text{Y}_{0.1}\text{Cu}_2\text{O}_{8+\delta}$ was determined to be ~ 56 meV. In the same manner as, $\Delta(23^\circ, p)$, $\Delta(\varphi, p)$ was precisely determined at various angles of φ .

By plotting $\Delta(\varphi, p)$ as a function of $\cos\varphi$, we quantitatively evaluated $\Delta_0(p)$ for there different samples possessing different value of p . The determined $\Delta_0(p)$ was plotted in Fig. 2. as a function of p together with those previously determined for $\text{Bi}_2(\text{Sr,RE})_2\text{CuO}_{6+d}$ (RE = La, Nd, Sm).

We found, in our previous study, that $\Delta_0(p)$ of $\text{Bi}_2(\text{Sr,RE})_2\text{CuO}_{6+d}$ falls on a universal curve regardless of the rare earth elements involved in the samples: it obviously increases with decreasing hole

concentration at overdoped region and turns out to be reduced with decreasing hole concentration after becoming maximal at around $p = 0.23$ holes/Cu. Notably, $\Delta_0(p)$ of present samples ($\text{Bi}_{1.7}\text{Pb}_{0.4}\text{Sr}_2\text{Ca}_{1-x}\text{Y}_x\text{Cu}_2\text{O}_{8+\delta}$) shows a fairly different behavior from the universal curve observed for $\text{Bi}_2(\text{Sr,RE})_2\text{CuO}_{6+d}$. The much larger magnitude of $\Delta_0(p)$ of the present samples than that of $\text{Bi}_2(\text{Sr,RE})_2\text{CuO}_{6+d}$ would be closely related with the difference in the maximum critical temperature: $T_{c-\text{max}} \sim 90$ K of $\text{Bi}_{1.7}\text{Pb}_{0.4}\text{Sr}_2\text{Ca}_{1-x}\text{Y}_x\text{Cu}_2\text{O}_{8+\delta}$ and $T_{c-\text{max}} \sim 40$ K of $\text{Bi}_2(\text{Sr,RE})_2\text{CuO}_{6+d}$.

It would be more important to note that $\Delta_0(p)$ of present samples shows a shape peak at around $p \sim 0.16$ while that of $\text{Bi}_2(\text{Sr,RE})_2\text{CuO}_{6+d}$ exhibits a shallow hump in the $\Delta_0 - p$ plot. The mechanism leading to the different carrier concentration dependence of $\Delta_0(p)$ would be closely related to the difference in critical temperature of Cooper-pair formation.

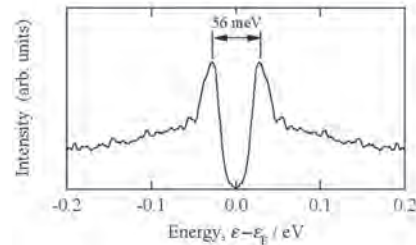


Fig. 1. Symmetrized ARPES spectrum at \mathbf{k}_F measured for $\text{Bi}_{1.7}\text{Pb}_{0.4}\text{Sr}_2\text{Ca}_{0.9}\text{Y}_{0.1}\text{Cu}_2\text{O}_{8+\delta}$ at around $\varphi = 23^\circ$. The temperature of measurement was ~ 13 K.

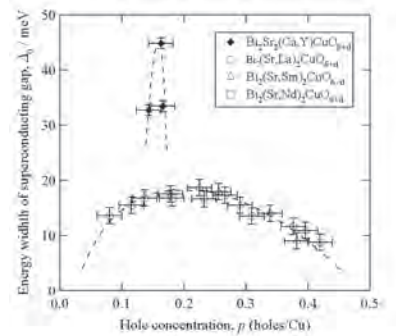


Fig. 2. Hole-concentration dependence of Δ_0 determined for $\text{Bi}_{1.7}\text{Pb}_{0.4}\text{Sr}_2\text{Ca}_{1-x}\text{Y}_x\text{Cu}_2\text{O}_{8+\delta}$ and $\text{Bi}_2(\text{Sr,RE})_2\text{CuO}_{6+d}$.

BL7U

Angle-Resolved Photoemission Study of Heusler-Type $\text{Fe}_2\text{V}_{1+x}\text{Al}_{1-x}$ Alloys

H. Miyazaki, K. Ando, W. Nagasaka and Y. Nishino

Department of Frontier Materials, Nagoya Institute of Technology, Nagoya 466-8555, Japan

Band structure calculations of Fe_2VAl alloy have predicted that a pseudo-gap is formed around the Fermi level [1]. Because of the possession of a sharp pseudo-gap across the Fermi level, Fe_2VAl -based alloys have attracted a great deal of interest as potential candidates for next-generation thermoelectric materials [2]. The peak temperature of the n-type thermoelectric power factor of previous Fe-based Heusler alloys is around 300 - 400 K [3]. For the application of thermoelectric materials to power generation, it is desirable that the peak temperature of both the n- and p-type be increased to 400-600 K. Recently, the substitution of Al or V atoms with V or Al atoms in the off-stoichiometric $\text{Fe}_2\text{V}_{1+x}\text{Al}_{1-x}$ compounds has proven to improve significantly the p- and, especially, n-type thermoelectric properties, such as electronic resistivity and Seebeck coefficient, and allows a shift of the peak performances towards interesting higher temperatures (300 - 600K) [4]. In order to clarify the origin of the improvement in the thermoelectric properties for the off-stoichiometric $\text{Fe}_2\text{V}_{1+x}\text{Al}_{1-x}$ alloys, we thus performed high-resolution three-dimensional angle-resolved photoemission spectroscopy (3D-ARPES) measurements to investigate the change in the electronic structure due to the V/Al off-stoichiometry.

SR-PES measurements were carried out in the beamline BL7U of the UVSOR-III. Photoemission spectra were recorded at 10 K. Clean surfaces for 3D-ARPES measurements were obtained by *in-situ* fracturing with a knife edge at 10 K under ultra-high vacuum. Fermi level and total energy resolution were determined by the Fermi edge of evaporated gold films. The total energy and momentum resolutions for the 3D-ARPES measurement were set to 15 meV and 0.006 \AA^{-1} at the X point ($h\nu = 26 \text{ eV}$).

Figure 1(a) and (b) shows the second derivative 3D-ARPES images of $\text{Fe}_2\text{V}_{1.03}\text{Al}_{0.97}$ (electron-doping) and $\text{Fe}_2\text{V}_{0.97}\text{Al}_{1.03}$ (hole-doping) alloys along X- Γ line, respectively. We observed three dispersion of the band around X point, which is consistent with the band structure calculation. All bands of $\text{Fe}_2\text{V}_{0.97}\text{Al}_{1.03}$ alloy shift to lower binding energy side compared to that of $\text{Fe}_2\text{V}_{1.03}\text{Al}_{0.97}$ alloy. This indicates that, the number of valence electrons around Fe, V and Al atoms decreases with increasing Al content (hole doping), and that the core level of Fe, V and Al gradually shifts to lower binding energy side because of the chemical potential shift. However, the energy dispersion ($\sim 30 \text{ meV}$) of $\text{Fe}_2\text{V}_{1.03}\text{Al}_{0.97}$ alloy is smaller than that ($\sim 70 \text{ meV}$) of $\text{Fe}_2\text{V}_{0.97}\text{Al}_{1.03}$ alloy. This result indicates that the electronic structure near

the Fermi level is modified due to the off-stoichiometric effect and the pseudo-gap widens. According to band structure calculations, a wider pseudo gap leads to a further shift in the peak temperature of the maximum thermoelectric power to the higher temperature side [5]. Therefore, it is thought that the origin of the improvement in n-type Seebeck coefficient and its peak temperature should be attributed to the modification in the electronic structure due to the off-stoichiometric effect.

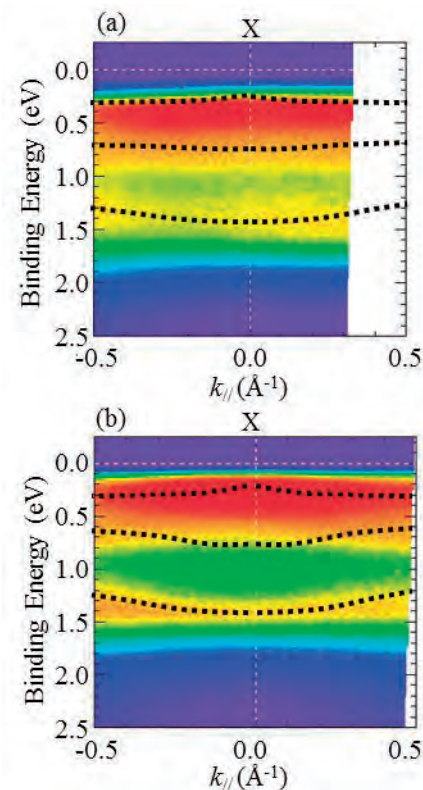


Fig. 1. Second derivative 3D-ARPES images of $\text{Fe}_2\text{V}_{1.03}\text{Al}_{0.97}$ (electron-doping) and $\text{Fe}_2\text{V}_{0.97}\text{Al}_{1.03}$ (hole-doping) alloys along X- Γ line. The dashed lines indicate the peaks in the second-derivative spectra that correspond to the shoulder and peaks in the spectra.

- [1] G. Y. Guo, G. A. Botton, and Y. Nishino, *J. Phys.: Condens. Matter* **10** (1998) L119.
- [2] Y. Nishino, *The Science of Complex Alloy Phases* (Warrendale: TMS) (2005) 325.
- [3] Y. Nishino, S. Deguchi and U. Mizutani, *Phys. Rev. B* **74** (2006) 115115.
- [4] H. Miyazaki, S. Tanaka, N. Ide, K. Soda and Y. Nishino, *Mater. Res. Express* **1** (2014) 015901.
- [5] D. Do, M. Lee and S. D. Mahanti, *Phys. Rev. B* **84** (2011) 125104.

BL7U

Angle-Resolved Photoemission Spectroscopy of YbB₁₂ (001) Surface

K. Hagiwara¹, J. Kishi¹, Y. Ohtsubo^{2,1}, H. Miyazaki³, T. Ito⁴, M. Matsunami⁵,
F. Iga⁶ and S. Kimura^{2,1}

¹Department of Physics, Osaka University, Toyonaka 560-0043, Japan

²Graduate School of Frontier Biosciences, Osaka University, Suita 565-0871, Japan

³Department of Frontier Materials, Nagoya Institute of Technology, Nagoya 466-8555, Japan

⁴Department of Materials Engineering, Nagoya University, Nagoya 464-8603, Japan

⁵UVSOR Facility, Institute for Molecular Science, Okazaki 444-8585, Japan

⁶Department of Physics, Ibaraki University, Mito 310-0056, Japan

Ytterbium dodecaboride YbB₁₂ is known as one of typical Kondo insulators/semiconductors (KIs), which has a tiny energy gap owing to the hybridization between conduction and localized 4*f* electrons, namely *c-f* hybridization [1]. Since so many experimental and theoretical studies on the physical properties have been performed over three decades, the overall physical properties have been revealed. The electronic structure has also been investigated by using optical conductivity [2], angle-integrated photoemission spectroscopy (AIPES) [3], time-resolved AIPES [4], and so on. However, the band dispersion as well as *E-k* curves probed by angle-resolved photoemission spectroscopy (ARPES) along the high symmetry lines has never been clarified experimentally because the sample cannot be cleaved along principal axes. Here, we report the ARPES result of a well-defined surface of YbB₁₂.

A single crystalline sample was fabricated by a floating-zone method. The sample was cut along the (001)-plane and polished up to a mirror surface by using a diamond lapping film sheet. The clean sample surface was obtained by annealing indirectly heated by SiC plate at the sample temperature of 1250 °C under an ultra-high vacuum better than 5×10⁻⁸ Pa. The obtained low-energy electron diffraction (LEED) image is shown in Fig. 1. The LEED image indicates the square lattice pattern that is the same as the bulk crystal.

The obtained ARPES image near the Fermi level (*E_F*) at the excitation photon energy of 16 eV is shown in Fig. 2. The observed highly dispersive bands at the binding energy below 0.3 eV mainly originates from the Yb 5*d* conduction band because of the higher cross-section at the photon energy than expected other bands, for instance Yb 4*f*. The peaks of momentum-distribution curves (MDCs) and energy-distribution curves (EDCs), which indicate the trace of the band dispersion, are plotted by open circles and triangles, respectively. The trace indicates that the conduction band becomes gentle below the binding energy of 0.1 eV suggesting that the conduction band is hybridized to localized Yb 4*f* bands located near *E_F*. The energy gap between the bonding and antibonding states of the *c-f* hybridization is expected to be about 50 meV, which

is consistent with that observed in the optical conductivity spectrum [2].

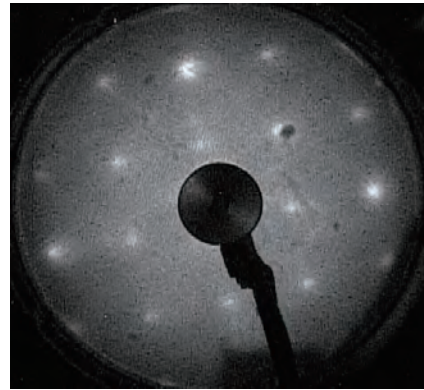


Fig. 1. LEED pattern of the YbB₁₂ (001) surface with an electron energy of 26.3 eV. Spots represent diffractions of 1×1.

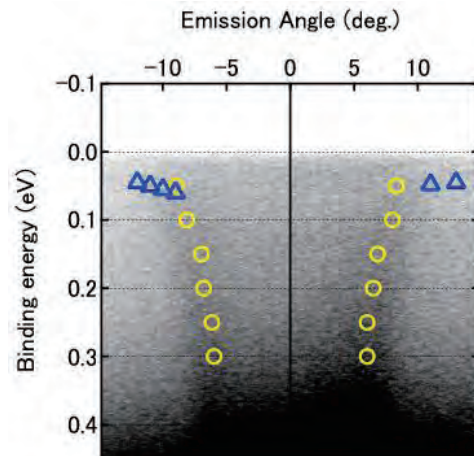


Fig. 2. ARPES image of the YbB₁₂ (001) surface along the (100) direction at the excitation photon energy of 16 eV. Open circles and triangles are peaks taken from the MDCs and EDCs, respectively.

[1] F. Iga *et al.*, J. Magn. Magn. Mater. **177–181** (1998) 337.

[2] H. Okamura *et al.*, J. Phys. Soc. Jpn. **74** (2005) 1954.

[3] T. Susaki *et al.*, Phys. Rev. Lett. **77** (1996) 4269.

[4] M. Okawa *et al.*, arXiv: 1407.0578.

BL7U

Quadratic Fermi Node in a 3D Strongly Correlated Semimetal

T. Kondo¹, M. Nakayama¹, R. Chen², J. J. Ishikawa¹, E.-G. Moon²,
 W. Malaeb¹, Y. Ishida¹, M. Matsunami³, S. Kimura^{3,4},
 S. Nakatsuji¹, L. Balents⁵ and S. Shin¹

¹ISSP, University of Tokyo, Kashiwa, 277-8581, Japan

²Physics Department, University of California, Santa Barbara, California 93106, USA

³UVSOR Facility, Institute for Molecular Science, Okazaki 444-8585, Japan

⁴Graduate School of Frontier Biosciences, Osaka University, Suita 565-0871, Japan

⁵Kavli Institute for Theoretical Physics, Santa Barbara, California 93106, USA

Following the discovery of topological insulators, the next frontier is the regime in which both spin-orbit coupling and correlation effects are strong. Theory has suggested that the pyrochlore iridates ($Ln_2Ir_2O_7$; Ln =rare earth elements), a family of cubic $5d$ transition metal oxides, realize both band inversion [1,2], the essential ingredient of topological insulators, and strong correlations. The phenomenological suggestion is that the Fermi surface of $Pr_2Ir_2O_7$ contains a single Fermi node at the Γ point protected by cubic and time-reversal symmetries, which emerges as the touching point of two quadratically dispersing “conduction” and “valence” bands [Fig.1(a) and Fig.2(e)]. If the assumption is correct, the $Pr_2Ir_2O_7$ could be a “parent” state tunable to new-types of strongly correlated topological phases [Fig.1(b)-(d)] [1,2]. As the ionic radius of Ln site increases (for example, $Ln=Nd$ and Eu), the all-in-all-out antiferromagnetic order emerges, which causes the time-reversal symmetry breaking in bulk. This could provide a realization of Weyl fermions that obeys a two-component Dirac equation. It was also predicted to establish remarkable topological properties manifested by surface states in the form of Fermi arcs. The pyrochlore iridates study therefore has enormous potential to open up the next frontier of condensed matter physics.

By ARPES, we have experimentally realized the Fermi node state in $Pr_2Ir_2O_7$ [see Fig.2]. A parabolic band-dispersion approaches E_F with increasing photon energies (or k_z values), and finally touches it at the Γ [Fig.2 (e)]. With a further increase of k_z , the dispersion gets away from E_F again, which signifies that the 3D band structure of $Pr_2Ir_2O_7$ has a single Fermi point. Other scans of different k_z values up to the L point revealed no other states touching or crossing E_F [Fig.2(c)]. This satisfies the charge neutrality, and it could be a further evidence for the realization of the Fermi nodal state. As demonstrated in Fig.2(e), we found that our ARPES data is consistent with the result of band calculations.

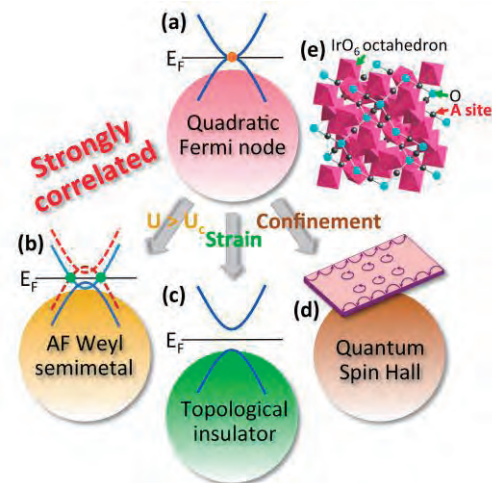


Fig. 1. Schematic diagram illustrating (a) the quadratic Fermi node state of $Pr_2Ir_2O_7$ and its role as a parent of (b)-(d) interacting topological phases.

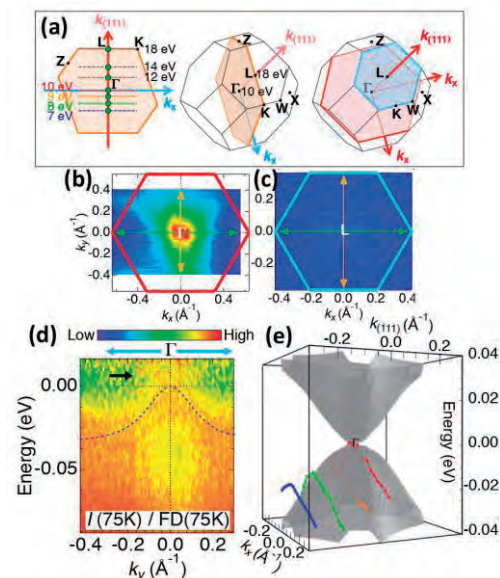


Fig. 2. (a) Brillouin zone. ARPES intensity maps around Γ (b) and L (c). (d) Band dispersion around Γ , divided by the Fermi function. (e) Comparison between ARPES data and band calculation.

[1] D. Pesin *et al.*, Nat. Phys. **6** (2010) 376.

[2] E.-G. Moon *et al.*, Phys. Rev. Lett. **111** (2013) 206401.

BL7U

ARPES Study on the Stripe-Ordered $(\text{La,Nd,Sr})_2\text{CuO}_4$ Superconductor

K. Tanaka¹, M. Matsunami¹, S. Miyasaka² and S. Tajima²

¹UVSOR Facility, Institute for Molecular Science, Okazaki 444-8585, Japan

²Department of physics, Osaka University, Toyonaka 560-0043, Japan

The “stripe order” is a periodic modulation of one-dimensional charge and spin densities observed in some hole-doped transition metal oxides. It was observed by means of neutron scattering, X-ray diffraction and so on [1,2]. In hole-doped La-214 cuprates, such as $\text{La}_{2-x}\text{Ba}_x\text{CuO}_4$ (LBCO) and $\text{La}_{2-x-y}\text{Nd}_y\text{Sr}_x\text{CuO}_4$ (LNSCO), represent this charge and magnetic order coexisting with superconductivity. Recently direct evidence for new charge density wave (CDW) order in $\text{YBa}_2\text{Cu}_3\text{O}_{7-\delta}$ (YBCO) has been observed in high magnetic field using nuclear magnetic resonance [3] and in zero-field diffraction, with resonant soft x-ray and hard x-ray scattering (RSXS) [4]. Since the superconductivity often emerges in the proximity of, or in competition with, symmetry-breaking ground states such as antiferromagnetism or CDW, the stripe order also has attracted much interests again.

Despite the intense interest and volume of research, there were not many angle-resolve photoemission (ARPES) studies on stripe samples. There were only a few studies on LBCO samples [5,6], which is mainly because it is hard to obtain a sharp peak in ARPES spectrum to discuss the detail of the superconducting gap size. Moreover, the carrier concentration and the strength of the stripe order change simultaneously by changing Ba concentration x in LBCO, which makes it difficult to understand the effect of the stripe order on the electronic structure, because the electronic structure is sensitive to the carrier concentration in cuprates. To figure out the intrinsic electronic structure of the stripe order, we choose LNSCO system, where the strength of the stripe order solely can be controlled by Nd concentration y . In this study, to clarify the intrinsic electronic structure of the stripe order, we tried to seek the best ARPES measurement condition for LNSCO samples, namely, an energy and a polarization of the incident light.

LNSCO single crystal ($x = 0.16$, $y = 0.1$) was grown by a traveling solvent floating-zone (TSFZ) method. As-grown sample was annealed on the gold plate in O_2 atmosphere at 800 degree for 1 week and quenched to the room temperature to make the hole concentration uniform. Superconducting transition temperature of the sample was determined as $T = 35$ K from the onset in the magnetization measurements. The ARPES measurements were carried out at beamline BL7U of UVSOR-III at the Institute for Molecular Science, using an MBS A-1 analyzer. The energy resolution was set to 10 meV and the angular resolution was about 0.17° . The Fermi level (E_F) was

calibrated using an evaporated gold film.

Figure 1 shows photon energy dependence of spectra from 14 eV to 40 eV at nodal k_F at 1st Brillouin Zone (BZ) taken at temperature 12 K. Here the polarization of the light was set along $(\pi,0)$ - $(0,\pi)$ direction. One can clearly see the peak structure at photon energy 20 and 36 eV. In those photon energies, the Fermi arc can be clearly seen in the Fermi surface mapping (not shown). We also performed measurements with polarization along $(0,0)$ - (π,π) direction, however, there were almost no peak and the whole spectral intensity was suppressed. This polarization dependence is consistent with previous calculation [5].

We clarify that the photon energies of 20 and 36 eV can be used for LNSCO measurements at BL7U to perform the detailed superconducting gap study.

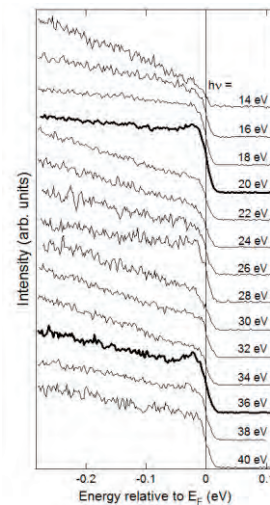


Fig. 1. Photon energy dependence of ARPES spectra of $\text{La}_{1.74}\text{Nd}_{0.1}\text{Sr}_{0.16}\text{CuO}_4$ at nodal k_F at 1st BZ taken at temperature 12 K.

- [1] J. M. Tranquada *et al.*, Nature, **375** (1995) 561.
- [2] M. Hucker *et al.*, Phys. Rev. B **83** (2011) 104506.
- [3] T. Wu *et al.*, Nature, **477** (2011) 191.
- [4] G. Ghiringhelli *et al.*, Science **337** (2012) 821.
- [3] T. Valla *et al.*, Science **314** (2006) 1914.
- [4] R. H. He *et al.*, Nature Physics **5** (2009) 119.
- [5] A. Bansil *et al.*, Phys. Rev. Lett. **83** (1999) 5154.

BL7U

ARPES Studies of Hydrogen Exposed MoS₂

S. Cho¹, B. Kim¹, B. Kim¹, Y. Kim¹, Y. Koh¹, J. Seo¹, J. Kwon¹, M. Matsunami², K. Tanaka², S. R. Park³ and C. Kim¹

¹Institute of Physics and Applied Physics, Yonsei University, Seoul, Korea

²Editorial Board, UVSOR Facility, Institute for Molecular Science, Okazaki 444-8585, Japan

³Department of physics, Incheon National University, Incheon 406-772, Korea

The physics associated with transition metal dichalcogenides (TMDCs) is one of the most intriguing issues in condensed matter physics. These materials have several interesting aspects inter physical properties, especially the direct to indirect band gap transition from monolayer to bulk and spin band splitting at the K-point. [1,2] There are many studies on the electronic structures of the monolayer TMDCs because of the direct band gap. [3,4,5] At these days, monolayer MoS₂ with direct band gap can be manufactured and it is interested in a variety of areas, such as field effect transistor, optoelectronic applications and so on. But thorough systematic studies on the electronic structures of bulk TMDCs regarding those issues have not been done.

In the early 21 century, molybdenum disulfide (MoS₂) was used by catalyst for hydrodesulfurization which mean capture and remove sulfur from the crude oil called thiophene by hydrogen sulfide. During this process, there is intermediate state that only sulfur released from MoS₂ such as defect state. We mainly interested in this intermediate state which was known for the mid gap state between conduction band and valence band. [6]

We bought the MoS₂ single crystal from the SPI then we made the cell with low vacuum. For the hydrogen treatment, we put the MoS₂ in the cell and flow the hydrogen under 20 bar pressure at about 350K for 10 hours. [7] Samples were cleaved in situ at room temperature and the chamber pressure was better than 5×10^{-11} Torr. ARPES spectra were acquired with a hemispherical photoelectron analyzer (MBS A-1). We used linearly polarized light with 40eV photon energy.

We present the electronic structure studies of hydrogen exposed MoS₂ by angle resolved photoemission in UVSOR. Figure 1a is the Γ -K fine cut raw data of hydrogen exposed MoS₂. To see band dispersion more clearly, Fig. 1b is shown as the second derivative data of Fig. 1a. In the K-point, there is a band splitting about 170meV due to strong spin-orbit coupling. [8] It is well matched by theoretical prediction for size of band splitting. The dotted white lines in Fig. 1b are guide to the eye indicating the band dispersions. It was recently reported that the number of band in topmost valence band at Γ -point are corresponding to be the number of layers. [3] The bulk MoS₂ case, it has a one thick band at Γ -point. In our data of Fig. 1b, the valence band at Γ -point shows five distinguished dispersions.

Therefore we assume that the bulk MoS₂ turns into the one of multilayer near surface after high pressure hydrogen treatment.

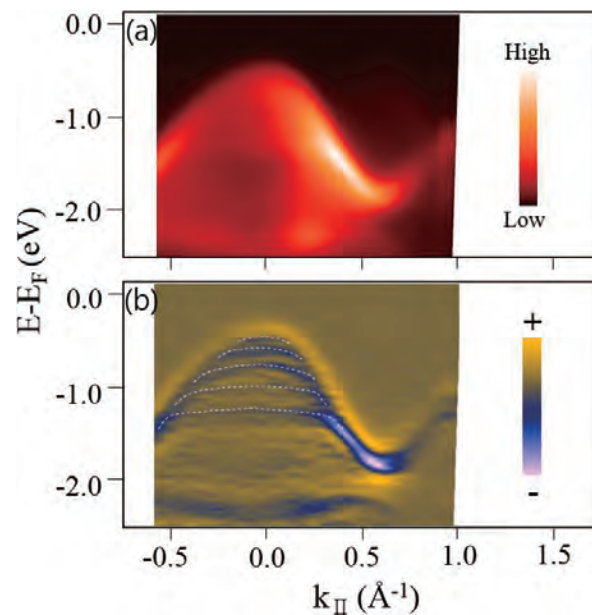


Fig. 1. (a) Γ -K fine cut raw data of hydrogen exposed MoS₂. Right side is intensity plot of raw data. (b) Γ -K fine cut second derivative data of hydrogen exposed MoS₂. Right side is sign plot of second derivative data.

- [1] Q. H. Wang *et al.*, Nat. Nanotechnol. **7** (2012) 699.
- [2] Z. Y. Zhu *et al.*, PRB. **84** (2012) 153402.
- [3] Y. Zhang *et al.*, Nat. Nanotechnol. **9** (2014) 111.
- [4] B. Radisavljevic *et al.*, Nat. Nanotechnol. **6** (2011) 147.
- [5] H. J. Conley *et al.*, Nano Lett. **13** (2013) 3626.
- [6] D. Liu *et al.*, Appl. Phys. Lett. **105** (2014) 213508.
- [7] B. H. Kim *et al.*, RCS Advances **3** (2013) 18424.
- [8] J. E. Padilha *et al.*, PR **90** (2014) 205420.

BL7U

Non-Uniform Temperature-Dependent Band Shift of an Iron Pnictide Superconductor LiFeAs

 T. Hajiri^{1,2}, T. Ito^{1,3}, M. Matsunami^{2,4}, B. H. Min⁵, Y. S. Kwon⁵, K. Kuroki⁶ and S. Kimura^{2,6,7}
¹Graduate School of Engineering, Nagoya University, Nagoya 464-8603, Japan

²UVSOR Facility, Institute for Molecular Science, Okazaki 444-8585, Japan

³Nagoya University Synchrotron Radiation Research Center, Nagoya University, Nagoya, 464-8603, Japan

⁴School of Physical Sciences, SOKENDAI (The Graduate University for Advanced Studies), Okazaki 444-8585, Japan

⁵Department of Emerging Materials Science, DGIST, Daegu 711-873, Republic of Korea

⁶Department of Physics, Graduate School of Science, Osaka University, Toyonaka 560-0043, Japan

⁷Graduate School of Frontier Biosciences, Osaka University, Suita 565-0871, Japan

Iron pnictide superconductors are recently attracted in the change of physical properties above superconducting temperature (T_c), such as the in-plane anisotropic resistivity [1], the softening of the C_{66} mode [2], the orbital-polarized electronic structure between d_{xz} and d_{yz} orbitals [3], and the appearance of a pseudogap [4]. Thus, it is considered that the electronic structure as well as the physical property above T_c is closely related to the appearance of the superconductivity, the electronic structure above T_c should be investigated to elucidate the origin of the superconductivity of the iron pnictides. In this report, we show the temperature-dependent angle-resolved photoemission spectroscopy (ARPES) results of LiFeAs ($T_c \sim 19.7$ K) using UVSOR BL7U "SAMRAI" end-station.

Figures 1(a)-1(d) show the ARPES image at the Γ ($h\nu = 23$ eV) and Z ($h\nu = 35$ eV) points along the Γ -M and Z-A directions at $T = 100$ K (above T_c) and 12 K (below T_c) taken by using S polarization. There are two hole bands at both of the Γ and Z points; the outer and inner hole bands are attributed to d_{xy} and d_{yz} orbitals, respectively [5]. Figures 1(e) and 1(f) show the comparison of each band dispersion at two temperatures of $T = 100$ and 12 K at the Γ and Z points, respectively. At the Γ point in Fig. 1(e), the observed two bands do not shift with temperature. At the Z point in Fig. 1(f), on the other hand, the inner hole band rigidly shifts to the higher binding energy side by 28 meV with decreasing temperature, though the outer hole band has almost no temperature dependence. Figures 1(g) and 1(h) show the temperature-dependent ARPES images divided by a Fermi-Dirac function at the Γ and Z points, respectively. It is clear that the energy of the top of the inner hole band at the Z point shifts below $T = 40$ K, but that at the Γ point is constant with temperature.

Recent ultrafast optical measurement reports an appearance of the pseudogap like feature below $T = 55$ K due to antiferromagnetic fluctuations [6]. Indeed, the spin fluctuation is enhanced with decreasing temperature below about $T = 50$ K [7]. These temperatures are consistent with that of an appearance of the orbital-dependent band shift, i.e., the band shift

is considered to be strongly related to the spin fluctuation.

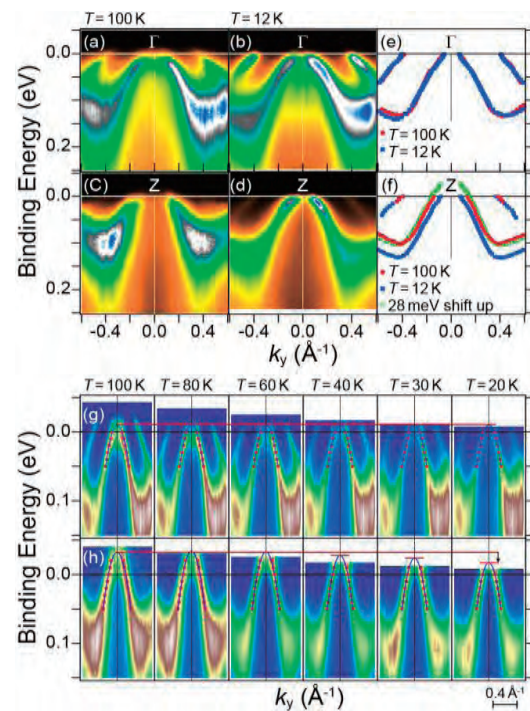


Fig. 1. (a-d) ARPES images along Γ -M/Z-A directions obtained by using S polarization at $T = 100$ and 12 K. (e, f) Comparison of each band dispersion. (g, h) Temperature-dependent ARPES images divided by a Fermi-Dirac function.

- [1] M. Nakajima *et al.*, Phys. Rev. Lett. **109** (2012) 217003.
- [2] M. Yoshizawa *et al.*, J. Phys. Soc. Jpn. **81** (2012) 024604.
- [3] M. Yi *et al.*, Proc. Natl. Acad. Sci. **108** (2011) 6878.
- [4] T. Shimojima *et al.*, Phys. Rev. B **89** (2014) 045101.
- [5] T. Hajiri *et al.*, Phys. Rev. B **85** (2012) 094509.
- [6] K.-H. Lin *et al.*, arXiv:1407.3539 (2014).
- [7] L. Ma, J. Zhang, G. F. Chen and W. Yu, Phys. Rev. B **82** (2010) 180501(R).

BL7U

Angle Resolved Photoemission Spectroscopy of Iron Pnictide Superconductor $\text{NdFeP}_{1-x}\text{As}_x(\text{O},\text{F})$

A. Takemori¹, S. Miyasaka¹, M. Uekubo¹, T. Kobayashi¹, S. Tajima¹, T. Hajiri^{2,3},
M. Matsunami^{3,4} and K. Tanaka^{3,4}

¹Department of Physics, Graduate School of Science, Osaka University, Toyonaka 560-0043, Japan

²Department of Crystalline Materials Science, Graduate School of Engineering, Nagoya University, Nagoya 464-8603, Japan

³UVSOR Facility, Institute for Molecular Science, Okazaki 444-8585, Japan

⁴School of Physical Sciences, The Graduate University for Advanced Studies (SOKENDAI), Okazaki 444-8585, Japan

The iron-based superconductors are multiband systems and have various Fermi surface states. These compounds show unconventional superconductivity with high superconducting transition temperature (T_c) and have been extremely investigated by many experimental and theoretical groups. Recently, we studied the transport properties in 1111-type P/As solid solution system, $R\text{FeP}_{1-x}\text{As}_x\text{O}_{1-y}\text{F}_y$ ($R=\text{La}, \text{Pr}$ and Nd). The results have indicated that this system has two different T_c -rising mechanism, related to two different Fermi surface states and nesting conditions below and above $x=0.6\sim 0.8$. [1, 2] To clarify x -dependent change of electronic structures and Fermi surfaces, we have investigated the angle resolved photoemission spectroscopy using single crystals of $\text{NdFeP}_{1-x}\text{As}_x(\text{O},\text{F})$ with $x=0.4, 0.8$ and 1.0 for F concentration $y\sim 0.1$.

The single crystals of $\text{NdFeP}_{1-x}\text{As}_x(\text{O},\text{F})$ were grown by high pressure technique using cubic anvil press and self-flux method. [3] T_c of the single crystals in the present work were 12 K for $x=0.4$, 23 K for $x=0.8$ and 44 K for $x=1.0$, respectively. The angle resolved photoemission spectroscopy were measured at BL7U of UVSOR facility in Institute for Molecular Science. The measurements of Fermi surfaces and electronic band dispersion around Γ and M points were performed at 12 K using incident light with the energy of 36 eV.

The results of the angle resolved photoemission spectroscopy indicate the existence of three hole and two electron Fermi surfaces in $x=0.4$, and two hole and two electron Fermi surfaces in $x=0.8$ and 1.0 samples. These Fermi surfaces have two dimensional features (cylindrical shapes), and the hole and electron Fermi surfaces are located around Γ and M points, respectively. The present experiments have clearly revealed that the change of Fermi surface state occurs around $x=0.8$. The orbital characters of these Fermi surfaces and electronic bands have been assigned by the polarization-dependent angle resolved photoemission spectroscopy [4], and the d_{xz} band particularly shows the systematic and important x dependence. Figure 1 shows the band dispersion around Γ point of $\text{NdFeP}_{1-x}\text{As}_x(\text{O},\text{F})$ with $x=0.4, 0.8$ and 1.0 by the P -polarization measurement. In this

polarization configuration, the bands with d_{xz} and d_z^2 orbital characters have been observed, and the d_{xz} band exists very near Γ point. As shown in this figure, the d_{xz} band crosses the Fermi energy and resultantly the d_{xz} hole Fermi surface exists around Γ point at $x=0.4$. The energy level of d_{xz} band decreases with increasing As concentration x , and this band almost sinks below Fermi energy around Γ point in the $x=0.8$ sample. With further increasing x , this d_{xz} Fermi surface completely disappears at $x=1.0$. The clear changes of Fermi surfaces and electronic structures around $x=0.8$ are related with the x -dependent changes of transport and other properties, and support the scenario of two T_c -rising mechanisms and two Fermi surface states in this system.

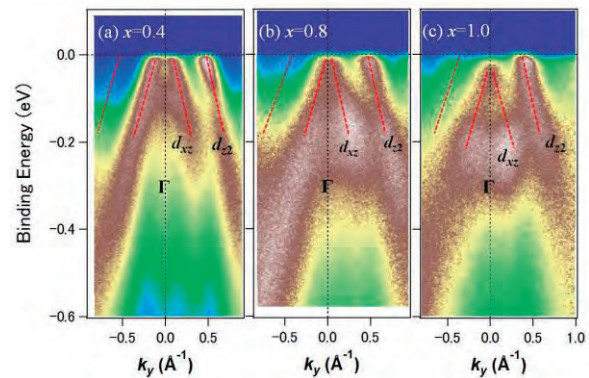


Fig. 1. Band dispersions along Γ -M direction of $\text{NdFeP}_{1-x}\text{As}_x(\text{O},\text{F})$ with (a) $x=0.4$, (b) 0.8 and (c) 1.0 by the P -polarization configuration measurement. [4] The broken red lines are guide for eyes and indicate the bands with d_{xz} and d_z^2 orbital characters around Γ point.

[1] S. Miyasaka *et al.*, J. Phys. Soc. Jpn. **82** (2013) 124706.

[2] K. T. Lai *et al.*, Phys. Rev. B **90** (2014) 064504.

[3] A. Takemori *et al.*, JPS Conf. Proc. **1** (2014) 012111.

[4] Y. Zhang *et al.*, Phys. Rev. B **83** (2011) 054510.

BL7U

Polarization Dependent ARPES Study on Iron-Based Superconductor $K_xFe_{2-y}Se_2$

M. Sunagawa¹, K. Terashima^{1,2}, M. Tanaka³, H. Takeya³, Y. Takano³,
K. Suzuki⁴, H. Usui⁴, K. Kuroki⁴, T. Wakita^{1,2}, Y. Muraoka^{1,2} and T. Yokoya^{1,2}

¹The Graduate School of Natural Science and Technology and Research Laboratory for Surface Science, Okayama University, Okayama 700-8530, Japan

²Research Center of New Functional Materials for Energy Production, Storage, and Transport, Okayama University, Okayama 700-8530, Japan

³National Institute for Material Science, Tsukuba 305-0047, Japan

⁴Department of Physics, Osaka University, Toyonaka 560-0043, Japan

An accurate description of the overall electronic structure is extremely important for understanding the mechanism of superconductivity. For iron-arsenide superconductors, their Fermi surface (FS) topology consists of hole- and electron-like FSs at the Brillouin zone center and corner, respectively. Theoretical studies based on weak-coupling approach have proposed that spin fluctuations arising from the FS nesting can realize a s_{\pm} superconducting state [1,2]. A nearly isotropic s -wave superconducting gap and a spin resonance peak at the nesting vector measured by ARPES and neutron scattering measurements [3,4], respectively, are consistent with the s_{\pm} superconducting state.

However, this theory has faced a serious challenge ever since the discovery of alkali-metal doped iron-selenide superconductors (AFS), where only electron-like FSs with nodeless superconducting gap have been observed by ARPES [5-7]. These results are not consistent with the d -wave symmetry expected by some of weak-coupling theories [8-10]. Therefore, it remains open whether the weak-coupling theories are suitable for explaining the superconductivity in AFS.

The low-lying electronic structure in iron-based materials consists of multi-band with different orbital character. Due to the photoemission selection rule, the spectral intensity of the bands exhibits photon polarization dependence. Moreover, in several iron-based superconductors, it has been reported that the strength of band intensity also depends on the excitation photon energy. So, there is a possibility that a hole-like FS actually exists and has eluded previous ARPES experiments because of the significant photon polarization and/or photon energy dependence of spectral intensity. Previously, we performed ARPES measurements with careful tuning of photon energy and photon polarization on a high quality single crystal of $K_{0.62}Fe_{1.7}Se_2$ [11], and we succeeded to observe a hole-like band with approaching E_F in two different momentum regions around the Γ point, suggesting the possible presence of a hole-like FS in $K_xFe_{2-y}Se_2$ [12].

In the present research, we performed the temperature-dependent ARPES study on $K_xFe_{2-y}Se_2$

with tuning the photon polarization at BL-7U of UVSOR, and confirmed the reproducibility of the observation of the hole-like band, as shown in Fig 1.

We acknowledge M. Matsunami and K. Tanaka for technical assistance in this photoemission experiment.

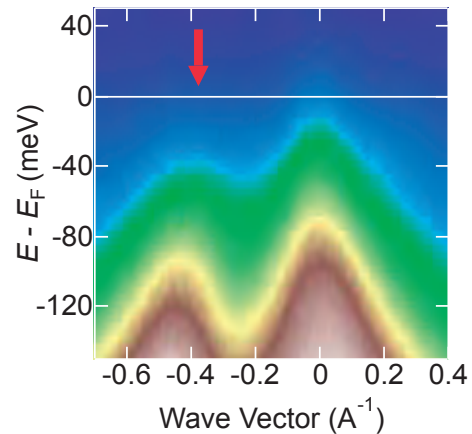


Fig. 1. ARPES E - k map along Γ -X line taken with p-polarized 23 eV photon at $T = 80$ K. In Fig.1, red arrow indicates the new hole-like band.

- [1] I. I. Mazin *et al.*, Phys. Rev. Lett. **101** (2008) 057003.
- [2] K. Kuroki *et al.*, Phys. Rev. Lett. **101** (2008) 087004.
- [3] P. Richard *et al.*, Rep. Prog. Phys. **74** (2011) 124512.
- [4] A. D. Christianson *et al.* Nature **456** (2008) 930.
- [5] M. Xu *et al.*, Phys. Rev. B **85** (2012) 220504.
- [6] D. Mou *et al.*, Phys. Rev. Lett. **106** (2011) 107001.
- [7] X. -P. Wang *et al.*, Europhys. Lett. **99** (2012) 67001.
- [8] I. I. Mazin, Phys. Rev. B **84** (2011) 02459.
- [9] M. Khodas *et al.*, Phys. Rev. Lett. **108** (2012) 247003.
- [10] A. Kreisel *et al.*, Phys. Rev. B **88** (2013) 094522.
- [11] T. Ozaki *et al.*, Europhys. Lett. **98** (2012) 27002.
- [12] M. Sunagawa *et al.*, submitted.

BL7U

CD-ARPES Studies on Rashba & Dresselhaus Effects

W. Jung¹, S. Cho¹, Y. Kim¹, B. Kim¹, J. Seo¹, J. Kwon¹, M. Matsunami², K. Tanaka²,
S. R. Park³ and C. Kim¹

¹*Institute of Physics and Applied Physics, Yonsei University, Seoul, Korea*

²*Editorial Board, UVSOR Facility, Institute for Molecular Science, Okazaki 444-8585, Japan*

³*Department of physics, Incheon National University, Incheon 406-772, Korea*

Semiconductor materials have recently been extensively studied for their spintronic applications. An important example is spin-field-effect transistor (spin-FET) proposed by Datta and Das [1] in light of controllability of spin precession motion of electrons through the Rashba and Dresselhaus spin-orbit coupling effects. [2,3,4]. Based on previous work, orbital angular momentum (OAM) plays a vital role in the Rashba effect. We expect OAM in these materials also has strong influence on the Dresselhaus effect, therefore, in turn on the spintronic properties.

Compound semiconductors such as CdTe and InSb have zinc blende structure with inversion symmetry breaking (ISB) in the bulk. They have three hole bands at the valence band top located at the Γ -point. They are defined as heavy and light hole bands with $J=3/2$, and a split off band with $J = 1/2$. The energy splitting (Δ) between $J=3/2$ and $1/2$ states due to spin-orbit coupling is on the order of hundred meV. To describe the complex spin configuration of these bands, they normally apply Dresselhaus Hamiltonian. However, the conventional Dresselhaus Hamiltonian does not consider OAM. Therefore, we aimed to investigate the OAM configuration in these bands of CdTe by using circular dichroism (CD) ARPES. We also performed density function theory calculation to theoretically study the role of OAM in the Rashba and Dresselhaus effect in these materials.

CdTe single crystals were purchased as wafers. ARPES measurement was performed at the beam line 7U of UVSOR-III. Samples were cleaved in situ at room temperature and the chamber pressure was better than 5×10^{-11} Torr. ARPES spectra were acquired with a hemispherical photoelectron analyzer (MBS A-1). We used horizontally polarized as well as left- and right-circularly polarized (LCP and RCP) light.

The dispersion of heavy and light hole bands are clearly seen in Γ -X high symmetry cut data taken by horizontal polarized light with 24 eV photon energy as shown in Fig. 1a. Figure 1b is the CD-pattern. The CD-pattern is defined as the subtraction data from RCP and LCP (RCP-LCP). The dotted black line is a guide to the eye, indicating the dispersion of the light hole band. We can only confirm the CD-pattern of light hole band because the heavy hole band is not clearly seen in low photon energy region. The CD-pattern of light hole band seems to have mirror-symmetry breaking about the Γ -point.

The above observation means that the OAM has

similar textures to the spin textures of Dresselhaus type, implying the existence of OAM in this system. It also implies that OAM plays an important role in the Dresselhaus effect. To confirm more precise OAM texture, we will obtain the energy constant contour data using CD-ARPES.

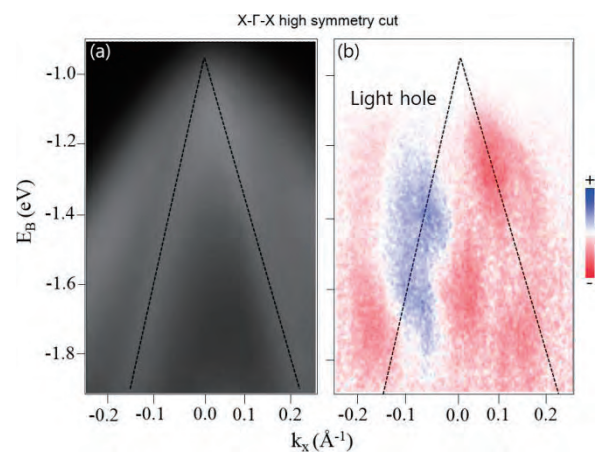


Fig. 1. ARPES results from CdTe (110) bulk state measured with 24 eV photon (a) and CD pattern of one with 9.75 eV (b) at the Γ -point.

- [1] S. Datta *et al.*, Appl. Phys. Lett. **56** (1990) 665.
- [2] Y. A. Bychkov *et al.*, JETP Lett. **39** (1984) 78.
- [3] J. Schliemann *et al.*, PRL. **90** (2003) 146801.
- [4] X. Cartoixà, D *et al.*, APL. **83** (2003) 1462.
- [5] S. R. Park *et al.*, PRL **107** (2011) 156803.
- [6] B. Y. Kim *et al.*, PRB **85** (2012) 195402.

BL7B

Electronic Structures and Reflectance Spectra of AZnF₃ (A=Na, K, Rb) Single Crystals

S. Ishii¹, S. Tanaka¹, A. Yamaji², S. Tanaka³, S. Kurosawa^{2,4}, S. Watanabe⁵, M. Kitaura¹, A. Ohnishi¹ and M. Sasaki¹

¹Department of Physics, Faculty of Science, Yamagata University, Yamagata 990-8560, Japan

²Institute for Materials Research, Tohoku University, Sendai 980-8577, Japan

³Department of Electric and Electronic Engineering, Faculty of Science and Engineering, Kinki University, Higashi-Osaka 577-8502, Japan

⁴New Industry Creation Hatchery Center, Tohoku University, Sendai 980-8579, Japan

⁵Department of Materials, Physics and Energy Engineering, Graduate School of Engineering, Nagoya University, Nagoya 464-8063, Japan

Studies on Auger-free luminescence (AFL) are of importance in both sides of basic science and industrial application. In this viewpoint, we have looked for new types of AFL materials so far [1, 2]. The present study is an extension of such previous studies; the possibility of AFL in AZnF₃ (A=Na, K, Rb) crystals has been investigated by measurements of reflection and x-ray photoelectron spectroscopy (xps) spectra.

The crystals of NaZnF₃, KZnF₃, and RbZnF₃ were grown from melt by a micro puling-down method. Reflectance spectra of NaZnF₃, KZnF₃, and RbZnF₃ crystals are shown in Figs. 1(a)-1(c), respectively. These data were measured at 8 K. The lowest energy reflectance peak due to excitonic transition locates around 10 eV. Since the peak position is independent of alkali metals, it is likely that such excitonic transition occurs by F 2*p* → Zn 4*s* transitions. The reflectance spectrum of NaZnF₃ is structureless in the energy region above 10 eV, and is different from the reflectance spectra of KZnF₃ and RbZnF₃. According to Ref. 3, the outermost core bands of NaZnF₃, KZnF₃, and RbZnF₃ are mainly of alkali *p* orbitals. The binding energies are estimated to be 25, 12, and 9 eV, respectively. In NaZnF₃, the electronic transition from the outermost core band does not occur in the energy region below 30 eV, and thus the reflectance spectrum exhibits only tail. In KZnF₃ and RbZnF₃, the transitions from outermost core bands are observed as many peaks in the reflectance spectra.

There is a general rule on the occurrence of AFL. It is observed in the case that the band gap energy is larger than the energy difference between the valence band top and the outermost core band top. This rule is satisfied in KZnF₃. Although KZnF₃ is expected to be an AFL material, AFL has not yet been found at present.

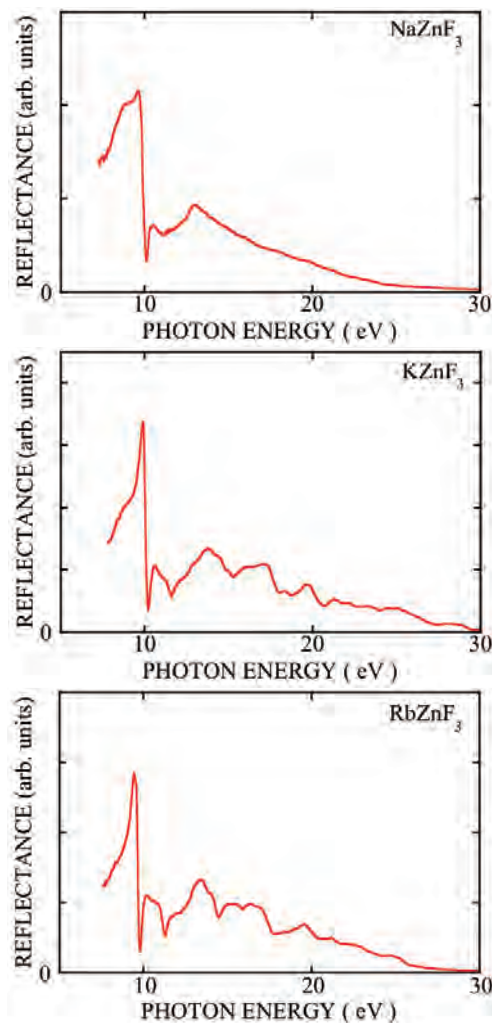


Fig. 1. Reflectance spectra of NaZnF₃ (upper), KZnF₃ (middle), RbZnF₃ (lower) single crystals measured at 8 K.

[1] A. Ohnishi *et al.*, J. Lumi. **132** (2012) 2639.

[2] M. Kitaura *et al.*, Phys. Status Solidi C **10** (2008) 993.

[3] J. F. Moulder, W. F. Stickle, P. E. Sobol and K. D. Bomben, *Hand- book of X-Ray Photoelectron Spectroscopy*, edited by J. Chastain Perkin-Elmer Corporation, Eden Prairie, MN, 1992.

BL7B

Luminescence and Scintillation Properties of CdF₂ Crystal

T. Yanagida^{1,2}, Y. Fujimoto², M. Koshimizu² and K. Fukuda³

¹*Kyushu Institute of Technology, Fukuoka 808-0196, Japan*

²*Department of Applied Chemistry, Graduate School of Engineering, Tohoku University, Sendai 980-8579, Japan*

³*Tokuyama Corp., Shunan 745-8648 Japan*

Auger-free luminescence (AFL) is a luminescence process in which a valence electron radiatively recombine with an outermost core hole. Typical decay time constant of the AFL is subnanosecond or on the order of nanoseconds. Owing to the fast decay, insulator crystals exhibiting the AFL is often used as fast scintillators. The AFL has been observed in various insulators, mainly halide crystals.

Among the halide crystals, the occurrence of the AFL was predicted in CdF₂ [1]. Scintillation properties of CdF₂ crystals have been reported in several papers [2-4]. Fast scintillation components has been observed, however, the ascription of these components to the AFL is not conclusive. In this report, the luminescence and scintillation properties of a single crystal of CdF₂, with an emphasis on the luminescence properties under vacuum ultraviolet (VUV) photon irradiation.

Single crystal of CdF₂ was grown by Tokuyama Corp. The luminescence and excitation spectra of CdF₂ was obtained by using VUV light as an excitation source at BL7B, UVSOR. Temporal profiles of photoluminescence was obtained at UVSOR operated in a single bunch mode. Radioluminescence (RL) spectrum was obtained under X-ray irradiation. Temporal profile of scintillation was obtained by a single photon counting technique using a pulsed X-ray as an excitation source.

Figure 1 shows the RL spectrum. We observed a prominent band at 420 nm and a shoulder at ca. 350 nm.

Figure 2 shows the excitation spectra monitored at 350 nm. The excitation band maxima were located between 200 and 300 nm. This is also the case for the monitoring wavelength of 420 nm. Taking into account the band gap energy, this excitation band is judged to be located within the band gap. In addition, the band was hardly observed under VUV irradiation.

Figure 3 shows the temporal profile of luminescence at 420 nm. A fast component was observed. The fast components in scintillation can be ascribed to this luminescence component.

The results mentioned above indicate that the fast scintillation component in CdF₂ cannot be ascribed to the AFL but to the defects or impurities.

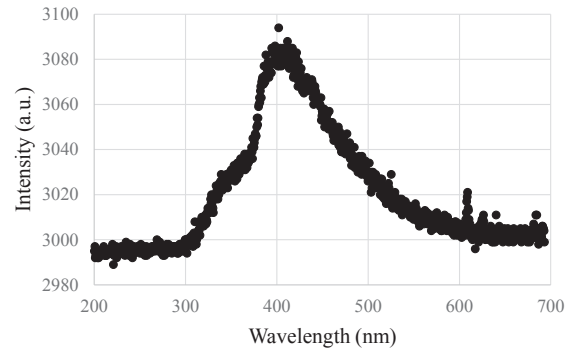


Fig. 1. Radioluminescence spectrum.

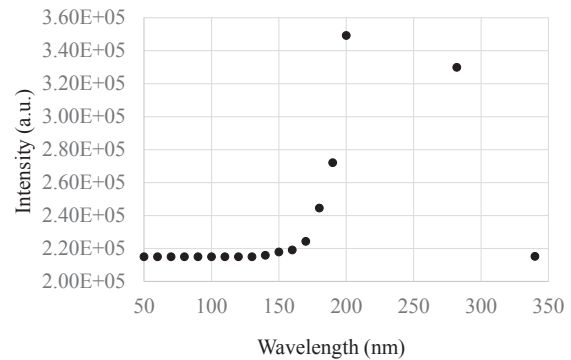


Fig. 2. Excitation spectra monitored at 350 nm.

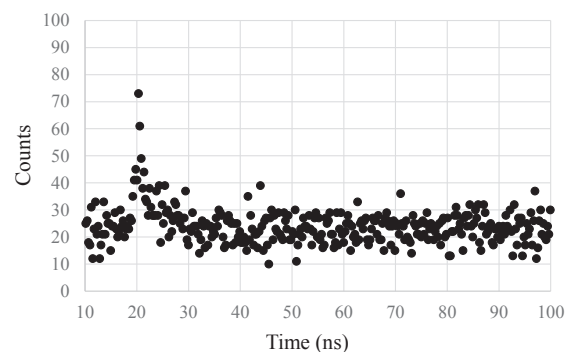


Fig. 3. Temporal profile of luminescence at 420 nm.

[1] J. Andiessen, P. Dorenbos and C. W. E. Van Eijk, *Radiat. Meas.* **24** (1995) 347.

[2] R. V. Jones and J. H. Pollard, *Proc. Phys. Soc.* **79** (1962) 358.

[3] S. E. Derenzo, W. W. Moses, J. L. Cahoon and R. C. C. Perera, *IEEE Trans. Nucl. Sci.* **37** (1990) 203.

[4] E. Radzhabov and R. Shendrik, *IEEE Trans. Nucl. Sci.* **61** (2014) 402.

BL7B

Reflection Spectra of Ternary Zinc Bismuth Phosphate Glasses in the Ultraviolet Region

N. Kitamura

National Institute of Advanced Industrial Science and Technology, Ikeda 563-8577, Japan

Bismuth phosphate glasses, which have high refractive index and low deformation temperature, are candidate materials for producing high performance optical components such as compact lenses and diffractive optics. It is of interest that a zinc bismuth phosphate glass system has two distinct glass-forming regions; orthophosphate and isolated phosphate structures are dominant in the region that the atomic ratio O/P is higher than 3.5 and metaphosphate and pyrophosphate structures are dominant in the region of O/P < 3.5 [1,2]. We have reported the glass structure and local structure around bismuth ions in a previous work [2,3]. However, the energy level in the glass system is not clear yet. In the present study, reflectivity of the bismuth phosphate glasses has been measured to investigate compositional dependence of the band structure in the vacuum ultraviolet region.

Ternary $x\text{ZnO}-(30-x/2)\text{Bi}_2\text{O}_3-(70-x/2)\text{P}_2\text{O}_5$ glasses ($x=10, 20$ and 30 mol%) and $(85-3x/2)\text{ZnO}-x\text{Bi}_2\text{O}_3-(15+x/2)\text{P}_2\text{O}_5$ glasses ($x=15, 20$ and 25 mol%) were prepared by using a conventional liquid-quench method. Nominal chemical compositions are plotted in the glass forming region of the present system as shown in Fig. 1. Reflectivity of optically polished samples was measured in the photon energy region of 4-18 eV with an incident angle of 10° at the BL7B. Figure 2 shows reflection spectra of the binary and un-doped $x\text{ZnO}-(30-x/2)\text{Bi}_2\text{O}_3-(70-x/2)\text{P}_2\text{O}_5$ glasses. Distinct reflection peak and broad contour were respectively observed at around 5 eV and 6-8 eV. The peak and contour are assigned to the $6s^2 \rightarrow 6s^1 6p^1$ transition in the Bi^{3+} ion [2, 4]. We know that transitions from the ground state (1S_0) to excited states 3P_0 and 3P_2 are spin-forbidden. Therefore, the lower distinct peak is expected to the $^1S_0 \rightarrow ^3P_1$ transition and the next contour could be due to the $^1S_0 \rightarrow ^1P_1$ transition. K-K transformed absorption peaks having Gaussian shape have been fitted to these reflection spectra by least square method. The first peak assigned to the $^1S_0 \rightarrow ^3P_1$ transition was located at 4.9 eV and the position was almost constant in spite of large change in ZnO and Bi_2O_3 concentration.

On the other hand, reflection spectra of ternary $(85-3x/2)\text{ZnO}-x\text{Bi}_2\text{O}_3-(15+x/2)\text{P}_2\text{O}_5$ glasses are shown in Fig. 3. The first peaks located around 4.2 eV and shifted toward lower energy side with the increase of ZnO content. In the previous work [5], we have found that the fraction of the Bi-O bond having short length in BiO_6 polyhedra increased with increasing ZnO content. The low energy shift of the first band might be due to the change in local structure around bismuth ions.

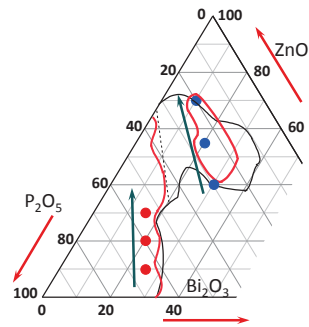


Fig. 1. Glass forming region and chemical compositions of glass of the present system.

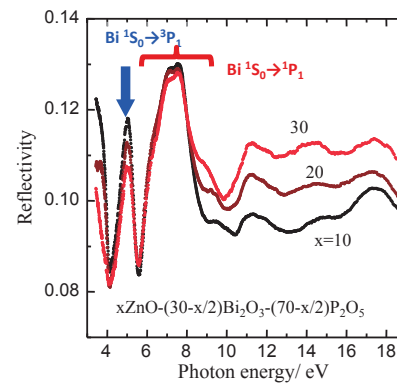


Fig. 2. Reflection spectra of ternary $x\text{ZnO}-(30-x/2)\text{Bi}_2\text{O}_3-(70-x/2)\text{P}_2\text{O}_5$ glasses.

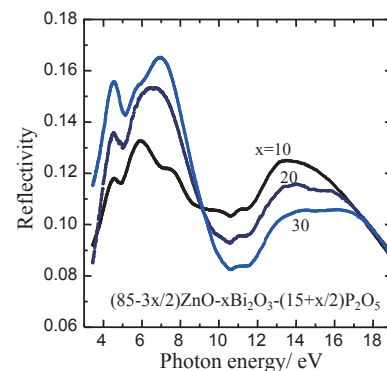


Fig. 3. Reflection spectra of ternary $(85-3x/2)\text{ZnO}-x\text{Bi}_2\text{O}_3-(15+x/2)\text{P}_2\text{O}_5$ glasses.

- [1] B. Elouadi *et al.*, Phase Trans. **13** (1988) 219.
- [2] N. Kitamura *et al.*, Mater. Sci. Eng. B **161** (2009) 91.
- [3] N. Kitamura and K. Fukumi, J. Ceram. Soc. Jpn. **121** (2013) 355.
- [4] G. Blasse and A. Bril, J. Chem. Phys. **48** (1968) 217.
- [5] N. Kitamura, *et al.*, 23th International Congress on Glass 2013, in preparation.

BL7B

Control of Spectral Response Using Compound Fluoride Materials $\text{Ca}_x\text{Sr}_{1-x}\text{F}_2$

S. Otani, H. Ishikawa, M. Yanagihara and S. Ono
Nagoya Institute of Technology, Nagoya 466-8555, Japan

Vacuum ultraviolet (VUV) light source is used in various applications such as surface treatment, optical cleaning of semiconductor substrates and sterilization. Accordingly, the detector for monitoring the light source is also required. Currently, many researchers developed VUV detectors based on oxide, nitride and diamond. However, the detectors require the filters for cutting off deep-UV when being used for monitoring of the light source. On the other hand, our group is proceeding to development of the VUV detectors using fluorides [1, 2]. Some fluorides have extremely wider band gap than oxides and nitrides so that they transmit deep-UV region [3]. Until now, we achieved filterless VUV detectors by applying such fluorides. And spectral response of the detectors varies according to band gap of the material. Therefore, we may realize the detectors possessing arbitrary response region by controlling band gap of the material. Here, we report on controlling band gap of compound fluoride materials $\text{Ca}_x\text{Sr}_{1-x}\text{F}_2$ and spectral response of filterless VUV photoconductive detectors.

$\text{Ca}_x\text{Sr}_{1-x}\text{F}_2$ crystals were grown by Bridgman method and they were controlled composition ratio as $\text{Ca}_{0.85}\text{Sr}_{0.15}\text{F}_2$ and $\text{Ca}_{0.5}\text{Sr}_{0.5}\text{F}_2$. The transmission spectrum of $\text{Ca}_x\text{Sr}_{1-x}\text{F}_2$ crystals was measured in beamline BL7B at the UVSOR facility. Absorption coefficient was calculated by measuring transmission spectrum of UV region, as shown in Fig. 1. Herewith, band gaps of $\text{Ca}_{0.85}\text{Sr}_{0.15}\text{F}_2$ and $\text{Ca}_{0.5}\text{Sr}_{0.5}\text{F}_2$ were calculated as 10.09 eV and 9.93 eV, respectively. Therefore, band gap of $\text{Ca}_x\text{Sr}_{1-x}\text{F}_2$ is expanded by increasing composition ratio of CaF_2 in the crystals.

Filterless VUV photoconductive detectors were fabricated by depositing a pair of interdigitated aluminum electrodes on the crystals. Spectral responses of the detectors were also measured in beamline BL7B at the UVSOR facility. The detectors of $\text{Ca}_{0.85}\text{Sr}_{0.15}\text{F}_2$ and $\text{Ca}_{0.5}\text{Sr}_{0.5}\text{F}_2$ responded until below 151 nm and 156 nm, respectively. The result shows the response region of the detectors shift to the short-wavelength by expanding band gap of the crystals.

In summary, we found capable of controlling the size of band gap of $\text{Ca}_x\text{Sr}_{1-x}\text{F}_2$ crystals. Additionally, the spectral response change of filterless VUV photoconductive detectors was observed by using $\text{Ca}_x\text{Sr}_{1-x}\text{F}_2$ crystals.

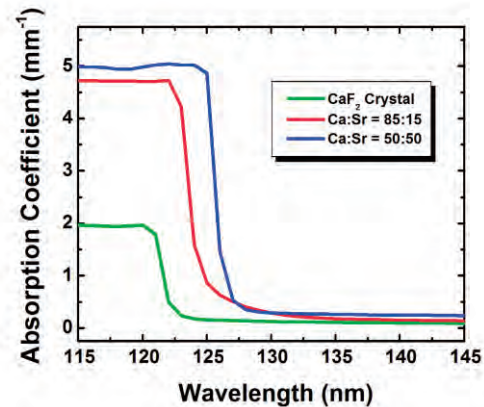


Fig. 1. Transmission spectrum of $\text{Ca}_x\text{Sr}_{1-x}\text{F}_2$ crystals.

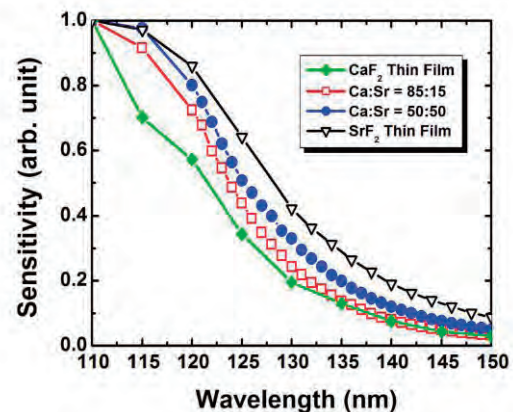


Fig. 2. Spectral responses of the detectors using $\text{Ca}_x\text{Sr}_{1-x}\text{F}_2$.

- [1] M. Ieda, T. Ishimaru, S. Ono, K. Yamanoi, M. Cadatal, T. Shimizu, N. Sarukura, K. Fukuda, T. Suyama, Y. Yokota, T. Yanagida and A. Yoshikawa, *Jpn. J. Appl. Phys.* **51** (2012) 022603.
- [2] T. Ishimaru, M. Ieda, S. Ono, Y. Yokota, T. Yanagida and A. Yoshikawa, *Thin Solid Films* **534** (2013) 12.
- [3] S. Ono, R. E. Ouenzerfi, A. Quema, H. Murakami, N. Sarukura, T. Nishimatsu, N. Terakubo, H. Mizuseki, Y. Kawazoe, A. Yoshikawa and T. Fukuda, *Jpn. J. Appl. Phys.* **44** (2005) 7285.

BL7B

Optical Spectroscopy of $\text{Ba}(\text{Fe}_{1-x}\text{Co}_x)_2\text{As}_2$ in Vacuum-Ultraviolet Energy Region

M. Nakajima, S. Miyasaka and S. Tajima

Department of Physics, Osaka University, Toyonaka 560-0043, Japan

Iron-based superconductors show high transition temperatures as high as 55 K, which is the second highest record after copper-oxide high-temperature superconductors, and have attracted much attention. BaFe_2As_2 is one of the representative parent compounds of iron-based superconductors and exhibits a magnetostructural phase transition at $T = 140$ K. With Co substitution for Fe, the magnetostructural order is suppressed and superconductivity emerges. Thus, how the electronic structure evolves with doping (chemical substitution) is one of the most important issues, and the investigation of the electronic structure over wide energy range by the measurements of the reflectivity spectra is essential.

In this beamtime, we measured reflectivity spectra of single-crystalline $\text{Ba}(\text{Fe}_{1-x}\text{Co}_x)_2\text{As}_2$ ($x = 0, 0.1,$ and 0.25) for an energy range from 2 eV to 35 eV at room temperature using BL7B. The measurement was performed for $x = 0.25$ using the light polarized parallel and perpendicular to FeAs layers (denoted as $E \perp c$ and $E // c$, respectively) and for $x = 0$ and 0.1 using the light of $E \perp c$. Reflectivity measurement in this energy region is necessary to understand the comprehensive electronic structure including valence bands away from the Fermi energy and to obtain reliable optical parameters derived from the Kramers-Kronig transformation for multi-band/orbital systems such as iron-based materials [1] or copper oxides [2], since a number of intraband and interband excitations overlap in the same energy region and extend up to 10 eV or higher.

Figure 1 shows the in-plane reflectivity spectra ($E \perp c$) for $x = 0, 0.1,$ and 0.25 . For all the three compositions, three distinct reflectivity edges are clearly observed at $< 2, \sim 10,$ and ~ 25 eV. Each edge indicates the end point of a series of intraband or interband excitations. The lowest-energy edge corresponds to the plasma edge of free carriers. In the present energy range, the lower limit of which is ~ 2 eV, only a tail of the edge is seen. With Co doping, an energy showing a dip shifts to a higher energy region, indicating that Co substitution increases electron carrier density. The second edge probably corresponds to the transition from $\text{As}4s$ to $\text{Fe}3d$. A height of a peak at ~ 7 eV decreases with increasing the Co content. This might result from a Lifshitz transition due to electron (Co) doping. The formation of the third edge observed at ~ 25 eV is contributed by the excitations involving all the valence electrons.

Polarization dependence of the reflectivity spectra for $x = 0.25$ is shown in Fig. 2. An overall feature is

similar, but fine structures are smeared for $E // c$, indicating that these structures result from excitations parallel to FeAs layers. The most prominent difference is observed for the 7-eV peak. The clearer peak for $E \perp c$ implies that the in-plane response is dominant for the transition from $\text{As}4s$ to $\text{Fe}3d$.

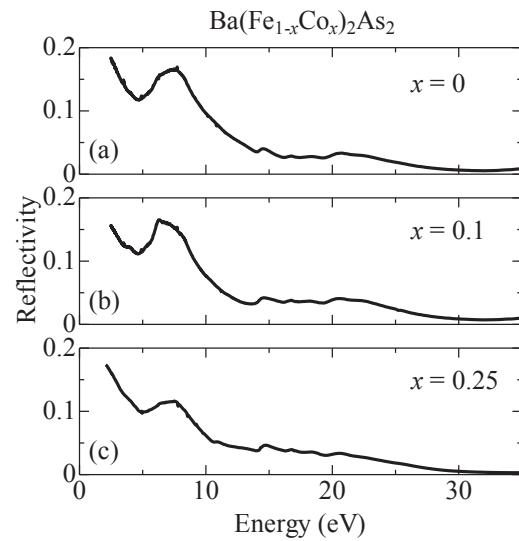


Fig. 1. Reflectivity spectra of $\text{Ba}(\text{Fe}_{1-x}\text{Co}_x)_2\text{As}_2$ up to 35 eV for (a) $x = 0$, (b) 0.1, and (c) 0.25.

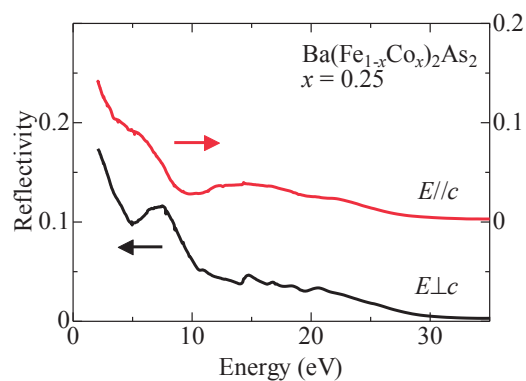


Fig. 2. Reflectivity spectra of $\text{Ba}(\text{Fe}_{0.75}\text{Co}_{0.25})_2\text{As}_2$ for the polarization parallel and perpendicular to the FeAs layers. The spectrum for $E // c$ is offset to avoid overlapping.

[1] M. Nakajima *et al.*, Proc. Natl. Acad. Sci. U.S.A. **108** (2011) 12238.

[2] S. Tajima *et al.*, J. Opt. Soc. Am. B **6** (1989) 475.

BL7B

Influence of Niobium Concentration on the Reflection Spectra for Ternary Niobium Bismuth Phosphate Glasses

N. Kitamura¹, K. Fukumi¹, Y. Hisano², N. Hirao², S. Tuji², A. Uchiyama² and H. Kozuka²

¹National Institute of Advanced Industrial Science and Technology, Ikeda 563-8577, Japan

²Kansai University, Suita 564-8680, Japan

BaO-Nb₂O₅-P₂O₅ glass is one of niobium phosphate glass systems having a wide glass forming region with high Nb₂O₅ contents¹. In this system, NbO_x polyhedra construct glass network structure with PO₄ tetrahedra. Since the glass shows high refractive index due to high niobium concentration. It is of interest for the application to optical glasses in precision optical devices. However, the glass with high niobium content gives yellowish and blue colours and the relationship between optical properties, such as refractive index, dispersion, absorption edge, etc., and structure around niobium ions or connection of niobium-oxygen polyhedra in the network structure are not clear yet. In the present study, reflectivity of the bismuth phosphate glasses has been measured to investigate compositional dependence of the band structure in the vacuum ultraviolet region.

Ternary xNb₂O₅-(100-x)Ba(PO₃)₂ glasses (x=0, 15, 35 and 50 mol%) and ternary xNb₂O₅-50BaO-(50-x)P₂O₅ glasses (x=0, 10, 20 and 30 mol%) were prepared by using a conventional liquid-quench method. Reflectivity of optically polished samples was measured in the photon energy region of 4-25 eV with an incident angle of 10° at the BL7B. Figure 1 shows reflection spectra of the xNb₂O₅-(100-x)Ba(PO₃)₂ glasses. Strong reflection peak was observed at around 9.5 eV and 22 eV, and a weak shoulder at 12-18 eV was observed for the glasses with low Nb₂O₅ content. The peaks are assigned to the transition from O 2p and P 3p states to Nb 4d and Ba 5d states from a report of DFT calculation for barium niobium phosphate compounds [2]. The origin of the higher band at 22 eV is not clear yet. The weak shoulder around 12-18 eV suppressed with increasing Nb₂O₅ content. Therefore, the shoulder could be due to the Ba 5d state. In a crystal which NbO₆ polyhedra construct chain-like structure, Ba 5d state locates at higher energy side than Nb 5d state [2]. This does not contradict the present results. The 9.5 eV peak became broad with the increase of Nb₂O₅ content. Low energy shift of absorption edge and yellowish color [3] might be due to the broadening of this band.

On the other hand, reflection spectra of ternary xNb₂O₅-50BaO-(50-x)P₂O₅ glasses are shown in Fig. 2. As shown in the figure, the similar peaks and shoulder were observed. The weak shoulder around 12-18 eV suppressed with increasing Nb₂O₅ content. The 9.5 eV band broadened with the increase of Nb₂O₅ content too. The broadening of the 9.5 eV band

might be due to the distortion of NbO₆ polyhedra which was found by Raman, FT-IR and XAFS measurements of these glasses [3].

This work was supported by Nippon Sheet Glass Foundation for Materials Science and Engineering.

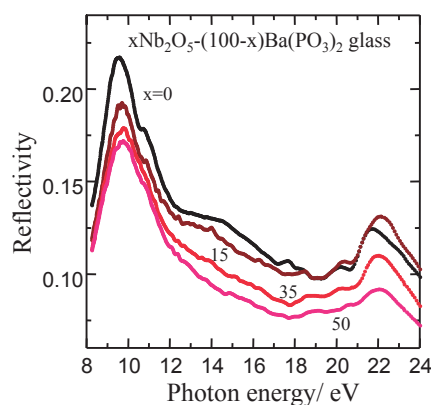


Fig. 1. Reflection spectra of ternary xNb₂O₅-(100-x)Ba(PO₃)₂ glasses.

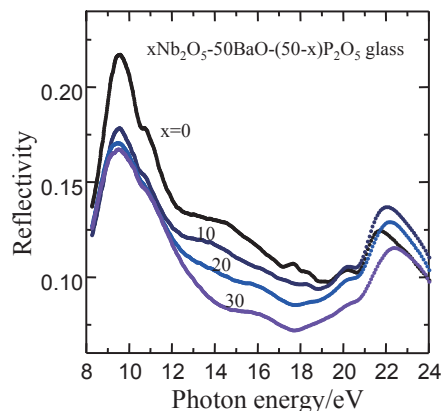


Fig. 2. Reflection spectra of ternary xNb₂O₅-50BaO-(50-x)P₂O₅ glasses.

- [1] N. Shcheglova and T. V. Avlas, *Fiz. Khim. Stekla* **16** (1990) 879.
- [2] I. Cho *et al.*, *Eur. J. Inorg. Chem.* **2011** (2011) 2206.
- [3] N. Kitamura *et al.*, Extended abstract 1st Int. Nat'l. Conf. Phosphate glasses, Pardvice, 2014.

BL8B

Ultraviolet Photoelectron Spectra of $\text{Ce}_2@C_{80}$ and $\text{La}_2@C_{80}$

T. Miyazaki¹, S. Okita¹, T. Ohta¹, H. Yagi¹, R. Sumii², H. Okimoto³, Y. Ito³,
H. Shinohara³ and S. Hino¹

¹Graduate School of Science and Engineering, Ehime University, Matsuyama 790-8577, Japan

²Institutes for Molecular Science, Okazaki 444-858, Japan

³Graduate School of Science, Nagoya University, Nagoya 464-8602, Japan

Fullerene cages often encapsulate metal atoms. C_{80} endohedral fullerenes attract attention because of the reasons such as empty I_h-C_{80} is not stable and cannot be isolated [1] but it becomes stable upon encapsulation of metal atoms [2]. Early theoretical calculation on $\text{La}_2@C_{80}$ suggested that entrapped two La atoms rotated in the $D_{2h}-C_{80}$ cage. Vibrational mode analysis using DFT calculation of $\text{La}_2@C_{80}$ suggested D_{3d} symmetry that is the global minimum in total energy. $\text{Ce}_2@C_{80}$ was isolated and its predicted geometry was not D_{2h} but D_{3d} . The reason of $\text{Ce}_2@C_{80}$ having D_{3d} geometry was attributed to specific bonding condition of Ce atoms to the cage: they bonded to C atoms on the opposite side of C_6 axis of C_{80} . We succeeded to measure ultraviolet photoelectron spectra (UPS) of $\text{La}_2@C_{80}$ and $\text{Ce}_2@C_{80}$. In this report their UPS will be presented and they are compared with simulated spectra obtained from DFT calculation.

The UPS were measured using a photoelectron spectrometer at BL8B2 of UVSOR. Energy calibration of the spectra was carried out using the Fermi edge of a gold-deposited sample disk before the UPS measurements of $\text{La}_2@C_{80}$ and $\text{Ce}_2@C_{80}$. Molecular orbitals of $\text{La}_2@C_{80}$ and $\text{Ce}_2@C_{80}$ were calculated with a Gaussian 03 program module. Their geometry was optimized at the Hartree-Fock level using the CEP-31G basis set. Simulated spectra generated by broadening the calculated Eigen values at the Hartree-Fock level with Gaussian functions of 0.2 eV full width at half maximum.

Figure 1 shows the UPS of $\text{La}_2@C_{80}$ and $\text{Ce}_2@C_{80}$ obtained with $h\nu = 30\text{eV}$. The spectral onset of $\text{La}_2@C_{80}$ and $\text{Ce}_2@C_{80}$ was 0.77 and 0.89 eV below the Fermi level, respectively. Except for the onset energy, their UPS are almost identical. There are 10 structures labeled A to J in their UPS. Their relative intensity is almost the same. The bars in Fig. 1 indicate the calculated ionization energies (Eigenvalues of occupied states). Scale of the simulated spectra and Kohn-Sham orbital energies is shifted by 4.4 eV for an easy comparison. The simulated spectra generated from D_{3d} and D_{2h} geometry seem to reproduce the UPS; the first four structures A – D are well reproduced and deeper structures F – J are also reproduced reasonably well. Only attractive difference in the simulated spectra might be associated with the position of the HOMO; the HOMO of $\text{Ce}_2@C_{80}$ appears at slightly shallower

than the HOMO-1 or -2, whereas that of $\text{La}_2@C_{80}$ locates rather close to the HOMO-1. From these data, present findings suggest that the simulated spectra obtained from D_{3d} geometry reproduced the UPS of $\text{Ce}_2@C_{80}$ and $\text{La}_2@C_{80}$ very well.

The UPS of $\text{La}_2@C_{80}$ are the same as those of $\text{Ce}_2@C_{80}$, both have the same electronic structure. Comparison of the UPS with theoretically generated simulation spectra indicates that the most plausible structure of $\text{Ce}_2@C_{80}$ and $\text{La}_2@C_{80}$ has D_{3d} symmetry. Charge population analysis suggests $\text{Ce}_2^{6+}@C_{80}^{6-}$ and $\text{La}_2^{6+}@C_{80}^{6-}$ oxidation state.

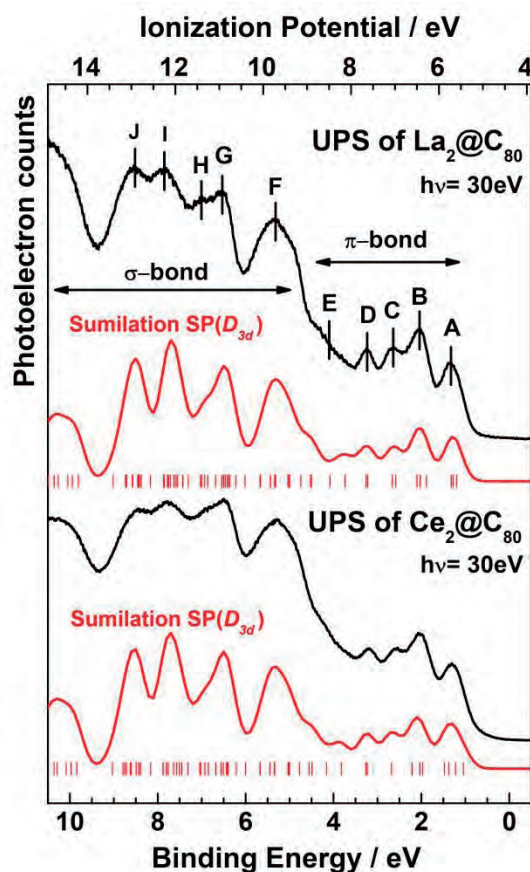


Fig. 1. Simulation spectra from the optimized D_{3d} structure and ultraviolet photoelectron spectra of $\text{La}_2@C_{80}$ and $\text{Ce}_2@C_{80}$.

[1] F. H. Hennrich, *et al.*, *Angew. Chem. Int. Ed.* **35** (1996) 1732.

[2] M. M. Alvarez, *et al.*, *J. Phys. Chem.* **95** (1991) 10561.

III-3

Chemistry

BL1U

Induced Chirality by Circularly Polarized UV Light for Photofunctional Organic/Inorganic Hybrid Materials

T. Akitsu¹, N. Sunaga¹, N. Ishida¹, M. Ito¹, T. Konomi² and M. Kato²

¹Department of Chemistry, Faculty of Science, Tokyo University of Science, Tokyo 162-8601, Japan

²UVSOR Facility, Institute for Molecular Science, Okazaki 444-8585, Japan

Photofunctional organic/inorganic hybrid materials containing chiral Schiff base Ni(II), Cu(II), and Zn(II) complexes involving azobenzene moiety have been prepared and investigated (supra)molecular orientation induced by linearly polarized UV light irradiation (optical dichroism, namely Weigert effect) with polarized electronic and IR spectroscopy or induced by circularly polarized UV light irradiation (supramolecular chirality) with CD spectra [1-3]. However, in oriented samples, artifact CD peaks prevents from obtaining proper data generally. So we have employed wavelength selective UV light generated by UVSOR BL-1U beamline. At the first term, circularly polarized UV light induced chiral supramolecular orientation was observed with difference CD spectra (before and after UV irradiation), while at the second term, that linearly polarized UV light induced changes resulted in little changes of CD spectra was confirmed as control experiments.

New diastereomers of (achiral or chiral) Schiff base Ni(II), Cu(II), and Zn(II) complexes with or without azobenzene moiety in ligands were prepared as PMMA cast films (namely total 6 types of organic/inorganic photofunctional hybrid materials). These samples were irradiated linearly or circularly polarized UV light at UVSOR BL-1U and compared CD spectra before and after UV light irradiation to confirm molecular orientation inside of the hybrid materials.

Circularly polarized UV light at 260, 318, and 380 nm was irradiated for (0), 3, 5, and 8 min and differences of CD spectra (considered blank data to remove the effect artifact peaks) indicated increasing CD peaks which suggested that chiral supramolecular orientation was induced. Light at 260 nm was effective for inducing bands at about 300 nm for all complexes (in addition about 400 nm only for Zn(II) complex). Light at 318 and 380 nm was effective for inducing bands at about 300 and 500 nm for all complexes (in addition about 500 nm for Ni(II) and Zn(II) complexes, and about 700 nm for Cu(II) complex).

On the other hand, similar discussion by difference CD spectra before and after linearly polarized UV light irradiation at selective wavelengths suggested that no CD peaks could be observed at long-wavelength region without noise peaks.

Generally in isotropic environment like solutions, proper CD spectra can be obtained for chiral metal

complexes, which was ascribed to molecular chirality. While no CD spectra could be observed for achiral metal complexes. However, it was well known that in anisotropic environment like oriented samples (for example, solid state or well-oriented films) not only proper CD bands but also artifact CD bands could be observed. In difference CD spectra, artifact peaks were cancelled when changes about chirality did not occurred even if there are molecular or supramolecular chirality. In other words, although linearly polarized UV light induced optical anisotropy of metal complexes in hybrid materials, supramolecular chiral ordering was not influenced even for chiral metal complexes.

In conclusion, emerging CD peaks in difference CD spectra is attributed to supramolecular helical orientation induced by circularly polarized UV light irradiation for achiral as well as chiral metal complexes. Additionally, UV light of certain wavelengths can effectively induced molecular orientation.

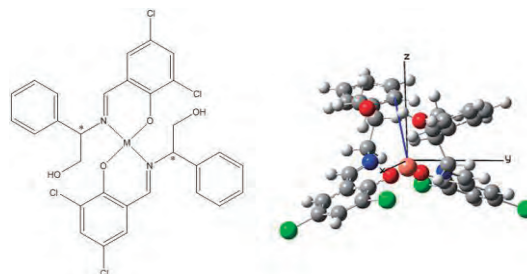


Fig. 1. Chiral Schiff base metal complex without azobenzene moiety [left] and its optimized structure [left].

[1] M. Ito and T. Akitsu, *Contemporary Engineering Sciences* **7** (2014) 869.

[2] N. Hariu, M. Ito and T. Akitsu, *Contemporary Engineering Sciences* **8** (2015) 57.

[3] N. Sunaga, S. Furuya, M. Ito, C. Kominato and T. Akitsu, *Computational Chemistry: Theories, Methods and Applications* (Nova Science Publishers, Inc., NY, USA, 2014) 85.

BL1U

Photoionization Study of Helium Atoms Using Variable Polarization Undulator

T. Kaneyasu¹, Y. Hikosaka², T. Konomi³, M. Katoh³, H. Iwayama³ and E. Shigemasa³¹SAGA Light Source, Tosu 841-0005, Japan²Department of Environmental Science, Niigata University, Niigata 950-2181, Japan³UVSOR Facility, Institute for Molecular Science, Okazaki 444-8585, Japan

The n_{th} harmonic radiation from a helical undulator carries orbital angular momentum (OAM) of $(n-1)\hbar$ per photon [1,2]. This accelerator-based method efficiently generates the OAM photon beam in a wide wavelength range. The APPLE-II undulator U1 in UVSOR storage ring is suitable for generating the OAM photon beam in the EUV region. We are planning to investigate the interaction of the OAM photon with gas-phase atoms in which violation of the dipole selection rules is predicted [3].

For the feasibility study on performing the gas-phase experiment by using the undulator U1, we constructed a test endstation equipped with the photoelectron imaging spectrometer [4] as shown in Fig.1. As a performance test of the experimental setup, we measured the angular distributions of the He 1s photoelectrons using the fundamental radiation with horizontal linear and circular polarization. The peak energy of the undulator radiation was roughly set to 30 eV. The experiments were performed during the machine study using the single-bunch mode. For eliminating the background signals due to secondary electrons emitted from the repeller plate of the imaging spectrometer, we applied the time gate signal to the detector system.

Figure 2 shows the photoelectron images which correspond to the projections of the three-dimensional velocity distributions. The photon propagation direction is along the Y-axis, while the electric vector of the horizontally polarized radiation is parallel to the X-axis. The images present broad structures corresponding to the photoelectrons having 5 eV kinetic energy. The broadness of the photoelectron structures is mainly due to the bandwidth (~ 2 eV fwhm) of the undulator radiation.

Figure 3 shows the photoelectron angular distributions converted from the images in Fig. 2. using the peeling-analysis. The measured angular distributions are in reasonable agreement with those calculated for the dipole asymmetry parameter $\beta=2$. This result confirms the usefulness of the present method for measuring the photoelectron angular distributions. We note that small deviations from the $\beta=2$ patterns are probably due to image distortions resulting from the stray magnetic field and imperfection in the background subtraction. For the experiment on the OAM photoionization, we are preparing a magnetic shield and a modified repeller plate for the imaging spectrometer, both of which are essential for improving the image quality.

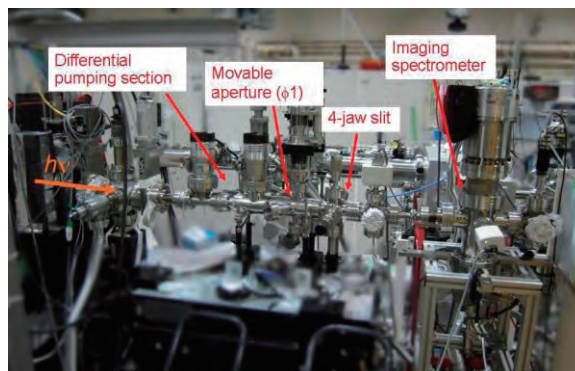


Fig. 1. Photo of the experimental setup constructed at BL1U.

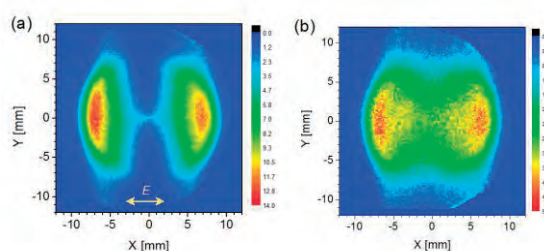


Fig. 2. He 1s photoelectron images measured for (a) horizontal linear and (b) circular polarization.

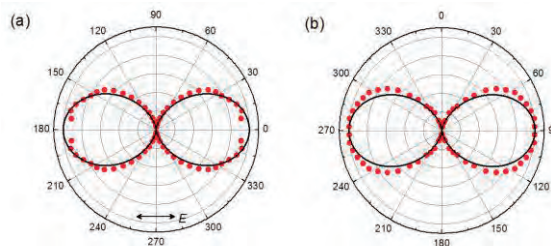


Fig. 3. He 1s photoelectron angular distributions measured for (a) horizontal linear and (b) circular polarization. Circles: experimental data, Solid curves: calculation for $\beta=2$.

[1] S. Sasaki and I. McNulty, Phys. Rev. Lett. **100** (2008) 124801.

[2] J. Bahrtdt *et al.*, Phys. Rev. Lett. **111** (2013) 034801.

[3] A. Picón *et al.*, New J. Phys. **12** (2010) 083053.

[4] Y. Hikosaka and E. Shigemasa, J. Electron Spectrosc. Relat. Phenom. **148** (2005) 5.

BL3U

In Situ Soft X-Ray Absorption Spectroscopy Applied to Solid-Liquid Heterogeneous Cyanopyrazine Hydration on Titanium Oxide Catalyst

H. Yuzawa, M. Nagasaka and N. Kosugi

Institute for Molecular Science, Okazaki 444-8585, Japan

In situ observation of liquid substrate conversion process in solid-liquid heterogeneous catalytic reaction is difficult because the bulk liquids (substrate and/or solvent) hinder the objective spectral change [1]. This type of spectroscopy has been often carried out by using ATR-IR and NMR, but these methods still have some problems of the sensitivity and the overlap of the target spectral signals.

We have developed a transmission-type in situ liquid flow cell, which is able to optimize easily the liquid layer thickness for the soft X-ray XAS [2] and demonstrated that this spectroscopic method is effective to clarify the local structure of various liquid solutions [3]. Thus, in the present study, we have applied this method to time and temperature dependent in situ XAS measurements of solid-liquid heterogeneous cyanopyrazine hydration to produce pyrazinamide (PzCN + H₂O → PzCONH₂) on TiO₂ catalyst [4].

The experiments were carried out in BL3U. Suspension of catalyst was prepared by mixing of PzCN (3 ml, 0.78 M), EtOH (5 ml), H₂O (35 ml) and TiO₂ (0.15 g). The suspension of thin layer (< 1 μm thickness) was sandwiched between two 100 nm-thick Si₃N₄ membranes for C K-edge XAS (SiC membranes for N K-edge XAS). Then, the measurement was carried out under various reaction temperatures from 323.2 to 344.5 K.

Figure 1a shows the C K-edge XAS spectra of PzCN and PzCONH₂ at 298K, and the hydration of cyanopyrazine at 335 K. Three absorption peaks (285.4, 286.0 and 286.6 eV) are observed in PzCN (red line) and one absorption peak (285.3 eV) in PzCONH₂ (blue line) are observed. All these peaks are assigned to the C1s → π* excitation. In the spectra of PzCN hydration (green lines), the intensity ratio of the absorption peaks varies with the reaction time, corresponding to the production of PzCONH₂. Figure 1b shows a logarithmic plot for the normalized XAS intensity of PzCN, which is obtained from the fitting analysis of Fig. 1a (green lines) by using the standard spectra of PzCN and PzCONH₂. This plot shows linear relationship to the reaction time, indicating that the observed catalytic reaction is the first-order reaction for the concentration of PzCN and the slope of the line is a reaction rate constant. The same results are obtained from C K-edge XAS at other temperatures and N K-edge XAS. Furthermore, the obtained rate constants show linear relationship in the Arrhenius plot (E_a = 80 kJ/mol). Thus, it is confirmed that this analytical procedure is reasonable.

We have compared this method with FT-IR spectroscopy, which is typically used for the in situ observation of catalytic reaction. FT-IR cannot detect the characteristic peaks of PzCN (Fig. 2, purple line) in the PzCN solution used for the catalytic reaction (red line) because of the hindrance by the absorption of H₂O and EtOH. Therefore, in situ soft X-ray XAS has a merit to detect minor liquid components in the catalytic reaction.

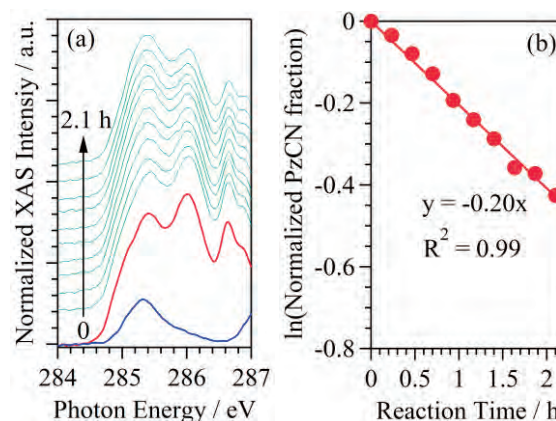


Fig. 1. (a) C K-edge XAS spectra for the PzCN (0.78 M) (red line) and PzCONH₂ (0.20 M) suspensions (blue line) at 298 K and catalytic hydration of PzCN on TiO₂ (green lines) at 335 K. (b) A logarithmic plot of the normalized XAS intensity of PzCN obtained from the fitting analysis of green lines in (a).

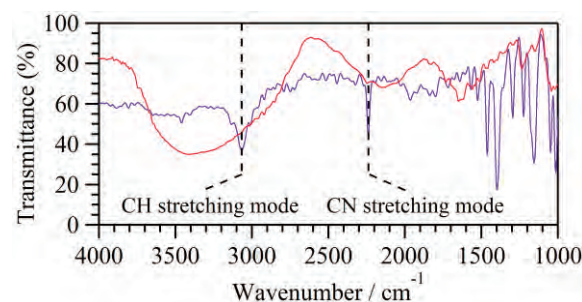


Fig. 2. FT-IR spectra in transmission mode of pure PzCN (purple line) and 0.78 M PzCN solution (red line) used in the catalytic hydration. They were measured by using the same liquid cell as in the XAS.

- [1] F. Zaera, *Chem. Rev.* **112** (2012) 2920.
- [2] M. Nagasaka *et al.*, *J. Electron Spectrosc. Relat. Phenom.* **177** (2010) 130.
- [3] M. Nagasaka *et al.*, *J. Phys. Chem. B* **118** (2014) 4388.
- [4] H. Yuzawa *et al.*, *J. Phys. Chem. C*, accepted.

BL3U

Electronic Structure of Interfacial Water on Nanodiamonds in Colloidal Dispersions

T. Petit¹, H. Yuzawa², M. Nagasaka², R. Yamanoi³, E. Osawa³, N. Kosugi² and E. F. Aziz^{1,2,4}

¹*Institute of Methods for Materials Development, Helmholtz-Zentrum Berlin, Albert-Einstein-Str. 15, 12489 Berlin, Germany*

²*Institute for Molecular Science, Myodaiji, Okazaki 444-8585, Japan*

³*NanoCarbon Research Institute, AREC, Shinshu University, Ueda 386-8567, Japan*

⁴*Freie Universität Berlin, FB Physik, Arnimallee 14, 14195 Berlin, Germany*

The organization of water molecules close to solid surfaces or around proteins differs significantly from pure water [1]. Reorganization of solvent molecules is likely to occur around colloidal nanoparticles and its understanding is of outermost importance to better estimate their reactivity and interaction with biological moieties in aqueous environment. Nevertheless, the structure of solvent molecules around nanomaterials in colloidal dispersion remains largely unexplored. Nanodiamonds (NDs) are of particular interest for the investigation of interfacial water since the existence of an ordered water shell ranging from 2 to 4 water layers was recently suggested.

The experiments were performed at BL3U in UVSOR-III. Aqueous dispersions of NDs with different sizes (ranging from 3 to 18 nm) and surface chemistries were characterized by X-ray absorption spectroscopy (XAS) in pure transmission using a flow cell described elsewhere [2]. By comparing these XA spectra at oxygen K edge to pure water spectra, the organization of water molecules in hydration layers of NDs could be investigated.

Orientation of water molecules in the first solvation shell is found to depend on the Zeta potential of NDs as seen by changes in the pre-edge feature of O K edge XA spectra. In particular, more hydrogen bonds are broken at the surface of negatively-charged NDs due to electrostatic interaction with carboxylate groups while water molecules donating two hydrogen bonds are dominant on positively-charged NDs.

Furthermore a long range order, having an electronic signature close to high density amorphous ice, was evidenced. As seen on Fig. 1, the X-ray absorption increases dramatically at high NDs concentration. This increase is significant compared to aqueous ionic solution. The electronic structure of water is extremely different from bulk water due to the strong contribution from interfacial water layers around NDs. Unlike ions, NDs are too large to be engulfed in a hydration cage which would break a limited amount of hydrogen bonds [3]. At the same time, they are small enough to offer a large interface and the surface polarization orients water molecules around them. It has to be noted that dispersions of detonation NDs at concentration around 8-10 wt% forms highly viscous gel, which may be a

consequence of the long range ordering of water molecules around NDs.

We could evidence that the electronic structure of interfacial water layers on NDs is very uncommon. The long range ordering of water molecules on their surface may explain the high affinity of NDs for proteins adsorption or participate to their low toxicity. These results have recently been submitted for publication.

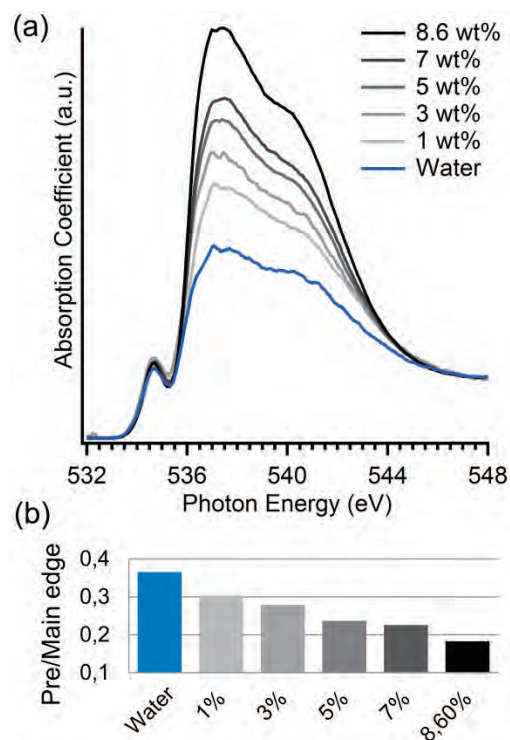


Fig. 1. (a) XAS of oxygen K-edge from water and aqueous dispersion of NDs at different concentrations ranging from 1 to 8.6 wt%. (b) Pre/Main-edge ratios for the different concentrations.

[1] J.-J. Velasco-Velez *et al.*, *Science* **346** (2014) 831.

[2] M. Nagasaka *et al.*, *J. Phys. Chem. C* **117** (2013) 16343.

[3] D. Chandler, *Nature* **437** (2005) 640.

BL3U

Fluorination-Dependent Molecular Orbital Occupancy in Perfluorocarbons

T. Brandenburg^{1,2}, T. Petit¹, A. Neubauer¹, K. Atak^{1,2}, M. Nagasaka³, R. Golnak^{1,2},
N. Kosugi³ and E. F. Aziz^{1,2,3}

¹ Institute of Methods for Material Development, Helmholtz-Zentrum Berlin für Materialien und Energie,
Albert-Einstein-Straße 15, 12489 Berlin, Germany

² Department of Physics, Freie Universität Berlin, Arnimallee 14, 14195 Berlin, Germany

³ Institute for Molecular Science, Okazaki 444-8585, Japan

The family of perfluorocarbons has a wide range of applications in biomedicine and physical chemistry due to their extraordinary properties. Many liquid perfluorocarbons are known to show high density, high viscosity as well as an especially high gas solubility, and are often chemically and biological inert. Their ability to dissolve gases and their biological inertness are exploited in the main applications, such as tissue oxygenation or post-operative treatment.

The perfluoro effect, inherent to all perfluorocarbons, describes the energetic shifts of the spectral features upon complete fluorination of hydrocarbons. This also led to a general rule for the dimensions of the energetic shifts depending on σ - or π -character of the molecular orbitals (MO). Hence, this effect can be used for experimental orbital classification. In this context, a few experimental studies have already been performed in the 1970s. Many of them were based on photoelectron spectroscopy. Since then, more complex theoretical models and the introduction of new experimental techniques give opportunities to investigate perfluorocarbons.

Through the measurements performed at the beamline BL3U in UVSOR-III we could obtain X-ray absorption (XA) spectra of several perfluorocarbons with sufficient signal intensity and without experimental saturation effects. These spectra are complemented by resonant inelastic X-ray scattering (RIXS) spectra obtained at the LiXedrom endstation in BESSY II (Germany) [1, 2].

We could present fundamental insight into the energetic shift induced by fluorination, the so-called perfluoro effect, and a comprehensive picture of the electronic structure of decalin as the parent hydrocarbon molecule for perfluorodecalin based on the XA, X-ray emission (XE) and RIXS spectroscopic data [3]. In addition DFT calculations for decalin, perfluorodecalin and stepwise fluorinated decalin derivatives were performed. We observed a change in occupancy of MOs occurring for the fluorinated hydrocarbons when reaching complete fluorination in PFD.

This MO alteration may be one of the main reasons for the chemical and biological inertness of the ring-shaped perfluorodecalin compared to decalin and the corresponding partially fluorinated hydrocarbons. Interestingly, the discovered orbital change in the XA

spectra could also be observed in the XE spectra in a complementary way. To the best of our knowledge, the observability of the perfluoro effect via XE spectra was confirmed for the first time, and the orbital change originating from unoccupied decalin to occupied PFD MOs was also discussed in relation to the well-known high electronegativity of fluorine atoms. Hence, the validity of this concept and its extension to linear and also larger perfluoro systems is of particular interest for a better understanding of the special properties of perfluoro compounds and their application development.

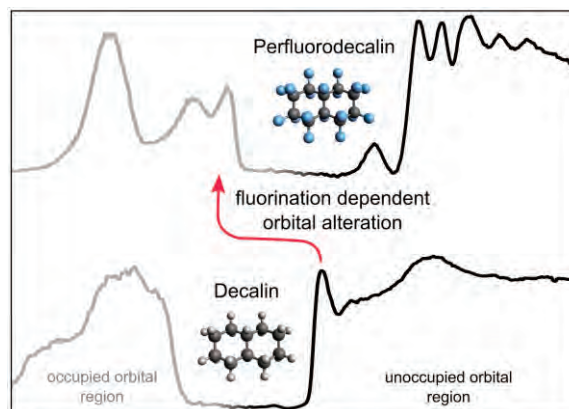


Fig. 1. Sketch of the acquired data with an indication of the discovered orbital alteration.

[1] K. M. Lange *et al.*, Phys. Rev. B **85** (2012) 155104.

[2] C. Jung *et al.*, Nucl. Instrum. Methods Phys. Res. Sect. Accel. Spectrometers Detect. Assoc. Equip. **467-468** (2001) 485.

[3] T. Brandenburg *et al.*, under review.

BL3U

Local Structures of Liquid Benzene Studied by Temperature-Dependent C K-Edge Soft X-Ray Absorption Spectroscopy

M. Nagasaka¹, H. Yuzawa¹, K. Mochizuki^{1,2}, E. Rühl³ and N. Kosugi¹

¹Institute for Molecular Science, Myodaiji, Okazaki 444-8585, Japan

²Department of Chemistry, Okayama University, Okayama 700-8530, Japan

³Physikalische Chemie, Freie Universität Berlin, Takustr. 3, D-14195 Berlin, Germany

Benzene is liquid at room temperature. We reported C K-edge X-ray absorption spectroscopy (XAS) of benzene clusters formed by supersonic gas expansion method, and investigated molecular interaction from the energy shift of C 1s \rightarrow π^* peak of benzene clusters from benzene gas [1]. We also investigated the energy shift of C K-edge XAS of solid benzene, which was grown in multilayers on Ru(0001) crystal surface under vacuum condition revealing the gas-to-solid shift in the C 1s-regime [2]. However, the molecular interaction in liquid benzene has not yet been investigated. In the present study, we have measured C K-edge XAS of liquid benzene at different temperatures, and studied the temperature effect of the molecular interaction.

The experiments were performed at BL3U in UVSOR-III. XAS spectra of liquid samples were measured by a transmitted-type liquid flow cell [3]. The liquid layer was sandwiched between two 100 nm-thick Si₃N₄ membranes. The thickness of the liquid layer is controllable between 20 nm and 2000 nm by adjusting the He pressure.

Figure 1 shows C K-edge XAS of gaseous and liquid benzene at different temperatures. The C 1s \rightarrow π^* peak shows adiabatic (0, 0) transition and vibrational fine structures at higher photon energy. Figure 2 shows the energy shifts of (0, 0) transition peaks of liquid benzene from gaseous benzene as a function of temperature. The π^* peak shows a shift to lower photon energy by increasing the temperature of the sample. The energy shift of liquid benzene relative to the gas phase is 29.4 meV at 25.3 °C. This shift is smaller than in solid benzene and clusters, which is 55 meV [2] and 70 meV [1], respectively.

The energy shift of the π^* peak is caused by the balance between the red-shift effect by induced polarization with surrounding molecules and the blue-shift effect by exchange interaction between the unoccupied π^* orbital with surrounding molecules [4]. Exchange interaction is effective in the short range, so that the peak is shifted in condensed benzene to lower photon energy when the molecular distance becomes longer. This is consistent with the fact that benzene molecules are increasingly separated from each other in the liquid as the temperature is raised. Furthermore, the radial distribution function between benzene molecules changes as a function of temperature as evidenced by molecular dynamics simulations. We have also investigated the

interactions between benzene molecules by exciting the C-H out-of-plane and C-H stretching vibration mode by infrared spectroscopy. In the future, we will discuss the molecular interaction in liquid benzene by correlating C K-edge XAS results with infrared spectroscopy and molecular dynamics simulations.

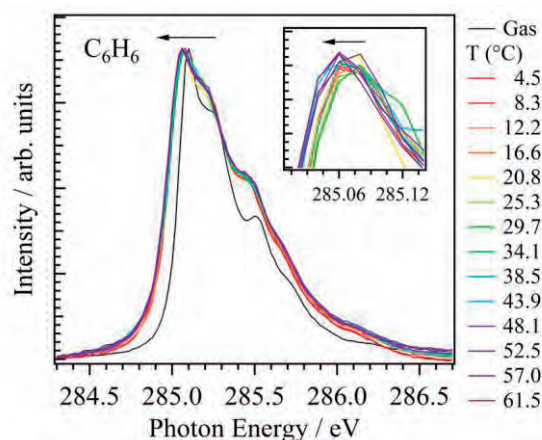


Fig. 1. C K-edge XAS of gaseous and liquid benzene at different temperatures. The inset shows the maximum of the C 1s \rightarrow π^* transition in greater detail.

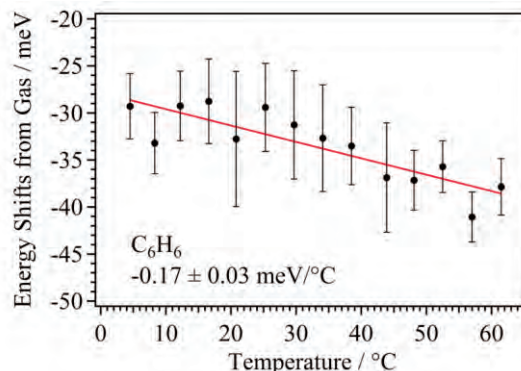


Fig. 2. Energy shifts of C 1s \rightarrow π^* (0, 0) transition peak of liquid benzene relative to gaseous benzene as a function of temperature.

[1] I. L. Bradeanu *et al.*, Phys. Chem. Chem. Phys. **8** (2006) 1906.

[2] R. Flesch *et al.*, Phys. Chem. Chem. Phys. **14** (2012) 9397.

[3] M. Nagasaka *et al.*, J. Electron Spectrosc. Relat. Phenom. **177** (2010) 130.

[4] M. Nagasaka *et al.*, J. Electron Spectrosc. Relat. Phenom. **183** (2011) 29.

BL3U

Optimization of the Sample Position of the Liquid Thin Layer for Soft X-Ray Absorption Spectroscopy

M. Nagasaka, H. Yuzawa, T. Horigome and N. Kosugi
Institute for Molecular Science, Okazaki 444-8585, Japan

In order to measure X-ray absorption spectroscopy (XAS) of liquid samples in transmission mode, it is necessary to control the liquid thickness. Recently, we have developed a transmitted-type liquid flow cell to measure XAS of liquid samples [1]. The liquid layer is sandwiched between two Si_3N_4 membranes, and the thickness is controllable from 20 nm to 2000 nm by adjusting helium pressures outside the membranes. However, in this system, it is not able to control the sample position and it is difficult to confirm the flatness, or uniform thickness, of the thin liquid layer. In the present study, we have developed an XAS measurement system to sweep the position of the liquid layer, and have measured O K-edge XAS of liquid water at different positions to find a flat area of the sample.

The experiments were performed at BL3U in UVSOR-III. The system consists of ultrahigh vacuum and atmospheric helium conditions, which are separated by Si_3N_4 membranes ($0.2 \times 0.2 \text{ mm}^2$). The liquid cell that is sandwiched between two Si_3N_4 membranes ($2 \times 2 \text{ mm}^2$) is in atmospheric condition, and is swept to different positions. XAS in transmission mode is measured by a photodiode detector set behind the liquid cell. This system also equips a silicon drift detector to measure XAS in fluorescence mode.

Figure 1 shows O K-edge XAS of liquid water at different sample positions. The inset of Fig. 2 shows the images of X-ray transmission at 550 eV. O K-edge XAS were measured by scanning the sample positions shown in the arrow. O K-edge XAS shows three features: The pre-edge at 535 eV, main-edge at 537 eV, and post-edge at 540 eV. The ratio of pre- and main-edge is important to evaluate O K-edge XAS of liquid water in transmission mode, and is proposed to be 0.38 [2]. Figure 2 shows the ratio of pre- and main-edge at different positions estimated by the O K-edge XAS shown in Fig. 1. The liquid thickness at different positions are also shown, which is estimated from the edge-jump and the absorption coefficient of liquid water. From 100 μm to 250 μm , the liquid thickness is nearly constant. The ratio of pre- and main-edge becomes 0.36-0.38 in this region. On the other hand, the liquid thickness is rapidly increased above 300 μm . The ratio of pre- and main-edge is also increased in this region. Because the beam size of soft X-rays is $200 \times 200 \mu\text{m}^2$, XAS in this region includes different thickness of liquid layers. The previous study suggests that the ratio of pre- and main-edge is increased at the mixtures of different

thickness of the liquid layers [2].

In summary, we have developed the XAS measurement system that adjusts the liquid thickness by controlling not only the helium pressure to optimize the absorbance but also the sample position to find a flat area of the sample thickness.

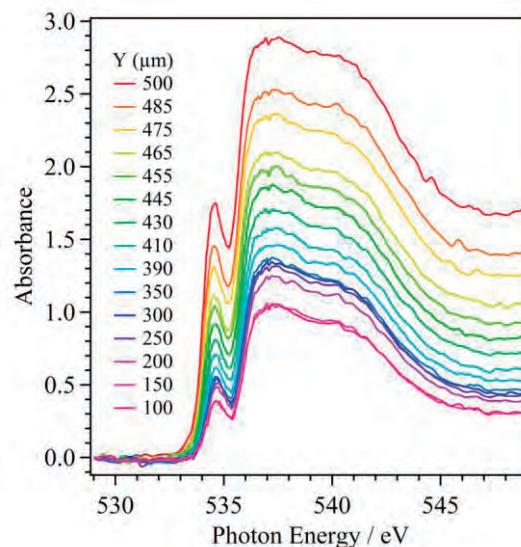


Fig. 1. O K-edge XAS spectra of liquid water at different sample positions (Y).

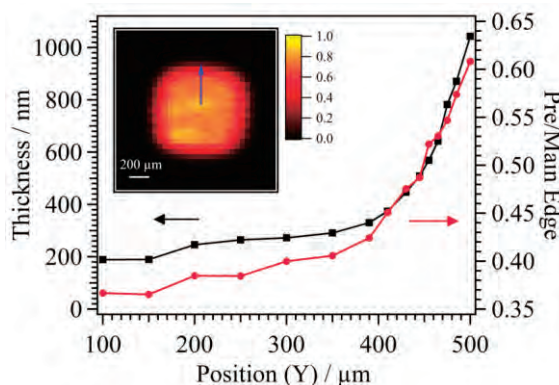


Fig. 2. Ratio of pre- and main-edge and the liquid thickness at different sample positions (Y) estimated from XAS shown in Fig. 1. The inset shows the images of X-ray transmission at 550 eV. The arrow indicates the sample position to measure XAS.

[1] M. Nagasaka *et al.*, *J. Electron Spectrosc. Relat. Phenom.* **177** (2010) 130.

[2] S. Schreck *et al.*, *Rev. Sci. Instrum.* **82** (2011) 103101.

BL3U

Detection of Intra- and Inter-Molecular Charge Transfer in Solution by N K-Edge X-Ray Absorption Spectroscopy

R. Golnak^{1,2}, J. Xiao¹, M. Tesch¹, M. Yablonskikh¹, M. Nagasaka³, T. Brandenburg^{1,4}, N. Kosugi³ and E. F. Aziz^{1,2,3}

¹*Institute of Methods for Material Development, Helmholtz-Zentrum Berlin für Materialien und Energie, Albert-Einstein-Straße 15, 12489 Berlin, Germany*

²*Department of Chemistry, Freie Universität Berlin, Takustraße 3, 14195 Berlin, Germany*

³*Institute for Molecular Science, Myodaiji, Okazaki 444-8585, Japan*

⁴*Department of Physics, Freie Universität Berlin, Arnimallee 14, 14195 Berlin, Germany*

Biological functions and chemical reactions mostly happen in solution. To understand these processes it is of paramount interest to know the electronic structure of liquids and solutions. Core level spectroscopy provides a probe to the electronic structure. In this work we investigated some derivatives of the Urea molecule (Fig. 1(A)) in water and in dimethyl sulfoxide (DMSO).

Through the measurements performed at the beamline BL3U at UVSOR-III we could obtain X-ray absorption (XA) spectra of the derivatives with sufficient signal intensity and without experimental saturation effects. These spectra are complemented by resonant inelastic X-ray scattering (RIXS) spectra obtained at the LiXEdrom endstation at BESSY II (Germany) [1, 2]. Partial fluorescence yield (PFY) measurements were also done at BESSY II to compare transmission mode absorption spectra obtained at UVSOR-III.

What we observed is that the different intra-molecular charge transfer, caused by different molecular dipole moments in these three species, leads to the energy shift of the N π^* orbital below the ionization potential (IP) (Fig. 1(A)), while the different inter-molecular charge transfer, caused by different surrounding solvent dipoles, results in an energy shift of the N σ^* orbital above the IP (Fig. 1 (B)). Occupied states are normally more localized in nature than the unoccupied states, and thus less influenced by the charge transfer effect, as shown in Fig. 2 that exhibits no energy shift between Urea and Thiourea for the occupied states. N K-edge XAS is sensitive to the molecular charge transfer, and therefore can be used as a good indicator detecting even minor changes of the chemical environment around the specific site of interest.

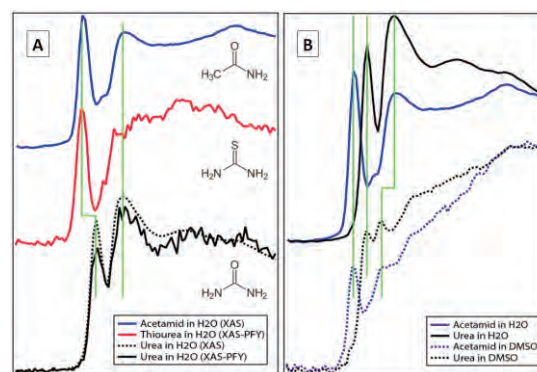


Fig. 1. (A) N π^* orbital below IP, indicated by the left green line, has an energy shift, while N σ^* above the IP, marked by the right green line, share the same energy. (B) Different solvents do not shift the N π^* orbital, but the σ^* instead, suggesting that the solvent only affects the orbital above the IP.

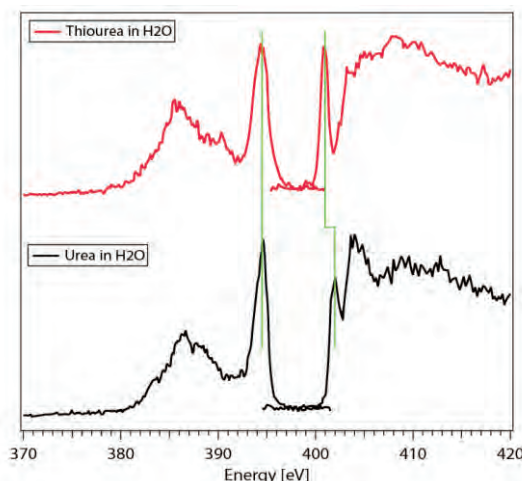


Fig. 2. Occupied states of Urea and Thiourea in water have almost identical energy positions, while the unoccupied states have an energy shift, as already discussed in Fig. 1 (A), resulting in an local energy gap opening for Urea, when compared with Thiourea.

[1] K. M. Lange *et al.*, Phys. Rev. B **85** (2012) 155104.

[2] C. Jung *et al.*, Nucl. Instrum. Methods Phys. Res. Sect. Accel. Spectrometers Detect. Assoc. Equip. **467-468** (2001) 485.

BL4U

Electrochemical Studies at BL4U STXM

S. M. Rosendahl^{1,2}, A. P. Hitchcock¹, M. Nagasaka³, Y. F. Wang³,
T. Horigome³, T. Ohigashi³ and N. Kosugi³

¹Chemistry & Chemical Biology, McMaster University, Hamilton, L8S4M1, Canada

²Canadian Light Source, Saskatoon, SK S7N 5C9, Canada

³Institute for Molecular Science, Okazaki 444-8585, Japan

UVSOR BL4U STXM provides chemical imaging with ~30 nm spatial resolution using 200-750 eV X-rays. This project uses STXM to investigate electrochemical systems, either prepared *ex situ* in defined electrochemical states, or with *in situ* modification of the electrochemical state of the system. Several generations of a device for *in situ* flow electrochemistry have been developed at UVSOR and in Canada. Here we report on progress in 2014, with data from two systems: (i) *in situ* solution oxidation of FeSO₄ (aq), and (ii) conversion of polyaniline (s) between emeraldine, the oxidized quinoid form and leucoemeraldine, the reduced aromatic form. Figure 1 is a photo of the latest version of the *in situ* UVSOR flow cell. Reproducible *in situ* flow in STXM has been achieved with this device but, for various reasons, an *in situ* data set has not yet been achieved.

In situ cyclic voltammetry and Fe 2p spectroscopy of FeSO₄ solutions have been carried out at BL3U using an electrochemical cell [1,2]. We have developed the Norcada/McMaster *in situ* cell from the concept of this cell [3]. This system was examined by STXM at the Fe 2p edge with *in situ* change of the electrochemical state. Figure 2a presents Fe 2p_{3/2} spectra of the reduced and oxidized Fe ions extracted from an image stack and set on an absolute intensity scale (OD per nm). The Fe 2p_{3/2} stack was fit to these spectra and a constant (water and Au electrodes), resulting in quantitative component maps which are presented as a color coded composite in Fig.2b. Surprisingly, the distribution of oxidation states was opposite that expected since the WE was positive relative to the CE when the stack was measured. It is also surprising that the solution has a redox gradient across it - one would expect diffusion to remove this. This, and the lack of blue tinge in the inter-electrode region, indicate there was very little water such that the solution phase is a gel.

Due to deterioration of the Au/Cr electrodes in Fe(II) solutions, the system used to further develop electrochemical STXM was changed to polyaniline (PANI), which has been studied with *in situ* STXM earlier [4]. However the 1 M HCl used as electrolyte damaged the stainless steel flow lines used in the UVSOR *in situ* flow cell (Fig. 1). We were only able to measure a dry sample, prepared *ex situ* at McMaster on an early 2-electrode chip ('PANI in a drop'). PANI was electrodeposited on the left electrode and left in the as-prepared oxidized state. PANI electrodeposited on the right electrode was

electrochemically reduced after deposition. Figure 3a presents C 1s spectra of the oxidized and reduced states extracted from selected regions of the dry, *ex situ* sample, nice examples of the C 1s performance of the BL4U STXM. The spectra were used to fit C 1s stacks of the PANI deposits on each electrode; color coded composites are presented in Fig.3b & 3c. The left electrode has only oxidized PANI, while the right electrode has a combination of reduced and oxidized PANI. The oxidized PANI is probably from PANI that was not electrically linked to the electrode.

Progress is steadily being made toward *in situ* flow electrochemical STXM at BL4U



Fig. 1. photograph of the UVSOR *in situ* flow cell.

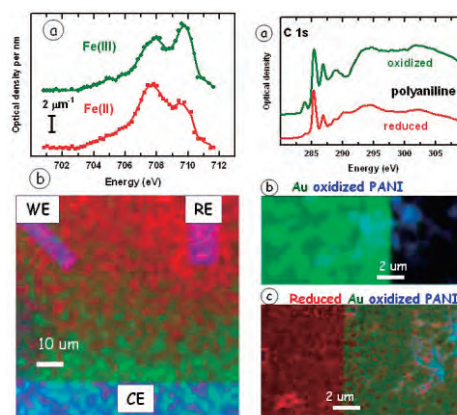


Fig. 2. (a) Fe(II) and Fe(III) spectra from stack of static cell with 0.1 M FeSO₄ (aq). (b) color coded composite of maps of Fe(II) (red), Fe(III) (green) and constant (blue) - electrodes.

Fig. 3. (a) C 1s spectra of *ex situ* deposited polyaniline, in the reduced and oxidized states. Color coded composites of (b) left, and (c) right electrodes which were converted electro-chemically to oxidized and reduced states in Canada.

[1] M. Nagasaka *et al.*, J. Phys. Chem. C **117** (2013) 16343.

[2] M. Nagasaka, Rev. Sci. Instrum. **85** (2014) 104105.

[3] A. P. Hitchcock *et al.*, J. Phys. Conf. Ser. (2015) in press.

[4] D. Guay *et al.*, Anal. Chem. **77** (2005) 3479.

BL4B

Stability of Molecular Dications Studied by an Electron-Electron-Ion Coincidence Method

K. Nakamura¹, R. Mashiko¹, K. Soejima¹, E. Shigemasa² and Y. Hikosaka¹

¹Department of Environmental Science, Niigata University, Niigata 950-2181 Japan

²UVSOR Facility, Institute for Molecular Science, Okazaki 444-8585 Japan

Inner-shell ionization of a molecule and subsequent Auger decay usually produce the doubly-charged molecular ion. The dication is inherently unstable against the ion-pair dissociation, but it is known that, while the lifetime is of course state-dependent, some low-lying dication states can be metastable in micro second time scale or longer.

In this work, we have performed an electron-electron-ion coincidence study of the OCS dication states. We have employed a magnetic-bottle electron spectrometer adapted to ion detection. The description is elsewhere [1]; here only brief accounts are given. The spectrometer equipped with a strong permanent magnet and a long solenoid coil, which create an inhomogeneous magnetic field forming a magnetic mirror to collect the electrons from almost the whole 4π solid angle. For coincidence detection of the counterpart ions, a pulsed high voltage was applied to the ionization region, according to an electron detection, and the formed ions were introduced into the same microchannel plate detector for electron detection.

Figure 1 shows a time-of-flight spectrum of electrons and ions produced from OCS at $h\nu=318.6$ eV. While electron structures are exhibited below 4000 ns, the peaks due to molecular ions are observed later than 4000 ns. Figure 2 shows an energy correlation map displaying the correlations between S2p photoelectrons and Auger electrons. The horizontal axis covers an electron energy range in which the S2p photoelectrons appear, and the vertical axis does a range for the Auger electrons. At the photoelectron energies for the formations of the spin-orbit components of $S2p^{-1}$, several structures associated with different OCS^{2+} states are observed. The vertical cuts at the photoelectron energies are plotted with black and blue curves in Fig. 3, where two groups of peaks (0-4 eV and 4-10 eV) are observed. The red and green curves are the coincidence Auger spectra which are obtained by filtering with further coincidence with OCS^{2+} ions. In the coincidence spectra, the peaks in 4-10 eV are presented, but the peaks below 4 eV disappear. This observation implies that, while the states in the 4-10 eV range are metastable, the states in the 0-4 eV range have much shorter lifetimes.

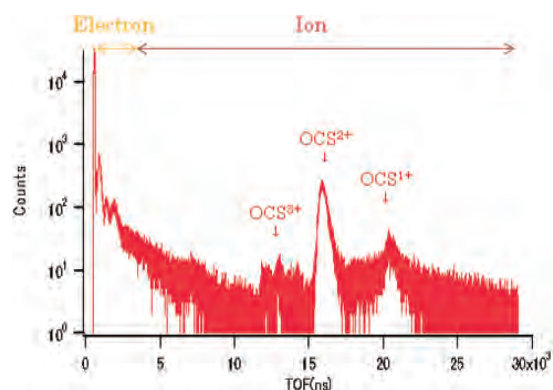


Fig. 1. Time-of-flight spectrum of electrons and ions produced from OCS at $h\nu=318.6$ eV.

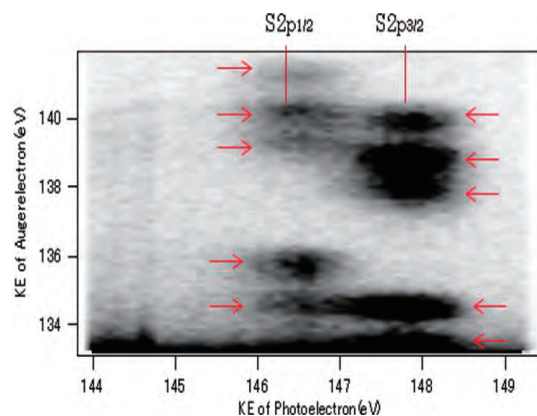


Fig. 2. Correlation map for ion pairs detected in coincidence with C1s photoelectron from CH_3OD .

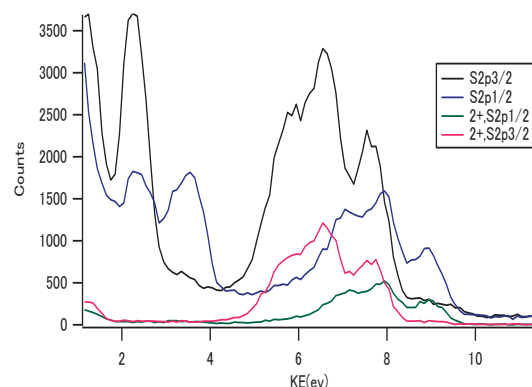


Fig. 3. Coincidence Auger spectra (black and blue) and those with further coincidence with OCS^{2+} ions (red and green).

[1] A. Matsuda, M. Fushitani, C.-M. Tseng, Y. Hikosaka, J. H. D. Eland and A. Hishikawa, *Rev. Sci. Instrum.* **82** (2011) 103105.

BL6U

Dissociation of CH₃OH Dication Studied by an Electron-Ion Coincidence Method

M. Higuchi¹, T. Shiota², K. Hoshina², H. Iwayama³, E. Shigemasa³ and Y. Hikosaka¹

¹Department of Environmental Science, Niigata University, Niigata 950-2181, Japan

²Faculty of Pharmaceutical Sciences, Niigata University of Pharmacy and Applied Life Sciences, Niigata 956-8603, Japan

³UVSOR Facility, Institute for Molecular Science, Okazaki 444-8585, Japan

Molecular absorption of a soft x-ray photon often induces inner-shell photoionization, and the formed core-hole usually relaxes via Auger decay. Because two electrons are emitted through this sequential process, the molecule with two positive charges is produced. This dication is inherently unstable due to the Coulomb repulsion of the two positive charges, and thus most of the dication states dissociate into ion pairs. In this work, we have studied the ion-pair dissociation of the CH₃OH dication states, by an electron-ion coincidence method.

The experiment was performed at the undulator beamline BL6U. We utilized an electron-ion coincidence spectrometer [1,2] composed of a toroidal electron analyzer and ion momentum imaging analyzer. Figure 1 shows time-of-flight spectra of ions produced after the C1s inner-shell ionization of CH₃OH and CH₃OD, observed in coincidence with C1s photoelectrons emitted at $h\nu=292.3$ eV. While the structure around 2340 ns in the CH₃OH spectrum is allocated to the OH⁺ fragments, the CH₃OD spectrum also shows sizable intensity in the same TOF range. In addition, the structure due to the OD⁺ fragments can be observed around 2410 ns in the CH₃OD spectrum. These observations imply that the hydrogen atom in the OH⁺ fragment is not always the one originally placed at the oxygen side in the neutral ground state of CH₃OH, and thus suggests that the molecular structure can be largely deformed in the dissociation pathway producing the OH⁺ fragment.

The correlation map in Fig. 2 presents ion pairs detected in coincidence with C1s photoelectron from CH₃OD. One finds on the map structures corresponding to the ion pairs of OD⁺ + CH₂⁺ and OH⁺ + CDH⁺. While the former ion pair can be produced by a simple CO bond breaking,

the formation of latter needs a hydrogen exchange before the bond breaking.

Figure 3 shows coincidence Auger spectra (red) which are filtered by detections with OD⁺ + CH₂⁺ and OH⁺ + CDH⁺, compared to the normal Auger spectrum (black). The coincidence Auger spectrum associated with OD⁺ + CH₂⁺ (simple CO bond breaking case) shows a peak at 41.3 eV. On the other hand, the peak location is 39.3 eV in the coincidence Auger spectrum associated with OH⁺ + CDH⁺ (hydrogen exchange case). This observation implies that fairly-stable dication state(s) lies around 39.3 eV, where hydrogen exchange precedes the bond

breaking.

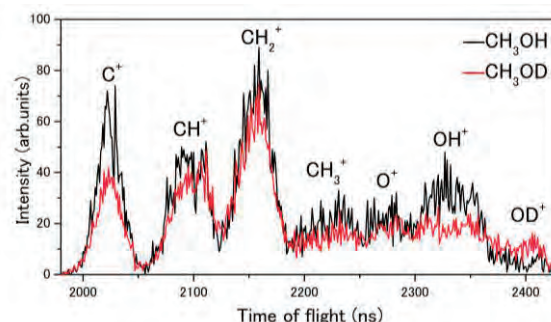


Fig. 1. Time-of-flight spectra of ions produced after the C1s inner-shell ionizations of CH₃OH (black) and CH₃OD (red), observed in coincidence with C1s photoelectrons emitted at $h\nu=292.3$ eV.

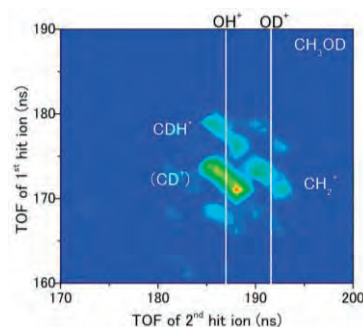


Fig. 2. Correlation map for ion pairs detected in coincidence with C1s photoelectron from CH₃OD.

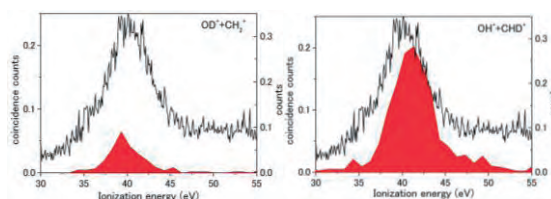


Fig. 3. Coincidence Auger spectra (red) which are filtered by detections with OD⁺ + CH₂⁺ and OH⁺ + CDH⁺, compared to the normal Auger spectrum (black).

[1] T. Kaneyasu, Y. Hikosaka and E. Shigemasa, *J. Electron Spectrosc. Rel. Phenom.* **156-158** (2007) 279.

[2] Y. Hikosaka, Y. Shibata, K. Soejima, H. Iwayama and E. Shigemasa, *Chem. Phys. Lett.* **603** (2014) 46.

BL6U

Spectator Auger Decays of 1,1,1-Trifluoroethane across the F K Threshold

T. Kaneda¹, K. Okada¹, H. Iwayama^{2,3} and E. Shigemasa^{2,3}¹Department of Chemistry, Hiroshima University, Higashi-Hiroshima 739-8526, Japan²UVSOR Facility, Institute for Molecular Science, Okazaki 444-8585, Japan³School of Physical Sciences, The Graduate University for Advanced Studies (SOKENDAI), Okazaki 444-8585, Japan

Inner-shell excitation of gaseous molecules results in a specific dissociation through Auger processes. Recently, we found in the F KVV Auger spectra of *cis*-hexafluorocyclobutane (*cis*- $c\text{-C}_4\text{H}_2\text{F}_6$, HFCB) that spectator decay predominates and that the peaks change almost linearly with photon energy [1]. These shifts are known as “spectator shifts” arising from the core-hole screening of a spectator electron for an outgoing electron. In addition to the spectator shifts, a fluorine atomic Auger peak was observed. This peak implies the presence of ultrafast dissociation (UFD). It takes place during the lifetime of the core-hole state before Auger electron emission. It is rare that the UFD can be observed clearly in relatively large molecules.

In this study, to investigate spectator shifts quantitatively, we measured resonant/normal Auger spectra of 1,1,1-trifluoroethane (CH_3CF_3) across the F K threshold as a function of photon energy with a small energy step and a higher electron energy resolution. Because the CH_3CF_3 molecule has a higher symmetry than that of HFCB, we expect a simple spectrum, making spectator shifts clearer.

The experiments were performed on the soft X-ray beamline BL6U. A main chamber was equipped with a high-resolution hemispherical electron analyzer (MBS-A1). The monochromatized radiation was focused onto a center of a gas cell containing the sample gas and the pressure of the main chamber was kept at 1.0×10^{-3} Pa during the measurements. Electron spectra were recorded in the F 1s region ($h\nu = 682.0\text{--}702.0$ eV) with a photon energy step of 0.5 eV.

Figure 1 shows some of the resonant/normal Auger spectra plotted on the electron kinetic energy scale. The spectra have been obtained by subtracting the contribution from the photoelectron acquired at $h\nu = 683.0$ eV. The spectator shifts can be evaluated using the F 1s ionization threshold of CH_3CF_3 : 694.1 eV [2]. One can see that the electronic relaxation processes are dominated by spectator Auger decay, in contrast with low probability of participator Auger decay. This is the same trend as in the case of HFCB [1]. On the analogy of HF [3], we assign the intense bands around 650, 625 and 605 eV to the transitions to the final state of $\nu_o^{-1}\nu_o^{-1}$, $\nu_o^{-1}\nu_i^{-1}$ and $\nu_i^{-1}\nu_i^{-1}$, respectively. The notation ν_o represents an outervalence orbital such as F 2p, and ν_i is an innervalence. The positions of spectator Auger bands (S1–S3) shift with the photon energy leading to the normal Auger bands (N1–N3).

This is similar to the results of HFCB, but the positions seem to vary in a non-linear manner because each of these spectator peaks is composed of several components. In addition, the shapes of these spectra change dramatically with the excitation energy. We need to find the correct components to evaluate the spectator shifts. The analysis is in progress now.

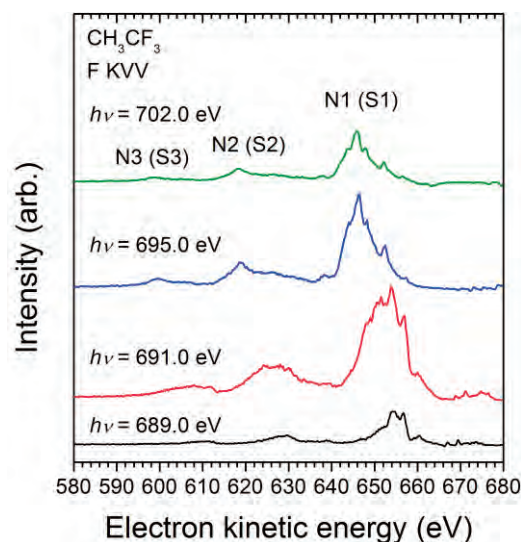


Fig. 1. Resonant and normal Auger spectra of CH_3CF_3 acquired at some photon energies across the F K threshold.

- [1] T. Kaneda, S. Ishikawa, K. Okada, H. Iwayama, L. Ishikawa and E. Shigemasa, UVSOR Activity Report 2013 **41** (2014) 119.
- [2] W. L. Jolly, K. D. Bomben and C. J. Eyermann, At. Data Nucl. Data Tables **31** (1984) 433.
- [3] R. W. Shaw, Jr. and T. D. Thomas, Phys. Rev. A. **11** (1975) 1491.

BL6U

Specific Auger Decay and Photofragmentation of *cis*-Hexafluorocyclobutane

S. Ishikawa¹, K. Okada¹, H. Iwayama^{2,3} and E. Shigemasa^{2,3}¹Department of Chemistry, Hiroshima University, Higashi-Hiroshima 739-8526, Japan²UVSOR Facility, Institute for Molecular Science, Okazaki 444-8585, Japan³School of Physical Sciences, Graduate University for Advanced Studies (SOKENDAI), Okazaki 444-8585, Japan

Inner-shell excited states of molecules relax into various molecular cationic states through Auger decays. The resultant cations are in general unstable and dissociate into fragment ions. In our previous study we observed site-specific fragmentation of the inner-shell excited *cis*-hexafluorocyclobutane (HFCB, *cis*- $c\text{-C}_4\text{H}_2\text{F}_6$) molecule. The yield spectra of the fragment ions with C–F bond(s) have a peak at the σ_{CC}^* resonance, while those of the ions without C–F bonds do not. This infers that the resonant state decays to particular Auger-final states, connecting to specific fragmentation channels. The purpose of this study is to illuminate such Auger processes with the measurements of Auger-electron–photoion coincidence (AEPICO) spectra.

The experiments have been performed on the soft X-ray beamline BL6U. The experimental setup has been described in a previous report [1]. Synchrotron radiation was irradiated at right angles to the effusive beam of the gaseous HFCB sample. The electrons traveling through a double toroidal analyzer tube were detected with a position sensitive detector (RoentDek, DLD40). The pass energy was set to 400 eV in this study. Photofragment ions were extracted toward the time-of-flight spectrometer by a pulsed electric field applied just after the Auger electron detection. The light intensity was monitored downstream on the beamline during the measurements. The coincidence data were acquired at the photon energies of 707.5, 695.0, 688.5, 310.0, 297.0 and 292.8 eV.

The branching fraction of the Auger processes is found to depend on the resonant states. Figure 1a shows some typical resonant Auger spectra plotted on the final-state energy scale. The normal Auger spectrum measured under the same experimental conditions is also given at the top on the double ionization energy scale. Two peaks are found in this energy range. They are assigned to spectator Auger decays [2]. The intensity ratio of the two peaks varies with the photon energy: 0.36 at 707.5 eV, 0.33 at 695.0 eV and 0.41 at 688.5 eV. This indicates that the presence of a spectator electron clearly affects the Auger decays.

A noticeable feature can be seen in the coincidence spectra. Panel b shows the Auger electron yield curves coincident with the $\text{C}_2\text{H}_{0,1}\text{F}^+$ and $\text{C}_2\text{H}_{0,2}^+$ ions, which have been obtained by editing the AEPICO data acquired at 695.0 eV. Auger electrons forming the S2 peak are almost exclusively coincident with

the ions without C–F bonds, except for $\text{CH}_{0,1}\text{F}^+$ (not shown in Fig. 1). This fact represents that the suppression of the S2 peak is responsible for the site-specific fragmentation at the F K-edge: smaller branching fraction to form the S2 peak makes the yield of the ions without C–F bonds lower.

The resonant Auger spectra at the C K-edge are in clear contrast to those at the F edge. The spectrum for the σ_{CC}^* resonance at 297.0 eV has a strong, broad peak at around the final-state energy of 40 eV. Abundant photofragments in coincidence with the corresponding Auger electrons are the ions with C–F bond(s). The processes to show the site specificity are different between at the F edge and at the C edge.

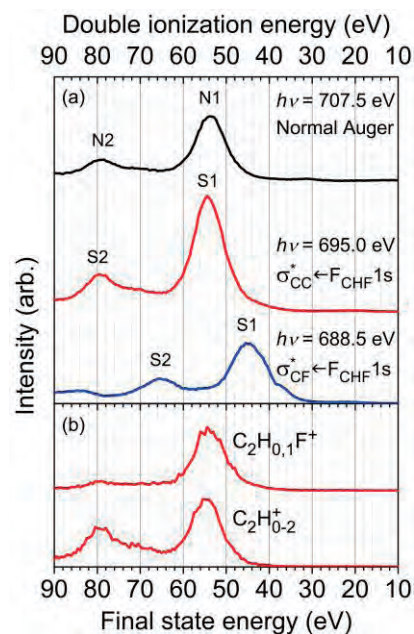


Fig. 1. Resonant and normal Auger spectra of HFCB measured at three excitation energies (a) and the components coincident with $\text{C}_2\text{H}_{0,1}\text{F}^+$ and $\text{C}_2\text{H}_{0,2}^+$ at the photon energy of 695.0 eV (b).

[1] S. Ishikawa, K. Okada, H. Iwayama, L. Ishikawa and E. Shigemasa, UVSOR Activity Report 2012 **40** (2013) 58.

[2] T. Kaneda, S. Ishikawa, K. Okada, H. Iwayama and E. Shigemasa, UVSOR Activity Report 2013 **41** (2014) 119.

BL6U

Ultrafast Dissociation of Core Excited CF_4 Molecules Studied by an Auger-Electron-Ion Coincidence Method

H. Iwayama^{1,2} and E. Shigemasa^{1,2}¹UVSOR Facility, Institute for Molecular Science, Okazaki 444-8585, Japan²School of Physical Sciences, The Graduate University for Advanced Studies (SOKENDAI), Okazaki 444-8585, Japan

Molecular inner-shell excitation into an anti-bonding orbital causes a nuclear motion. In some cases, the nuclear dynamics is so fast that dissociation takes place before Auger electron emission. This process is referred to as ultrafast dissociation and observed in hydrogen halide molecules such as HBr [1] and HCl [2].

Recently, we found a signature of ultrafast dissociation following $\text{C } 1s \rightarrow \sigma^*(t_2)$ core excitation in CF_4 by using two dimensional electron spectroscopy [3]. We observed Auger electrons from both CF_3^* fragment and CF_4^* parent molecule. This means that the Auger decay and dissociation processes take place on the same time scale and significantly compete with each other.

In the present work, we have investigated anisotropic angular distributions of ejected CF_3^+ ions by using an Auger-electron-ion coincidence method. Since the CF bond involved in the $\text{C } 1s \rightarrow \sigma^*(t_2)$ core excitation is immediately broken due to the ultrafast dissociation, anisotropic angular distributions of ejected the CF_3^+ ions are expected.

The Auger-electron-ion coincidence measurements were carried out on the undulator beamline BL6U at UVSOR. The radiation from an undulator was monochromatized by a variable included angle varied line-spacing plane grating monochromator. The electrons ejected at 54.7° with respect to the electric vector of the incident radiation were analyzed in energy by a double toroidal analyzer (DTA), while ions were extracted from the interaction region into a momentum spectrometer by a pulsed electric field according to the electron detection. Arrival position on the detector and time-of-flights of ions were recorded for every event. The pass energy of the DTA was set to 200 eV for observing the Auger electrons. The energy resolution was about 1.9 eV. All signals from the detectors were recorded with an 8ch TDC board. We used the photon energy of 298.5 eV, which corresponds to the $\text{C } 1s \rightarrow \sigma^*(t_2)$ resonance.

Figure 1 shows total and coincidence Auger spectra with CF_3^+ ions. It is seen that the CF_3^+ ions are coincident with electrons at the binding energy of 15–25 eV, where two peaks A and B are detected. For higher binding energies, we observed smaller fragment ions such as CF_2^+ , CF^+ and C^+ (not shown here). From the previous work [3], the peaks A and B are attributable to the Auger electrons from the CF_3^* fragment and CF_4^* parent molecules, respectively.

Figures 2(a) and 2(b) show ion images of CF_3^+ ion fragments, which were taken in coincident with electrons at the peaks A and B, respectively. The angular distribution of CF_3^+ ions is considerably anisotropic in Fig. 2(a), while almost isotropic angular distributions are seen in Fig. 2(b). Two island-like structures along the polarization vector are clearly observed in Fig. 2(a). This means that the core-excited CF_4 molecules lead to immediate CF bond breaking, which is the direct evidence of the ultrafast dissociation for the peak A. The detailed data analyses are now in progress.

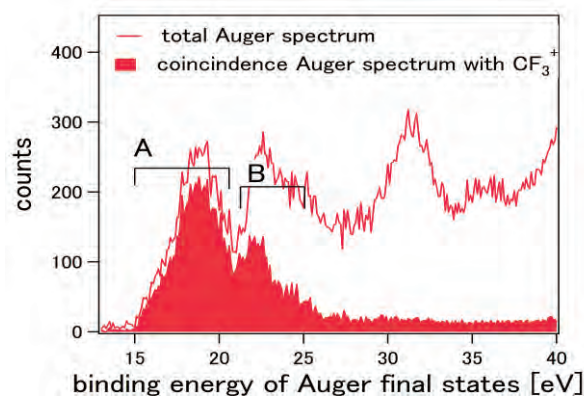


Fig. 1. Total and coincident Auger electron spectrum with CF_3^+ ions.

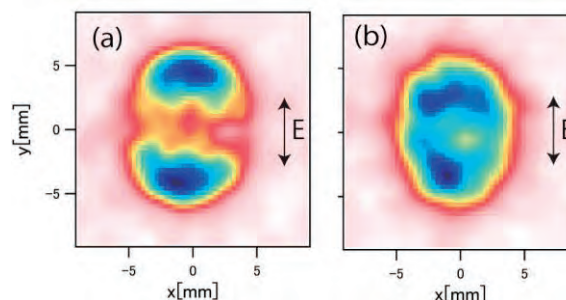


Fig. 2. Ion images of CF_3^+ ions coincident with Auger electrons at (a) peak A and (b) peak B.

[1] M. Morin and I. Nenner *Phys. Rev. Lett.* **56** (1986) 1913.

[2] H. Aksela *et al.*, *Phys. Rev. A* **41** (1990) 600.

[3] M. N. Piancastelli, R. Guillemin, M. Simon, H. Iwayama and E. Shigemasa, *J. Chem. Phys.* **138** (2013) 23430.

III-4

Surface,
Interface and
Thin Films

BL2B

An Optimization Study for Multi-Alkali Photocathode as the Ultimate Electron Source

M. Kuriki¹, Y. Seimiya¹, T. Konomi², M. Katoh² and R. Inagaki³

¹Graduate school of Advanced Science of Matter, Hiroshima University, Higashi-hiroshima, 739-8530, Japan

²UVSOR Facility, Institute for Molecular Science, Okazaki 444-8585, Japan

³Graduate School of Engineering, Nagoya University, Nagoya 464-8603, Japan

Multi-alkali photocathode, CsK₂Sb is the strongest candidate as the ultimate photocathode for high-brightness electron accelerator. Recently, advanced accelerator projects based on the linear accelerator (Linac) have been proposed and some of them, e.g. X-ray FEL, are already in operation. To realize a high brightness beam with Linac, the electron source is one of the key components, because the beam brightness normalized with its energy is kept during the acceleration over Linac. From the view point of electron source, a small emittance and large current beam from a small spot size has to be generated. As the cathode requirements, not only the small emittance, but also high quantum efficiency (QE) and high robustness are required. In addition, if the visible light laser instead of UV laser which is commonly used for metal cathode is applicable, it relaxes the technical requirements for the laser. CsK₂Sb cathode fulfills these requirements; high QE as high as more than 10%, driven by a green laser, and high robustness [1]. CsK₂Sb is then suitable for the high brightness Linac application. On the other hand, CsK₂Sb cathode is made with evaporation in a vacuum chamber as a thin film in order of several 10s nm. The cathode activity is lost by air exposure. The evaporation condition to maximize the cathode performance is not established and material property is not well understood. The aim of our study is to understand the cathode performance from the material science point of view.

We made the multi-alkali evaporation chamber which is capable to form the thin film in an extreme vacuum environment. The thin-film cathode is made on a substrate fixed on a sample holder. The pressure of the chamber was 5.0×10^{-8} Pa.

Figure 1 shows an example of CsK₂Sb evaporation. The horizontal axis shows time in minutes and $t=0$ gives the start of the evaporation. On boron doped p-type Si substrate (100), Sb, K, and Cs were evaporated in this order. The thickness was measured with a quartz monitor. QE was measured with 405 nm laser. It was more than 8%.

Figure 2 shows UPS spectrum for CsK₂Sb. By comparing Sb peaks[2][3], Sb 4d peaks split into 5. The valence band peaks are enhanced. Peak at 18 and 10 eV are consistent with K 3p[4] and Cs 5p[5], respectively, but need more careful investigation for the identification.

As the summary, we successfully took UPS spectra for (multi) alkali cathode evaporated on Si substrate.

To identify the optimized evaporation condition for the thin film cathode, UPS spectra of the cathode evaporated with various different conditions should be taken. UPS spectral change during the cathode degradation should give curious information about the process.

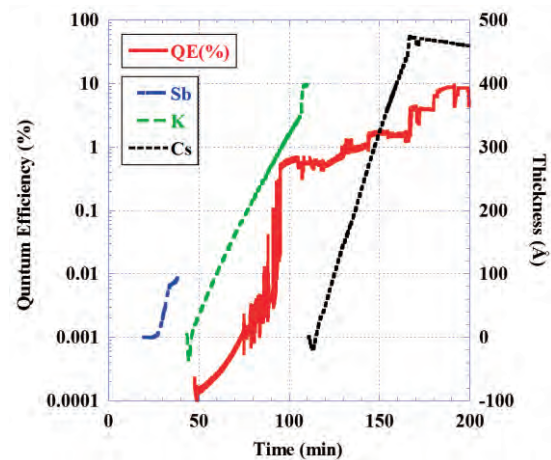


Fig. 1. An example of evaporation of CsK₂Sb. The right and left vertical axes show thickness (Angstrom) and QE (405nm) in %.

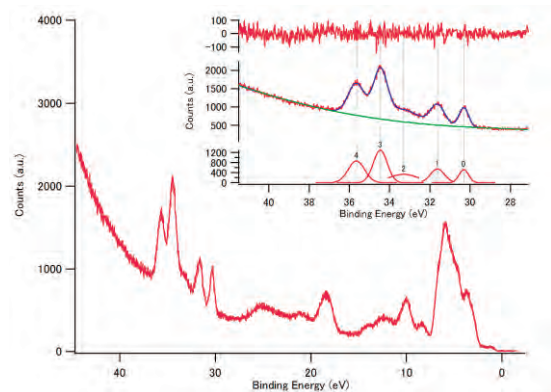


Fig. 2. CsK₂Sb UPS spectrum as a function of binding energy.

- [1] B. Dunham *et al.*, Appl. Phys. Lett. **102** (2013) 034105.
- [2] M. Scrocco *et al.*, J. Electron Spectrosc. Relat. Phenom. **50** (1990) 171.
- [3] G. E. Franklin *et al.*, Phys. Rev. B **45** (1992) 3426.
- [4] H. H. Weitering *et al.*, Phys. Rev. B **48** (1993) 8119.
- [5] A. N. Belsky *et al.*, J. Electron Spectrosc. Relat. Phenom. **80** (1996) 109.

BL2B

Electronic Structure of Chlorophyll-a Investigated by Photoelectron Spectroscopy and Photoelectron Yield Spectroscopy

Y. Takeda¹, H. Ezawa², T. Miyauchi¹, H. Kinjo¹, K. R. Koswattage³,
Y. Nakayama¹ and H. Ishi^{1,3}

¹Advanced Integration Science, Chiba University, Chiba 263-8522, Japan

²Department of Engineering, Chiba University, Chiba 263-8522, Japan

³Center for Frontier Science, Chiba University, Chiba 263-8522, Japan

Observing the electronic structures of bio-molecules in their living environment is indispensable to elucidate their functionalities. Especially understanding how photosystem of plants realizes energy conversion in high efficiency is an important factor for the development of artificial photosynthesis. In photosystem, photon energy is converted to electron energy by photoexcitation reaction of Chlorophyll-a (Chl-a) aggregation. In addition, in actual systems, Chl-a is surrounded by solvent. In water-rich acetone-water binary solvent, Chl-a exists predominantly as oligomer, which have been utilized as artificial model of Chl-a in vivo [1]. For general materials, photoelectron spectroscopy (PES) is a powerful and widely used technique to examine their electronic structures. However, PES needs vacuum environment and its application to bio-related systems has been much limited. In this study, we tried to observe the electronic structure of Chlorophyll-a (Chl-a) with the techniques.

Chl-a powder was bought from Wako Pure Chemical Industries and was used as purchased. Sample of UPS was spin-coated film which was deposited acetone solution of chlorophyll a on ITO. For PYS, Chl-a powder was dissolved in water-rich (83.3 vol%) acetone-water binary solution (0.7 mM), in which almost all Chl-a molecules are known to exist as oligomers, which have been utilized as an artificial in vivo model of RC [1]

Figure 1 a) shows UPS results by Synchrotron radiation at BL2B. Blue line is estimated DOS and red line is the observed spectra. The observed spectral feature is consistent with calculated DOS. Weak sample-charge-up seems to slightly induce the spectral broadening. Moreover, we measured Low Energy UPS and the determined that the ionization energy of Chl-a film was 5.0eV. In addition, gap state was observed above HOMO as shown in Fig. 1 b). The spectra HOMO state may spread due to the variation of molecular packing. Figure 2 shows PYS spectra of Chl-a solution and a film which was measured after drying up of the solution. The ionization energies of Chl-a in the solution and solid phase were determined to be $I_1 = 4.9_5$ eV and $I_s = 4.9_3$ eV, respectively. Its ionization energy in the gas phase had been reported to be $I_g = 6.1$ eV [2] which was collaborated by DFT calculation. Hence the polarization energies P_+ of Chl-a in the solvent is

estimated to be 1.2 eV by the formula: $P_+ = I_g - I_1$. Interestingly this value is 0.5 eV smaller than a literature value of P_+ (=1.7eV [3]) for a water molecule induced by adjacent H₂O molecules. This suggest that large molecules like Chl-a reduce polarization energy by water.

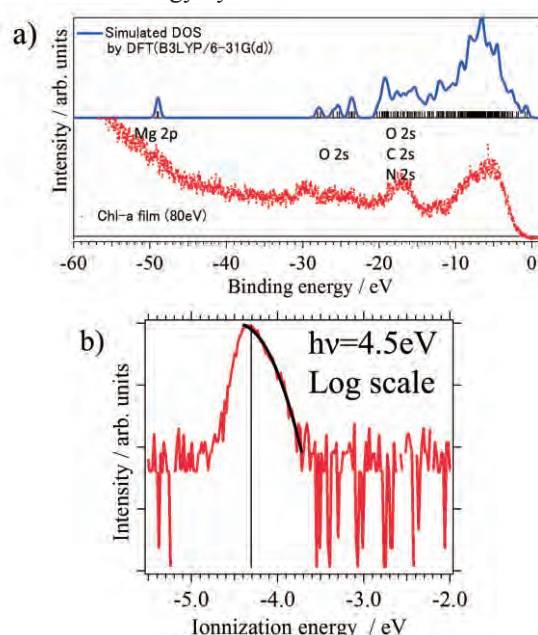


Fig. 1. UPS spectrum of the Chl-a film
a)UPS by Synchrotron radiation, b)Low Energy UPS.

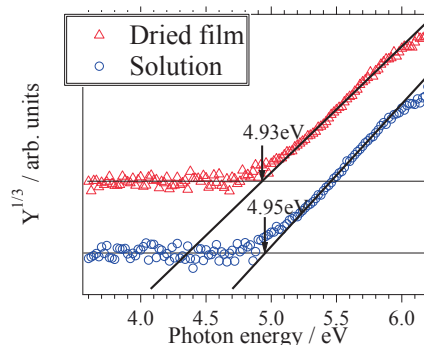


Fig. 2. PYS spectra of Chl-a in the solution and solid phases.

[1] Agostiano *et al.*, BBA BIOENER. **936** (1988) 171.

[2] Y. Nakato *et al.*, Chem. Soc. Jpn. **47** (1974) 3001.

[3] M. Faubel *et al.*, J. Chem. Phys. **106** (1997) 9013.

BL3U

Cobalt-Borate Oxygen Evolution Catalyst Studied by Electrochemical XAFS Technique Using Soft X-Ray

Y. Mitsutomi¹, M. Yoshida^{1,2}, T. Mineo¹, M. Kawamura¹, M. Nagasaka³, H. Yuzawa³,
N. Kosugi³ and H. Kondoh¹

¹Department of Chemistry, Keio University, Yokohama 223-8522, Japan

²Cooperative Research Fellow, Catalysis Research Center, Hokkaido University, Sapporo 001-0021, Japan

³Institute for Molecular Science, Okazaki 444-8585, Japan

Photoelectrochemical water splitting using solar energy is an attractive candidate to produce hydrogen gas from water. This system consists of two half reactions of hydrogen and oxygen evolutions. Among of them, the rate of oxygen evolution is generally slower than that of hydrogen evolution. Thus, the development of efficient oxygen evolution catalyst has been required toward highly active energy conversion system. Recently, a cobalt-borate electrodeposited from a dilute Co^{2+} solution in a borate-buffered electrolyte (Co-B_i) was reported to function as an efficient electrocatalyst for oxygen evolution reaction [1]. The structural information was investigated by X-ray pair distribution function (PDF), which indicates that Co-B_i catalyst is formed by coherent domains consisting of 3–4 nm cobaltate clusters with up to three layers [1]. However, the correlation between structure and activity is still unclear. Therefore, in this study, the Co-B_i catalyst was investigated by *in-situ* O K-edge XAFS measurements under potential control conditions.

Electrochemical XAFS measurements with transmission mode using soft X-rays were performed at BL3U in the UVSOR Synchrotron, according to the previous work [2]. A home-made electrochemical cell was used with Au/Cr/SiC thin film substrates as working electrodes, a Pt mesh counter electrode, and a Ag/AgCl (saturated KCl) reference electrode. Co-B_i catalyst was prepared on the Au/Cr/SiC working electrode at 1.0 V in 0.1 M K-B_i electrolyte containing 0.5 mM $\text{Co}(\text{NO}_3)_2$.

Figure 1 shows the linear sweep voltammograms of bare and Co-B_i-modified Au electrodes in 0.1 M K-B_i electrolyte. The current density of oxygen evolution reaction for Co-B_i-modified electrode was higher than that for bare Au electrode, which exhibits that Co-B_i can function as an efficient oxygen evolution catalyst. Figure 2 shows the O K-edge XAFS spectra for Co-B_i catalyst at 1.0 V in a 0.1 M K-B_i. Two absorption peaks were observed at ca. 529.3 eV and 530.9 eV for Co-B_i sample. Empirically, the O K-edge absorption peak position shifts to lower energies with increasing the formal oxidation state. Thus, the absorption peak at ca. 529.3 eV is likely to be attributed to a high-valent cobalt species. Further investigation is in progress in order to reveal the relationship between production of high-valent cobalt species and oxygen evolution activity.

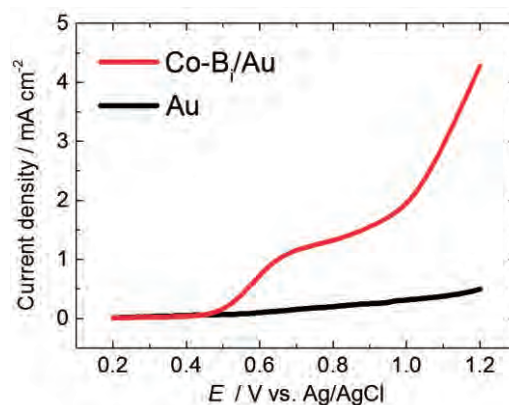


Fig. 1. Linear sweep voltammograms of the bare and Co-B_i-modified Au electrodes in 0.1 M K-B_i (pH 9.2) electrolyte at 100 mV/s.

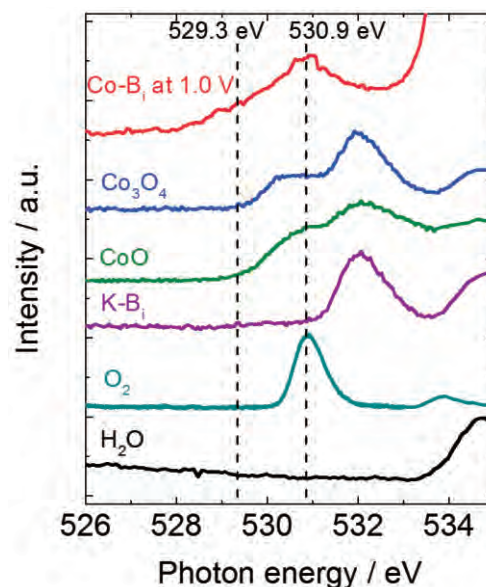


Fig. 2. O K-edge XAFS spectra of Co-B_i catalyst on the Au/Cr/SiC electrode at 1.0 V in 0.1 M K-B_i. The spectra of Co_3O_4 , CoO, K-B_i, O_2 , and H_2O are shown as reference samples.

[1] D. G. Nocera *et al.*, J. Am. Chem. Soc. **135** (2013) 6403.

[2] M. Nagasaka *et al.*, J. Electron. Spectrosc. Relat. Phenom. **177** (2010) 130., J. Phys. Chem. C **117** (2013) 16343., Rev. Sci. Instrum. **85** (2014) 104105.

BL4U

STXM Analysis of Adsorbent for Effective Recovery of Radioactive Elements

Y. Sano¹, S. Watanabe¹, H. Matsuura² and A. Nezu²

¹Japan Atomic Energy Agency (JAEA), Tokai-mura 319-1194, Japan

²Research Laboratory for Nuclear Reactors, Tokyo Institute of Technology, Tokyo 152-8550, Japan

Spent nuclear fuels generated from nuclear power plants contain U and Pu which can be reused, and several long-lived radioactive elements. It will be quite important for effective utilization of energy and environmental loading reduction to process the spent fuel adequately. JAEA has been developing the selective recovery process of radioactive elements, which uses adsorbents of SiO₂ supports coated with styrene-divinylbenzene copolymer (SiO₂-P) and extractants on its surface [1]. Our recent work shows that the separation and recovery abilities of adsorbent, i.e. adsorption/elution behavior of radioactive elements, in this process are strongly dependent on the condition of its surface in which polymer and extractants are impregnated [2]. In this study, some information about the adsorbent surface, such as uniformity of extractants and SiO₂/polymer/extractants interaction, were investigated by scanning transmission X-ray microscope (STXM).

Some adsorbents with different crosslinking degree of polymer (CDP) were synthesized and octyl (phenyl)-N, N-diisobutylcarbonylmethylphosphine oxide (CMPO) was impregnated as an extractant by the flowsheet reported by Wei et al. [3]. The average diameter and pore size of the synthesized adsorbents were 50 μ m and 50nm, respectively (Fig.1). These adsorbents were sliced to 1~3 μ m in thickness by focused ion beam (FIB), and were supplied to STXM analysis.

Figures 2 and 3 show the STXM image of adsorbent surface and the change of O-NEXAFS spectra with CDP at 530eV (O-K edge), respectively. The intensity of pre-edge peak at 532eV increased with CDP at any positions in the adsorbent. The impregnation of CMPO into the adsorbent showed no significant effect on these results.

The appearance of pre-edge peak at 530eV in O-NEXAFS spectra with increasing CDP indicates the some interactions between SiO₂ and the polymer or/and the capture of some kinds of molecules, such as H₂O, by the polymer. These will give some interpretation of our previous experiment, in which it was more difficult to elute adsorbed metal ions from the adsorbent with higher CDP [2]. To obtain more detailed information about the adsorbent surface, STXM analyses at 300eV (C-K edge) and 189eV (P-K edge) will be carried out. It should be further required for effective recovery of radioactive elements to evaluate and compare the STXM data and adsorption/elution behavior using several kinds of adsorbents with different pore sizes and extractants.

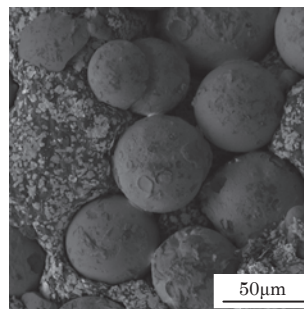


Fig. 1. Photo of the SiO₂-P adsorbents (CDP: 10%).

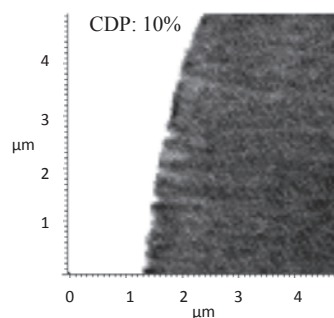


Fig. 2. STXM image of the surface of the SiO₂-P adsorbent at 530eV (O-K edge).

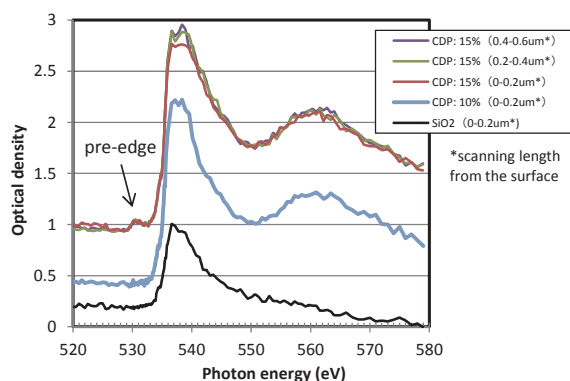


Fig. 3. Change of O-NEXAFS spectra with CDP at 530eV (O-K edge)

[1] Y. Koma *et al.*, Proc. OECD Nuclear Energy Agency 11th Information Exchange Meeting on Actinide and Fission Product Partitioning and Transmutation, San Francisco, USA, November 1-4, (2010) IV-4.

[2] S. Watanabe *et al.*, Procedia Chemistry 7 (2012) 411.

[3] Y. Wei, M. Kumagai and Y. Takashima, Nucl. Technol. 132 (2000) 413.

BL4B

XMCD Study on Magnetic Multilayer of CoNi₂ on W(110)

 T. Yasue¹, M. Suzuki¹, T. Nakagawa², K. Takagi³, T. Yokoyama³ and T. Koshikawa¹
¹Fundamental Electronics Research Institute, Osaka Electro-Communication University,
Neyagawa 572-8530, Japan

²Department of Molecular and Material Sciences, Kyusyu University, Fukuoka 816-8580, Japan

³Institute for Molecular Science, Okazaki 444-8585, Japan

Co/Ni₂ multilayer shows the perpendicular magnetic anisotropy (PMA) and hence is attracted much attention as a candidate for the spintronics device based on the current induced domain wall motion. We have investigated the dynamic behavior of emerging PMA during the multilayer growth process on W(110) by a high-brightness and highly spin polarized low energy electron microscopy (SPLEEM) [1]. In the beginning of the growth below 3 Co/Ni₂ pairs, the perpendicular magnetization appears during Ni deposition, while the magnetization becomes in-plane by Co deposition. PMA becomes stable after 4 pairs even after Co deposition. In order to understand the behavior, XMCD measurements were performed at BL4B in the present work.

Ni L_{2,3} and Co L_{2,3} XMCD spectra were taken at the incident angle of X-ray of 60° (GI) and 0° (NI) with applying the external high magnetic field enough to saturate the magnetization. The magnetic field was parallel to the X-ray direction. The spin magnetic moments m_s and the orbital magnetic moments m_o of Ni and Co were derived from the measured XMCD spectra using the sum rules.

The white line intensities of Ni and Co L_{2,3} absorption spectra were almost constant over different multilayer repetitions examined. The white line intensity is proportional to the number of 3d holes, so that the charge transfer between Ni, Co and the substrate W could be negligible. On the contrary, XMCD spectra strongly depend on the multilayer repetition. This indicates that the spin and orbital moments vary in the multilayer stacking sequence. Figure 1 shows m_o/m_s ratio of Ni taken at NI (red) and GI (blue). At NI configuration, the m_o/m_s ratio increases with coverage, and decreases at GI. This result clearly indicates that the orbital moment of Ni plays an important role for the perpendicular magnetization at higher coverage. Figure 2 shows the spin (squares) and orbital moments (circles) of Ni (top) and Co (bottom). The parallel (blue) and perpendicular (red) components are separated for the orbital moment. Both spin and orbital moments of Co do not show clear coverage dependence, while those of Ni increase with coverage up to 3 pairs and reach to the constant value above 4 pairs. The perpendicular orbital moment of Ni becomes more dominant with increasing coverage. Therefore it is concluded that PMA of the Co/Ni₂ multilayer is mainly induced by the perpendicular orbital moment of Ni.

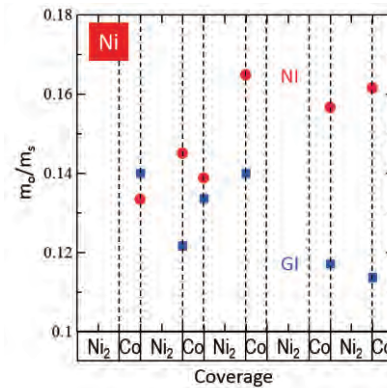


Fig. 1. Ratio of the orbital moment to the spin moment of Ni. Red circles are taken at NI and blue squares at GI.

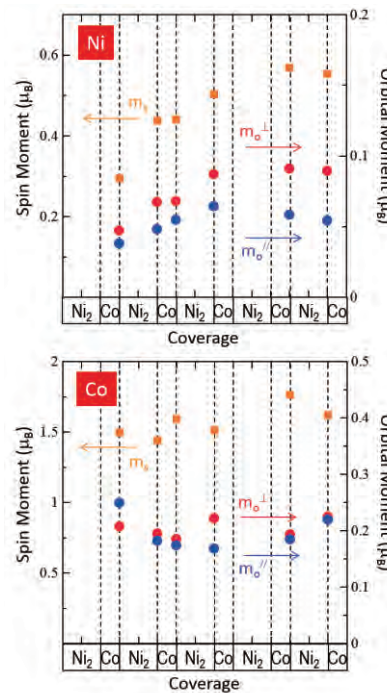


Fig. 2. Spin and orbital magnetic moments of Ni (top) and Co (bottom) obtained by XMCD measurements.

[1] M. Suzuki, K. Kudo, K. Kojima, T. Yasue, N. Akutsu, W. A. Diño, H. Kasai, E. Bauer and T. Koshikawa, *J. Phys.: Condens. Matter* **25** (2013) 406001.

BL4B

XMCD Study of Anisotropic Magnetism of Fe/W(112)

K. Yamaguchi, T. Kawashima, S. Mizuno and T. Nakagawa

Department of Molecular and Material Sciences, Kyushu University, Kasuga 816-8580, Japan

Ordered atoms on surfaces have highly anisotropic structures which is not available for the bulk materials. Such strained or low dimensional structures bring anisotropic electronic structures, resulting in interesting magnetic properties. One-dimensional structures are successfully prepared on stepped surfaces and shows intriguing magnetic properties, which has attracted much attention [1,2]. On the other hand, other works on bcc(112), highly anisotropic surfaces, are also interesting due to its furrow structure (Fig.1), which would exhibit high magnetic anisotropy. However few investigation of magnetic overlayers on bcc(112) have been examined so far [3], and its magnetic properties are unknown. We have prepared Fe quasi-chain structure on W(112) surface and investigated its magnetic properties.

X-ray magnetic circular dichroism (XMCD) measurements were done at BL4B using high field and low temperature end station. All the measurements were performed *in situ* under the vacuum of 1×10^{-10} Torr.

Figure 1 shows anisotropic Fe quasi chain structure on W(112), as determined by tensor low energy diffraction (LEED) analysis (Fig.1 (a)), and visualized by STM (Fig.1(b)). Fe atoms occupy the furrow of W(112), and forms 1×1 structure, irrespective of the large size mismatch between Fe and W ($\sim 10\%$), in accordance with other Fe monolayer structures on W(111), W(110), and W(100) surfaces.

Figure 2 shows Fe-L XAS for 0.6 ML Fe/W(112) and its XMCD. Figure 3 shows magnetization curves (M - H curves) for 0.6 ML Fe/W(112), which was measured by monitoring Fe L_3 XAS intensity. The M - H curve along the $[11\bar{1}]$ direction shows hysteresis with the large coercivity of 3.7 T, while the M - H curves along the $[112]$, surface normal, and the $[1\bar{1}0]$ directions do not show hysteresis and do not saturate even at $H = 5$ T. This M - H curve measurement reveals that the magnetization easy axis is along the $[11\bar{1}]$ direction, parallel to the quasi Fe chains and that the magnetic anisotropy energy is 0.6 meV/Fe atom.

In summary, XMCD study reveals that Fe/W(112) exhibits the large magnetic anisotropy and coercivity as expected from its anisotropic structure.

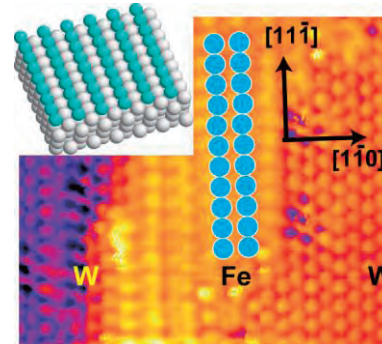


Fig. 1. A structure model of Fe(1 ML)/W(112) determined by tensor LEED and its atomically resolved STM image.

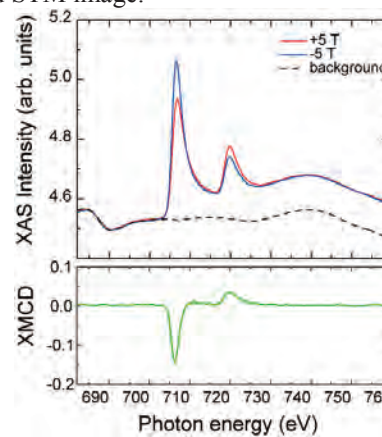


Fig. 2. XAS and XMCD spectra for Fe(0.6 ML)/W(112) for $H = \pm 5$ T along the $[11\bar{1}]$ direction with the background contribution from W(112) clean surface.

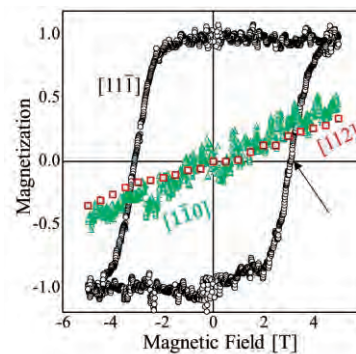


Fig. 3. Magnetization curves for Fe(0.6 ML)/W(112) taken along three different directions.

[1] M. Pratzner *et al.*, Phys. Rev. Lett. **87** (2001) 127201.
 [2] P. Gambardella *et al.*, Nature **416** (2002) 301.
 [3] J. Kołaczekiewicz and E. Bauer, Surf. Sci. **144** (1984) 495.
 [4] T. Nakagawa *et al.*, Phys. Rev. B **86** (2012) 144418.

BL4B

X-Ray Magnetic Circular Dichroism Study of Mn- and Fe-Phthalocyanine Molecules Self-Assembled on the Si(111)-($\sqrt{7}\times\sqrt{3}$)-In Surface

T. Uchihashi and S. Yoshizawa

International Center for Materials Nanoarchitectonics (MANA), National Institute for Materials Science, Tsukuba 305-0044, Japan

Recently, atomic-layer superconductors on silicon surface (surface reconstructions) were investigated by electron transport measurement and scanning tunneling microscopy. The superconductivity of this class of atomically thin materials can be tuned by adsorption of molecules due to its high surface sensitivity. In this work, we studied the magnetic properties of Mn-Phthalocyanine (Pc) and FePc self-assembled on the Si(111)-($\sqrt{7}\times\sqrt{3}$)-In surface reconstruction [referred to as ($\sqrt{7}\times\sqrt{3}$)-In], which is made of atomic indium layers on a clean silicon surface [1,2]. Since the ($\sqrt{7}\times\sqrt{3}$)-In surface exhibits superconducting phase transition at 3 K, interesting competition effects between superconductivity and magnetism are expected to occur in this system.

X-ray absorption spectroscopy (XAS) and X-ray magnetic circular dichroism (XMCD) measurements [3,4] were taken to detect the magnetic properties of the MnPc and FePc. The experiment was performed in the ultrahigh vacuum XMCD system with a superconducting magnet, which was set at the UVSOR beam line BL4B in the Institute for Molecular Science. First, preparation of the ($\sqrt{7}\times\sqrt{3}$)-In surface was confirmed by low energy electron diffraction (LEED) (Fig. 1). MnPc was then evaporated to a monolayer level. Parallel molecular adsorption geometry on the surface was confirmed from the XAS measurement of N K-edge. Similar results were obtained for or FePc on the ($\sqrt{7}\times\sqrt{3}$)-In surface. XMCD spectra were determined from the difference between the XAS spectra taken at $T=5\text{K}$ and $B = \pm 5\text{T}$.

We found clear XMCD signal for both MnPc and FePc molecules, which showed that the spins of Mn and Fe atoms coordinated at the Pc molecules were retained even when they are adsorbed onto the ($\sqrt{7}\times\sqrt{3}$)-In surface (Fig. 2). Detailed analysis of the XMCD data using the sum rule gives the following results. MnPc (1ML, $\theta=55^\circ$): $\langle S_{\text{eff}} \rangle = 0.94 \pm 0.18 \mu_B$, $\langle L \rangle = 0.61 \pm 0.08 \mu_B$, FePc (1ML, $\theta=55^\circ$): $\langle S_{\text{eff}} \rangle = 0.50 \pm 0.23 \mu_B$, $\langle L \rangle = 0.31 \pm 0.12 \mu_B$. Therefore, it is concluded that MnPc and FePc have about one and half spins, respectively, on adsorption. The observed orbital magnetic moments were also found to be relatively large in both cases. These magnetic moments should influence the superconductivity of the ($\sqrt{7}\times\sqrt{3}$)-In surface at low temperatures.

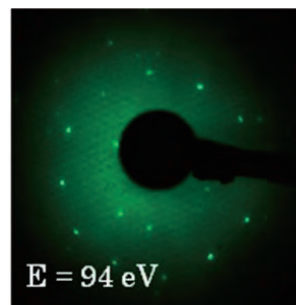


Fig. 1. LEED patterns of the ($\sqrt{7}\times\sqrt{3}$)-In sample before evaporation of Pc molecules.

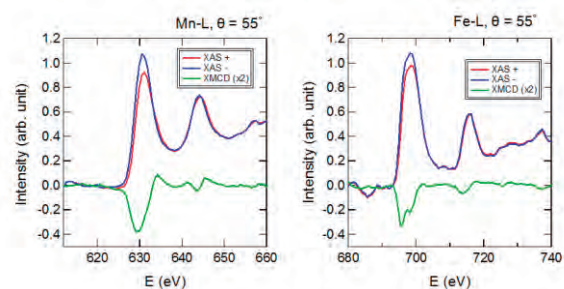


Fig. 2. XAS and XMCD spectra taken for Mn-L edge (MnPc) and Fe-L edge (FePc) at $T = 5\text{K}$, $B = \pm 5\text{T}$, and $\theta=55^\circ$. The coverage of the molecule is 1ML for both cases.

- [1] T. Uchihashi *et al.*, Phys. Rev. Lett. **107** (2011) 207001.
- [2] S. Yoshizawa *et al.*, Phys. Rev. Lett. **113** (2014) 247004.
- [3] S. Stepanow *et al.*, Phys. Rev. B **82** (2010) 014405.
- [4] K. Eguchi *et al.*, J. Phys. Chem. C **118** (2014) 17633.

BL4B

Magnetic Properties of Ordered Iron Nitride Monatomic Layer

T. Miyamachi¹, Y. Takahashi¹, Y. Takagi^{2,3}, M. Uozumi^{2,3}, T. Yokoyama^{2,3} and F. Komori¹

¹*Institute for Solid State Physics, University of Tokyo, Kashiwa 277-8581, Japan*

²*Department of Materials Molecular Science, Institute for Molecular Science, Okazaki 444-8585, Japan*

³*Department of Structural Molecular Science, The Graduate University for Advanced Studies (SOKENDAI), Okazaki 444-8585, Japan*

Iron nitrides, especially in iron-rich phases as represented by Fe_{16}N_2 [1], or F_4N [2], are of great interest for the field of materials science due to their extraordinarily large magnetic anisotropy and room-temperature ferromagnetism. Towards practical applications, deep understanding of their magnetic properties in the form of thin films and extremely of a monatomic layer is required. For this purpose, we fabricated well-ordered iron nitride monatomic layer (Fe_2N layer) on a $\text{Cu}(001)$ substrate and performed x-ray magnetic circular dichroism (XMCD) measurements at BL4B in UVSOR by total electron yield mode.

The Fe_2N layer was fabricated by three processes, i.e., (1) ionic bombardment of N^+ onto a clean $\text{Cu}(001)$ surface with a beam energy of 500 eV, (2) Fe deposition onto N^+ -bombarded $\text{Cu}(001)$ at room temperature, and (3) subsequent annealing up to ~ 700 K. The high-quality surface of the Fe_2N layer with a $p4gm(2 \times 2)$ reconstruction was confirmed before XMCD measurements by scanning tunneling microscopy and low energy electron diffraction.

Figure 1(a) displays XMCD spectra obtained at $B = 5$ T and $T = 7.2$ K in the in-plane ($\theta = 55^\circ$) and the out-of-plane ($\theta = 0^\circ$) geometries by detecting $\mu_+ - \mu_-$, where μ_+ (μ_-) denote the x-ray adsorption spectrum (XAS) with the photon helicity parallel (antiparallel) to the sample magnetization. θ is defined as the angle between the sample normal and the incident x-ray. We find that the XMCD intensity in the in-plane geometry is greater than that in the out-of-plane geometry, which indicates the magnetic easy axis of the Fe_2N layer is towards in-plane direction.

The easy magnetization direction of the Fe_2N layer is clearly recognized by the magnetization curves. Figure 1(b) displays the magnetization curves obtained in the in-plane and out-of-plane geometries. The data points represent the $\text{Fe } L_3$ intensity as a function of applied magnetic field. A steplike magnetization curve with a clear hysteresis loop near $B = 0$ T [see inset of Fig. 1(b)] is observed in the in-plane geometry, while the magnetization curve in the out-of-plane geometry can be fit rather well by a simple Langevin function. Furthermore, the intensity of the in-plane remanent XMCD signal in Fig. 1 (c) monotonously decreases with increasing temperature, but the reduction was only by $\sim 20\%$ when temperature is increased from 7.2 to 41 K. These facts would reveal that the Fe_2N layer is ferromagnetic with a strong in-plane magnetic anisotropy, in good

agreement with a recent study [3].

Detailed analyses of the XMCD spectra and the temperature dependence of the remanent XMCD signal give further information on the magnetic moments and the Curie temperature of the Fe_2N layer. In future work, combined XMCD with surface analysis techniques, the correlation between magnetism and surface quality of the Fe_2N layer will be also discussed.

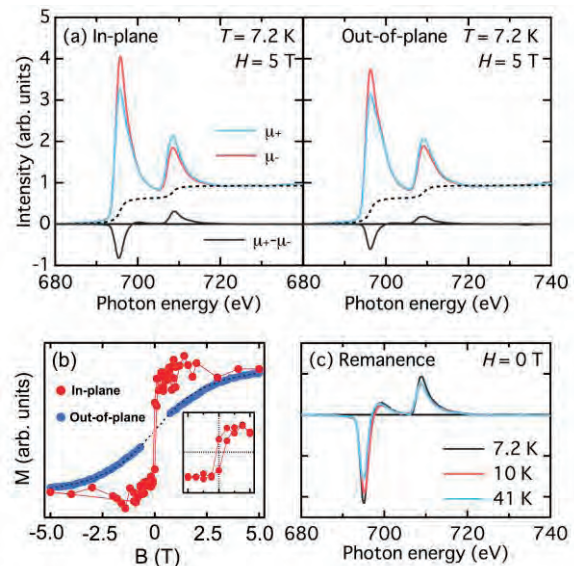


Fig. 1. (a) XAS and XMCD spectra obtained at $B = 5$ T and $T = 7.2$ K in the in-plane and out-of-plane geometries. (b) Magnetization curves obtained at $T = 7.2$ K in the in-plane and out-of-plane geometries. (c) Remanent XMCD spectra obtained at $T = 7.2, 10,$ and 41 K.

[1] K. H. Jack, Proc. R. Sot. London, Ser. A **208** (1951) 200.

[2] J. M. Gallego *et al.*, Phys. Rev. B **70** (2004) 115417.

[3] Y. Takagi *et al.*, Phys. Rev. B **81** (2010) 035422.

BL4B

Magnetism of Oxygen Covered Fe Monolayer on Mo(110)

T. Nakagawa¹, Y. Higuchi¹, K. Yamaguchi¹, S. Mizuno¹, Y. Takagi² and T. Yokoyama²

¹Department of Molecular and Material Sciences, Kyushu University, Kasuga 816-8580, Japan

²Institute for Molecular Science, Okazaki 444-8585, Japan

Iron oxides have a variety of structures, which show intriguing magnetic ordering such as antiferromagnetism in FeO, ferrimagnetism in Fe₃O₄. Thin film iron oxides have been studied since they are important for basic research and solid devices, but few studies have been devoted to understand their magnetic properties of the single layer unit [1].

Experiments were done at x-ray magnetic circular dichroism (XMCD) endstation with a superconducting magnet ($H \sim 6$ T). Fe was deposited on Mo(110) which was cleaned by repeated cycles of oxidation at 1500 K and high temperature annealing up to 2200 K. Subsequently the monolayer Fe film was exposed to oxygen with the crystal temperature kept at room temperature. We found three Fe oxide structures, namely $p(3 \times 2)$, $p(5 \times 1)$, and quasi-FeO(111), which is in good agreement with the previously reported structures for O/Fe/W(110)[1]. The structural consistency is plausible since both of W and Mo substrates have similar crystal and electronic structures.

Figure 1(a) shows Fe L edge XAS spectra for Fe/Mo(110) with different exposures to oxygen. Here 1 L corresponds to 1×10^{-6} Torr s. With increasing the exposure, the white line intensity gradually increases, indicating the increase of Fe 3d hole. The L_2 peak around $h\nu = 720$ eV shows clear difference due to the oxidation. The spectrum with the exposure of 150 L shows a splitting at L_2 with 718 and 721 eV, while the spectra for the Fe films exposed up to 17 L does not show the splitting. According to the previous XAS result [2], the oxygen covered Fe at 150 L is FeO.

Oxygen adsorption on Fe/Mo(110) drastically modifies the magnetization. Figure 1(b) shows XMCD spectra for various oxygen adsorption. The application of the conventional sum rule gives the effective magnetic moment of $2.0 \mu_B$ for the clean Fe monolayer, which is the sum of the orbital and effective spin moment including the dipole term. When Fe is exposed to 0.2 L oxygen, corresponding to the appearance of the first super structure, $p(3 \times 2)$, the XMCD intensity decreases, resulting in $0.3 \mu_B$ of the magnetic moments. When the $p(3 \times 2)$ is completed, the magnetic moment is suppressed to $0.2 \mu_B$. With further expose to oxygen, the magnetic moment slightly increases to $0.4 \mu_B$ at 17 L, but it is almost zero at 150 L.

In conclusion, the oxygen adsorption on monolayer Fe drastically deactivates ferromagnetism, and the resulting structures are antiferromagnetic or paramagnetic structures.

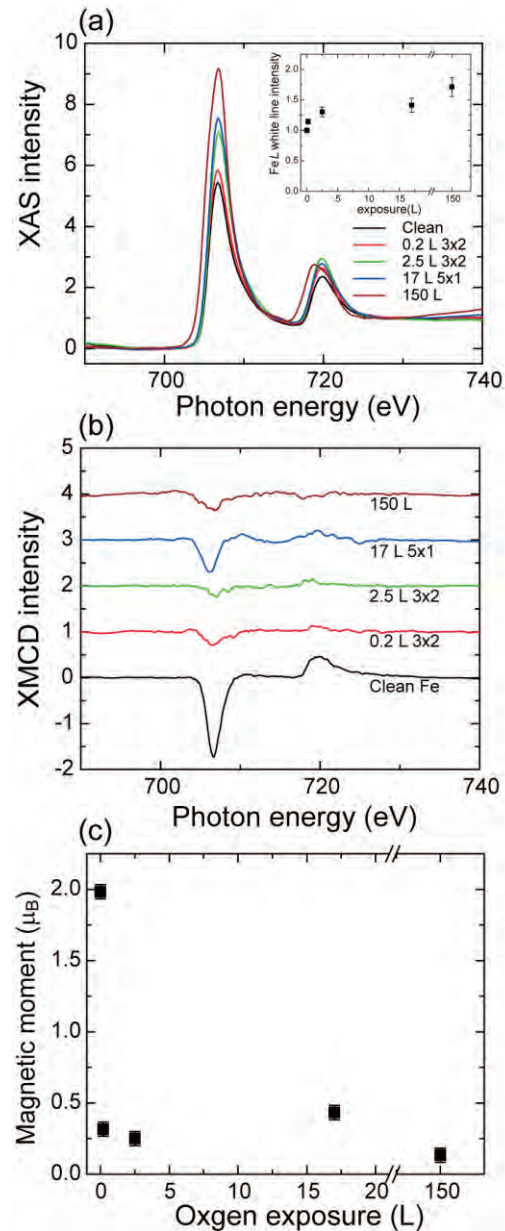


Fig. 1. (a) XAS spectra for Fe films exposed to 0, 0.2, 2.5, 17, and 150 L oxygen taken at $T_s = 5$ K with the light incidence normal to the surface. The inset is the Fe L edge white line intensity. (b) The same as (a), but XMCD spectra taken at $H = \pm 5$ T. (c) Magnetic moment obtained from the sum rule analysis.

[1] K. Feindl *et al.*, Surf. Sci. **617** (2013) 183.

[2] P. S. Miedema and F. M. F. de Groot, J. Electron Spectrosc. Relat. Phenom. **187** (2013) 32.

BL5B

Characterization of Amorphous Chalcogenide Thin Films by Vacuum Ultraviolet Transmission Spectroscopy

K. Hayashi

Department of Electrical, Electronic and Computer Engineering, Gifu University, Gifu 501-1193, Japan

Amorphous chalcogenide semiconductor materials are very expected as a potential material for optoelectronic devices. Because, in these materials are very sensitive to the light, and show a variety of photoinduced phenomena [1-3]. For device applications, it is necessary to sufficiently understand the fundamental properties of these materials. Although a large number of studies have been done on the photoinduced phenomena of these materials, little is known about the details of these mechanisms. These phenomena were studied by exciting outer core electrons with the irradiation of light with the energy corresponding to the optical bandgap or sub-bandgap. The interest has been attracted for the change of the optical properties in the energy region of the visible light. We are interesting for the changes of the optical properties in the higher energy region. To obtain a wide knowledge of the photoinduced phenomena, it is necessary to investigate to the photoinduced effects on wide energy region. In previous reports, we reported the photoinduced change at the VUV transmission spectra of amorphous thin films [4]. In this report, we investigated the photoinduced effects on the as-deposited film by VUV transmission spectroscopy. We also report on the annealing effects at glass transition temperature.

Samples used for the measurement of the VUV transmission spectra were amorphous chalcogenide ($a\text{-As}_2\text{Se}_3$ and $a\text{-As}_2\text{S}_3$) semiconductor thin films prepared onto aluminum thin films by conventional evaporation technique. Typical thickness of the samples and the aluminum films were around 180nm and 100nm respectively. The aluminum film of the thickness of 100 nm was also used in order to eliminate the higher order light from the monochromator in the VUV region. The measurements were carried out at room temperature at the BL5B beam line of the UVSOR facility of the Institute for Molecular Science. And the spectrum was measured by using the silicon photodiode as a detector. Two pinholes of 1.5mm in a diameter were inserted between the monochromator and sample to remove stray light. The intensity of the VUV light was monitored by measuring the TPEY of a gold mesh. The positions of the core levels for the samples were calibrated by referencing to the 2p core level absorption peak of the aluminum film.

Figure 1 shows the VUV transmission spectra of $a\text{-As}_2\text{Se}_3$ film in each state. Two main absorption peaks were observed in this wavelength region. One absorption peak around 22nm corresponds to the 3d

core level of Se atom. Another absorption peak around 28nm corresponds to the 3d core level of As atom. As shown in the figure, the photoinduced changes are observed on the transmission spectra before and after the irradiation of the bandgap (BG) light. We think that those changes are related to the local structures of the amorphous network. The annealing effect on the film after the irradiation by the BG light did not appear clearly as a change in spectrum shape. More detailed experiments are necessary to clarify the origin of the photoinduced changes of the VUV transmission spectra.

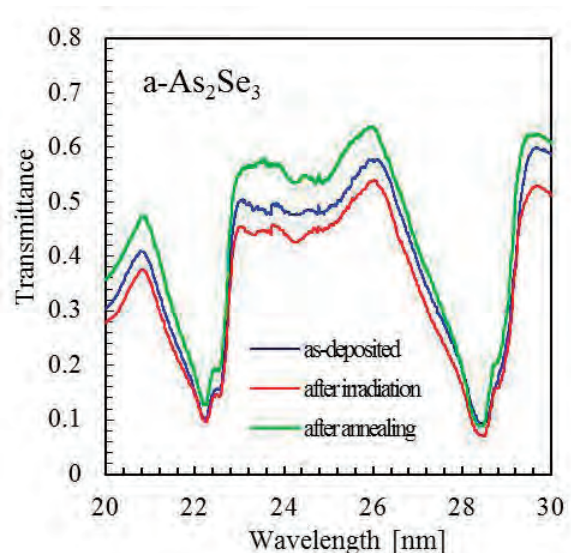


Fig. 1. VUV transmission spectra of $a\text{-As}_2\text{Se}_3$ thin film in each state.

- [1] K. Tanaka, *Rev. Solid State Sci.* **4** (1990) 641.
- [2] K. Shimakawa, A. Kolobov and S. R. Elliott, *Adv. Phys.* **44** (1995) 475.
- [3] K. Tanaka, *Encyclopedia of Nanoscience and Nanotechnology* **7** (2004) 629.
- [4] K. Hayashi, *UVSOR Activity Report 2013* **41** (2014) 140.

BL6U

Phase-Dependent Electronic Structure of Superstructure Monolayer of Hexa-*peri*-Hexabenzocoronene on Au(111)

H. Yamane and N. Kosugi

Department of Photo-Molecular Science, Institute for Molecular Science, Okazaki 444-8585, Japan

The intermolecular interaction is a key issue in molecular electronic properties. It has been reported that hexa-*peri*-hexabenzocoronene (HBC) on Au(111) forms various ordering phases in the monolayer, e.g., $(5 \times 5)R0^\circ$ “R0 phase”, $(\sqrt{27} \times \sqrt{27})R30^\circ$ “R30 phase”, and their mixed phase, depending on the preparation condition [1,2]. In the present work at BL6U, in order to examine the lateral intermolecular interaction in flat-lying molecular layers, we investigated the electronic structure of the R0 and R30 phases of HBC on Au(111), which was realized by controlling the substrate temperature during the thin-film growth.

Figure 1 shows the low-energy electron diffraction (LEED) image, the surface Brillouin zone (SBZ), and the energy-*versus*-momentum [$E(\mathbf{k})$] map of the R0 and R30 phases of the HBC monolayer on Au(111) at 15 K, obtained from angle-resolved photoemission spectroscopy (ARPES). In the R0 phase, the highest occupied molecular orbital (HOMO, H_0) disperses in a narrow width by 20 meV only along the k_{TK} direction, and the HOMO-1 (H_1) disperses by 25 meV only along the k_{TM} direction, which is more evident in the selected energy distribution curve (EDC) in Fig. 1. The opposite trend was observed in the R30 phase; that is, the HOMO disperses by 20 meV along the k_{TM} direction, and the HOMO-1 disperses by 25 meV along the k_{TK} direction. The observed dispersion periodicity is dependent on the high symmetric points of $\bar{\Gamma}$, \bar{K}' , and \bar{M}' in SBZ of the HBC superstructure; therefore, the observed π -band dispersion rationally arises from the intermolecular interaction.

The lateral intermolecular π -band dispersion in organic monolayers has been reported for strongly chemisorbed interfaces with the 0.2-0.3 eV dispersion width [3,4], which is 10 times larger than the present dispersion. Such large dispersions are caused by the substrate-mediated intermolecular interaction due to the strong orbital hybridization and the highly ordered structure at the interface [3,4]. In the present case, the interfacial electronic coupling is weak because of the observation of the vibrationally-resolved HOMO line shape, as indicated by the downed arrow. In addition, we observed no evidence for the interfacial charge transfer. These evidences are the indication of the weak interaction at the interface. Furthermore, the substrate-mediated π -band dispersion should be observed along the underlying metal-atom array [3,4]. Since the present π -band dispersion is dependent not on the substrate SBZ but on the molecular SBZ, the observed π -band dispersion might be introduced by a lateral intermolecular interaction.

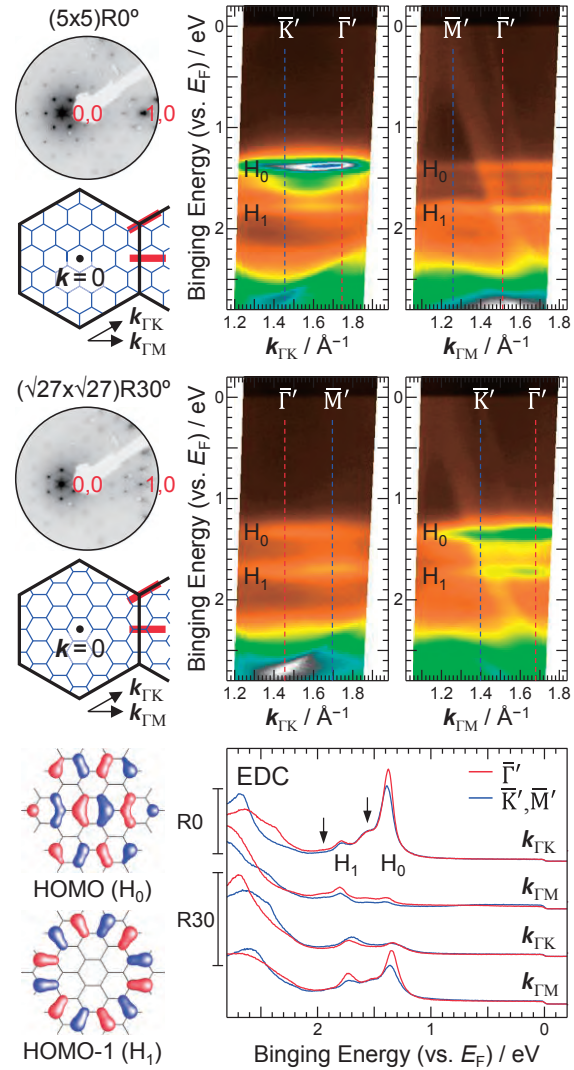


Fig. 1. LEED, SBZ [thick-black hexagon for Au(111) and thin-blue hexagon for HBC], wherein the red line indicates the scanned region in ARPES, the $E(\mathbf{k})$ map, and the EDCs at the high symmetric point of the superstructure monolayer of HBC/Au(111) with the $(5 \times 5)R0^\circ$ and $(\sqrt{27} \times \sqrt{27})R30^\circ$ phases at 15 K. The LCAO patterns of the HOMO and HOMO-1 of HBC are also shown.

- [1] D. Kasemann *et al.*, *Langmuir* **25** (2009) 12569.
- [2] C. Wagner *et al.*, *Phys. Rev. B* **81** (2010) 035423, and references therein.
- [3] H. Yamane *et al.*, *Phys. Rev. B* **76** (2007) 165436; *J. Electron Spectrosc. Rel. Phenom.* **174** (2009) 28.
- [4] M. Wießner *et al.*, *Nat. Commun.* **4** (2013) 1514; *Phys. Rev. B* **88** (2013) 075437.

BL6U

Formation of Delocalized π Band and Interface State in Superstructure Monolayer of Coronene on Au(111)

H. Yamane and N. Kosugi

Department of Photo-Molecular Science, Institute for Molecular Science, Okazaki 444-8585, Japan

Polycyclic aromatic hydrocarbons have attracted attention again as a fragment of graphene. In the present work, by using angle-resolved photo emission spectroscopy (ARPES), we have studied the electronic structure of a (4×4) superstructure monolayer of coronene on Au(111).

The experiment was performed at the in-vacuum undulator beamline BL6U. The cleanliness of the Au(111) surface was confirmed by the low-energy electron diffraction (LEED) and the Shockley state in ARPES, as obtained from the repeated cycles of the Ar^+ sputtering and the subsequent annealing at 700K. The total energy resolution in ARPES was 13 meV.

Figures 1 shows (a) a LEED image at 15 K and (b) the corresponding surface Brillouin zone (SBZ) of the coronene monolayer on Au(111). The LEED image shows the (4×4) superstructure with respect to the Au(111) hexagonal lattice, as reported in Ref. [1]. The ARPES spectra were measured by considering the high symmetric points of $\bar{\Gamma}'$, \bar{K}' , and \bar{M}' in the molecular SBZ [blue hexagon in Fig. 1(b)].

The energy-*vs*-momentum $E(\mathbf{k})$ relation map of the coronene (4×4) /Au(111) along the $\bar{\Gamma}'$ - \bar{K}' and $\bar{\Gamma}'$ - \bar{M}' (\mathbf{k}_{TK} and \mathbf{k}_{TM}) directions, obtained from ARPES, is shown in Figs. 1(c) and 1(d), respectively. The highest occupied molecular orbital (HOMO, π) derived peak of coronene is observed at the binding energy (E_b) of 1.6 eV. Although no direct intermolecular π - π overlap exist in the coronene monolayer, the HOMO peak shows a quite weak

lateral band dispersion by 30 meV at $\bar{\Gamma}'$ - \bar{K}' and by 15 meV at $\bar{\Gamma}'$ - \bar{M}' . The observed dispersion is larger than that for the (5×5) hexa-*peri*- hexabenzocoronene (HBC) superstructure monolayer on Au(111) [2]. This difference is explained by the smaller molecular unit cell and the shorter inter- molecular spacing of the coronene monolayer than those of the HBC monolayer. The observed π -band dispersion is ascribed to the lateral intermolecular interaction in flat-lying aromatic hydrocarbons.

On the other hand, the interface-specific electronic states are observed around the $\bar{\Gamma}'$ point as labeled IS_1 , IS_2 , and IS_3 in Figs. 1(c) and 1(d), which show the relatively large dispersion with the evidence for the spin-orbit splitting. These interface states may originate from the backfolded Shockley- and Tamm-type electronic states of the Au(111) surface at the $\bar{\Gamma}$ and \bar{M} points, respectively, induced by the superstructure. Note that, the observed dispersions are modified from the original Shockley and Tamm states in terms of the effective mass, the Rashba parameter, and so on. Such modifications might be introduced by the Pauli repulsion of surface electrons due to adsorbates and by the scattering due to the superstructure lattice.

[1] C. Seidel *et al.*, Phys. Rev. B **64** (2001) 195418.

[2] H. Yamane *et al.*, a separate page in this volume, UVSOR Activity Report 2014.

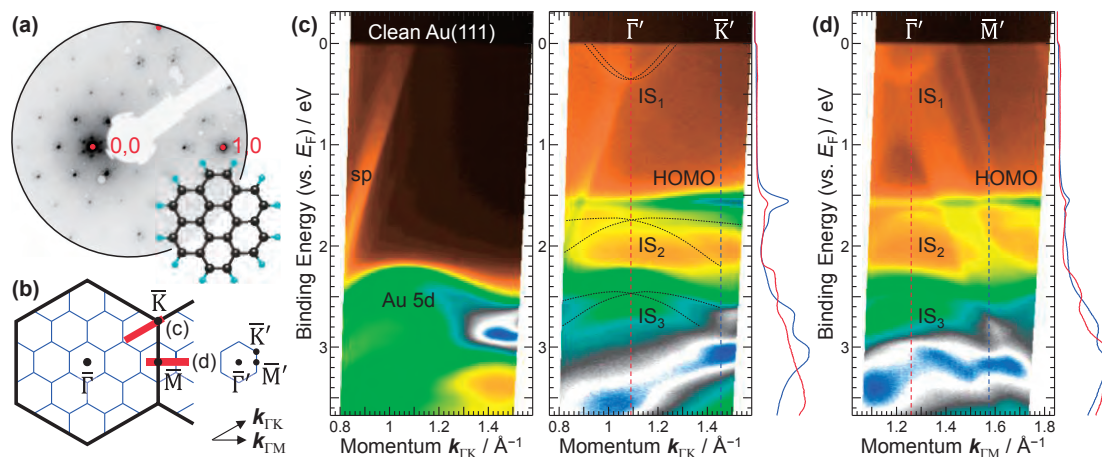


Fig. 1. (a) LEED of the coronene (4×4) /Au(111) at 15 K, wherein the red dot indicates the substrate's spot. The molecular structure of coronene is also shown. (b) SBZ of the Au(111) (black) and the coronene (4×4) / Au(111) (blue). The red line indicates the scanned region in ARPES. (c,d) The $E(\mathbf{k})$ maps of the clean Au(111) and the coronene (4×4) /Au(111) at 15 K along the \mathbf{k}_{TK} and \mathbf{k}_{TM} directions. The energy distribution curves at $\mathbf{k}_{\text{TK}} = 1.08 \text{ \AA}^{-1}$ ($\bar{\Gamma}'$), 1.44 \AA^{-1} (\bar{K}') and $\mathbf{k}_{\text{TM}} = 1.25 \text{ \AA}^{-1}$ ($\bar{\Gamma}'$), 1.56 \AA^{-1} (\bar{M}') are also shown.

BL6U

Manybody Interactions in Rb-Doped Graphene

W. J. Shin^{1,2}, S. H. Ryu^{1,2}, H. Yamane³, N. Kosugi³, K. S. Kim^{1,2} and H. W. Yeom^{1,2}

¹Center for Artificial Low Dimensional Electronic Systems, Institute for Basic Science (IBS), 77 Cheongam-Ro, Pohang 790-784, Korea

²Department of Physics, Pohang University of Science and Technology, 77 Cheongam-Ro, Pohang 790-784, Korea

³Department of Photo-Molecular Science, Institute for Molecular Science, Okazaki 444-8585, Japan

Graphene has served as a prototypical model system for study of various low-dimensional physics [1]. It has rather simple lattice and electronic structures, and the energy scale of phonons, collective excitations of periodic atoms, is relatively large (up to ~200 meV), making it ideal to investigate the electron-phonon interaction and its interplay with electron correlations [2]. Angle-resolved photo emission spectroscopy (ARPES) is an ideal technique that can directly observe energy band dispersion of electrons. Also, ARPES is capable of probing not only a signature of electron-phonon interactions that appear as an abrupt slope change in band dispersion (kink) [2,3], but also electron correlations that lead to the multiple Dirac points. Indeed, high-resolution ARPES spectra from heavily doped graphene have shown such kink structures and band renormalizations [4,5].

In this work, we have measured a systematic evolution of graphene π bands as increasing the Rb density (Fig. 1). We found the phase separation of Rb dopants that the two distinct doping levels coexist at the moderate Rb density. This can be understood by the different degree of charge transfer between the scatter Rb atoms and Rb islands. From the kinked dispersion we could compare electron-phonon and electron-electron coupling constants, which turn out to be different from those for K atoms as dopants. This shows a different degree of screening (or dielectric constant of dopant islands) between Rb and K. We anticipate that this work would provide a meaningful step forward to understanding manybody correlations in heavily-doped graphene as well as to searching for superconductivity in graphene with a relatively high transition temperature.

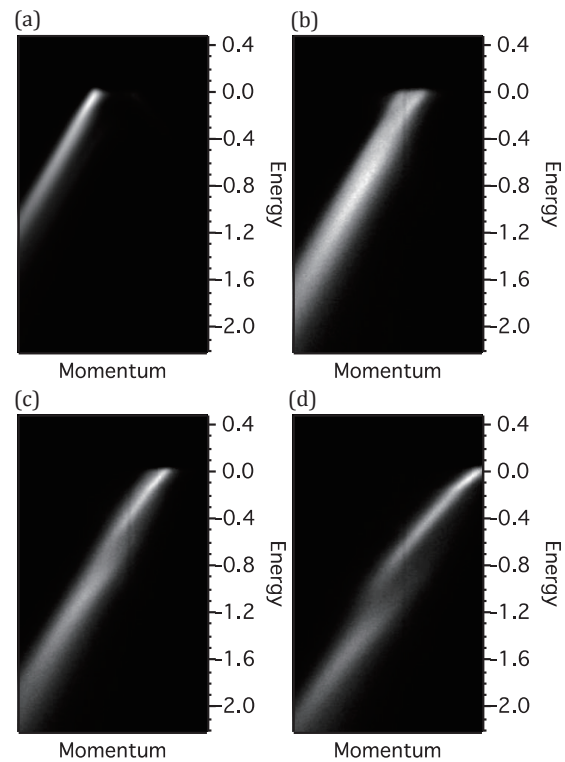


Fig. 1. Doping dependence of band dispersions of rubidium doped graphene.

- [1] H. Castro Neto *et al.*, Review of Modern Physics **81** (2009) 109.
- [2] C. S. Leem *et al.*, Physical Review Letters **100** (2008) 016802.
- [3] A. Damascelli *et al.*, Review of Modern Physics **75** (2003) 473.
- [4] A. Bostwick *et al.*, Nature Physics **3** (2007) 36.
- [5] S. Y. Zhou *et al.*, Physical Review B **78** (2008) 193404.

BL6U

Surface Coordination Chemistry to Control the Charge Transfer at Organic/Metal Interface: SnCl₂Pc on Ag(111)

S. Kera^{1,2}, K. Yonezawa², T. Tago², F. Bussolotti¹, H. Yamane¹,
N. Kosugi¹ and K. K. Okudaira²

¹Department of Photomolecular Science, Institute of Molecular Science, Okazaki, 444-8585, Japan

²Department of Nanomaterial Science, Graduate School of Advanced Integration Science, Chiba University, Chiba 263-8522, Japan

For more than two decades molecular adsorbates on metal surfaces represent a very active field of research in surface and interface science. Fundamental understanding the basic physical properties is a key issue for tuning the geometric and electronic structure at the interfaces, hence to improve and control the organic device performance. To understand the mechanism of charge transfer (CT) at organic/metal interfaces, the binding energy of frontier orbitals (HOMO and LUMO) and the adsorption height of the molecules on the metal are critical parameters.

Using coordination chemistry we introduce “spacers” which change the contact distance to the surface, and investigate the consequences for geometric (adsorption height, molecular bending, etc.) and electronic structure (amount of CT). In contrast to planer phthalocyanines (Pc), dichlorotin Pc (SnCl₂Pc) is an n-type semiconductor and its conductivity is 1–3 orders larger than most of the other Pcs. In this study, we performed ARUPS and XPS for SnCl₂Pc films prepared on Ag(111). Since the size of the SnCl₂ group is large, the molecule is considered to be non-planar, but there is no permanent dipole.

The experiments were conducted at BL6U. The clean surface was obtained by the repeated cycles of Ar⁺ sputtering and annealing. After preparing the monolayer film (0.4nm) on the Ag(111) at room temperature, valence band (VB) and secondary cut-off (SECO) was measured at 45eV, then each core levels are scanned for C1s, N1s, Cl2p, and Sn4d. The same measurements are repeated for the annealed monolayer film (633K for 3h). We evaluated the photoelectron angular distribution of HOMO and concluded the flat-lying orientation both for as-grown and annealed films (not shown).

Figure 1 shows the Cl2p XPS spectra of SnCl₂Pc/Ag(111) before and after the annealing. For the as-grown film, spin-orbit splitting of Cl2p is detected in different binding energies for upper- (towards the vacuum) and lower-side (to the substrate) of Cl atoms. However the peaks disappear totally for the annealed film. Considering energy shifts in other core levels, the chemical structure may change to SnPc by removing the Cl atoms.

Figure 2 shows the angle-integrated UPS for VB and SECO regions. Regardless of Cl atoms, clearly

the gap state due to the CT from the metal to the LUMO state is observed as for other metal-Pcs on Ag(111) [1]. By detaching the Cl atoms, HOMO shifts to high energy side to show a very similar spectrum to SnPc/Ag(111) [1]. The work function is reduced by 0.2eV upon annealing, which might be caused by differences in total CT amount and/or push-back effects induced by rearrangement of the adsorption height.

It is an open question if this chemisorption with CT involves the anchored Cl atom via an expanded LUMO orbital, or whether basically the indole groups bond to the surface due to a strongly distorted or tilted geometry. A geometrical study including a precise determination of adsorption height will give a clear answer for these.

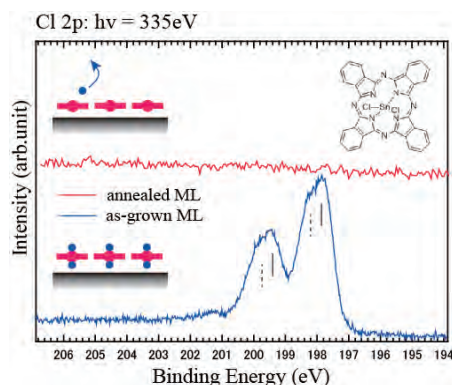


Fig. 1. Cl2p XPS spectra for SnCl₂Pc/Ag(111) taken at 297K for as-grown and annealed film.

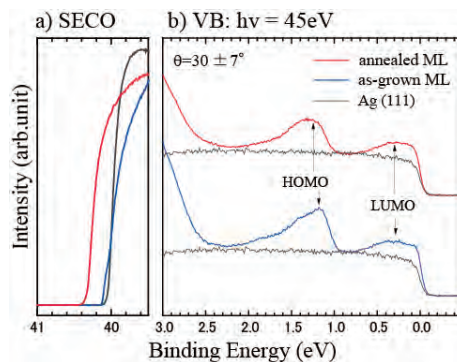


Fig. 2. a) SECO and b) VB for SnCl₂Pc/Ag(111) taken at 297K for as-grown and annealed film. The spectra for the clean substrate are also shown.

[1] M. Häming *et al.*, Phys. Rev. B **82** (2010) 235432.

BL7U

Electronic Structure of a MnSe/Bi₂Se₃ Ultrathin Film Heterostructure

T. Hirahara¹, T. Kubo², A. Takayama², T. Hajiri³, M. Matsunami³,
K. Tanaka³ and S. Hasegawa²

¹Department of Physics, Tokyo Institute of Technology, Tokyo 152-8551, Japan

²Department of Physics, University of Tokyo, Tokyo 113-0033, Japan

³UVSOR Facility, Institute for Molecular Science, Okazaki 444-8585, Japan

Topological insulators (TI) are extensively studied recently due to its peculiar properties [1]. The Dirac-cone surface states of TI are protected by time-reversal symmetry (TRS) and backscattering among these surface states is prohibited. But when TRS is broken by application of a magnetic field or incorporating magnetic materials, a gap opening in the Dirac cone is expected and an intriguing phase called the quantum anomalous Hall state can be realized [2]. This phase is expected to show even more exotic phenomena such as the topological magnetoelectric effect. To realize such state, two types of sample fabrication techniques have been employed up to now: (1) magnetic doping while growing the single crystal or thin film of TI [3], and (2) magnetic impurity deposition on the surface of TI [4]. While method (1) was successful and showed evidence of the TRS violation, no one has succeeded using method (2), which should be a more direct way to examine the interaction between the topological surface states and magnetism.

In the present work, we have attempted an alternative approach to break the TRS in TI: making a heterostructure of TI and magnetic insulators (MI) and making use of the magnetic proximity effect at the interface. For this purpose, we have fabricated a heterostructure of MnSe (MI) and Bi₂Se₃ (TI) since the lattice mismatch between the two materials is relatively small (~6%). MnSe is a layered structure and is antiferromagnetic as a whole, but in each Mn layer, the spin is oriented in one direction (ferromagnetic within the layer and antiferromagnetic among the adjacent layers) [5]. Thus one can expect that the ferromagnetic Mn layer will break TRS of TI. Figures 1 (a) and (b) show the band dispersion of the surface states of Bi₂Se₃ and the 2BL MnSe/Bi₂Se₃ heterostructure. While the Dirac-cone surface states are massless in (a), one can find a clear gap of ~ 80 meV at the Dirac point in (b), meaning that it has turned into a massive Dirac cone. This result shows that our method is indeed a successful way to induce TRS breaking in TI surface states. Spin- and angle-resolved photoemission measurements will be performed to see the change of the spin-polarization of the Dirac cone upon the gap opening.

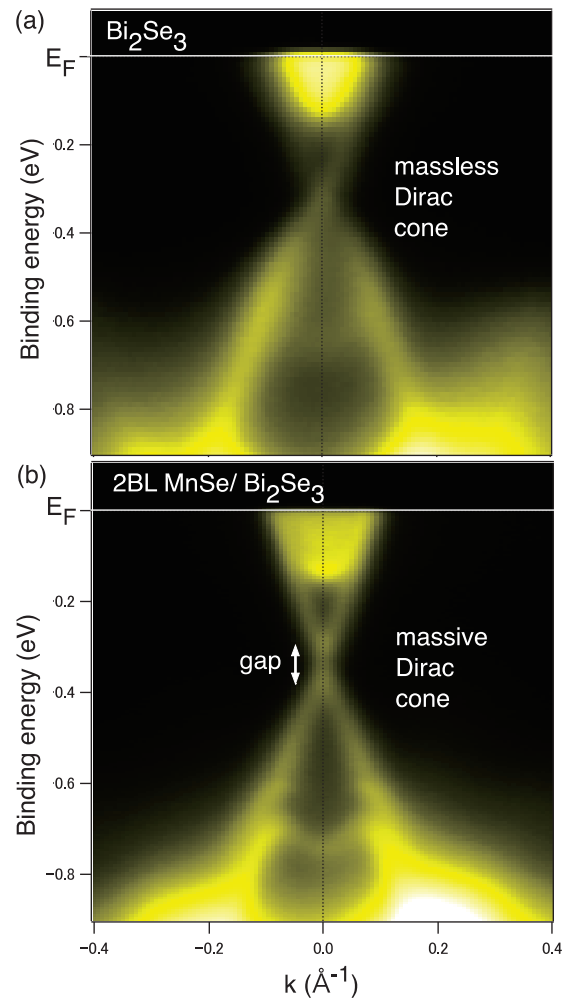


Fig. 1 The band dispersion of Bi₂Se₃ (a), and a heterostructure of MnSe/Bi₂Se₃, respectively measured at $h\nu = 21$ eV with p -polarization.

[1] M. Hasan and C. Kane, *Reviews of Modern Physics* **82** (2010) 3045.

[2] X.-L. Qi and S.-C. Zhang, *Reviews of Modern Physics* **83** (2011) 1057.

[3] For example, C. Z. Chang *et al.*, *Science* **340** (2013) 167.

[4] For example, M. Ye *et al.*, *Physical Review B* **85** (2012) 205317.

[5] R. J. Pollard *et al.*, *J. Phys. C: Solid State Phys.* **16** (1983) 345.

BL7U

Angle-Resolved Photoelectron Spectroscopy Study of One-Dimensional Electronic States on Bi/InSb(001)

 Y. Ohtsubo^{1,2}, J. Kishi², K. Hagiwara², M. Matsunami³, K. Tanaka³ and S. Kimura^{1,2}
¹Graduate School of Frontier Biosciences, Osaka University, Suita 565-0871, Japan

²Department of Physics, Graduate School of Science, Osaka University, Toyonaka 560-0043, Japan

³UVSOR Facility, Institute for Molecular Science, Okazaki 444-8585, Japan

One-dimensional (1D) metals behave in completely different ways from ordinal 3D metals [1]. Tomonaga Luttinger liquid (TLL) is one of the most extensively studied phases as an example of the exotic 1D metals. It is theoretically predicted that TLL should exhibit exotic power-law scaling and spin-charge separation [2]. So far, various 1D systems with 1D structure were studied as candidates of TLL and only a few of them showed metallic states with power-law spectral features *e.g.* carbon nanotube [3] and Lithium purple bronze (LiPB) [4, 5].

On the surface of semiconductor, various self-assembled 1D atomic structures are known and they have been regarded as suitable systems to study 1D metallic states [1]. However, most of them do not behave as TLL at low temperature, because of 2D undulation of the surface states and/or metal-insulator transition driven by strong nesting. Up to now, the only system claimed as a surface TLL is the Au nanowire assembled on Ge(001) [6]. However, even on Au/Ge(001), the direction of conduction path and even the nature of TLL itself is still under debate.

In this project, we have performed angle-resolved photoelectron spectroscopy (ARPES) study on the surface 1D system Bi/InSb(001). Bi/InSb(001) is reported to form an 1D atomic structure with metallic electronic states [7] and hence the encouraging candidate of surface TLL. ARPES measurements were performed at the beamline BL7U of UVSOR-III. The InSb(001) substrate is cleaned by repeated cycles of sputtering and annealing and then Bi is evaporated from a home-made Knudsen cell. The sample preparation process was performed *in situ*.

Figure 1 (a) shows the Fermi surface of Bi/InSb(001) taken at room temperature. The Fermi surface clearly shows the 1D and metallic features of the surface electronic states of Bi/InSb(001). No k_z dispersion of the metallic state was observed with different photon energies (not shown here), indicating that it is the 1D surface state. The 1D state disperses along the 1D chain direction (the relationship between the surface periodicity and 1D atomic-chain direction has been already reported in Ref. [7]).

We examined the polarization dependence of the metallic 1D state. As shown in Fig. 1 (b) and (c), the surface state is observed only with *P*-polarized photons. Broad features below 0.6 eV come from bulk bands. The clear polarization dependence on the surface state indicates the even symmetry of the 1D

state with respect to the photon-incident plane.

Further analysis based on temperature dependence and spectral shape around the Fermi level is in progress in order to examine whether the 1D surface state on Bi/InSb(001) behaves as TLL or not.

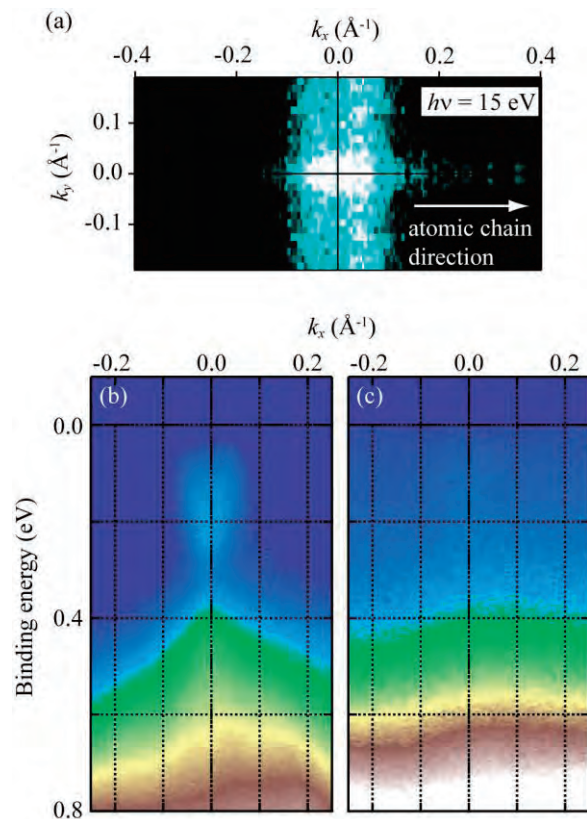


Fig. 1. The Fermi surface (a) and band dispersion (b, c) of the Bi/InSb(001) surface taken at $h\nu = 15$ eV. (b) and (c) are measured with *P*- and *S*- linearly polarized photons, respectively.

[1] M. Grioni *et al.*, J. Phys.: Condens. Matt. **21** (2009) 023201.

[2] S. Tomonaga, Prog. Theor. Phys. **5** (1950) 544.

[3] H. Ishii *et al.*, Nature **426** (2003) 540.

[4] F. Wang *et al.*, Phys Rev. Lett. **96** (2006) 196493.

[5] L. Dudy *et al.*, J. Phys.: Condens. Matt. **25** (2013) 014007.

[6] C. Blumenstein *et al.*, Nat. Phys. **7** (2011) 776.

[7] P. Laukkanen *et al.*, Phys. Rev. B **81** (2010) 035310.

BL7U

Formation of the Dirac Cone at the Γ -Point on the Epitaxial Graphene Sheet Observed by the Angle-Resolved Photoelectron Spectroscopy with the Low Energy Photon

S. Tanaka¹, T. Maruyama², M. Matsunami³ and K. Tanaka³¹*Institute of Scientific and Industrial Research, Osaka University, Ibaraki 567-004, Japan*²*Department of Materials Science and Engineering, Meijo University, Nagoya 468-8502, Japan*³*UVSOR Facility, Institute for Molecular Science, Okazaki 444-8585, Japan*

Graphene, a single-atomic-layer consisting of a carbon sp^2 -orbital-network, is one of the materials that have been most extensively studied these years. Here, for the first time, we report a peculiar behavior of the epitaxial single-layer graphene formed on the SiC crystal; a backfolding of the Brillouin zone which enables an observation of the characteristic Dirac cone at the Γ -point, which is located at the K-point in the normal Brillouin zone of the graphene.

The experiments were made at the BL-7U, UVSOR-III. The sample used was provided by the “Graphene Platform” inc, and cleaned by heating at 700C° in UHV. The sample was then moved to the experimental chamber and slowly cooled down to 13K for measuring the angle-resolved photoelectron spectra (ARPES) near the surface-normal direction as a function of the photon energy. Figure 1 shows volume and plane ($k_y=0$) maps of the ARPES intensity taken at $h\nu=10.8\text{eV}$ as functions of the momentum parallel to the graphene sheet and the electron binding energy. The feature in the ARPES spectra is absolutely agreed with the so called “Dirac cone”, which is consisting of linearly dispersed π -bands and most prominent characteristics of the graphene. The Dirac point is located 0.4 eV below the Fermi level, which indicates that a single-layer of the graphene is formed. This behavior is very surprising, since the Dirac cone of the graphene exists not at the Γ -point but at the K-point of the Brillouin zone, (separated by 1.7 \AA^{-1} from the Γ -point) which cannot be accessed with the ARPES technique below the photon energy of 15.4eV if the work function of 4.5eV is assumed. Since the defects or electron-phonon scattering cannot be a candidate considering the momentum and energy conservation rule, the most probable interpretation is the surface Umklapp process, in which the electron is diffracted from K to Γ due to the formation of the superstructure (e.g., $(\sqrt{3} \times \sqrt{3})R30^\circ$) formed on the graphene layer. As shown in Fig.2, this Dirac cone is only observed when the photon energy is near 11eV. This clearly indicates that the final state located 11eV above the Fermi level plays a key role for this observation. Thus, it seems reasonable the scattering occurs among the unoccupied bands located this energy region.

We found that the surface normal photoelectron emission due to the Dirac cone is extinguished when the sample is warmed to 50K. This behavior is similar

to the superstructure formation on the graphite surface, where the CDW transition was proposed[1], and similar transition may occur on the graphene surface and/or the step edge. However, this superstructure on the graphene surface is less stable than the graphite surface, and we could not find a definite condition for the observation of the Dirac cone, and more work is needed for a deeper understanding the physical nature of this surprising phenomenon.

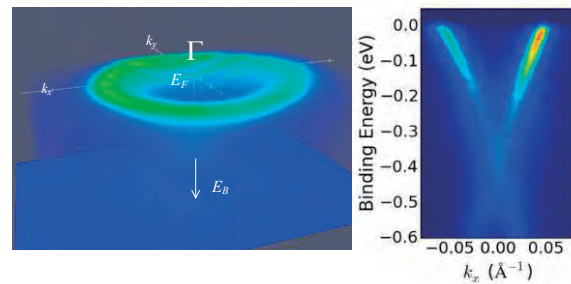


Fig. 1. ARPES results of epitaxial graphene on SiC (13K) near Fermi level at the Γ -point (surface normal) taken at $h\nu=10.8\text{eV}$.

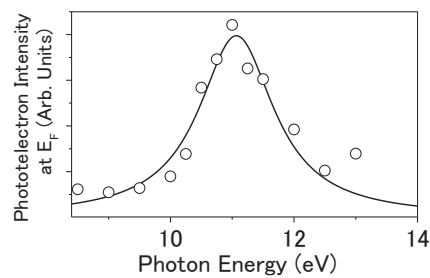


Fig. 2. Photoelectron intensity near the Fermi level in the ARPES spectra of graphene as a function of the excitation photon energy. The line is a Lorentzian curve centered at 11.1eV.

[1] S. Tanaka, M. Matsunami and S. Kimura, Phys. Rev. B **84** (2011) 121411(R) .

BL7U

Inelastic Scattering of Photoelectrons at Organic/Graphite Interface

 T. Yamaguchi¹, F. Bussolotti², J. Yang¹, K. Kimura¹, M. Matsunami², N. Ueno¹ and S. Kera^{1,2}
¹Graduate School of Advanced Integration Science, Chiba University, Chiba 263-8522, Japan

²Institute for Molecular Science, Okazaki 444-8585, Japan

Understanding electron-phonon coupling as well as *weak* intermolecular interaction is required to discuss the mechanism of charge transport in functional molecular materials. The experimental study of electron-phonon coupling of the highest occupied molecular orbital (HOMO) state in the ordered monolayer film is essential to comprehend hole-hopping transport and small-polaron related transport [1]. In this work, we succeeded to observe a modulation of energy loss of photoelectron from graphite by exciting *intramolecular* vibration of adsorbed organic molecule at the substrate surface.

Low-energy excited angle-resolved ultraviolet photoelectron spectroscopy (ARUPS) was performed at beamline BL7U. A highly oriented pyrolytic graphite (HOPG) substrate was cleaned by heating at 900K for 2h. Pentacene (PEN) and zinc phthalocyanine (ZnPc) were deposited on the HOPG at < 0.1nm/min at room temperature, then the film was annealed to obtain the well-ordered monolayer.

First derivative of ARUPS intensity maps for PEN/HOPG and ZnPc/HOPG are shown in Fig.1 (a) and (b), respectively. Strong peaks beneath the Fermi level due to scattering from k-point of graphite (red arrows) are observed similarly to the previous report [2]. To exclude the impact of intensity background by the strong peaks, energy distribution curve, $I_0(E)$ was integrated for $\theta = 0 \pm 3^\circ$. In Fig. 2, photon energy dependence of $I_0(E)$ (top panel) and their derivatives, $-dI_0(E)/dE$ (bottom) taken for photon energies of 7~11eV are shown for PEN/HOPG.

Clearly one can find peaks observed strongly at $E_b=170$ meV for higher energy excitation and weakly at $E_b=90$ meV for lower energy excitation in Fig. 2(b). Tanaka *et al.*, reported ARUPS result of a bare HOPG where features of energy loss of photoelectron (60~70 and 154~175 meV) due to inelastic scattering by graphite phonon are observed with phonon dispersion [3]. Comparing to the bare surface, the loss energy increases from 154 meV to 170 meV and 67 meV to 90 meV at Γ point, respectively with no energy dispersion. Similar results are observed for ZnPc (not shown). The energy loss of 170 meV may correspond to the effective vibronic coupling mode of 167 meV for PEN/HOPG and 170 meV for ZnPc/HOPG detected for HOMO in high-resolution UPS [1]. We observed that the energy dependences of the intensity of both peaks are similar to that of the bare surface, indicating that the process of the inelastic scattering would be bounded by the resonance excitation channels of the graphite [3], however the frequency

of emitted phonon is arranged by exciting *intramolecular* vibrations. Obviously, the observed intensity is too large for *extrinsic* energy loss in propagation process to the surface as found for HREELS (on the order of 10^{-3}), indicating that the inelastic scattering could be dominated by *intrinsic* loss of photoelectron at molecule/graphite interface where the wavefunction of electron couples strongly to that of *intramolecular* vibrations.

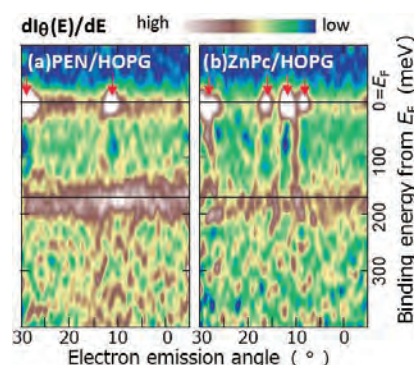


Fig. 1. First derivative of ARUPS intensity map taken at $h\nu=11$ eV for PEN/HOPG at 11 K (a) and ZnPc/HOPG at 14 K (b).

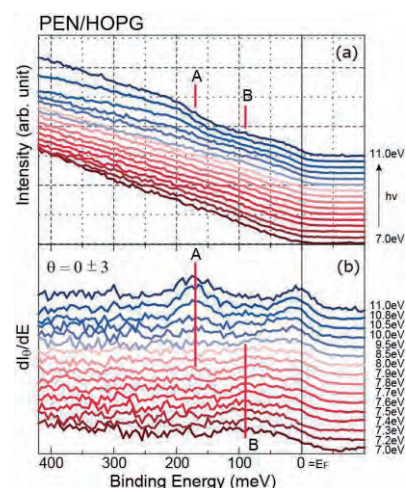


Fig. 2. Photon-energy dependence of $I_0(E)$ and $dI_0(E)/dE$ for PEN/HOPG ($\theta=0 \pm 3^\circ$).

- [1] S. Kera *et al.*, Prog. Surf. Sci. **84** (2009) 135.
- [2] H. Yamane *et al.*, UVSOR Activity Report 2013 **41** (2014) 144.
- [3] S. Tanaka *et al.*, Sci. Rep. **3** (2013) 3031.

BL8B

Direct Observation of Electronic Structure of Nylon-6,6 to Clarify the Contact Electrification Mechanism

T. Sato¹, K. R. Koswattage², Y. Nakayama¹ and H. Ishii^{1,2}

¹Graduate School of Advanced Integration Science, Chiba University, Chiba 263-8522, Japan

²Center for Frontier Science, Chiba University, Chiba 263-8522, Japan

Contact electrification of insulating polymers has been widely used in several technologies such as laser printing and photocopying. But the fundamental mechanism of this phenomenon is still controversial, and several models have been discussed [1]. In most models such as surface state model [2] and molecular-ion-state model [3], the existence of the some gap states is often assumed between highest occupied molecular orbital (HOMO) and lowest unoccupied molecular orbital (LUMO). These states can work as charge reservoir for the charge transfer upon the contact electrification. However, the direct observation of the electronic structure including gap states was examined only for very limited insulating polymers. Therefore, the investigation of the electronic structure of insulating polymers is important to clarify the contact electrification mechanism. In this study, the electronic structure of Nylon-6,6 including gap states was observed by not only ultraviolet photoemission spectroscopy (UPS) at BL8B of UVSOR but also high sensitivity UPS and photoelectron yield spectroscopy (PYS) at handmade apparatus of our laboratory [4].

Figure 1 shows the UPS spectrum of Nylon-6,6 thin film, which was made by spin coating on indium-tin oxide (ITO) substrate. The ionization energy (I) of Nylon-6,6 is determined as 7.49 eV from the onset of the photoemission from the HOMO. Moreover, the photoemission was detected from the vicinity of 4.3 eV by high sensitivity PYS. This result suggests that the gap states of Nylon-6,6 exist from the HOMO to at least 3.2 eV above, and the existence of such gap states was also confirmed by high sensitivity UPS by using pure deep UV light with extremely low stray light. These gap states are related to the charge transfer upon the contact electrification.

In PYS measurement, the information on the density of states (DOS) of the sample can be obtained in principle by differentiating the PYS spectrum with respect to photon energy [5]. Accordingly, we determined the DOS distribution of nylon-6,6 including gap states by combining the UPS at BL8B, high sensitivity UPS, and high sensitivity PYS results (Fig. 2). As a result, the density of states of gap states near the Fermi level of the substrate was about 10^{-5} times smaller than that of HOMO. Besides, using this observed DOS distribution, we estimated the charge density during the contact electrification if the charge transfer occurs via only gap states. Consequently, the order of estimated charge density was consistent with

that of the literature data observed by Kelvin Probe. This result suggests that contact electrification of insulating polymers can be explained by charge transfer via only gap states.

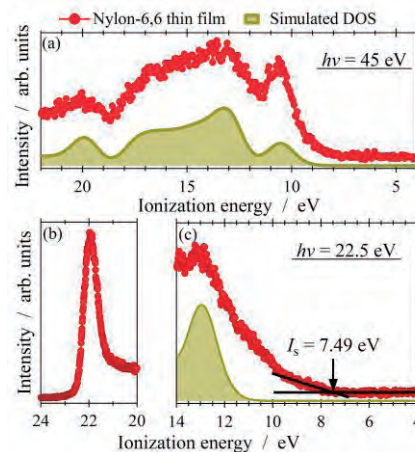


Fig. 1. (a) UPS spectrum of Nylon-6,6 thin film and a simulated density of states curve of Nylon-6,6 based on quantum chemical calculation (Gaussian09 with B3LYP/6-31g basis set). (b) UPS spectrum of the SECO region. (c) UPS spectrum of the top valence region.

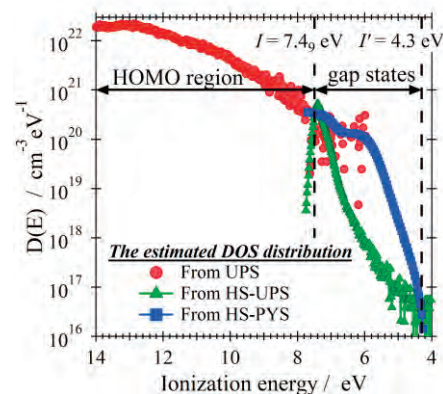


Fig. 2. The density of states of Nylon-6,6 estimated from UPS and PYS spectra.

[1] S. Matsusaka *et al.*, Chem. Eng. Sci. **65** (2010) 5781.

[2] J. Lowell, Adv. In Phys. **29** (1980) 947.

[3] C. B. Duke *et al.*, J. Appl. Phys. **49** (1978) 315

[4] S. Machida *et al.*, Appl. Phys. Express **6** (2013) 025801.

[5] J. Szuber, Vacuum **57** (2000) 209.

BL8B/BL2B

Investigation of Charge-Transfer Interaction by Metal Deposition on Organic Semiconducting Thin Films

T. Hosokai¹, K. Yonezawa², R. Makino², K. R. Koswattage², K. K. Okudaira² and S. Kera^{2,3}¹National Institute of Advanced Industrial Technology and Science, Tsukuba 305-8568, Japan²Graduate School of Advanced Integration Science, Chiba 263-8522, Japan³Department of Photo-Molecular Science, Institute for Molecular Science, Okazaki 444-8585, Japan

Understanding the impact of the electronic structure on the charge-transfer (CT) interaction between organic semiconductors and noble metals is highly important for *Organic Electronics*, because their interfacial energy-level alignment determines an efficiency of charge-carrier injection. Previously, we have proposed that such a CT can happen for organic-on-metal systems (as seen in Figs. 1(a) and 1(b) top) due to surface-induced aromatic stabilization (SIAS), and the SIAS takes place owing to a specific chemical structure of the adsorbates [1,2,3]. However, it is still not clear whether the SIAS can also occur for metal-on-organic systems, which is usually used in organic devices as a top-contact fabrication. Here, we investigated the electronic structure of a prototypical organic semiconductor, diindenoperylene (DIP: C₃₂H₁₆, Fig. 1(b)), thin films by using angle-resolved ultraviolet photoelectron spectroscopy (ARUPS).

All the experiments were conducted at BL8B in UVSOR. After preparing a clean SiO₂/Si wafer or Au-coated Si wafer, DIP films were thermally grown on the surfaces in situ with a nominal film thickness of 20 nm. There, DIP molecules orient with up-right standing on SiO₂ surface or lying-down on Au surface, which exhibit a large difference in energy of molecular features relative to the Fermi level (see the bottom spectrum in Figs. 1(a) and 1(b)). Then, Ag or Cu was thermally deposited step-by-step on those DIP films. ARUPS was measured at each deposition amount of the metals, with a photoelectron emission angle $\theta=40^\circ$ at $h\nu=28$ eV. All the depositions and measurements were performed at room temperature.

Figures 1(a) and 1(b) show the ARUPS results of Ag or Cu/DIP systems as a function of the metal deposition amount, where spectra of DIP monolayer/Ag or Cu polycrystalline (poly) surface systems are also depicted. The bottom spectrum of each DIP film clearly shows no gap states. As metals are deposited on the DIP films, abundant gap states immediately appear and grow together with a distinct feature colored by green, which is resembled to the DIP/Ag or DIP/Cu systems. These results imply that the observed distinct feature in the metal/DIP systems is caused by CT interaction between the deposited metals and DIP. Thus, it can be concluded that SIAS can occur even for a top-contact condition as the same as a bottom-contact condition, which should be a key to realize Ohmic contacts in various organic devices. Furthermore, the molecular orientations do not effect formation of the CT state.

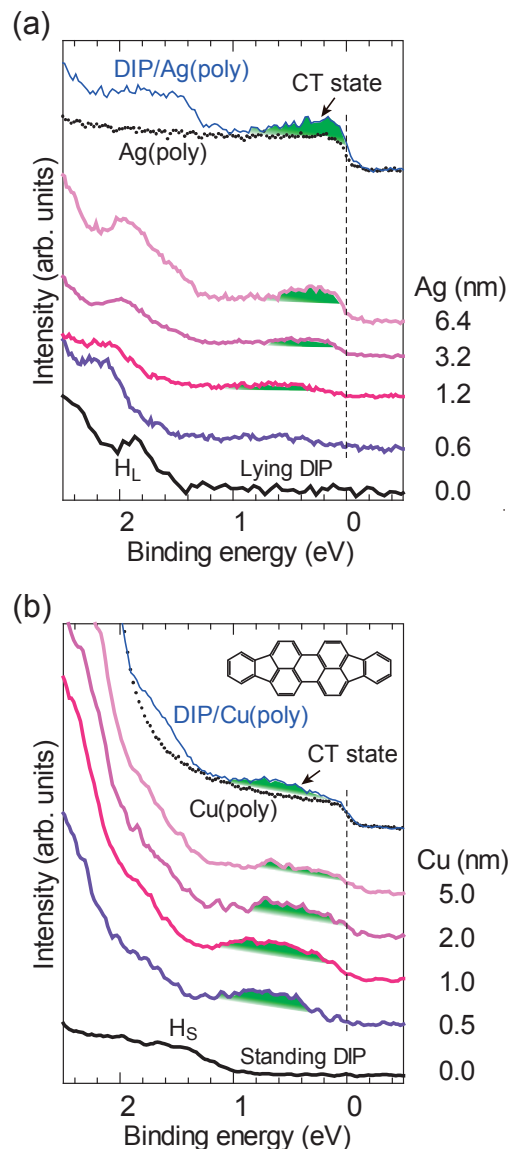


Fig. 1. ARUPS of Ag (a) and Cu (b) deposited on DIP (inset in (b)) thick films, where spectra of DIP monolayer on Ag(poly) or on Cu(poly) systems are also depicted. H_s and H_L indicates the highest occupied molecular orbital band of standing and lying DIP films.

[1] G. Heimel *et al.*, *Nature Chem.* **5** (2013) 187.[2] T. Hosokai *et al.*, *MRS proceedings 2013, 1647, mrsf13-1647-gg01-03.*[3] T. Hosokai *et al.*, *UVSOR Activity Report 2013* **41** (2014) 152.

The background is a solid purple color with several abstract geometric patterns. A large, semi-transparent circular graphic is centered on the right side, featuring concentric rings and a dotted border. Diagonal lines and a grid of small dots are also visible in the lower-left quadrant.

III-5

Life, Earth and
Planetary Sciences

BL4U

Quantitative Penetration Profiles of Free and Nanocarrier-Bound Dexamethasone in Human Skin Studied by Soft X-Ray Spectromicroscopy

K. Yamamoto¹, T. Ohigashi², Y. F. Wang², S. Hedtrich³, F. Rancan⁴, R. Flesch¹, A. Klossek¹, E. Fleige¹, S. Ahlberg⁴, A. Vogt⁴, U. Blume-Peytavi⁴, P. Schrade⁵, S. Bachmann⁵, R. Haag¹, M. Schäfer-Korting³, N. Kosugi² and E. Rühl¹

¹Institute for Chemistry and Biochemistry, Freie Universität Berlin, Takustr. 3, 14195 Berlin, Germany

²UVSOR Facility, Institute for Molecular Science, Okazaki 444-8585, Japan

³Institut für Pharmazie, Freie Universität Berlin, 14195 Berlin, Germany

⁴Charité Universitätsmedizin, 10117 Berlin, Germany

⁵Abteilung für Elektronenmikroskopie at CVK, 13353 Berlin, Germany

The penetration of topically applied drugs in skin is known to be enhanced by drug nanocarriers [1]. However, quantitative drug uptake studies with high spatial resolution in which the exposure time and drug formulation are systematically varied are lacking to date. We have investigated the uptake of the anti-inflammatory drug dexamethasone by human skin using soft X-ray spectromicroscopy.

Chemical selectivity of this approach is gained by excitation of the O 1s→ π^* -transition of dexamethasone at 530.65 eV, which is suitable to suppress the background absorption of fixed human skin as well as drug nanocarriers (core-multi-shell nanocarriers (CMS)), which were loaded by 5% dexamethasone. In addition, we used two different exposure times (4 h and 16 h) and varied the drug formulation, where either ethanolic solution or HEC gel (drug concentration: 0.5%) were used, respectively. Any cross sensitivities from absorption of untreated skin were subtracted, so that exclusively the drug concentration was monitored.

The experiments were performed at the BL4U beamline at UVSOR III using a scanning X-ray microscope (STXM), similar to previous work, in which the feasibility of this approach was explored [2,3].

Figure 1 shows a comparison of depth profiles of dexamethasone in different skin samples along with an optical micrograph, in which the skin regions are labeled (stratum corneum (SC), viable epidermis (VE), and dermis (D)). Figure 2 shows the integrated drug concentration for the samples under study, which facilitates to derive quantitative information regarding the drug distribution, if the exposure time and drug formulation are varied. Specifically, Fig. 1(a) indicates that after 4 h most of the drug is found in the SC, whereas a lower fraction is found in the VE (cf. Fig. 2). No drug is observed in the dermis (D). This situation changes, when 16 h of drug exposure in HEC gel are used (cf. Fig. 1(b) and Fig. 2). The intense maximum in the SC is weaker and the drug concentration in the VE is enhanced. If drug nanocarriers in HEC gel are used instead of the neat drug (cf. Fig. 1(c)), no drug signal was observed after 16 h in the SC rather than in the VE. This underscores the expected drug transport into deeper skin layers by

nanocarriers. A drop in local drug concentration is observed for all samples in the dermis (D). This indicates that in this region rapid clearance is possible, so that no enhanced drug concentration is observed.

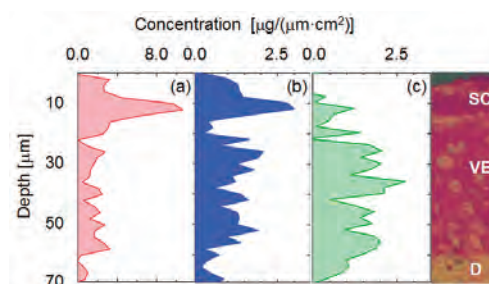


Fig. 1. Distribution of dexamethasone in the top skin layers (right hand side: typical optical micrograph, see text for details): (a) dexamethasone in ethanol: exposure time: 4 h; (b) dexamethasone in HEC gel: exposure time: 16 h; (c) CMS nanocarriers in HEC gel, exposure time: 16 h.

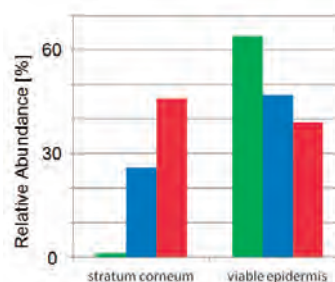


Fig. 2. Relative abundance of dexamethasone in the stratum corneum and viable epidermis (green: drug-loaded CMS nanocarriers in HEC gel, exposure time: 16 h; blue: dexamethasone in HEC gel: exposure time: 16 h; red: dexamethasone in ethanol: exposure time: 4 h) compared to the dose applied to skin.

[1] N. Alnasif, C. Zoschke, E. Fleige, R. Brodewolf, A. Boreham, E. Rühl, K.-M. Eckl, H.-F. Merk, H.-C. Hennies, U. Alexiev, R. Haag, S. Kuchler and M. Schäfer-Korting, *J. Control. Rel.* **185** (2014) 45.

[2] R. Flesch *et al.*, *UVSOR Activity Report 2013* **41** (2014) 156.

[3] K. Yamamoto, *et al.*, *Anal. Chem.*, *accepted* (2015) DOI : 10.1021/acs.analchem.5b00800

BL4U

Evaluation of Sample Damage of XANES and Application to the Analysis of Carbonaceous Materials in Hayabusa-Returned Samples

M. Uesugi and A. Nakato

Institute of Space and Astronautical Science, Japan aerospace exploration agency, Sagami-hara 252-5210, Japan

Hayabusa spacecraft has successfully retrieved regolith particles from the surface of asteroid Itokawa. Silicate materials found in the sample catcher of the Hayabusa spacecraft were typically 50 μ m in diameter, and their origin was confirmed by mineralogical, chemical and isotopic analyses in the preliminary examination of the Hayabusa- returned particles [e.g. 1-6].

Carbonaceous particles, those have been found in the sample catcher together with silicate particles, were still under the investigations, including precise determination of their origin. Results of isotopic analysis of H, C and N of the carbonaceous materials by NanoSIMS did not show any signatures of their extraterrestrial origin, i.e. isotopic anomalies against the terrestrial composition [7]. Some of the results of analyses by Transmission Electron Microscopy (TEM, [8]) and X-ray absorption near edge structure (XANES, [9]) indicated relation to the terrestrial material. Thus, those particles might indicate the contamination of terrestrial material into the sample catcher before, during and/or after the operation of Hayabusa spacecraft.

XANES analysis of C, N and O is useful for the characterization of molecular structure of the unknown carbonaceous material, which would relate to their origin. We expected to obtain the information for the source of contamination of Hayabusa spacecraft by comparing possible contaminants and Hayabusa-returned samples using XANES/STXM installed in UVSOR.

It is well known that high voltage electron beam of TEM could modify the C-XANES spectrum largely [9]. Thus TEM observation has generally been applied after XANES analysis. However, in this study, we focused on the sample damage induced C-XANES. To evaluate the damage, TEM observations were done before and after C-XANES analysis. As the results, TEM observations (Fig. 1) clearly show that if the sample contains NaCl or KCl inclusions, they would be damaged heavily by the XANES analysis. The phenomenon was also observed in the samples analyzed by other XANES/STXM instrument, though the detail of the process is uncertain.

This result should be important not only for the analyses of Hayabusa-returned samples, but also for the future analyses of Hayabusa2 returned samples. Because the amount of sample obtained directly by spacecraft is very small, sequential analysis will be inevitable for the characterization of those samples. In this case, we should construct the analytical flow

based on the sample damage effective to the downstream analyses. Results of XANES analyses of a Hayabusa-returned sample, RA-QD02-0180-03, showed clear relation to the particles collected by witness plates those exposed to the cleanroom of Hayabusa2 spacecraft, though the data should be re-examined carefully (in progress).

In future work, we will apply the XANES/STXM analysis to further possible contaminants such as rubbers and particles of biological materials, for the precise determination of the origin of carbonaceous particles in Hayabusa-returned samples.

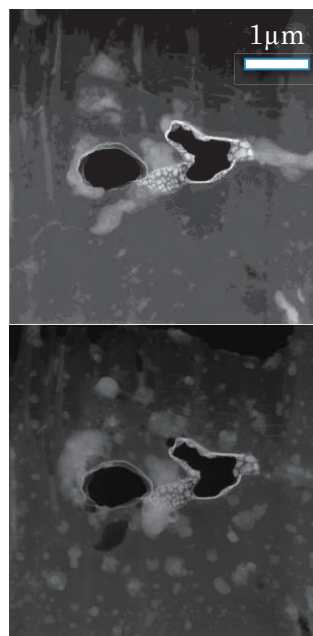


Fig. 1. STEM/DF image of the Ultra-thin section of carbonaceous material of a Hayabusa-returned sample, RA-QD02-0180-03 before (upper) and after (lower) the C-XANES analysis. White objects are the NaCl and KCl inclusions. We can observe the disrupted inclusions entire section after the C-XANES analysis.

- [1] T. Nakamura *et al.*, *Science* **333** (2011) 1113.
- [2] H. Yurimoto *et al.*, *Science* **333** (2011) 1116.
- [3] M. Ebihara *et al.*, *Science* **333** (2011) 1119.
- [4] A. Tsuchiyama *et al.*, *Science* **333** (2011) 1121.
- [5] T. Noguchi *et al.*, *Science* **333** (2011) 1125.
- [6] K. Nagao *et al.*, *Science* **333** (2011) 1128.
- [7] M. Ito *et al.*, *Earth planet. Space* **66** (2014) 102.
- [8] M. Uesugi *et al.*, *Earth planet. Space* **66** (2014) 102.
- [9] H. Yabuta *et al.*, *Earth planet. Space* **66** (2014) 156.

BL4U

Absorption Spectra of Bio-Cell Organelles in Cultural Fluid

T. Ejima¹, M. Kado², M. Aoyama³, K. Yasuda³ and T. Tamotsu³

¹IMRAM, Tohoku University, Sendai 980-8577, Japan

²Japan Atomic Energy Agency, Kizugawa 619-0215, Japan

³Dept. of Biological Sciences, Fac. of Science, Nara Women's University, Nara 630-8263, Japan

Organelles in bio-cells are composed of proteins, and the proteins consist of specific 20 kinds of amino acids. Spectra of these amino acids are known at C-K and N-K absorption edges [1], therefore absorption spectrum of a small organelle will be interpreted by a spectral combination of these amino acids in zero-th order approximation. If both position of organelles in a bio-cell and C-K and/or N-K absorption spectra at the organelles are measured simultaneously, positions and compositions of the organelles will be obtained in the bio-cell. Water-window wavelength region ($\lambda=2.3-4.5\text{nm}$) is suitable for this simultaneous measurements, because water is transparent and carbides and nitrides are absorbable, which are the principal components of proteins. On the other hand, the measurements have hardly been made especially for bio-cells of eukaryotes, because thickness of the eukaryotes cells is thick for absorption spectroscopy even in Water-window wavelength region. In addition, usual analytical method takes much time to separate the positions and spectra from measured SX images.

In this study, a Leydig cell in a mouse testis was used and thickness of the bio-cell was controlled with culture fluid under 5 μm thick by a sample holder. The thickness of the Leydig cell contained in the sample holder was measured by an interference

method, therefore the thickness of the bio-cells were confirmed as 5 μm or less. The SX images of the Leydig cells were taken under the spatial resolution of 200nm at around N-K absorption edge. Spectra and positions of the organelles in the Leydig cell were separated from the measured SX images by the use of image analysis methods [2], and absorption coefficients of the separated structures are also obtained. Obtained spectra are composed mainly of σ^* and π^* bonds, and shapes of small structures in the bio-cell depend on the density of the organelles.

[1] for example, Y. Zubavichus, A. Shaporenko, V. Korolkov, M. Grunze and M. Zharnikov, *J. Phys. Chem. B* **112** (2008) 13711.

[2] M. Lerotic, C. Jacobsen, J. B. Gillow, A. J. Francis, S. Wirick, S. Vogt and J. Maser, *J. Elec. Spectro. Rel. Phenom.* **144-147** (2005) 1137.

Acknowledgements

This work was supported by JSPS KAKENHI Grant Numbers 23241038 and by Nanotechnology Platform Program (S-13-MS-1002) of MEXT, Japan.

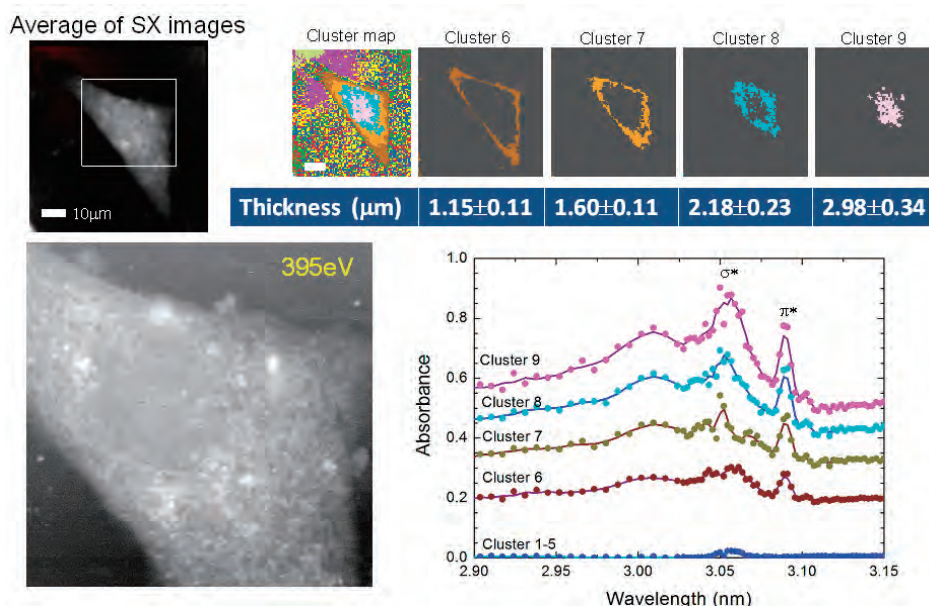


Fig. 1. From the measured sx images, cluster structures were separated according to the similar spectrum of each dot in the images. It are presented in the figure that an average sx image of the measured sx images (upper left), details of sx image at 395 eV (lower left), clusters separated and its thicknesses measured by an interference method (upper right), and absorption spectra of the clusters obtained from sx images (lower right).

BL4U

Evaluation of FIB Beam Damage in XANES Spectra of Organics in Meteorites: Preliminary Measurements for Implementation Planning of a Synchrotron Cosmochemistry Research Base at UVSOR BL4U

H. Yabuta¹, A. Takahashi¹, Y. Inagaki² and T. Ohigashi²

¹Department of Earth and Space Science, Osaka University, Osaka 560-0043, Japan

²UVSOR Facility, Institute for Molecular Science, Okazaki, 444-8585, Japan

This study aimed to evaluation of FIB beam damage in XANES spectra of organics in meteorites. However, unfortunately, it was impossible to carry out the analysis during the beam time in June, 2014, due to a mistake by a manufacturer (a maker) of placing a diffraction grating upside down, after their cleaning the carbon contamination. For this reason, the schedule had to be changed, and the analogue of organic materials in meteorite was analyzed by STXM during the beam time in December 2014. Carbon contamination on the surface of the mirror was still remained and it was difficult to acquire an ideal Carbon-XANES spectrum, and the measurements were limited to Nitrogen-XANES.

Paraformaldehyde (120 mg), glycolaldehyde (120 mg), $\text{NH}_3(\text{aq})$ (54 μl), $\text{Ca}(\text{OH})_2$ (30 mg) in 2 ml of water in a glass tube was heated at 90°C for 3-100 days [1-2]. After heating, the precipitation was rinsed with HCl and dried. The purified organic solids were suspended in ethanol and the suspension was dripped to the Cu-TEM grid (200 mesh) with SiO film using a micropipette. N-XANES spectra of the samples were acquired using a scanning transmission x-ray microscope (STXM) at the BL 4U, UVSOR.

Our previous study revealed that the organic solids include a number of micro spherules of 3-20 μm in diameter. Their size and shape distributions changed with a heating period of time. In contrast, N-XANES spectra of the organic solids were similar throughout a heating period of time (Fig. 1), exhibiting absorption peaks of imine ($\text{C}=\text{N}$) at 398.8 eV, protonated imine ($\text{C}=\text{NH}^+$) at 400.8 eV, and amide ($\text{NHx}(\text{C}=\text{O})\text{C}$) around at 401.6 eV, respectively. Combining the results by infrared analysis, these features imply that the organic microspherule is a self-organized polymer of a amphiphilic molecule including alkyl group and pi-bonding.

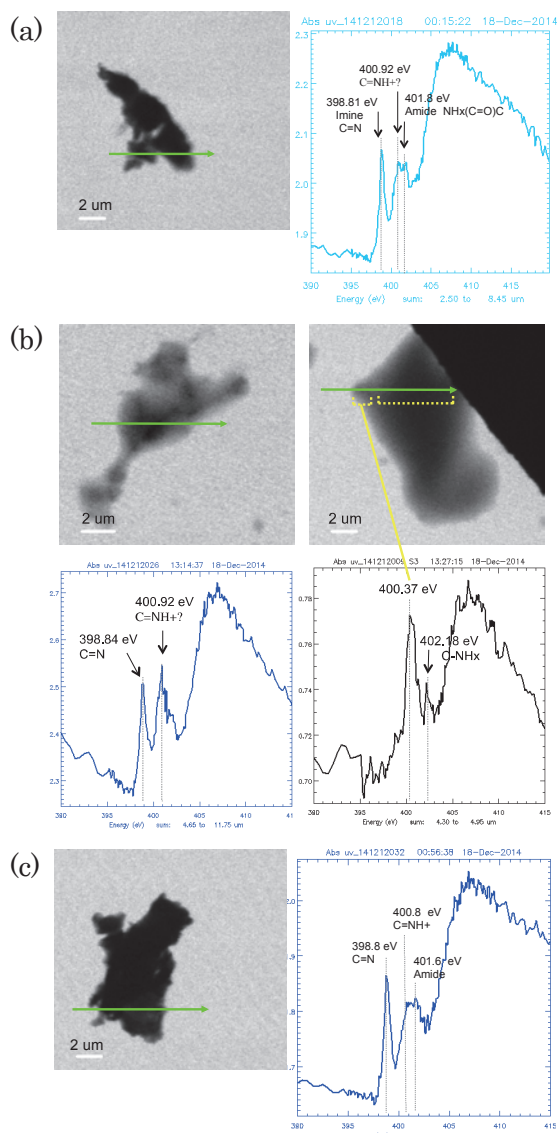


Fig. 1. N-XANES spectra of analogues of organic materials in meteorite, which were synthesized from formaldehyde and ammonia for different heating periods of times (a) 10 days, (b) 20 days, and (c) 60 days.

[1] G. D. Cody, E. Heying, C. M. O.'D. Alexander, L. R. Nittler, A. L. D. Kilcoyne, S. A. Sandford and R. M. Stroud, *PNAS* **108** (2011) 19171.

[2] Y. Kebukawa, A. L. D. Kilcoyne and G. D. Cody, *Astrophys. J.* **771** (2013) 19.

BL4U

Chemical Mapping of DNA and Protein in Isolated Cell Nuclei during Apoptotic Process Using STXM

A. Ito^{1,2}, T. Ohigashi^{2,3}, K. Shinohara¹, S. Tone⁴, M. Kado⁵, Y. Inagaki² and N. Kosugi²

¹*School of Engineering, Tokai University, Hiratsuka 259-1292, Japan*

²*UVSOR Facility, Institute for Molecular Science, Okazaki 444-8585, Japan*

³*The Graduate University for Advanced Studies (SOKENDAI), Okazaki 444-8585, Japan*

⁴*Department of Biochemistry, Kawasaki Medical School, Kurashiki 701-0192, Japan*

⁵*Japan Atomic Energy Agency, Kizugawa 619-0215, Japan*

Apoptosis is characterized as a programmed cell death controlled by the expression of the relating genes. One of the remarkable morphological features of cells which undergo apoptosis is the deformation of nuclei during the apoptotic process. Tone et al. observed the distribution change of DNA in isolated cell nuclei with the progression of apoptosis by labelling DNA with fluorescent dye [1]. They classified the apoptotic process into three characteristic stages, stage 1, 2 and 3. DNA in the normal nuclei (stage 0) proceeds to ring-shape structure (stage 1) accumulated in the peripheral region, followed by necklace-shape structure where the ring structure is broken intermittently (stage 2). Finally the nuclei are collapsed toward the center (stage 3). In the present study, we observed distributions of DNA as well as nuclear protein including histone, using chemical mapping of STXM with higher spatial resolution than optical microscope. Our previous study for the DNA mapping in mammalian cell nuclei was successfully achieved with the aid of the different XANES profiles between DNA and protein at the N-K absorption edge [2]. Chemical mapping was extended to apoptotic nuclei in this study.

XANES profiles of DNA and histone were measured by the STXM around the N-K absorption edge from 390 to 410 eV as reference spectra. Solution of these biomolecules was dropped on collodion membrane supported by an EM grid, and then dried in the air. S/M extract of chicken DU249 cells was used to induce apoptosis on isolated nuclei of human HeLa S3 cells. The nuclei were fixed with glutaraldehyde at the timing of four different stages described above, and dropped on Formvar membrane supported by EM grid, and then dried in the air.

The 61 X-ray transmission images (an energy stack) for each stage were acquired from 397 to 403 eV. The dwell time and scanning pitch were 10 ms and 0.1 μm , respectively. DNA and histone (protein) distributions were obtained fitting the reference spectra of DNA and histone to the energy stack by using aXis2000 software (fitting method). Alternatively the maps were obtained by the subtraction of images taken between at the top and the bottom of the resonance peak of DNA or histone (subtraction method).

Figure 1 shows distributions of DNA and protein in

four stages of apoptosis. In the case of normal nuclei at the stage 0 shown by the panel a, b and c, DNA and protein were distributed in the nearly whole nucleus with similar pattern, since nucleus mainly consists of chromatin, a complex structure of DNA and proteins. At the stage 1, DNA and protein were accumulated in the ring shape on the rim of nucleus (panel e and f). The width of the ring was less than 0.5 μm . Note that in the central part of the nucleus DNA seems to be distributed more preferentially than protein. In addition, an image of “constant” (panel g), which means the existence of molecules with no spectral feature at the N-K absorption edge, shows significant distribution in the inner region. The identification of the molecules is an issue for the future research. These distributions of DNA and protein were also confirmed by the subtraction method. For the stages 2 and 3, remarkable difference was not observed between DNA and protein maps. Necklace structure in the stage 2 as shown by arrows in panel h was evident in both DNA and protein maps. To improve the quality of the images, reproducibility of reference spectra and the acquisition time to assure enough photon counts per pixel should be considered.

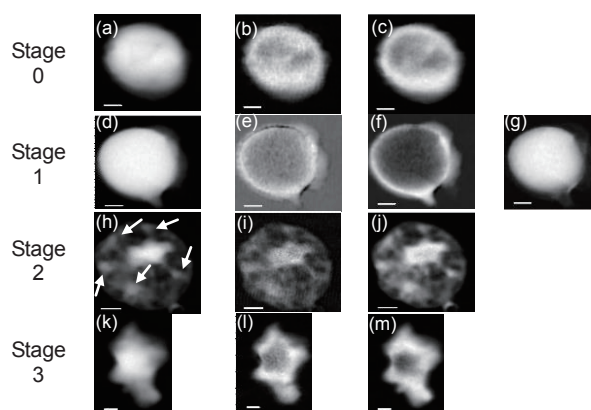


Fig. 1 Distributions of DNA and protein in four stages of apoptotic nuclei.

X-ray image at 397 eV: (a), (d), (h), (k); DNA map: (b), (e), (i), (l); protein map: (c), (f), (j), (m); constant map: (g)

bar: 1 μm (stage 0, 1, 3), 2 μm (stage 2)

[1] Toné *et al.*, *Exp. Cell Res.* **313** (2007) 3635.

[2] T. Ohigashi *et al.*, *UVSOR Activity Report* 2013 **41** (2014) 158.

BL4U

Observation of Prokaryotic Organelles of Musty-Odor Producing Filamentous Cyanobacterium Using STXM

K. Takemoto^{1,2}, M. Yoshimura², T. Ohigashi^{2,3} and H. Kihara^{2,4}

¹Department of Physics, Kansai Medical University, Hirakata 573-1010, Japan

²SR center, Ritsumeikan University, Kusatsu 525-8577, Japan

³UVSOR Facility, Institute for Molecular Science, Okazaki 444-8585, Japan

⁴Himeji Hinomoto College, Himeji 679-2151, Japan

In a source of potable water, musty-odor produced by blue-green algae suddenly appear all over the world. Since 1969, a problem of musty-odor in potable water has occurred due to sudden propagation of *Phormidium tenue* (*Pseudanabaena* sp.) green strain (PTG) in Lake Biwa. Because there are few studies on PTG, an exhaustive study of PTG is required of water resource managers.

PTG is a small filamentous cyanobacterium, and the trichome consists of cells 1.0–1.6 μm in width, and 2.5–10 μm in length. Due to a diffraction limit, light microscope (LM) is impossible to provide intracellular observation with a sufficient spatial resolution. Therefore, we applied a soft X-ray microscope (XM) to PTG observation. The XM is capable of imaging thick and untreated specimens, allowing viewers to investigate whole cells up to 10 μm thick with much higher resolution than LM. In our full field transmission soft XM observation, several intracellular granules were observed. [1].

Based on the transmission electron microscopy (TEM) observation and the energy dispersive X-ray (EDX) analysis on low temperature/low vacuum scanning electron microscope (LT/LV SEM), we inferred that the granules were polyphosphate and/or carboxysome. Carboxysome is one of the bacterial microcompartment that contains enzymes, RuBisCO, involved in carbon dioxide fixation. Polyphosphate granule is one of the bacterial microcompartment that is characterized by their high content of phosphorus. Polyphosphate has the general formula $M_{(n+2)}P_nO_{(3n+1)}$, where M is H^+ or monovalent metal cation [2]. However, there is no objective evidence to identify them. In this study, it is aimed to obtain the objective evidence to identify them using oxygen K-edge X-ray absorption near edge structure (XANES).

Oxygen K-edge XANES spectra were collected on the scanning transmission X-ray microscope (STXM) at UVSOR BL4U [3]. PTG was isolated from Lake Biwa and culture was carried out under the fixed condition for four weeks [1].

Figure 1 shows a STXM image of the distribution of oxygen in PTG. Four oxygen accumulated granules were confirmed. Characterization of intracellular granules was performed by oxygen K-edge XANES (Fig. 2). The spectrum from cytoplasm shows an intense pre-peak. On the other hand, the spectrum from granule shows a small pre-peak at the same

energy region. Although the pre-peak energies are almost similar, the main edge energy of the granule shifts towards lower than that of cytoplasm. To identify the granules, we intend to promote a more detailed analysis.

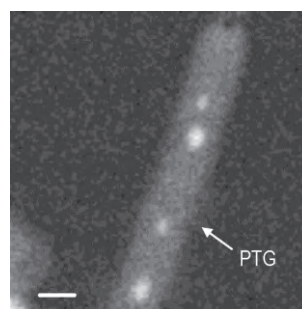


Fig. 1. Distribution of oxygen in PTG. Scale bar is 1 μm .

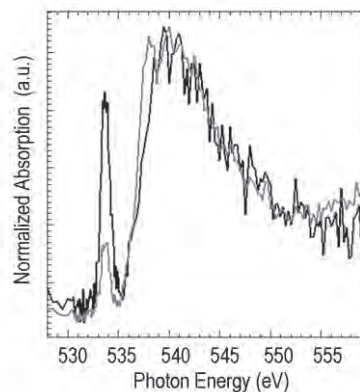


Fig. 2. Oxygen-XANES spectra of cytoplasm (black line) and granule (gray line).

[1] K. Takemoto *et al.*, Jpn. J. Water Treat. Biol. **48** (2012) 157. [in Japanese.]

[2] I.S. Kulaev *et al.*, The Biochemistry of Inorganic Polyphosphates, 2nd Ed., John Wiley & Sons, Inc., New York (2004) 3.

[3] T. Ohigashi *et al.*, J. Phys. Conf. Ser. **463** (2013) 012006.

BL4U

Skin Penetration Study of Drug Carriers Using Soft X-Ray Spectromicroscopy

P. Pan-In¹, T. Ohigashi^{2,3}, N. Kosugi^{2,3} and S. Wanichwecharungruang¹

¹Department of Chemistry, Faculty of Science, Chulalongkorn University, Bangkok 10330, Thailand

²UVSOR Facility, Institute for Molecular Science, Okazaki 444-8585, Japan

³School of Physical Sciences, The Graduate University for Advanced Studies (SOKENDAI), Okazaki 444-8585, Japan

Skin is a natural barrier to protect human body and control molecular transports from and into the body. Nanoparticles can be developed to deliver drugs both into the skin and through the skin into the circulation. Although it has been stated that drug/bioactive molecules can penetrate through skin barrier via intracellular, intercellular and follicular pathways [1, 2], recent researches have proven that the follicular pathway is important for the nanoparticulate drug delivery systems [3]. Researchers have shown that nanoparticles with appropriated sizes could penetrate well into skin via hair follicle because the rigid hair shafts acted as the geared pump that upon movement or massage the particles could be pushed down. The loaded drugs could then be stored more than 10 days in hair follicles [3].

Thus, the aim of this research is to study the skin penetration level of oxidized carbon nanoparticles with the size between 150-800 nm [4]. BODIPY® FL (4,4-Difluoro-5,7-Dimethyl-4-Bora-3a,4a-Diazas-indacene-3-Propionic Acid) was grafted on the particles. Porcine skin penetration of the particles was investigated *ex vivo*. The BODIPY-grafted particles were massaged on fresh porcine skin samples at the coverage of 100 µg/cm² and the applied skin was left for 30 minutes before being subjected to the treatment with 4% glutaraldehyde and then cryo-sectioning. The thickness of the skin sections was 400 nm. Then, the skin samples were mounted on Cu grids (300-mech) and subjected to the soft X-ray microscopic investigation. The experiment was carried out at the B 1s-edge (170-200 eV) for tracking the BODIPY-grafted particles.

The soft X-ray experiment was performed at the BL4U beamline at UVSOR using a scanning X-ray microscope (STXM) [5]. The experimental design was that the presence of the boron element in the BODIPY® FL (Fig. 1) could make a significant difference in X-ray signal when compared to signals from tissue with no BODIPY® FL. Chemical selectivity was obtained from excitation at the B 1s-edge (170-200 eV). The presence of the 182 eV peak observed in the B 1s-absorption of only the BODIPY-grafted particles, not the skin tissue (Fig. 2), provided a chemical selectivity for tracking the carrier uptake into porcine skin.

Unfortunately, the (BODIPY-grafted particle)-treated porcine skin samples did not show any obvious 182 eV peak in their B 1s spectra, even at the

very uppermost location where the carriers were applied. We speculate a too low concentration of the BODIPY moieties in the particles. To investigate for the skin penetration ability of this carrier in the future, a more intense BODIPY labeling will be required. In addition, skin application at a high dose will be needed.

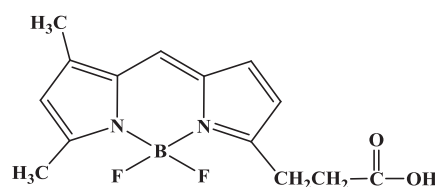


Fig. 1. Structure of BODIPY® FL.

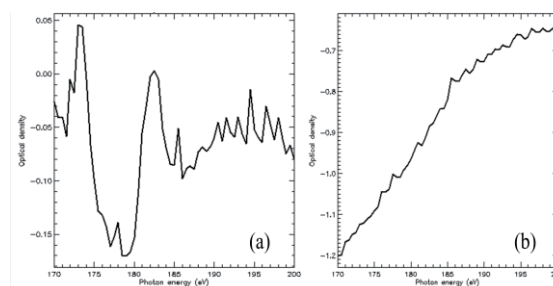


Fig. 2. B 1s excitation of BODIPY-grafted particles (a) and porcine skin (b).

[1] M. A. Bolzinger *et al.*, *Curr. Opin. Colloid Interface Sci.* **17** (2012) 156.

[2] K. Moser *et al.*, *Eur. J. Pharm. Biopharm.* **52** (2001) 103.

[3] J. Lademann *et al.*, *Skin Pharmacol. Physiol.* **19** (2006) 232.

[4] S. Arayachukiat *et al.*, *Nano Lett.* Accepted (2015).

[5] T. Ohigashi *et al.*, *J. Phys.: Conf. Ser.* **463** (2013) 012006.

Farewell Parties



The background is a vibrant red color with a complex, abstract design. It features several overlapping circular and linear elements. A prominent feature is a large, semi-transparent circular graphic on the right side, composed of concentric rings and a dotted border. Diagonal lines and smaller circles are scattered throughout the composition, creating a sense of depth and movement.

IV

List of Publications

List of Publications

- K. Eguchi, Y. Takagi, T. Nakagawa and T. Yokoyama, “**Growth Process and Magnetic Properties of Iron Nanoparticles Deposited on $\text{Si}_3\text{N}_4/\text{Si}(111)-(8 \times 8)$** ”, *Phys. Rev. B* **85** (2012) 174415.
- K. Eguchi, Y. Takagi, T. Nakagawa and T. Yokoyama, “**Magnetic Interactions of Vanadyl Phthalocyanine with Ferromagnetic Iron, Cobalt, and Nickel Surfaces**”, *J. Phys. Chem. C* **118** (2014) 17633.
- K. Eguchi, Y. Takagi, T. Nakagawa and T. Yokoyama, “**Molecular Orientation and Electronic States of Vanadyl Phthalocyanine on $\text{Si}(111)$ and $\text{Ag}(111)$ Surfaces**”, *J. Phys. Chem. C* **117** (2013) 22843.
- K. Eguchi, Y. Takagi, T. Nakagawa and T. Yokoyama, “**Passivating Effect of $\text{Si}(111)-(\sqrt{3} \times \sqrt{3})\text{Ag}$ and $\text{Si}_3\text{N}_4/\text{Si}(111)-(8 \times 8)$ Buffer Layers**”, *J. Phys.: Conf. Ser.* **430** (2013) 012129.
- T. Hajiri, T. Ito, M. Matsunami, B. H. Min, Y. S. Kwon and S. Kimura, “**Anomalous Superconducting-Gap Structure of Slightly Overdoped $\text{Ba}(\text{Fe}_{1-x}\text{Co}_x)_2\text{As}_2$** ”, *J. Phys. Soc. Jpn.* **83** (2014) 093703.
- T. Hajiri, T. Ito, M. Matsunami, B. H. Min, Y. S. Kwon and S. Kimura, “**Polarization-Dependent Three-Dimensional Angle-Resolved Photoemission Spectroscopy of $\text{BaFe}_{1.8}\text{Co}_{0.2}\text{As}_2$** ”, *JPS Conf. Proc.* **3** (2014) 015028.
- Y. Hikosaka, Y. Shibata, K. Soejima, H. Iwayama and E. Shigemasa, “**Site-Specific Formation of Metastable Dications Following Inner-Shell Ionization of CO_2** ”, *Chem. Phys. Lett.* **603** (2014) 46.
- U. Hörmann, C. Lorch, A. Hinderhofer, A. Gerlach, M. Gruber, J. Kraus, B. Sykora, S. Grob, T. Linderl, A. Wilke, A. Opitz, R. Hansson, A. S. Anselmo, Y. Ozawa, Y. Nakayama, H. Ishii, N. Koch, E. Moons, F. Schreiber and W. Brütting, “ **V_{oc} from a Morphology Point of View: the Influence of Molecular Orientation on the Open Circuit Voltage of Organic Planar Heterojunction Solar Cells**”, *J. Phys. Chem. C* **118** (2014) 26462.
- T. Hosokai, K. Yonezawa, K. Kato, R. Makino, J. Yang, K. R. Koswattage, A. Gerlach, F. Schreiber, N. Ueno and S. Kera, “**Structural Requirements for Surface-Induced Aromatic Stabilization**”, *MRS Proceedings* **1647** (2014).
- E. Ieki, K. Nakayama, Y. Miyata, T. Sato, H. Miao, N. Xu, X.-P. Wang, P. Zhang, T. Qian, P. Richard, Z.-J. Xu, J. S. Wen, G. D. Gu, H. Q. Luo, H.-H. Wen, H. Ding and T. Takahashi, “**Evolution from Incoherent to Coherent Electronic States and Its Implications for Superconductivity in $\text{FeTe}_{1-x}\text{Se}_x$** ”, *Phys. Rev. B* **89** (2014) 140506.
- S. Ishida, Y. Sugizaki, T. Nakamura, K. Edamoto, M. Matsunami, T. Hajiri and S. Kimura, “**Electronic Structure of $\text{Ni}_2\text{P}(0001)$ Studied by Resonant Photoelectron Spectroscopy**”, *e-J. Surf. Sci. Nanotech.* **13** (2015) 93.
- M. Kaneko, M. Saito, T. Ito, K. Imura, T. Hajiri, M. Matsunami, S. Kimura, H. S. Suzuki and N. K. Sato, “**Angle-Resolved Photoemission Study on Insulator-to-Metal Transition of $\text{Sm}_{1-x}\text{Y}_x\text{S}$** ”, *JPS Conf. Proc.* **3** (2014) 011080.
- M. Kitaura, S. Tanaka and M. Itoh, “**Optical Properties and Electronic Structure of Lu_2SiO_5 Crystals Doped with Cerium Ions: Thermally-Activated Energy Transfer from Host to Activator**”, *J. Lumi.* **158** (2015) 226.
- M. Kitaura, A. Sato, K. Kamada, S. Kurosawa, A. Ohnishi, M. Sasaki and K. Hara, “**Photoluminescence Studies on Energy Transfer Processes in Cerium-Doped $\text{Gd}_3\text{Al}_2\text{Ga}_3\text{O}_{12}$ Crystals**”, *Opt. Mater.* **41** (2015) 45.

- M. Koshimizu, T. Yanagida, Y. Fujimoto, A. Yamazaki, K. Watanabe, A. Uritani, K. Fukuda, N. Kawaguchi, S. Kishimoto and K. Asai, **“Origin of Fast Scintillation Components of LiCaAlF₆ Crystals”**, Appl. Phys. Express **6** (2013) 062601.
- M. Koshimizu, N. Yahaba, R. Haruki, F. Nishikido, S. Kishimoto and K. Asai, **“Scintillation and Luminescence Properties of a Single CsCaCl₃ Crystal”**, Opt. Mater. **36** (2014) 1930.
- S. Mitsunobu, M. Zhu, Y. Takeichi, T. Ohigashi, H. Suga, H. Makita, M. Sakata, K. Ono, K. Mase and Y. Takahashi, **“Nanoscale Identification of Extracellular Organic Substances at the Microbe-Mineral Interface by Scanning Transmission X-Ray Microscopy”**, Chem. Lett. **44** (2015) 91.
- T. Miyazaki, R. Sumii, H. Tanaka, K. Amemiya and S. Hino, **“Surface Electronic Structures of Lithium Nickel Oxide Solid Solutions: Selective Methane Oxidation”**, Res. Chem. Intermed DOI 10.1007/s11164-014-1820-5.
- T. Miyazaki, S. Okita, T. Ohta, H. Yagi, R. Sumii, H. Okimoto, Y. Ito, H. Shinohara and S. Hino, **“Ultraviolet Photoelectron Spectra of Ce₂@C₈₀ and La₂@C₈₀”**, Chem. Phys. **447** (2015) 71.
- M. Nagasaka, H. Yuzawa, T. Horigome and N. Kosugi, **“In Operando Observation System for Electrochemical Reaction by Soft X-Ray Absorption Spectroscopy with Potential Modulation Method”**, Rev. Sci. Instrum. **85** (2014) 104105.
- M. Nagasaka, K. Mochizuki, V. Leloup and N. Kosugi, **“Local Structures of Methanol-Water Binary Solutions Studied by Soft X-Ray Absorption Spectroscopy”**, J. Phys. Chem. B **8** (2014) 4388.
- A. Nakahira, H. Nishimoto, Y. Hamada and Y. Yamasaki, **“Synthesis and Characterization of Dense Mesoporous Alumina”**, Key Engineering Materials **616** (2014) 252.
- K. Nishimura, T. Yoshioka and T. Yamamoto, **“Substitution Mechanism of Mn and Fe Ions in Bi₄Ti₃O₁₂”**, IEEE Trans. Mag. **50** (2014) 2502306.
- J. Okabayashi, J. W. Koo, H. Sukegawa, S. Mitani, Y. Takagi, and T. Yokoyama, **“Perpendicular Magnetic Anisotropy at the Interface between Ultrathin Fe Film and MgO Studied by Angular-Dependent X-Ray Magnetic Circular Dichroism”**, Appl. Phys. Lett. **105** (2014) 122408.
- Y. Ozawa, Y. Nakayama, S. Machida, H. Kinjo and H. Ishii, **“Maximum Probing Depth of Low-Energy Photoelectrons in an Anamorphous Organic Semiconductor Film”**, J. Electron Spectrosc. Relat. Phenom. **197** (2014) 17.
- E. Roussel, C. Evain, C. Szwaj, S. Bielawski, J. Raasch, P. Thoma, A. Scheuring, M. Hofherr, K. Ilin, S. Wünsch, M. Siegel, M. Hosaka, N. Yamamoto, Y. Takashima, H. Zen, T. Konomi, M. Adachi, S. Kimura and M. Katoh, **“Microbunching Instability in Relativistic Electron Bunches: Direct Observations of the Microstructures Using Ultrafast YBCO Detectors”**, Phys. Rev. Lett. **113** (2014) 094801.
- E. Roussel, C. Evain, M. L. Parquier, C. Szwaj, S. Bielawski, M. Hosaka, N. Yamamoto, Y. Takashima, M. Shimada, M. Adachi, H. Zen, S. Kimura and M. Katoh, **“Transient Response of Relativistic Electron Bunches to Wave-Number Selected Perturbations near the Microbunching Instability Threshold”**, New J. Phys. **16** (2014) 063027.
- Y. Shimizu, K. Ueda, H. Takashima and Y. Inaguma, **“UV Cathodoluminescence of Gd³⁺ Doped and Gd³⁺-Pr³⁺ Co-Doped YAlO₃ Epitaxial Thin Films”**, Phys. Status Solidi A **212** (2015) 703.
- S. Tanaka, T. Otani, K. Fukuzawa, K. Ogawa, J. Azuma, I. Yamamoto, K. Takahashi, M. Kamada and I. Hiromitsu, **“Anomalous Photoelectric Emission from Ag on Zinc-Phthalocyanine Film”**, Appl. Phys. Lett. **104** (2014) 193304.
- M. Uesugi, H. Naraoka, M. Ito, H. Yabuta, F. Kitajima, Y. Takano, H. Mita, I. Ohnishi, Y. Kebukawa, T. Yada, Y. Karouji, Y. Ishibashi, T. Okada and M. Abe, **“Sequential Analysis of Carbonaceous Materials in Hayabusa-Returned Samples for the Determination of Their Origin”**, Earth, Planets and Space **66** (2014) 102.

K. Wakui, K. Hayasaka and T. Ido, **“Generation of Vacuum Ultraviolet Radiation by Intracavity High-Harmonic Generation Toward State Detection of Single Trapped Ions”**, Appl. Phys. B: Lasers and Optics **117** (2014) 957.

N. Yahaba, M. Koshimizu, Y. Sun, T. Yanagida, Y. Fujimoto, R. Haruki, F. Nishikido, S. Kishimoto and K. Asai, **“X-Ray Detection Capability of a Cs₂ZnCl₄ Single-Crystal Scintillator”**, Appl. Phys. Express **7** (2014) 062602.

N. Yamamoto, H. Zen, M. Hosaka, T. Konomi, M. Adachi, K. Hayashi, J. Yamazaki, Y. Takashima and M. Katoh, **“Beam Injection with Pulsed Multipole Magnet at UVSOR-III”**, Nucl. Instrum. Methods Phys. Res. A **767** (2014) 26.

T. Yanagida, Y. Fujimoto and M. Koshimizu,

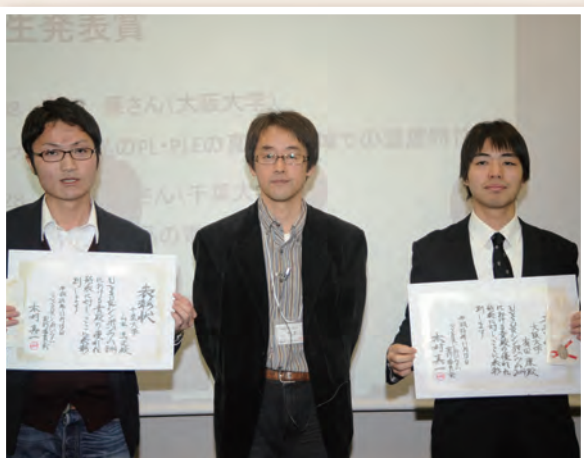
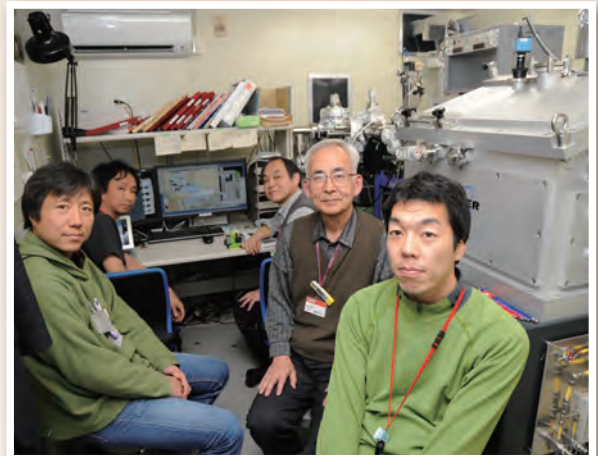
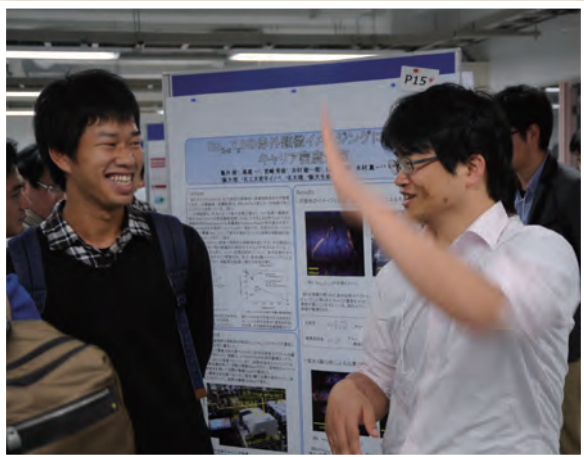
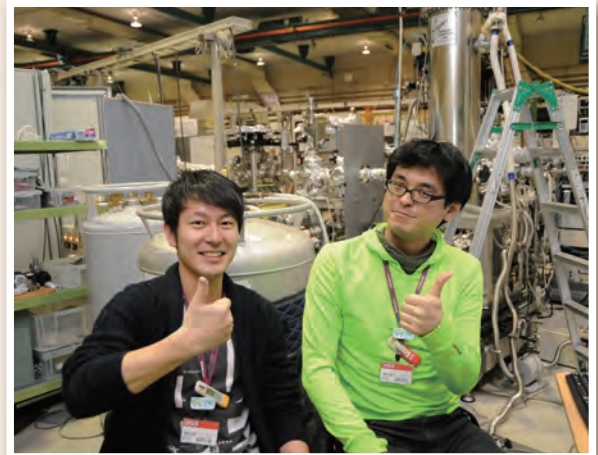
“Evaluation of Scintillation Properties of GaN”, e-J. Surf. Sci. Nanotech. **12** (2014) 396.

T. Yanagida, Y. Fujimoto, M. Koshimizu, K. Watanabe, H. Sato, H. Yagi and T. Yanagitani, **“Positive Hysteresis of Ce-Doped GAGG Scintillator”**, Opt. Mater. **36** (2014) 2016.

T. Yanagida, Y. Fujimoto, M. Koshimizu and K. Fukuda, **“Scintillation Properties of CdF₂ Crystal”**, J. Lumin. **157** (2015) 293.

K. Yoshida, T. Sonobe, H. Zen, K. Hachiya, K. Okumura, K. Mishima, M. Inukai, H. Negm, K. Torgasin, M. Omer, R. Kinjo, T. Kii, K. Masuda and H. Ohgaki, **“Effect of Microwave Irradiation on the Electronic Structure of ZnO”**, J. Phys. Chem. Sol. **83** (2015) 47.

User and Symposium



The background features a large, stylized graphic of concentric circles and radiating lines, resembling a sunburst or a stylized 'V' shape. The circles are composed of dashed lines and small dots, creating a textured effect. The overall color palette is a range of warm, earthy tones from light beige to deep brown.

V

Workshops

UVSOR Symposium 2014

Date: November 14-15, 2014

Place: Okazaki Conference Center, Okazaki, Japan

November 14th (Fri)

13:00 - 13:05 Opening remarks

T. Ohigashi (UVSOR)

<Session 1, Chair: **M. Kitaura**>

13:05 - 13:15 Present status of UVSOR light source accelerator

M. Katoh (UVSOR)

13:15 - 13:35 Development of application technology of coherent light source and solid state spectroscopy

S. Kimura (Osaka Univ.)

13:35 - 13:55 Spin-, orbital symmetry-, and momentum-resolved photoemission spectroscopy at new beamline BL5U

K. Tanaka (UVSOR)

13:55 - 14:15 Optical properties of $\text{Ca}_x\text{Sr}_{1-x}\text{F}_2$

K. Toyama (Nagoya Institute Tech.)

14:15 - 14:35 Morphological control and photoconductive properties of YF_3 thin films prepared by pulsed laser deposition

H. Ishikawa (Nagoya Institute Tech.)

14:35 - 15:05 Coffee break

<Session 2, Chair: **K. Tanaka**>

15:05 - 15:25 Development of the photoelectron spectroscopy beamline suited for organic molecular solids: BL2B reconstruction II

S. Kera (IMS)

15:25 - 15:45 Ultraviolet photoemission spectra of $\text{Sc}_2\text{C}_2@C_{82}$ and encapsulated cluster structure

T. Miyazaki (Ehime Univ.)

15:45 - 16:05 Application of scanning transmission X-ray microscopy into study on microbe-metal-mineral

S. Mitsunobu (Shizuoka Prefecture Univ.)

16:05 - 16:25 Auger decay and specific photofragmentation of *cis*-hexafluorocyclobutane

K. Okada (Hiroshima Univ.)

16:25 - 16:55 [Invited] Studies at UVSOR: From anthracene, supercritical Xe, C_{60} to amino acids and nuclear bases

K. Nakagawa (Kobe Univ.)

<Poster Session & Banquet>

17:30 - 18:00 Poster Session A

18:00 - 18:30 Poster Session B

18:30 - 21:00 Banquet

November 15th (Sat)

<Session 3, Chair: **T. Hirahara**>

9:00 - 9:20 Missions of IMS and UVSOR

N. Kosugi (UVSOR)

9:20 - 9:50 [Invited] Local structures of aqueous solutions studied by soft X-ray absorption spectroscopy

- 9:50 - 10:10 **N. Nagasaka** (IMS)
Angle- resolved photoemission study of $\text{Sm}_{1-x}\text{Y}_x\text{S}$ and YbPtSb
T. Ito (Nagoya Univ.)
- 10:10 - 10:30 Time-resolved measurements of photoluminescence from dielectrics using SR in a single-bunch mode
Y. Ohki (Waseda Univ.)
- 10:30 - 10:50 Coffee Break

<Session 4, Chair: **E. Shigemasa**>

- 10:50 - 11:10 Comprehensive study of photo-excited states of solids by VUV luminescence spectroscopy
M. Kitaura (Yamagata Univ.)
- 11:10 - 11:30 Relationship between chemical bond and perpendicularly magnetic anisotropy in FeCo alloy/MgO interfaces revealed by XMCD
J. Okabayashi (Tokyo Univ.)
- 11:30 - Discussion and closing remarks
S. Kimura (Osaka Univ.)

<Poster Session>

- P01 Intrinsic luminescence and energy transfer from self-trapped excitations in binary rare-earth borates under vacuum UV excitation
A. Abe (Akita Univ.)
- P02 Oxygen evolution catalyst studied by electrochemical soft X-ray XAFS
Y. Mitsutomi (Keio Univ.)
- P03 Observation of DNA and protein distributions in mammalian cell nuclei using STXM
T. Ohgashi (UVSOR)
- P04 Energy transfer from Tl^+ to In^+ in $\text{NaCl}:\text{Tl}^+$, In^+
A. Iguchi (Osaka Prefecture Univ.)
- P05 CEES measurements of the high concentration boron-doped diamond films
S. Kondou (Fukui Univ.)
- P06 Development of spectroscopic ellipsometry for VIS-VUV region
Y. Kubo (Fukui Univ.)
- P07 Emission and excitation spectrum of $\alpha\text{-CN}_x$
K. Ikeda (Fukui Univ.)
- P08 Temperature dependence of PL and PLE of fluoride crystals in VUV region
R. Arita (Osaka Univ.)
- P09 Electronic state calculation of Lu-containing fullerene by density function theory (DFT)
G. Takasumi (Ehime Univ.)
- P10 Optical properties and an APES model of RbCl crystals doped with Au- ions
S. Yamasuso (Osaka Prefecture Univ.)
- P11 Infrared spectroscopy of photo induced Defects in $\text{Ce}^{3+}:\text{GAGG}$ Crystals
R. Inaba (Yamagata Univ.)
- P12 Features and origin of the α luminescence band in NaCl: Au- crystals
T. Kawai (Osaka Prefecture Univ.)
- P13 Reflectance spectra of alanine single crystals in vacuum ultraviolet region
S. Tanaka (Yamagata Univ.)
- P14 Generation of gamma-ray by inverse Compton scattering at BL1U and its application
H. Zen (Kyoto Univ.)
- P15 Carrier density mapping of $\text{Sm}_{1-x}\text{Y}_x\text{S}$ by infrared micro-spectroscopic imaging

- S. Kamei** (Osaka Univ.)
- P16 Observation of solid-liquid interface by soft X-ray absorption spectroscopy in transmission mode
H. Yuzawa (IMS)
- P17 Electronic structure of chlorophyll a investigated by photoelectron spectroscopy and photoelectron yield spectroscopy
Y. Takeda (Chiba Univ.)
- P18 Site-specific formation of metastable dications following inner-shell ionization of CO₂
Y. Hikosaka (Niigata Univ.)
- P19 Photoinduced change of vacuum ultra-violet absorption spectra in amorphous chalcogenide thin films
K. Hayashi (Gifu Univ.)
- P20 Control of spectral response using compound fluoride materials Ca_xSr_{1-x}F₂
S. Otani (Nagoya Institute Tech.)
- P21 Band gap and luminescent property of infrared emission scintillator crystals
A. Yamaji (Tohoku Univ.)
- P22 Filterless VUV detector development by using CaF₂ thin films
H. Ishikawa (Nagoya Institute Tech.)
- P23 Direct observation of electronic structure of insulating polymer to clarify the mechanism of contact electrification
T. Sato (Chiba Univ.)
- P24 Spectator auger decay of *cis*-hexafluorocyclobutane across the F K threshold
T. Kaneda (Hiroshima Univ.)
- P25 Observation of the electronic structure of Au (111) /Octanethiol/Copper phthalocyanine by ultraviolet photoelectron spectroscopy
M. Yamamoto (Chiba Univ.)
- P26 Site-specific photofragmentation of the F K-shell excited *cis*-hexafluorocyclobutane molecule probed by the auger-electron-photoion coincidence method
S. Ishikawa (Hiroshima Univ.)
- P27 Multi-electron coincidence study of electron emission from condensed water
R. Mashiko (Niigata Univ.)
- P28 The electronic structure of pentacene single crystal
M. Yamamoto (Chiba Univ.)
- P29 Three-dimensional angle-resolved photoemission study on heusler-type Fe₂VAl thermoelectric materials
H. Miyazaki (Nagoya Institute Tech.)
- P30 Photoemission spectroscopy for valence fluctuating quasicrystal and approximant
M. Matsunami (UVSOR)
- P31 Angle-resolved photoemission study on LuPtSb
E. Tsuiki (Nagoya Univ.)
- P32 Low-photon-energy polarization-dependent angle-resolved photoemission study of quasi-one dimensional organic conductor (TMTSF)₂SbF₆
M. Mitamura (Nagoya Univ.)
- P33 Specification of the ionization energy of HAT-CN and its dependence on the atmosphere by ultraviolet photoelectron and photoelectron yield spectroscopies
A. Yoneyama (Chiba Univ.)
- P34 XAS measurements on leydig cell of mice tistis in cultural fluid
T. Ejima (Tohoku Univ.)
- P35 Preparation of evaporated films of amino acids and nuclear bases for SR spectroscopy
K. Ishiyama (Kobe Univ.)
- P36 Wide energy range absorption spectra of 20 amino acids and 5 nuclear bases
H. Tanaka (Kobe Univ.)





Editorial Board : T. Ohigashi H. Iwayama Y. Inagaki M. Sakai H. Hagiwara

**Institute for Molecular Science
National Institutes of Natural Sciences
Okazaki 444-8585, Japan**

Tel: +81-564-55-7402

Fax: +81-564-54-7079

<http://www.uvsor.ims.ac.jp>

ISSN 0911-5730

UVSOR ACTIVITY REPORT 2014

Preface

N. Kosugi

Obituary

News

I. Organization and Staff List 1

II. Current Status of Light Sources and Beamlines 7

Light Sources in 2014 (M. Katoh) 9

Beamlines in 2014 (E. Shigemasa) 13

III. Research Activities

III-1. Accelerators and Instruments 31

Measurement of Temporal Response of Transmission-Type Spin-Polarized Photocathodes [[Light Sources](#)] 33
T. Inagaki, N. Yamamoto, T. Konomi, Y. Okano, M. Adachi, X. G. Jin, M. Hosaka, Y. Takashima and M. Katoh

Narrow Band Coherent Edge Radiation from UVSOR-III Storage Ring [[Light Sources](#)] 34
M. Hosaka, D. Oodake, N. Yamamoto, T. Konomi, J. Yamazaki, K. Hayashi, Y. Takashima and M. Katoh

Beam Injection with a Pulsed Multipole Magnet at UVSOR-III [[Light Sources](#)] 35
N. Yamamoto, H. Zen, M. Hosaka, M. Adachi, K. Hayashi, J. Yamazaki, Y. Takashima and M. Katoh

Performance Evaluation of Mass Production Nuclear Emulsion for 2015 Balloon-Borne Experiment [[Others](#)] 36
N. Otsuka, H. Kawahara, H. Rokujo, K. Ozaki, S. Aoki, E. Shibayama, S. Takahashi, S. Tawa, F. Mizutani, K. Yamada, Y. Tateishi, T. Kosaka and GRAINE collaboration

Development of the Backward-Illuminated Photocathode for SRF GUN [[Others](#)] 37
T. Konomi, R. Inagaki, M. Hosaka, N. Yamamoto, Y. Takashima and M. Katoh

Generation of Laser Compton Scattered Gamma-Ray Using a 1.95- μm Fiber Laser at UVSOR Facility [[1U](#), [Accelerators](#)] 38
H. Zen, Y. Taira, T. Konomi, J. Yamazaki, T. Hayakawa, T. Shizuma, T. Kii, H. Toyokawa, M. Katoh and H. Ohgaki

Observation of Light's Orbital Angular Momentum from Helical Undulator Harmonics [1U]	39
S. Sasaki, A. Miyamoto, M. Hosaka, N. Yamamoto, T. Konomi and M. Katoh	
Reconstruction of the Beamline BL2B for Development of Photoelectron Spectroscopy for Organic Materials II [2B]	40
S. Kera, K. R. Koswattage, K. Yonezawa, Y. Nakayama, K. K. Okudaira and H. Ishii	
Microbunching Instability in Relativistic Electron Bunches: Direct Observations of the Microstructures Using Ultrafast YBCO Detectors [6B, 1U]	41
E. Roussel, C. Evain, C. Szwarz, S. Bielawski, J. Raasch, P. Thoma, A. Scheuring, M. Hofherr, K. Ilin, S. Wunsch, M. Siegel, M. Hosaka, N. Yamamoto, Y. Takashima, H. Zen, T. Konomi, M. Adachi, S. Kimura and M. Katoh	
Evaluation of the VUV Coating Performed on the Flight Mirrors of the CLASP Sounding Rocket [7B]	42
N. Narukage, M. Kubo, R. Ishikawa, Y. Katsukawa, S. Ishikawa, T. Kobiki, G. Giono, R. Kano, T. Bando and S. Tsuneta	
The Improvement and Evaluation of VIS-VUV Ellipsometry [7B]	43
Y. Kubo, K. Fukui, K. Yamamoto, T. Saito and T. Horigome	
III-2. Materials Sciences	45
Terahertz Reflectivity Spectra of Superionic Conductors [1B]	47
T. Awano	
THz Spectra of Hole-Doped CeO₂Al₁₀ [1B]	48
H. Takao, S. Kamei, Y. Yamada, J. Kawabata, T. Takabatake and S. Kimura	
Local Structure Investigation around P Atom in Ag and Cu Doped Hydroxyapatite [2A]	49
M. Sato, H. Sakaguchi, Y. Inoue and A. Nakahira	
Study of Formation Processes of Active Mo Species over V-Doped Mo/H-AlGaMFI by Mo L_{III}-Edge XANES [2A]	50
H. Aritani, S. Mogi, N. Naijo, T. Sugawara, T. Kawai and A. Nakahira	
Local Environment Analysis of Mg Ions Doped in CaZrO₃:Tb [2A]	51
H. Fukaya, Y. Kubo and T. Yamamoto	
Local Structure Analysis of the Charge-Discharge Process for Conversion Reaction of the Binary Metal Oxide Containing Aluminum Ion by XAFS Measurement [2A]	52
N. Sonoyama, Y. Ogasawara, T. Mizuno and T. Tukada	
Evaluation of Local Structure of Si for Perlite Synthesized from Natural Mineral [2A]	53
A. Nakahira, S. Togo, M. Kasai, Y. Kobayashi, T. Morinaga, Y. Inoue, M. Sato and H. Aritani	
XANES Analysis of Methylene Blue Adsorbed on WO₃ Nanomaterials [2A]	54
T. Yoshida, K. Komori, M. Yamamoto, C. Tsukada, S. Yagi, M. Yajima, S. Kajita and N. Ohno	

Local Structure Investigation around P Atom in Mn Substituted LiFePO ₄ [2A] M. Sato, M. Togo, Y. Inoue and A. Nakahira	55
Structural Evaluation of Local Structure of Si for LTA-Type Zeolite from Perlite Source [2A] A. Nakahira, M. Kasai, S. Togo, Y. Kobayashi and H. Aritani	56
Studies on Electronic Structure of Aluminum Oxide Thin Film under Voltage Applied Conditions by Near-Edge X-Ray Absorption Fine Structure [2A] E. Kobayashi, K. K. Bando, O. Takahashi and T. Okajima	57
Temperature Dependence of Self-Trapped Exciton Emission and Energy Transfer in Binary Rare-Earth Borates upon Vacuum UV Excitation [3B] N. Kodama, A. Abe, M. Kudo and T. Takahashi	58
Charging States of Oxygen Vacancies in Yttria-Stabilized Zirconia Analyzed by the Decay of Photoluminescence [3B] S. Kaneko, T. Morimoto and Y. Ohki	59
Band Gap of B1-Type M _x Zn _{1-x} O (M = Mg, Mn, Fe, Co, Ni) Synthesized under High Pressures [3B] K. Takahama, K. Usui, D. Shimada, M. Kato, K. Niwa, K. Kusaba, M. Hasegawa and K. Soda	60
Energy Transfer from Tl ⁺ Centers to In ⁺ Centers in Co-Doped NaCl:Tl ⁺ , In ⁺ Crystals [3B] A. Iguchi and T. Kawai	61
Luminescence Band with a Zero-Phonon Line in NaCl:Tl ⁺ Crystals [3B] T. Kawai	62
Anomalous Excitons and Screenings Unveiling Strong Electronic Correlations in SrTi _{1-x} Nb _x O ₃ [3B] P. K. Gogoi, L. Sponza, D. Schmidt, T. C. Asmara, C. Diao, J. C. W. Lim, S. M. Poh, S. Kimura, P. E. Trevisanutto, V. Olevano and A. Rusydi	63
Ultraviolet Photoluminescence of Gd ³⁺ in Gd ³⁺ -Pr ³⁺ Co-Doped Yttrium Aluminate under Vacuum Ultraviolet Excitation [3B] K. Ueda, Y. Shimizu, A. Takiguchi, Y. Taira and Y. Inaguma	64
Excitation and Emission Spectra of Ce ³⁺ in Ba ₃ Y ₂ B ₆ O ₁₅ [3B] M. Yoshino, M. Hotta and S. Watanabe	65
Optical Spectroscopy of Nd and Cr Codoped Y ₃ Sc _x Ga _y Al _{5-x-y} O ₁₂ Single Crystals [3B] M. Yamaga, T. Kishita, S. Fujiwara, Y. Takeda and A. Ogata	66
Relaxed Exciton Luminescence of RbCl Heavily Doped with RbI [3B] N. Ohno and K. Sakae	67
Near Band Edge Absorption Spectra and Green Band Excitation Spectrum of Boron-Doped Diamond Films [3B] S. Kondou, K. Fukui, K. Yamamoto and T. Inushima	68

Optical Properties of SrCeO₃ Crystals [3B] H. Numata, M. Kitaura, S. Watanabe, S. Kurosawa, K. Yubuta and A. Ohnishi	69
VUV Absorption Spectra of Alanine Single Crystals [3B] S. Tanaka, M. Kitaura, A. Ohnishi and M. Sasaki	70
Temperature Dependence of Absorption Spectra for Ce³⁺-Doped Y₃Al₅O₁₂ Single Crystals [3B] S. Watanabe, M. Nakaya, J. Onoe, M. Kitaura, K. Kamada and A. Ohnishi	71
Two-Band Luminescence from an Intrinsic Defect in Spherical and Terraced MgO Nanoparticles [3B] P. V. Pikhitsa, C. Kim, S. Chae, S. Shin, S. Jung, M. Kitaura, S. Kimura, K. Fukui and M. Choi	72
Scanning Transmission X-Ray Microscopy Study on Fluorescence Mechanism of Nanocarbon-Silica Composites [4U] S. Kawasaki, H. Song and Y. Takeuchi	73
The Effect of Carbon Bombardment of ZnO Probed by Scanning Transmission X-Ray Microscopy [4U] Y. F. Wang, S. H. Hsieh, J. W. Chiou, W. F. Pong, T. Ohigashi and N. Kosugi	74
Chemical Redox of Mesoscopic NiO/CH₃NH₃PbI₃ Perovskite Heterojunction by Scanning Transmission X-Ray Microscopy [4U] M. W. Lin, K. C. Wang, L. T. Chang, Y. L. Lai, T. Ohigashi, N. Kosugi, P. Chen and Y. J. Hsu	75
Characterization of Monolithic Polymers Containing Nanoparticles by Scanning Transmission X-Ray Microscopy (STXM) [4U] D. Arrua, C. Desire, A. Khodabandeh, T. Ohigashi, N. Kosugi and E. Hilder	76
O K-Edge Spectroscopy of High Valence State Mn(V) Oxides [4B] Y. Aoki, T. Kobayashi, K. Kuroda, E. Tsuji and H. Habazaki	77
XANES Analysis of Valence State of Co Doped in CeO₂ [4B] T. Oomori, K. Tarui and T. Yamamoto	78
Investigation on the Surface Structure of LiNbO₃-Coated LiCoO₂ Using the Soft X-Ray XANES Measurement [4B] H. Kobayashi, T. Okumura and M. Shikano	79
Perpendicular Magnetic Anisotropy in Mn₄N Studied by X-Ray Magnetic Circular Dichroism [4B] G. Shibata, J. Okabayashi, A. Chikamatsu, A. Fujimori and T. Hasegawa	80
Investigating Orbital Magnetic Moments in Spinel-Type MnV₂O₄ Using X-Ray Magnetic Circular Dichroism [4B] J. Okabayashi, S. Miyasaka, K. Hemmi, K. Tanaka, S. Tajima, H. Wadati, A. Tanaka, Y. Takagi and T. Yokoyama	81
Study of Ultrafast Spin-Switching of a Ferrimagnetic Alloy by Resonant Magneto-Optical Kerr Effect [5B] S. Yamamoto, M. Taguchi, Y. Kubota, S. Ito, M. Hasumoto, E. Shigemasa and I. Matsuda	82
Infrared Spectroscopy of Photo-Induced Defects in Ce³⁺:GAGG Crystals [6B] R. Inaba, M. Kitaura, K. Kamada, S. Kurosawa, A. Ohnishi and K. Hara	83

Formation Mechanism of Ultrashallow Thermal Donors Formed in Carbon- and Hydrogen-Doped Czochralski Silicon Crystals [6B] A. Hara and T. Awano	84
Domain Structure of Alkali Niobate Piezoelectrics by Far-Infrared Reflective Method [6B] Y. Taniguchi, T. Yamazaki, M. Kato and K. Kakimoto	85
Spatial Distribution of Carrier Density of $\text{Sm}_{1-x}\text{Y}_x\text{S}$ ($x = 0.17$) [6B] S. Kamei, H. Takao, Y. Ohtsubo, H. Miyazaki, K. Imura, N. K. Sato and S. Kimura	86
<i>Local</i> Electron-Phonon Coupling in Organic Single Crystals: Angle-Resolved Ultraviolet Photoemission Study [7U] F. Bussolotti, J. Yang, T. Yamaguchi, Y. Nakayama, H. Ishii, M. Matsunami, N. Ueno and S. Kera	87
Valence Band Dispersion of the Pentacene Single Crystal [7U] Y. Nakayama, M. Yamamoto, Y. Mizuno, M. Matsunami, H. Ishii and N. Ueno	88
Angle-Resolved Photoemission Study on Quasi-One Dimensional Organic Conductor $(\text{TMTTF})_2\text{PF}_6$ [7U] T. Ito, M. Mitamura, H. Horikawa, T. Hajiri, S. Kimura and T. Nakamura	89
Carrier Concentration Dependence of Superconducting Gap of $\text{Bi}_{1.7}\text{Pb}_{0.4}\text{Sr}_2\text{Ca}_{1-x}\text{Y}_x\text{Cu}_2\text{O}_{8+\delta}$ [7U] H. Sakamoto, A. Yamamoto and T. Takeuchi	90
Angle-Resolved Photoemission Study of Heusler-Type $\text{Fe}_2\text{V}_{1+x}\text{Al}_{1-x}$ Alloys [7U] H. Miyazaki, K. Ando, W. Nagasaka and Y. Nishino	91
Angle-Resolved Photoemission Spectroscopy of YbB_{12} (001) Surface [7U] K. Hagiwara, J. Kishi, Y. Ohtsubo, H. Miyazaki, T. Ito, M. Matsunami, F. Iga and S. Kimura	92
Quadratic Fermi Node in a 3D Strongly Correlated Semimetal [7U] T. Kondo, M. Nakayama, R. Chen, J. J. Ishikawa, E.-G. Moon, W. Malaeb, Y. Ishida, M. Matsunami, S. Kimura, S. Nakatsuji, L. Balents and S. Shin	93
ARPES Study on the Stripe-Ordered $(\text{La}, \text{Nd}, \text{Sr})_2\text{CuO}_4$ Superconductor [7U] K. Tanaka, M. Matsunami, S. Miyasaka and S. Tajima	94
ARPES Studies of Hydrogen Exposed MoS_2 [7U] S. Cho, B. Kim, B. Kim, Y. Kim, Y. Koh, J. Seo, J. Kwon, M. Matsunami, K. Tanaka, S. R. Park and C. Kim	95
Non-Uniform Temperature-Dependent Band Shift of an Iron Pnictide Superconductor LiFeAs [7U] T. Hajiri, T. Ito, M. Matsunami, B. H. Min, Y. S. Kwon, K. Kuroki and S. Kimura	96
Angle Resolved Photoemission Spectroscopy of Iron Pnictide Superconductor $\text{NdFeP}_{1-x}\text{As}_x(\text{O}, \text{F})$ [7U] A. Takemori, S. Miyasaka, M. Uekubo, T. Kobayashi, S. Tajima, T. Hajiri, M. Matsunami and K. Tanaka	97

Polarization Dependent ARPES Study on Iron-Based Superconductor $K_xFe_{2-y}Se_2$ [7U]	98
M. Sunagawa, K. Terashima, M. Tanaka, H. Takeya, Y. Takano, K. Suzuki, H. Usui, K. Kuroki, T. Wakita, Y. Muraoka and T. Yokoya	
CD-ARPES Studies on Rashba & Dresselhaus Effects [7U]	99
W. Jung, S. Cho, Y. Kim, B. Kim, J. Seo, J. Kwon, M. Matsunami, K. Tanaka, S. R. Park and C. Kim	
Electronic Structures and Reflectance Spectra of $AZnF_3$ (A=Na, K, Rb) Single Crystals [7B]	100
S. Ishii, S. Tanaka, A. Yamaji, S. Tanaka, S. Kurosawa, S. Watanabe, M. Kitaura, A. Ohnishi and M. Sasaki	
Luminescence and Scintillation Properties of CdF_2 Crystal [7B]	101
T. Yanagida, Y. Fujimoto, M. Koshimizu and K. Fukuda	
Reflection Spectra of Ternary Zinc Bismuth Phosphate Glasses in the Ultraviolet Region [7B]	102
N. Kitamura	
Control of Spectral Response Using Compound Fluoride Materials $Ca_xSr_{1-x}F_2$ [7B]	103
S. Otani, H. Ishikawa, M. Yanagihara and S. Ono	
Optical Spectroscopy of $Ba(Fe_{1-x}Co_x)_2As_2$ in Vacuum-Ultraviolet Energy Region [7B]	104
M. Nakajima, S. Miyasaka and S. Tajima	
Influence of Niobium Concentration on the Reflection Spectra for Ternary Niobium Bismuth Phosphate Glasses [7B]	105
N. Kitamura, K. Fukumi, Y. Hisano, N. Hirao, S. Tuji, A. Uchiyama and H. Kozuka	
Ultraviolet Photoelectron Spectra of $Ce_2@C_{80}$ and $La_2@C_{80}$ [8B]	106
T. Miyazaki, S. Okita, T. Ohta, H. Yagi, R. Sumii, H. Okimoto, Y. Ito, H. Shinohara and S. Hino	
III-3. Chemistry	107
Induced Chirality by Circularly Polarized UV Light for Photofunctional Organic/Inorganic Hybrid Materials [1U]	109
T. Akitsu, N. Sunaga, N. Ishida, M. Ito, T. Konomi and M. Kato	
Photoionization Study of Helium Atoms Using Variable Polarization Undulator [1U]	110
T. Kaneyasu, Y. Hikosaka, T. Konomi, M. Katoh, H. Iwayama and E. Shigemasa	
In Situ Soft X-Ray Absorption Spectroscopy Applied to Solid-Liquid Heterogeneous Cyanopyrazine Hydration on Titanium Oxide Catalyst [3U]	111
H. Yuzawa, M. Nagasaka and N. Kosugi	
Electronic Structure of Interfacial Water on Nanodiamonds in Colloidal Dispersions [3U]	112
T. Petit, H. Yuzawa, M. Nagasaka, R. Yamanoi, E. Osawa, N. Kosugi and E. F. Aziz	

Fluorination-Dependent Molecular Orbital Occupancy in Perfluorocarbons [3U] T. Brandenburg, T. Petit, A. Neubauer, K. Atak, M. Nagasaka, R. Golnak, N. Kosugi and E. F. Aziz	113
Local Structures of Liquid Benzene Studied by Temperature-Dependent C K-Edge Soft X-Ray Absorption Spectroscopy [3U] M. Nagasaka, H. Yuzawa, K. Mochizuki, E. Rühl and N. Kosugi	114
Optimization of the Sample Position of the Liquid Thin Layer for Soft X-Ray Absorption Spectroscopy [3U] M. Nagasaka, H. Yuzawa, T. Horigome and N. Kosugi	115
Detection of Intra- and Inter-Molecular Charge Transfer in Solution by N K-Edge X-Ray Absorption Spectroscopy [3U] R. Golnak, J. Xiao, M. Tesch, M. Yablonskikh, M. Nagasaka, T. Brandenburg, N. Kosugi and E. F. Aziz	116
Electrochemical Studies at BL4U STXM [4U] S. M. Rosendahl, A. P. Hitchcock, M. Nagasaka, Y. F. Wang, T. Horigome, T. Ohigashi and N. Kosugi	117
Stability of Molecular Dications Studied by an Electron-Electron-Ion Coincidence Method [4B] K. Nakamura, R. Mashiko, K. Soejima, E. Shigemasa and Y. Hikosaka	118
Dissociation of CH₃OH Dication Studied by an Electron-Ion Coincidence Method [6U] M. Higuchi, T. Shirota, K. Hoshina, H. Iwayama, E. Shigemasa and Y. Hikosaka	119
Spectator Auger Decays of 1, 1, 1-Trifluoroethane across the F K Threshold [6U] T. Kaneda, K. Okada, H. Iwayama and E. Shigemasa	120
Specific Auger Decay and Photofragmentation of <i>cis</i>-Hexafluorocyclobutane [6U] S. Ishikawa, K. Okada, H. Iwayama and E. Shigemasa	121
Ultrafast Dissociation of Core Excited CF₄ Molecules Studied by an Auger-Electron-Ion Coincidence Method [6U] H. Iwayama and E. Shigemasa	122
III-4. Surface, Interface and Thin Films	123
An Optimization Study for Multi-Alkali Photocathode as the Ultimate Electron Source [2B] M. Kuriki, Y. Seimiya, T. Konomi, M. Katoh and R. Inagaki	125
Electronic Structure of Chlorophyll-a Investigated by Photoelectron Spectroscopy and Photoelectron Yield Spectroscopy [2B] Y. Takeda, H. Ezawa, T. Miyauchi, H. Kinjo, K. R. Koswattage, Y. Nakayama and H. Ishi	126
Cobalt-Borate Oxygen Evolution Catalyst Studied by Electrochemical XAFS Technique Using Soft X-Ray [3U] Y. Mitsutomi, M. Yoshida, T. Mineo, M. Kawamura, M. Nagasaka, H. Yuzawa, N. Kosugi and H. Kondoh	127

STXM Analysis of Adsorbent for Effective Recovery of Radioactive Elements [4U] Y. Sano, S. Watanabe, H. Matsuura and A. Nezu	128
XMCD Study on Magnetic Multilayer of CoNi₂ on W(110) [4B] T. Yasue, M. Suzuki, T. Nakagawa, K. Takagi, T. Yokoyama and T. Koshikawa	129
XMCD Study of Anisotropic Magnetism of Fe/W(112) [4B] K. Yamaguchi, T. Kawashima, S. Mizuno and T. Nakagawa	130
X-Ray Magnetic Circular Dichroism Study of Mn- and Fe-Phthalocyanine Molecules Self-Assembled on the Si(111)-(√7×√3)-In Surface [4B] T. Uchihashi and S. Yoshizawa	131
Magnetic Properties of Ordered Iron Nitride Monatomic Layer [4B] T. Miyamachi, Y. Takahashi, Y. Takagi, M. Uozumi, T. Yokoyama and F. Komori	132
Magnetism of Oxygen Covered Fe Monolayer on Mo(110) [4B] T. Nakagawa, Y. Higuchi, K. Yamaguchi, S. Mizuno, Y. Takagi and T. Yokoyama	133
Characterization of Amorphous Chalcogenide Thin Films by Vacuum Ultraviolet Transmission Spectroscopy [5B] K. Hayashi	134
Phase-Dependent Electronic Structure of Superstructure Monolayer of Hexa-<i>peri</i>-Hexabenzocoronene on Au(111) [6U] H. Yamane and N. Kosugi	135
Formation of Delocalized π Band and Interface State in Superstructure Monolayer of Coronene on Au(111) [6U] H. Yamane and N. Kosugi	136
Manybody Interactions in Rb-Doped Graphene [6U] W. J. Shin, S. H. Ryu, H. Yamane, N. Kosugi, K. S. Kim and H. W. Yeom	137
Surface Coordination Chemistry to Control the Charge Transfer at Organic/Metal Interface: SnCl₂Pc on Ag(111) [6U] S. Kera, K. Yonezawa, T. Tago, F. Bussolotti, H. Yamane, N. Kosugi and K. K. Okudaira	138
Electronic Structure of a MnSe/Bi₂Se₃ Ultrathin Film Heterostructure [7U] T. Hirahara, T. Kubo, A. Takayama, T. Hajiri, M. Matsunami, K. Tanaka and S. Hasegawa	139
Angle-Resolved Photoelectron Spectroscopy Study of One-Dimensional Electronic States on Bi/InSb(001) [7U] Y. Ohtsubo, J. Kishi, K. Hagiwara, M. Matsunami, K. Tanaka and S. Kimura	140
Formation of the Dirac Cone at the Γ-Point on the Epitaxial Graphene Sheet Observed by the Angle-Resolved Photoelectron Spectroscopy with the Low Energy Photon [7U] S. Tanaka, T. Maruyama, M. Matsunami and K. Tanaka	141
Inelastic Scattering of Photoelectrons at Organic/Graphite Interface [7U] T. Yamaguchi, F. Bussolotti, J. Yang, K. Kimura, M. Matsunami, N. Ueno and S. Kera	142

Direct Observation of Electronic Structure of Nylon-6,6 to Clarify the Contact Electrification Mechanism [8B]	143
T. Sato, K. R. Koswattage, Y. Nakayama and H. Ishii	
Investigation of Charge-Transfer Interaction by Metal Deposition on Organic Semiconducting Thin Films [8B/2B]	144
T. Hosokai, K. Yonezawa, R. Makino, K. R. Koswattage, K. K. Okudaira and S. Kera	
Life and Planetary Sciences	145
 Quantitative Penetration Profiles of Free and Nanocarrier-Bound Dexamethasone in Human Skin Studied by Soft X-Ray Spectromicroscopy [4U]	147
K. Yamamoto, T. Ohigashi, Y. F. Wang, S. Hedtrich, F. Rancan, R. Flesch, A. Klossek, E. Fleige, S. Ahlberg, A. Vogt, U. Blume-Peytavi, P. Schrade, S. Bachmann, R. Haag, M. Schäfer-Korting, N. Kosugi and E. Rühl	
Evaluation of Sample Damage of XANES and Application to the Analysis of Carbonaceous Materials in Hayabusa-Returned Samples [4U]	148
M. Uesugi and A. Nakato	
Absorption Spectra of Bio-Cell Organelles in Cultural Fluid [4U]	149
T. Ejima, M. Kado, M. Aoyama, K. Yasuda and T. Tamotsu	
Evaluation of FIB Beam Damage in XANES Spectra of Organics in Meteorites: Preliminary Measurements for Implementation Planning of a Synchrotron Cosmochemistry Research Base at UVSOR BL4U [4U]	150
H. Yabuta, A. Takahashi, Y. Inagaki and T. Ohigashi	
Chemical Mapping of DNA and Protein in Isolated Cell Nuclei during Apoptotic Process Using STXM [4U]	151
A. Ito, T. Ohigashi, K. Shinohara, S. Tone, M. Kado, Y. Inagaki and N. Kosugi	
Observation of Prokaryotic Organelles of Musty-Odor Producing Filamentous Cyanobacterium Using STXM [4U]	152
K. Takemoto, M. Yoshimura, T. Ohigashi and H. Kihara	
Skin Penetration Study of Drug Carriers Using Soft X-Ray Spectromicroscopy [4U]	153
P. Pan-In, T. Ohigashi, N. Kosugi and S. Wanichwecharungruang	
IV. List of Publications	155
V. Workshops	161
UVSOR Symposium 2014	163

UVSOR User 1

